

Experimental and numerical study of chloride induced corrosion in reinforced concrete

Von der Fakultät Bau- und Umweltingenieurwissenschaften
der Universität Stuttgart zur Erlangung der Würde
eines Doktor-Ingenieurs (Dr.-Ing.)
genehmigte Abhandlung

Vorgelegt von
Emiliano Sola
aus Segni, Rom, Italien

Hauptberichter: Prof. Dr.-Ing. habil. Joško Ožbolt
Mitberichter: Prof. Dr.-Ing. Christoph Gehlen
Mitberichter: Prof. Dr.-Ing. Gojko Balabanić
Mitberichter: Prof. Dr.-Ing. Jan Hofmann

Tag der mündlichen Prüfung: 05.10.2017

Institut für Werkstoffe im Bauwesen der Universität Stuttgart

2017

ABSTRACT

Chloride-induced corrosion is considered as one of the major concern for durability of reinforced concrete (RC) structures. Especially vulnerable, are structures located in coastal marine environment or highways and garages treated with de-icing salts during winter seasons (Tuutti, 1993; Cairns, 1998). Consequences of chloride-induced corrosion of steel reinforcement have negative effects on structural behavior and involve several aspects related to the life cycle of the structure, such as serviceability, safety and structural performance. Direct and indirect costs of maintenance and repair are relatively high and constitute nowadays a huge economic exertion. Therefore, challenging task is to develop and improve a numerical tool, which can realistically predict corrosion processes and the related mechanism of deterioration in RC structures, supporting the service life prediction of damaged and undamaged structures.

The main objective of the present work is to validate the recently developed 3D Chemo-Hygro-Thermo-Mechanical model for concrete by means of an extensive experimental program, which includes tests under natural and laboratory controlled conditions. The comparison between numerical and experimental results is significantly important in order to quantitatively calibrate the parameters responsible for the computation of corrosion rate and distribution of rust in pores and cracks. To better describe the problem, hysteretic moisture behaviour is coupled with the transport of corrosion products in cracks and a relationship between diffusivity of corrosion compounds and crack width is proposed.

It has been demonstrated experimentally that the production of corrosion compounds are strongly dependent on the environmental conditions and presence of chemical reactants. Therefore, type of corrosion products and corresponding distribution are in the present work investigated on concrete thin section by means of microscope analysis and Raman spectroscopy.

Computation of corrosion rate and related corrosion induced damage is directly related to the assumed position of anode and cathode on the reinforcement surface and currently there is no algorithm which can predict the combination between anode and cathode surfaces that results to the highest corrosion induced damage. To investigate this influence, the expression for maximum entropy production, deduced from irreversible thermodynamics, is formulated. The entropy is considered produced by dissipative processes, which are in this special case the flow of ions through the electrolyte, the anodic and cathodic polarization and the diffusion oxygen process. Through several numerical examples, in which the size and position of anodic and cathodic surfaces are varied, is demonstrated that maximum entropy leads to maximum corrosion induced damage.

KURZFASSUNG

Die durch chloridinduzierte Korrosion verursachte Schädigung von Stahlbetonkonstruktionen ist eine der größten Einflussgrößen auf die Dauerhaftigkeit von Stahlbetonbauwerken. Besonders gefährdet sind Bauwerke, die sich in küstennaher Meeresumgebung befinden, oder Autobahnen und Parkdecks, die im Winter mit Tausalz behandelt werden (Tuutti, 1993; Cairns, 1998). Die chloridinduzierte Korrosion der Stahlbewehrung hat negative Folgen auf das Verhalten der Bauteile und beeinflusst verschiedene Aspekte im Zusammenhang mit der Lebensdauer der Konstruktion wie Gebrauchstauglichkeit, Sicherheit und Tragfähigkeit. Die Folgen der Korrosion zeigen sich am deutlichsten an Rissen und Abplatzungen, die durch die Ausdehnung der Korrosionsprodukte entstehen, die ein größeres Volumen als der Stahl haben. Da die direkten und indirekten Kosten der Wartung und Instandsetzung sehr hoch sind, ist es wichtig numerische Tools zu entwickeln, die die Korrosionsprozesse und die damit zusammenhängenden Mechanismen der Schädigung der Bauteile realistisch vorhersagen können.

Die vorliegende Arbeit stellt die Verifizierung und Kalibrierung des 3D Chemo-Hygro-Thermo-Mechanischen Modells (CHTM) dar. Aus diesem Grund, wurden experimentelle Versuche unter beschleunigten und natürlichen Bedingungen durchgeführt. Der Vergleich zwischen numerischen und experimentellen Ergebnissen ist wichtig, um die Parameter, die für die Berechnung der Korrosionsrate und der Rostverteilung in Poren und Rissen verantwortlich sind, quantitativ zu kalibrieren. Um das Problem besser zu beschreiben, wird ein hysteretisches Feuchtemodell für Beton mit dem Transport des Rosts in den Rissen gekoppelt und eine Relation zwischen der Diffusionsfähigkeit von Korrosionsprodukten und der Rissbreite vorgeschlagen.

Es wurde experimentell gezeigt, dass die Herstellung von Korrosionsprodukten stark von den Umgebungsbedingungen und der Anwesenheit von chemischen Reaktanten abhängig ist. Daher werden in der vorliegenden Arbeit die Art und die entsprechende Verteilung der Korrosionsprodukte auf Betondünnschnitten mittels Mikroskop-Analyse und Raman-Spektroskopie untersucht.

Die Berechnung der Korrosionsrate, und der damit verbundenen Korrosionsschäden, hängt direkt von der angenommenen Position der Anode und Kathode auf der Bewehrungsfläche ab. Allerdings gibt es derzeit keinen Algorithmus, der die Kombination von Anoden- und Kathodenoberflächen, die zu der höchsten korrosionsinduzierten Schädigung führt, voraussagen kann. Um diesen Einfluss zu untersuchen, wird die Gleichung der maximalen Entropieproduktion, abgeleitet von der irreversiblen Thermodynamik, formuliert. Die Entropie lässt sich aus der Summe von dissipativen Prozessen berechnen, die in diesem speziellen Fall aus der Strömung von Ionen durch den Elektrolyt, der anodischen und kathodischen Polarisation und dem

Diffusions-Sauerstoff-Prozess bestehen. Durch mehrere numerische Beispiele, bei denen die Größe und die Position von anodischen und kathodischen Oberflächen variiert wird, wird gezeigt, dass maximale Entropie zu maximaler Korrosionsschädigung führt.

ACKNOWLEDGEMENTS

In the first place, I would like to express my sincere gratitude to my advisor Prof. Ožbolt for giving me this opportunity, for the continuous support of my Ph.D study and related research, for his patience, motivation, and immense knowledge. His guidance helped me all the time of research and writing of this thesis. I could not have imagined having a better advisor and mentor for my Ph.D study.

Apart from work, Professor Ožbolt used to provide me with valuable career advice. He took the role of a mentor and helped me shape my career by providing valuable advices and mentoring. I am highly grateful to him in this regard.

Furthermore, I would like to thank Prof. Gojko Balabanić, for the contribution to my thesis, for the interesting challenging topics proposed during these years as well as for the support in the implementation of new formulations.

I am very much thankful to Prof. Christoph Gehlen and Prof. Jan Hofmann for kindly accepting to be the co-reporters of the thesis and for the comments which have contributed to the final form of the here presented work.

I am very grateful to the group of colleagues and friends which supported me on the time spent at IWB. Prof. Akanshu Sharma and Dr. Baris Irhan introduced me to working with MASA, CIF and Femap. Their help on technical and theoretical topics was very much appreciated.

I owe a very special thanks to Dr. Josipa Bosnjak for helping me in the organization of the very extensive experimental program planned in the framework of my Ph.D and for the experimental investigations on the compact tension specimens. She was not only a co-worker, but she devoted time to help me also in the private life, giving continuous support and valuable advices.

I would like to express my gratitude to Dr. Filip Orsanic for introducing me in the modelling of corrosion, in programming new features and for all the time spent together. He continued to give me advices also after the time spent at IWB. It was nice to have him as colleague and friend.

The evaluation of the test results was constantly supported by student assistants. In special case I would like to express my gratitude to Zahid Mohammad Mir for his kind and patient help, especially in the preparation of the challenging test program as well as evaluation of the numerical analysis.

I am very thankful also to Marina Stipetic for her friendship and the kind help in the basement. It has been a pleasure to work with Natalja Bede, Vinay Mahadik and Hitesh Lakhani.

The friendship of Kaipei Tian was very much appreciated, he is an example of politeness and fairness.

I am very grateful to Silvia Choynacki. She helped me to improve my german skills and she always had helpful tips about the working and non-working life during my stay in Stuttgart.

Evaluation and interpretation of my experimental tests was much easier with the help of Prof. Christian Fischer, who had always time to describe his point of view and shared with me many details of his research.

Monika Werner was extremely helpful with the literature review and she found every book and paper I needed. Thomas Rauscher always had time for a technical discussion in the framework of corrosion.

Kind help of Gerard Bahr, in building up the test setup of my experimental test is greatly acknowledged. I would also like to thank all the rest of the IWB staff (Simone Stumpp, Gisela Baur, Regina Jäger, Olga Weber) for their help on all administrative issues.

I enjoyed the nice discussions with Dr. Tobias Schmidt about working problems and non-working life. He always offered his hand to help me in my private life and helped me to improve my German.

Looking to the Italian staff of the IWB, I would like to thank Dr. Serena Gambarelli for the time spent together in Stuttgart, for her help and friendship as well as the enjoyable conversations in my native language.

I would like to thank my family: my parents Domenico and Ida and my brothers Giuseppe and Fabio for supporting me spiritually throughout writing this thesis and my life in general.

Last, but not the least, I express my deepest gratitude to my friend, my colleague and wife Daniela Ruta. She was from the first to the last day here with me at IWB sharing working and private life. This work could not be possible without her support and advices. This thesis is dedicated to her and to our son Flavio.

Stuttgart, 11.12.2016

CONTENTS

| | | |
|--------------|---|---------------|
| 1 | INTRODUCTION | 1 |
| 1.1 | Motivation, problem statement and context of the research..... | 1 |
| 1.2 | Research objectives..... | 3 |
| 1.3 | Scope of the work..... | 4 |
| 2 | LITERATURE REVIEW | 5 |
| 2.1 | Corrosion of reinforcement in concrete | 5 |
| 2.1.1 | Electrochemical kinetics..... | 7 |
| 2.1.2 | Chloride induced corrosion..... | 10 |
| 2.2 | Basics of reinforcement corrosion in concrete | 13 |
| 2.2.1 | Hysteretic moisture behaviour of concrete | 13 |
| 2.2.2 | Electrolytic resistivity of concrete | 16 |
| 2.2.2.1 | Experimental determination of electrolytic resistivity of concrete | 17 |
| 2.2.2.2 | Influence of moisture and <i>w/c</i> ratio on concrete resistivity..... | 18 |
| 2.2.2.3 | Influence of chlorides and cement type on concrete resistivity..... | 19 |
| 2.2.3 | Influence of oxygen on corrosion of steel in concrete | 20 |
| 2.2.4 | Corrosion products characterization | 21 |
| 2.2.5 | Corrosion products distribution..... | 23 |
| 2.2.5.1 | Penetration of corrosion products in pores and voids | 23 |
| 2.2.5.2 | Ingress of corrosion products in cracks..... | 25 |
| 2.3 | Experimental tests | 27 |
| 2.3.1 | Accelerated corrosion tests | 27 |
| 2.3.1.1 | Corrosion current density influence | 27 |
| 2.3.1.2 | Relationship between corrosion penetration and corrosion induced damage | 32 |
| 2.4 | Modelling corrosion of reinforcement in concrete | 34 |
| 2.4.1 | Empirical models..... | 36 |
| 2.4.2 | Mathematical models..... | 37 |
| 2.4.3 | Probabilistic models..... | 39 |
| 3 | EXPERIMENTAL INVESTIGATIONS | 40 |
| 3.1 | Objectives of the experimental program | 40 |
| 3.1.1 | Description of the specimens..... | 40 |
| 3.1.2 | Casting and concrete properties..... | 41 |
| 3.1.3 | Epoxy coating | 44 |
| 3.2 | Performed accelerated corrosion tests..... | 46 |
| 3.2.1 | Environmental exposure..... | 47 |
| 3.2.2 | Cracks evolution monitoring..... | 48 |

| | | |
|----------|--|-----------|
| 3.2.3 | Mass and cross-sectional loss | 48 |
| 3.3 | Preliminary experimental test results at different level of applied potential..... | 50 |
| 3.3.1 | Conclusions | 52 |
| 3.4 | Accelerated corrosion tests on reinforced concrete cylinders with different dimensions | 53 |
| 3.4.1 | Imposed electric potential and environmental exposure | 53 |
| 3.4.2 | Results of the experimental tests..... | 54 |
| 3.4.2.1 | Test results for the specimen type A: A/8, A/12 and A/16 – wetting/drying exposure | 54 |
| 3.4.2.2 | Test results for the specimen type A: A/8, A/12 and A/16 – submerged specimens..... | 61 |
| 3.4.2.3 | Test results for the specimen type B: B/8, B/12 and B/16 – wetting/drying exposure | 65 |
| 3.4.2.4 | Test results for the specimen type B: B/8, B/12 and B/16 – submerged specimens..... | 69 |
| 3.4.2.5 | Test results for the specimen type C: C/8, C/12 and C/16 – wetting/drying exposure | 71 |
| 3.4.2.6 | Test results for the specimen type C: C/8, C/12 and C/16 – submerged specimens..... | 74 |
| 3.5 | Characterization and distribution of corrosion products in pores and cracks | 77 |
| 3.5.1 | Microscope analysis and Raman spectroscopy | 77 |
| 3.5.1.1 | Microscope analysis and Raman spectroscopy results: specimens MR-1 and MR-2..... | 79 |
| 3.5.1.2 | Microscope analysis and Raman spectroscopy results: specimens MR-3, MR-4 and MR-5 | 82 |
| 3.6 | Summary of the experimental results | 86 |
| 4 | CHEMO-HYGRO-THERMO-MECHANICAL MODEL (CHTM MODEL) | 88 |
| 4.1 | Non-mechanical processes before depassivation of reinforcement..... | 89 |
| 4.1.1 | Transport of capillary water | 88 |
| 4.1.2 | Transport of oxygen | 90 |
| 4.1.3 | Transport of chloride ions | 91 |
| 4.1.4 | Heat transfer in concrete..... | 92 |
| 4.2 | Non-mechanical processes after depassivation of reinforcement..... | 93 |
| 4.2.1 | Oxygen consumption | 93 |
| 4.2.2 | Flow of electric current through electrolyte..... | 94 |
| 4.2.3 | Polarization of anode and cathode | 95 |
| 4.2.4 | Rate of rust production and distribution of corrosion products..... | 96 |
| 4.3 | Hysteretic moisture model for concrete | 97 |
| 4.3.1 | Moisture transport | 97 |

| | | |
|----------|--|------------|
| 4.3.2 | Water vapour permeability..... | 98 |
| 4.3.3 | Empirical model for determining the scanning curves..... | 99 |
| 4.3.4 | Chloride convective diffusion..... | 100 |
| 4.4 | Chemo-Hygro-Thermo-Mechanical coupling..... | 103 |
| 4.4.1 | Microplane model with relaxed kinematic constraint | 103 |
| 4.4.2 | One-dimensional corrosion contact elements | 105 |
| 4.4.3 | Numerical implementation..... | 106 |
| 4.5 | Entropy production in corrosion processes of steel reinforcement in concrete..... | 108 |
| 4.5.1 | Energy dissipation analysis..... | 108 |
| 5 | VALIDATION OF THE 3D CHTM MODEL: ACCELERATED CORROSION AT DIFFERENT LEVEL OF IMPOSED POTENTIAL..... | 111 |
| 5.1 | Specimen C/8 at different level of imposed potential..... | 111 |
| 5.1.1 | Numerical model | 111 |
| 5.1.2 | Numerical results under accelerated corrosion conditions (preliminary tests) | 113 |
| 5.1.3 | Numerical results under natural conditions | 117 |
| 5.1.4 | Conclusions | 119 |
| 6 | VALIDATION OF THE 3D CHTM MODEL: INVESTIGATION OF REINFORCED CONCRETE CYLINDERS WITH DIFFERENT DIMENSIONS | 120 |
| 6.1 | Validation of the transport of corrosion products against experimental test..... | 120 |
| 6.1.1 | Objectives of the numerical simulations | 120 |
| 6.1.2 | Numerical model | 121 |
| 6.1.3 | Penetration of the corrosion products in cracks: diffusivity dependency on crack width and water content | 122 |
| 6.2 | Results of the numerical simulations | 125 |
| 6.2.1 | Numerical results for the specimen type A: A/8, A/12 and A/16 – wetting/drying exposure | 125 |
| 6.2.1.1 | Prediction of corrosion current density and model parameters | 125 |
| 6.2.1.2 | Crack pattern and development of the corrosion induced damage | 127 |
| 6.2.1.3 | Hysteretic moisture behaviour and distribution of relative humidity..... | 129 |
| 6.2.1.4 | Distribution of the corrosion products..... | 132 |
| 6.2.2 | Numerical results for the specimen type A: A/8, A/12 and A/16 – submerged specimens | 135 |
| 6.2.2.1 | Corrosion current density and model parameters..... | 135 |
| 6.2.2.2 | Crack pattern and development of the corrosion induced damage | 136 |
| 6.2.2.3 | Distribution of the corrosion products..... | 138 |

| | | |
|----------|--|------------|
| 6.2.3 | Numerical results for the specimen type B: B/8, B/12 and B/16 – wetting/drying exposure | 140 |
| 6.2.3.1 | Prediction of corrosion current density and model parameters | 140 |
| 6.2.3.2 | Crack pattern and development of the corrosion induced damage | 142 |
| 6.2.3.3 | Hysteretic moisture behaviour and distribution of relative humidity | 144 |
| 6.2.3.4 | Distribution of the corrosion products | 145 |
| 6.2.4 | Numerical results for the specimen type B: B/8, B/12 and B/16 – submerged specimens | 148 |
| 6.2.4.1 | Corrosion current density and model parameters..... | 148 |
| 6.2.4.2 | Crack pattern and development of the corrosion induced damage | 149 |
| 6.2.4.3 | Distribution of the corrosion products | 151 |
| 6.2.5 | Numerical results for the specimen type C: C/8, C/12 and C/16 – wetting/drying exposure | 152 |
| 6.2.5.1 | Prediction of corrosion current density and model parameters | 152 |
| 6.2.5.2 | Crack pattern and development of the corrosion induced damage | 154 |
| 6.2.5.3 | Hysteretic moisture behaviour and distribution of relative humidity | 156 |
| 6.2.5.4 | Distribution of the corrosion products | 158 |
| 6.2.6 | Numerical results for the specimen type C: C/8, C/12 and C/16 – submerged specimens | 160 |
| 6.2.6.1 | Corrosion current density and model parameters..... | 160 |
| 6.2.6.2 | Crack pattern and development of the corrosion induced damage | 161 |
| 6.2.6.3 | Distribution of the corrosion products | 162 |
| 6.3 | Summary of the numerical results | 164 |
| 6.4 | Conclusions..... | 166 |
| 7 | ENTROPY PRODUCTION IN CORROSION PROCESSES OF STEEL REINFORCEMENT IN CONCRETE: NUMERICAL EXAMPLE | 167 |
| 7.1 | Objectives of the numerical applications | 167 |
| 7.1.1 | Numerical case study: Multi-rebar RC beam | 167 |
| 7.1.2 | Results and discussion | 171 |
| 7.2 | Conclusions..... | 176 |
| 8 | CONCLUSIONS AND OUTLOOK | 177 |
| | BIBLIOGRAPHY | 180 |

LIST OF INDICES

Literature review

| | |
|---------------|---|
| $E_{0,Fe}$ | standard equilibrium potential |
| $E_{eq,Fe}$ | thermodynamically reversible potential |
| R | universal gas constant |
| T | absolute temperature |
| F | Faraday's constant |
| z | valence of the metal ion |
| $a_{Fe^{2+}}$ | activity of the ferrous cation |
| E_{0,O_2} | standard equilibrium potential of oxygen reduction |
| $\prod[Ox]$ | product of the activities of the species (LHS) |
| $\prod[Red]$ | product of the activities of the species (RHS) |
| ν | stoichiometric coefficient of the species |
| i_0 | exchange current density |
| i | current density |
| η | overpotential |
| α | transfer coefficient |
| E_{eq} | equilibrium potential |
| E | potential |
| β | Tafel slope |
| β_a | Tafel slope for anodic reaction |
| β_c | Tafel slope for cathodic reaction |
| i_L | limiting current density |
| i_c | cathodic current density |
| D_o | oxygen diffusivity coefficient |
| C_o | oxygen concentration |
| n | outward normal to the cathodic surface |
| C_{ob} | oxygen concentration at the external boundary surface |

| | |
|---------------------|---|
| i_{0c} | cathodic exchange current density |
| w/c | water/cement ratio |
| σ | electrical conductivity of concrete |
| w_i | crack width on concrete surface |
| x_{corr} | corrosion penetration |
| $V_{r/s}$ | expansion factor of the corrosion product |
| V_{eff} | effective expansion factor |
| k_{st} | factor related to the effect of stirrups |
| w_{max} | maximum surface crack width |
| x_{aver} | average attack penetration |
| r_0 | initial steel bar radius |
| α_f, β_f | experimental parameters |
| c | concrete cover |
| d | reinforcement diameter |
| f_{ct} | average tensile strength of concrete |
| Cl | free chloride content |
| R_ϵ | ohmic resistance of concrete |
| t | corrosion time |
| C_{Cl} | chloride content |
| i_{rate} | corrosion rate |
| t_{cr} | cracking time |
| Q_{cr} | critical amount of corrosion products |
| t_p | time for depassivation of reinforcement |
| t_{cor} | time needed to damage the concrete cover |
| j_r | rate of rust production per unit of area |
| Δd | increase of diameter due to rust production |
| R_{pa} | anodic polarization resistance |
| R_{pc} | cathodic polarization resistance |
| R_s | steel resistivity |

| | |
|------------------|---|
| R_c | concrete resistivity |
| $\Phi_{eq,a}$ | anodic equilibrium potential |
| $\Phi_{eq,c}$ | cathodic equilibrium potential |
| Φ | electric potential |
| r | resistivity of the pore solution |
| n_{el} | direction normal to the equipotential lines |
| M | model factor |
| F_{Cl} | correction factor for chloride concentration |
| F_{Galv} | correction factor for macro-galvanic effects |
| F_{O_2} | correction factor for oxygen availability |
| Δr_s | increase of steel radius due to rust production |
| K_C | model factor for corrosion induced damage |
| K_R | model factor for time dependent behaviour |
| K_S | model factor for rebar spacing |
| $\Delta r_{r,A}$ | analytical resistance |
| Δr_r | resistance of the structure |
| pf | probability of structural failure |

Chemo-Hygro-Thermo-Mechanical (CHTM) model for concrete

| | |
|------------------|------------------------------------|
| \mathbf{j}_w | specific water discharge |
| θ_w | volume fraction of pore water |
| \mathbf{v}_w | mean water velocity |
| K_w | unsaturated hydraulic conductivity |
| ψ | capillary potential |
| D_w | water diffusivity |
| ρ_w | density of water |
| D_{lm} | limiting magnitude |
| $\bar{\theta}_w$ | reduced water content |
| θ_{wi} | initial water content |

| | |
|-----------------------|--|
| θ_{wd} | saturated water content |
| $\mathbf{j}_{o,diff}$ | macroscopic diffusive flux of oxygen |
| $\mathbf{j}_{o,conv}$ | macroscopic convective flux of oxygen |
| \mathbf{j}_o | macroscopic total flux of oxygen |
| h | relative humidity |
| p_{cp} | porosity of hardened cement paste |
| p_c | concrete porosity |
| a/c | aggregate/cement ratio |
| ρ_c | density of cement |
| ρ_a | density of aggregate |
| \mathbf{j}_c | total mass flux of chloride ions |
| C_c | concentration of free chloride in pore solution |
| D_c | chloride diffusion coefficient |
| C_{cb} | concentration of bound chlorides |
| k_r | binding rate coefficient |
| α_b | constant – chloride binding process |
| $D_{c,ref}$ | reference value of D_c at standard conditions |
| U | activation energy of chloride diffusion process |
| λ | thermal conductivity |
| c | heat capacity per unit mass of concrete |
| W | internal source of heating |
| Q | number of oxygen molecules reduced per unit surface of cathode and per unit time |
| j_o^c | oxygen diffusion flux at the cathode surface |
| j_o^a | oxygen diffusion flux at the anode surface |
| k_c | constant (stoichiometry of electrochemical reactions at cathode) |
| k_a | constant (stoichiometry of electrochemical reactions at anode) |
| i_a | current density at the anode surface |
| j_{fh} | rate of $\text{Fe}(\text{OH})_2$ production |

| | |
|----------------|--|
| \mathbf{j}_i | vector of flux of ions |
| \mathbf{i} | vector of the electric current density |
| i_{0a} | exchange current density at anodic surface |
| i_{0c} | exchange current density at cathodic surface |
| A_r | surface of steel reinforcement |
| J_r | rate of rust production |
| m_r | mass of hydrated red rust |
| Δt | time interval |
| R | corrosion products per volume of pore solution |
| D_r | corrosion products diffusion coefficient |

Hysteretic moisture behaviour of concrete

| | |
|-----------------------|--|
| u | water to dry mass of concrete ratio |
| w | moisture content w per volume of concrete |
| m_{wet} | weight of concrete specimen before drying |
| m_{dry} | weight of concrete specimen after drying |
| $\mathbf{j}_{w,mass}$ | vector of the moisture flux |
| δ_v | water vapour permeability |
| $p_{v,sat}$ | water vapour saturation pressure |
| ξ | moisture capacity |
| β_{hum} | surface humidity transfer coefficient |
| h_s | relative humidity at the exposed concrete surface |
| h_{env} | relative humidity of the ambient air |
| a_o | reference permeability at 25 °C |
| f_l | moisture transfer within the adsorbed water layers |
| h_c | transition humidity |
| ϑ | temperature |
| $\xi_{hys,a}$ | moisture capacity scanning curves (adsorption) |
| $\xi_{hys,d}$ | moisture capacity scanning curves (desorption) |

| | |
|--------------------------------|---|
| ξ_a | moisture capacity adsorption isotherm |
| ξ_d | moisture capacity desorption isotherm |
| w_a | moisture contents calculated from main adsorption curve |
| w_d | moisture contents calculated from main desorption curve |
| w_0 | initial moisture content |
| Δh | change in the relative humidity |
| $\mathbf{j}_{c,diff}$ | vector of the diffusive flux of chloride ions |
| $\mathbf{j}_{c,conv}$ | vector of the convective flux of chloride ions |
| $\mathbf{j}_{w,vol}$ | vector of the specific water discharge |
| σ | stress |
| ε | strain |
| σ_V | volumetric component of the microplane stress |
| σ_D | deviatoric component of the microplane stress |
| σ_N | normal component of the microplane stress |
| σ_K, σ_M | shear components of the microplane stress |
| ε_V | volumetric component of the microplane strain |
| ε_D | deviatoric component of the microplane strain |
| ε_N | normal component of the microplane strain |
| $\varepsilon_K, \varepsilon_M$ | shear components of the microplane strain |
| ε_{ij} | total strain tensor |
| ε_{ij}^m | mechanical strain |
| ε_{ij}^T | thermal strain |
| ε_{ij}^w | hygro strain |
| ε_{ij}^{corr} | strain due to expansion of corrosion products |
| E | macroscopic E modulus |
| ν | Poisson's coefficient |
| f_c | macroscopic compressive strength |
| f_t | macroscopic tensile strength |

| | |
|--------------|---|
| G_F | macroscopic fracture energy (tension) |
| S | surface area of the unit radius sphere |
| Δl_r | inelastic radial expansion due to corrosion |
| ρ_r | density of rust |
| ρ_s | density of steel |
| E_r | stiffness of the rust layer |
| m_s | mass of steel |
| r | ratio mass of steel / mass of rust |

Entropy production in corrosion processes of steel reinforcement in concrete

| | |
|---------------------|---|
| \dot{Q} | specific energy dissipation rate in the corrosion cell |
| \dot{Q}_{diff} | volumetric energy dissipation rate due to oxygen diffusion |
| \dot{Q}_{ohm} | energy dissipation rate due to the flow of ions through the electrolyte |
| $\dot{Q}_{polar,a}$ | energy dissipation rate due to the polarization of the anode |
| $\dot{Q}_{polar,c}$ | energy dissipation rate due to the polarization of the cathode |
| i_{na} | normal component of the electric current density at the anode surface |
| i_{nc} | normal component of the electric current density at the cathode surface |
| \dot{Q}_v | total rate of energy dissipation in a given volume of corrosion cell and electrode surfaces |
| V | volume of corrosion cell |
| A_a | anodic surface |
| A_c | cathodic surface |
| ξ | spatial coordinates |

1. INTRODUCTION

1.1 Motivation, problem statement and context of the research

Durability of concrete is defined by the American Concrete Institute as its ability to resist weathering action, chemical attack, abrasion or any other process of deterioration. The degradation mechanisms in concrete structures include physical effects and chemical effects. The most important physical effects come from abrasion and mechanical loads. On the other side, chemical effects are consequence of alkali aggregates reactions, microbiological induced attack, sulfate attack and corrosion of steel in reinforced concrete, which itself is subdivided into carbonation and chloride induced corrosion.

In particular, chloride-induced corrosion is considered as one of the major concern for durability of reinforced concrete (RC) structures. Especially vulnerable, are structures located in coastal marine environment or highways and garages treated with de-icing salts during winter seasons (Tuutti, 1993; Cairns, 1998). Consequences of chloride-induced corrosion of steel reinforcement have negative effects on structural behavior and involve several aspects related to the life cycle of the structure, such as serviceability, safety and structural performance. The main effect of the corrosive attack is manifested as cracking and spalling, due to the expansion of the corrosion products which have a greater volume than the original steel (see Fig. 1.1).



Fig. 1.1 Examples of deteriorating bridge elements (Yunovich et al., 2001)

Direct and indirect costs of maintenance and repair, are relatively high and constitute nowadays a huge economic exertion. In a recent corrosion cost study (Koch et al., 2002), the annual direct cost of corrosion on US highway bridges was estimated at 8.3 billion Dollars overall, with 4.0 billion Dollars of that on the capital cost and maintenance of reinforced concrete highway bridge decks and substructures (Broomfield, 2002). In

Germany a total amount of 120 million Euros in 2004 were needed for the maintenance of highway bridges damaged due to chloride induced corrosion (Jacob, 2008).

As chloride-induced corrosion is one the major cause of deterioration of RC structures, and especially bridges, deterioration prediction models of corrosion process in structural elements is essential for an efficient management of the structures. Therefore, challenging task is to develop and improve a numerical tool, which can realistically predict corrosion processes and the related mechanism of deterioration in RC structures, supporting the service life prediction of damaged and undamaged structures. Moreover, employing such a model is useful to formulate simple engineering models and design rules in order to increase the durability of structure and reduce its maintenance costs.

Principally, the calculation of corrosion current density requires modeling of the following physical, electrochemical and mechanical processes: (1) Transport of capillary water, oxygen and chloride through the concrete cover; (2) Immobilization of chloride in the concrete; (3) Crystallization and dissolution of free chloride as a consequence of drying and wetting of concrete as well as related hysteretic property of concrete; (4) Transport of OH^- ions through electrolyte in concrete pores; (5) Cathodic and anodic polarization; (6) Transport of corrosion products in concrete and cracks, (7) Creep and shrinkage of concrete and (8) Damage of concrete due to mechanical and non-mechanical actions.

Currently, there are a number of models in literature, which are able to simulate processes before and after depassivation of reinforcement in uncracked concrete (Tuutti, 1993; Bažant, 1979a; Glass and Buenfeld, 2000). For such computational models to be considered as realistic, chemo-hygro-thermo-mechanical processes have to be coupled with mechanical processes, and also vice versa. Presently, there are only a limited number of coupled 3D chemo-hygro-thermo-mechanical models capable to realistically predict corrosion process in cracked concrete (Ožbolt et al., 2010, 2011; Marsavina et al., 2009; Ishida et al., 2008). Furthermore, moisture behavior coupled with transport of corrosion products in cracked concrete and its effect on the corrosion-induced damage so far has not been addressed by any model, i.e. the existing models do not account for the transport of water and solution species that are involved in the process of corrosion.

However, the main problem in defining such models is quantifying controlling parameters for processes before and after depassivation. Therefore, additional theoretical and experimental work is needed on this subject.

Consequently, the main objective of this study is to validate the recently developed 3D Chemo-Hygro-Thermo-Mechanical model for concrete by means of an extensive experimental program, which includes tests under natural and laboratory controlled conditions. Particular attention is paid in characterizing the parameters of the hysteretic moisture model as well as the concrete conductivity. Moreover, based on the experimental results, computation of current density could be validated.

The comparison between numerical and experimental results, at this stage of the model development, is also important in order to quantitatively calibrate the parameters responsible for the distribution of rust in pores and cracks. In the here presented work, the hysteretic moisture behaviour is coupled with the transport of corrosion products in cracks and a relationship between diffusivity of corrosion compounds and crack width is proposed.

Further on, currently there is no algorithm which can predict the combination between anode and cathode surfaces on reinforcement that results to the highest corrosion induced damage. Therefore, to investigate this influence the expression for maximum entropy production, deduced from irreversible thermodynamics, is formulated. The entropy is produced by dissipative processes, which are in this special case the flow of ions through the electrolyte, the anodic and cathodic polarization and the diffusion oxygen process. Through several numerical examples, in which the size and position of anodic and cathodic surfaces are varied, is demonstrated that maximum entropy leads to maximum corrosion induced damage.

Finally, the model and the proposed improvements are validated for every geometry examined in the experimental tests, under laboratory controlled conditions and in natural environment. However, experimental tests under natural conditions are still underway and will be used to more accurately calibrate the model parameters and better highlight the differences between natural and accelerated corrosion.

1.2 Research objectives

1. Improve the 3D chemo-hygro-thermo-mechanical (CHTM) model in order to realistically predict the corrosion processes and the related mechanism of deterioration in RC structures.
2. Perform experimental investigation on RC specimens of different sizes under accelerated and natural conditions.
3. Account for the transport of capillary water in concrete and cracks in the CHTM model.
4. Validate the mechanical and non-mechanical processes in the CHTM model against the experiments.
5. Numerically investigate the influence of water content and concrete conductivity on current density and crack pattern through series of parametric studies.
6. Analyse the influence of concrete cover and reinforcement size on the corrosion induced damage

7. Validate and quantitatively calibrate the transport of corrosion products in the CHTM model.
8. Investigate the size and position of the anodic and cathodic regions which maximize the corrosion induced damage.
9. Investigate the influence of an imposed electrical potential on corrosion induced damage, by comparing with natural corrosion conditions.

1.3 Scope of the work

This research aims to investigate the effect of chloride induced corrosion of steel reinforcement on the mechanical behavior of RC structures, with particular reference to the physical, electrochemical and mechanical processes. By means of the CHTM model, rate of rust production and related effects on the RC structures have been studied.

Following the comparison between FE analyses and experiments results, in accelerated and natural conditions, the influence of the concrete cover and bar diameter was investigated. Experimental tests, under controlled laboratory conditions, were performed to validate the CHTM model and to provide a better insight into the controlling parameters used in the physical and electrochemical processes of the above mentioned model.

The study focuses also on the factors which influence the non-mechanical processes in presence of cracks due to reinforcement corrosion and using experimental methods. Furthermore, the influence of the position and size of anode and cathode on crack pattern and the corrosion rate, high challenging task from the experimental point of view, is numerically studied.

2. LITERATURE REVIEW

2.1 Corrosion of reinforcement in concrete

Corrosion can be caused by carbonation of the concrete cover or by reaching a critical concentration of free chloride ions in the vicinity of the reinforcement bar. Under normal conditions the steel reinforcement in concrete is in contact with pore solution, which has generally a high alkalinity. This is sufficient to generate an insoluble surface film of ferric oxides on the reinforcement. Under these conditions the steel reinforcement is passivated and the protection layer prevents it from corroding. However, during their life, structures could be exposed to several deterioration processes which reduce the alkalinity of the pore solution and allow the penetration of above mentioned aggressive agents. Generally, the value of pH of concrete cement paste is between 12.6 and 13.5 and the insolubility of the protective layer is preserved, as can be seen in Fig. 2.1 in which the domain of immunity, passivity and corrosion of iron in solution is described in the diagram equilibrium potential-pH (Pourbaix, 1966).

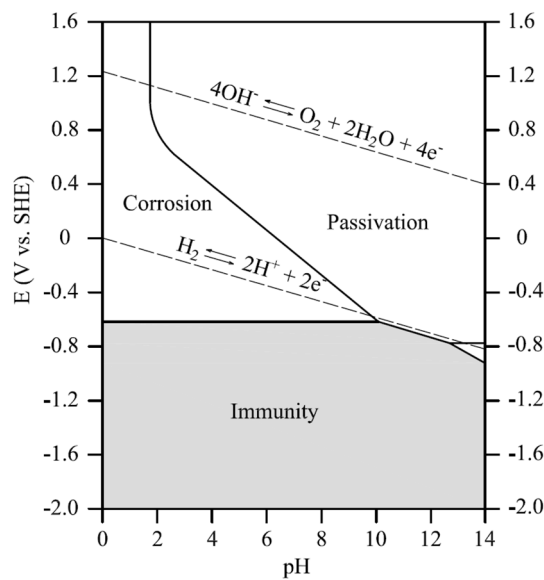
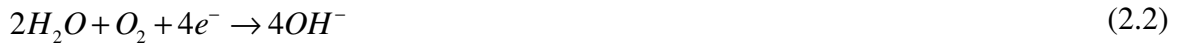


Fig. 2.1 Simplified Pourbaix diagram for iron in water at 25°C (Pourbaix, 1966)

If the protective layer is damaged (see Fig. 2.2a) or depassivated, the corrosion of reinforcement can be activated. Corrosion of steel in concrete is an electrochemical process with two half-cell reactions. (i) At the anodic site, electrons are produced, i.e. iron is oxidized to form ferrous ions (Fig. 2.2b):



Free electrons are consumed by oxygen at the cathodic site in presence of water (Fig. 2.2b) and form hydroxyl ions OH⁻:



The hydroxyl ions react with the ferrous ions (Fig. 2.2c) forming the ferric(II)-hydroxide:

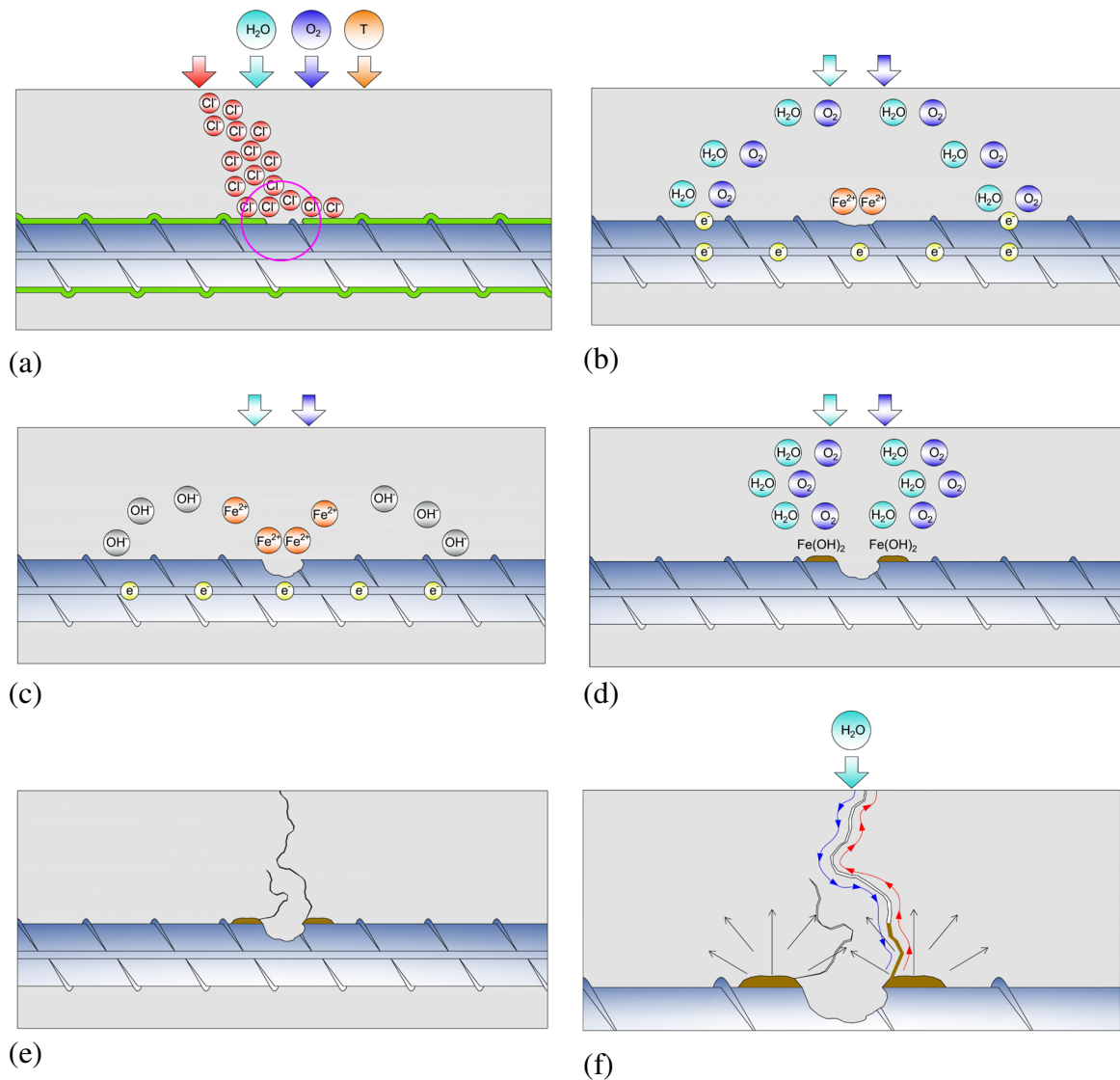


Fig. 2.2 Corrosion in concrete: depassivation of reinforcement because of chlorides (a); forming of ferrous and hydroxyl ions (b); forming of the ferric(II)-hydroxide (c); production of iron(III)-oxide (d); cracking of concrete cover (e) and transport of corrosion products (f)

Further reactions and production of corrosion products depend on the environmental conditions and available chemical reactants. One of the possible occurring reactions is the production of iron(III)-oxide or red rust (Fig. 2.2d) in the presence of oxygen and water:



Considering that the specific volume of the corrosion products is greater than the normal steel, corrosion induced cracks are formed in the surrounding concrete because of the pressure due to the volume increase (Fig. 2.2e). The expansion of the formed rust is highly influenced from the presence of pores and voids in concrete and the effectiveness of the products expansion is highly dependent on their diffusion through concrete itself. Moreover, it was recently demonstrated by means of experimental tests (Molina et al., 1993; Wong et al., 2010; Fischer, 2012) that corrosion products can migrate/diffuse not only in pores and voids but also in cracks (Fig. 2.2f) and that their transport is also influenced from wetting/drying cycles and corresponding entrance of outer solution (Zhao et al., 2012a). Because of this effect, it is generally noted a slowing of the corrosion damage in time.

2.1.1 Electrochemical kinetics

Generally, steel in electrolyte is in equilibrium with its ions (Fe^{2+}) according to the ferrous ions half-cell reaction (Eq. (2.1)). In such conditions, steel has an equilibrium potential ($E_{eq,Fe}$), in which the rate of oxidation is equal to the rate of reduction and the above equation is possible in both directions (Stern & Geary, 1957). In these conditions, of thermodynamic equilibrium, there is no corrosion, since there is no dissolution of ferrous ions. The potential that steel has in these conditions is called thermodynamically reversible potential which can be calculated with the equation of Nernst (Shreir et al., 1994):

$$E_{eq,Fe} = E_{0,Fe} + \frac{RT}{zF} \ln(a_{Fe^{2+}}) \quad (2.5)$$

where $a_{Fe^{2+}}$ is the activity or thermodynamic concentration of the ferrous cation, $E_{0,Fe}$ is the standard equilibrium potential (that for the ferrous ion is -0.440 V vs. the standard hydrogen electrode), R is the universal gas constant, T the temperature, F the Faraday constant, z the valence of the metal ion.

At the same time, the half-cell reaction at the cathodic site (see Eq. (2.2)) can be expressed by means of the Nernst equation in a more general way, considering that oxygen and hydrogen are involved in both sides of the reaction, i.e. the “oxidized side” and “the reduced side” (Stansbury & Buchanan, 2000). The equation can be written as:

$$E_{eq,O_2} = E_{0,O_2} + \frac{RT}{zF} \ln \frac{\Pi[Ox]^v}{\Pi[Red]^v} \quad (2.5)$$

in which E_{0,O_2} is the standard equilibrium potential of oxygen reduction, $\Pi[Ox]^v$ and $\Pi[Red]^v$ are the product of the activities of the species on the left and right side of the reaction, respectively. The stoichiometric coefficient of the species is represented by v .

Current density in equilibrium condition is commonly called exchange current density (i_0). If potential is different from that of equilibrium, electric current is generated. The Butler-Volmer equation is the central equation which describes the electrode kinetics, which gives the current density i as a nonlinear function of the overpotential η (Böckris et al., 2000):

$$i = i_0 \left[\exp\left(\frac{\alpha z F \eta}{RT}\right) - \exp\left(\frac{-(1-\alpha) z F \eta}{RT}\right) \right] \quad (2.6)$$

where

$$\eta = E - E_{eq} \quad (2.7)$$

α is the transfer coefficient, which describes how the electric potential alters the activation energy barrier of the reaction.

It has to be noted that the Butler-Volmer equation can be considered valid when the electrode reaction is controlled by electrical charge transfer at the electrode and not by the mass transfer from the electrode surface to the bulk electrolyte and vice versa. On the other hand when the electrode process is mass-transfer controlled, the value of the current density is equal to the limiting current density (Böckris et al., 2000).

Chemical reactions, including electrochemical reactions, involve energy barriers which must be overcome by the reacting species. This energy barrier is called the “activation energy” and results in activation or charge-transfer polarization, which is due to the transfer of charges between the electronic and the ionic conductors. The activation polarization may be regarded as the extra potential necessary to overcome the energy barrier of the rate-determining step of the reaction to a value such that the electrode reaction proceeds at a certain rate. Under high activation polarization, the first exponential term (Eq. (2.6)) is much greater than the second term, and the latter can be excluded from the equation (Chan et al., 2001). Rearranging the simplified equation yields:

$$E - E_{eq} = \frac{RT}{\alpha z F} \ln \frac{i}{i_0} = \frac{2.303RT}{\alpha z F} \log \frac{i}{i_0} = \beta \log \frac{i}{i_0} \quad (2.8)$$

which is well known as Tafel equation, where β is the Tafel slope.

In other words, the relationship between current density and surface overpotential is linear for small values of overpotential and for large values the current density varies exponentially (Newman & Thomas-Alyea, 2012) that in semi-log scale is a curve with the slope β_a e β_c , known as Tafel slope for anodic and cathodic reaction, respectively.

As mentioned above, corrosion of steel in partially saturated concrete is considered as a cathodically controlled (Broomfield, 2002), because the process is mass-transfer controlled. In this way, the cathodic sites on the steel surface can polarize through activation polarization and concentration polarization (Warkus et al., 2006; Kranc & Sagüés, 2001; Gulikers & Raupach, 2006; Isgor & Razaqpur, 2006a). The concentration polarization occurs when oxygen that is consumed by the cathodic reaction (Eq. (2.2)) cannot be replaced adequately in order to sustain the oxygen reduction process. In this situation the current density of the electrochemical process is controlled by a limiting current density i_L (Poursaee, 2016), as follows:

$$E - E_{eq,O_2} = \beta_c \log \frac{i_c}{i_{0c}} - \frac{2.303RT}{zF} \log \frac{i_L}{i_L - i_c} \quad (2.9)$$

where i_c is the cathodic current density and i_{0c} is the exchange current density of the cathodic reaction. The first term on the right hand side represents the activation polarization and the second one, the concentration polarization component. The limiting current density i_L , in the case when oxygen arriving at the cathode is instantaneously consumed, can be expressed as (Oršanić, 2015):

$$i_L = zFD_o \left. \frac{\partial C_o}{\partial n} \right|_{cathode} \quad (2.10)$$

where D_o is the oxygen diffusivity coefficient, C_o is the oxygen concentration per volume of pore water and n is the normal to the cathode surface.

As can be noted the limiting current density is proportional to the oxygen concentration on the electrode surface directly related to the oxygen diffusivity dependent on water content and cover thickness. When the limiting current density is large (high oxygen concentration) the concentration polarization approaches to unity (Gulikers, 2005) and the cathodic polarization is mainly controlled by activation polarization.

Another approach was proposed by Kranc & Sagüés (2001), which tried to incorporate the concentration polarization into Butler Volmer equation in a simplified way:

$$E - E_{0,O_2} = \frac{\beta_c}{2.303} \log \left(\frac{i_c}{i_{0c}} \frac{C_{ob}}{C_o} \right) \quad (2.11)$$

In which C_{ob} is the oxygen concentration at the external boundary surface. This relation, however, is overly simplistic. Among various shortcomings, the relation fails to reflect the asymptotic nature of the curve at limiting current density i_L , an important characteristic of the current density-potential curve for cathodic reaction.

2.1.2 Chloride induced corrosion

Structures located in coastal marine environment or highways and garages treated with de-icing salts during winter seasons have to be considered very exposed to chloride-induced corrosion (Tuutti, 1993; Cairns, 1998), whose main consequences have negative effects on structural behavior and involve several aspects related to the life cycle of the structure, such as serviceability, safety and structural performance. Chlorides that reach the concrete surface, transported through non-saturated concrete are generally modeled as a result of convection, diffusion and chemically binding by cement hydration product (Bear & Bachmat, 1991; Ožbolt et al., 2010) and are strongly influenced by the hysteretic moisture behaviour of concrete (Oršanić, 2015; Ožbolt et al., 2016). As discussed in Martín-Pérez (1999), when a partially-saturated concrete surface is being wet, the water is quickly absorbed through capillary suction bringing with itself dissolved chloride ions. During dry periods, the water at the surface evaporates leaving the chloride ions behind in the concrete pore solution. Due to these two phenomena (wetting/drying of concrete), the concentration of chlorides will be fluctuating near the concrete surface and will reach a maximum value some millimeters inside the concrete. Because of these observations, Tuutti (1993) made a distinction between a convection zone and a diffusion zone in the concrete cover as illustrated in Fig. 2.3.

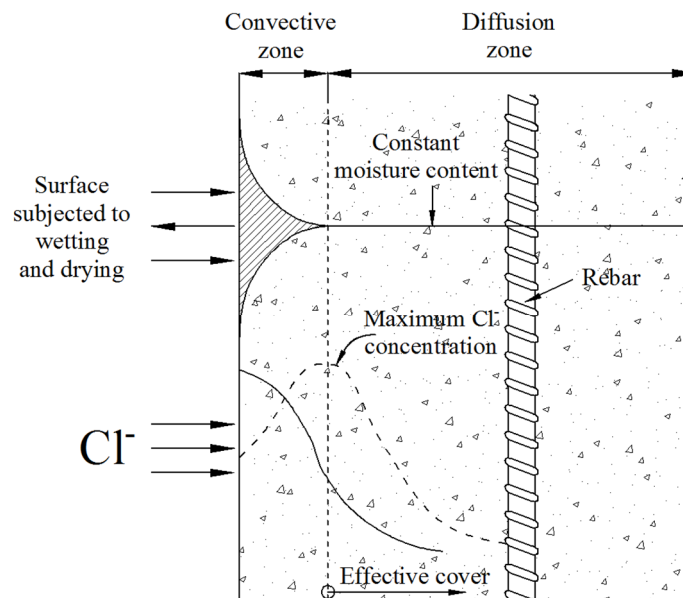


Fig. 2.3 Moisture and chloride variation in the concrete cover of structures subjected to cycles of wetting and drying (Tuutti, 1993)

Whereas a diffusion model is applicable to concrete with a constant moisture level (diffusion zone), the transport of chloride ions due to water flow has to be considered for the outer part where moisture conditions vary with time (convection zone). The depth of the convection zone depends on the concrete quality and exposure conditions (Andrade & Alonso, 1996). As can be seen, exposure to wetting and drying cycles can result in characteristic “peak” chloride profiles along the concrete depth (Saetta et al., 1993; Polder & Peelen, 2002; Fenaux, 2013), with the peak value of the total chloride content being translated away from the exposed surface progressively with the wet/dry cycling. The experimental results obtained by Polder & Peelen (2002) were also numerically predicted by Ožbolt et al. (2016) showing that the exposure to wetting and drying conditions is one of the governing mechanisms for obtaining characteristic peak shapes of the chloride profiles along the concrete depth. The increase of the w/c ratio is followed not only by a more prominent translation of the profile peak, but also leads to higher values of the total chloride content along the whole depth. Furthermore, it was shown that the extent of the chloride ingress during the wetting phase is highly dependent on the convective component of the transport process and on the other hand, in drying condition, the relatively low RH affects not only the convective, but also the diffusive contribution to the total chloride flux which has in this period a stronger influence pushing the chlorides and the profile peak even further inside

In general, when the chloride concentration exceeds 0.4% by weight of cement (for chlorides cast into concrete) or 0.2% (for chlorides diffusing in) active corrosion is observed (Apostolopoulos et al., 2013; Angst et al., 2009; Papadakis, 2000; Shi et al., 2012). According to different spatial location of anode and cathode, corrosion of steel in concrete can occur in different forms (Raupach et al., 2014): (i) as microcells, where anodic and cathodic reactions are immediately adjacent, leading to uniform iron dissolution over the whole surface, which is generally caused by carbonation of the concrete cover or by very high chloride content at the rebars and (ii) as macrocells, where a net distinction between corroding areas of the rebar (anode) and non-corroding, passive surfaces (cathode) is found.

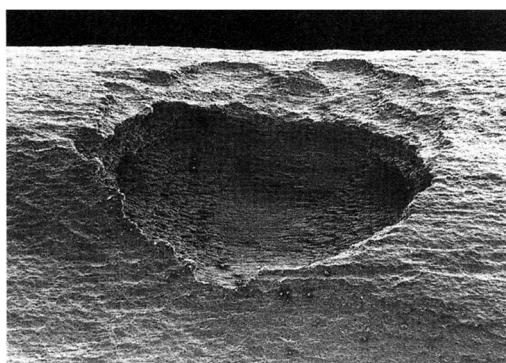


Fig. 2.4 Pitting at a locally depassivated place - individual corrosion pit (Nürnberger, 1995)

Macrocells occur mainly in case of chloride induced corrosion, known as pitting (see Fig. 2.4), in which generally the anode is very small with respect to the total (passive) rebar surface. According to Eq. (2.1), at the anodic site ferrous ions are formed and the electrons given up by the anode, flow to the cathode (passivated surface) where they are discharged in the cathodic reaction as in Eq. (2.2). As a result of these reactions the electrolyte enclosed in the pit gains positive electrical charge in contrast to the electrolyte surrounding the pit, which becomes negatively charged.

The positively charged pit attracts negative ions of chloride Cl^- increasing acidity of the electrolyte according to the reaction:



In this way, the pH value of the electrolyte inside the pit decreases (acidity increases) from 6 to 2-3, which causes further acceleration of corrosion process. Large ratio between the anode and cathode areas favors increase of the corrosion rate.

2.2 Basics of reinforcement corrosion in concrete

As already mentioned mechanical and transport properties of concrete strongly influence the mechanical and non-mechanical processes before and after depassivation having effects on the crack initiation time and on the development of the corrosion induced damage. In particular, most of the processes related to corrosion in concrete are strongly dependent on water/cement ratio (w/c) and moisture content. The water content, and its dynamic changes in time related to the hysteretic behaviour, influences the distribution of chloride ions and oxygen as well as electrical conductivity of concrete and distribution of corrosion products in pores and cracks.

2.2.1 Hysteretic moisture behaviour of concrete

Moisture hysteresis refers to the phenomenon that at the same relative humidity, the material experiences a different degree of moisture saturation or level of moisture content depending on its loading history (Derluyn et al., 2012). The difference in moisture content at the same relative humidity for cement or concrete during repeated cycles of adsorption and desorption under isothermal conditions is illustrated by different authors (De Belie et al., 2010; Anderberg and Wadsö, 2004; Baroghel-Bouny, 2007a; Maruyama and Igarashi, 2010). With the change of the environmental relative humidity (RH), the relative pore pressure is correspondingly changing and hence, affecting the water content in the concrete pores. Unsaturated conditions in concrete specimens have a strong influence on the distribution of chlorides. Convective flux of chloride ions due to moisture transport becomes more dominant compared to a slower, diffusive flux (Ožbolt et al., 2016). Therefore, the ingress of chlorides is more pronounced compared to the chloride attack under saturated conditions (Ababneh et al., 2003).

Numerous experiments on concrete and cement pastes were also performed for different level of relative humidity, in order to highlight the fundamental aspects of the phenomenon. The hysteretic moisture behavior, sorption data for the specific structural concrete and the main adsorption and desorption curves as well as some intermediate scanning curves were investigated at constant temperature by different authors. (Powers & Brownard, 1946; Feldman & Sereda, 1964; Hansen, 1986; Anderberg, 2004; Baroghel-Bouny, 2007; Nielsen, 2007). Although, it is very difficult to find detailed literature data for different concrete types and only several experimental results are available on cement pastes or mortars. This is consequence of time consuming experiments which require also very elaborate testing procedure and experimental settings, or specific test setup to carry out faster tests.

The connection between moisture content and relative humidity at equilibrium at a constant temperature is called sorption isotherm or simply isotherm. Equilibrium established during drying gives a desorption isotherm and equilibrium established during wetting gives an adsorption isotherm (see Fig. 2.5a). Different equilibrium conditions of

the two curves can be reached by changing of state from desorption or adsorption following the curves ABC or DEF, as can be seen in Fig. 2.5b, which are called scanning curves (Hansen, 1986).

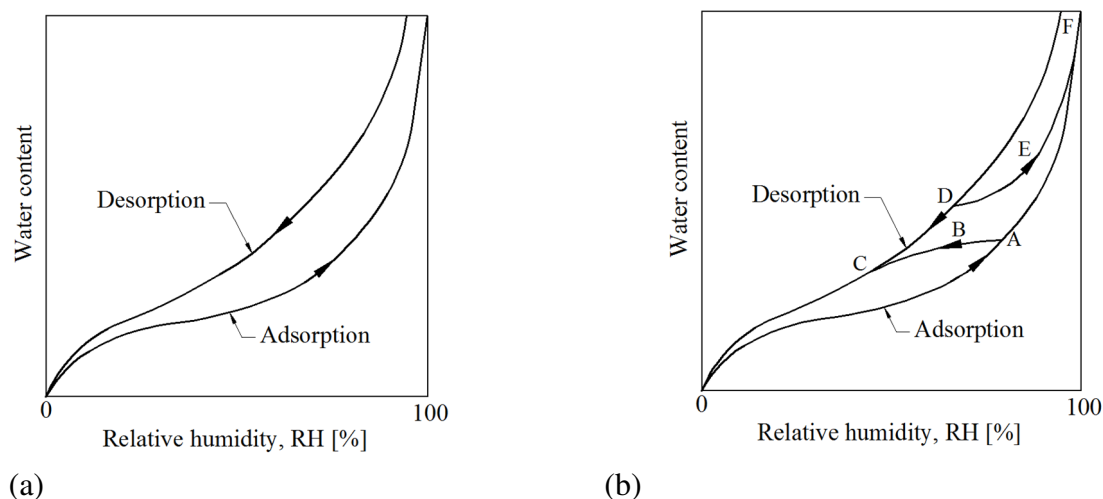


Fig. 2.5 Typical adsorption and desorption isotherms (a) and example of scanning curves (b) for building materials (Hansen, 1986)

In the literature, researchers proposed different theories to explain and model the sorption hysteresis. It has to be noted that in the hydrated cement paste, water can be present in different states: chemically bonded water, interlayer water, adsorbed water and capillary water (Mertens, 2009). Chemically bonded water is part of the microstructure of the various cement hydration products and cannot be lost during normal drying but is released during extreme heating. Interlayer water is water that is associated with the calcium silicate hydrates (C-S-H) structure and is removed only after extreme drying (<11% of relative humidity, RH). Under the influence of attractive forces, water molecules are physically adsorbed onto the surface of solid phase in the hydrated cement paste. Capillary water in the hydrated paste can be divided into free water in large voids and water held by capillary forces in so called capillary pores.

The process when water molecules are accumulating on a surface is called adsorption and the thin film formed is called an adsorbate. The opposite process is called desorption, when water molecules are released from the surface to the dry air. An example of monolayer adsorption is the Langmuir theory (1916), multilayer adsorption theories includes the (BET) Brunauer - Emmett - Teller theory (Brunauer et al., 1938). Later, it has been suggested that maximum five (Bažant et al., 1997) or six (Mehta, 1986) molecular layers of water can be physically held by hydrogen bonding or van der Waals forces.

Many studies tried to investigate the behaviour of moisture in concrete by adopting physical adsorption theory and condensation theory. As proposed by Hansen (1986), at low relative humidity RH (which represents the relative humidity of the gaseous phase in

equilibrium with the interstitial liquid phase in the pore network of the material) water molecules are bound in one layer to the surface of the concrete pores (see Figs. 2.6 and 2.7). When all the surfaces of pores are covered with one layer of molecules, the building of the next layer starts and the transition can be noted by the fact the curve is straight. Capillary condensation is the last mechanism that takes place.

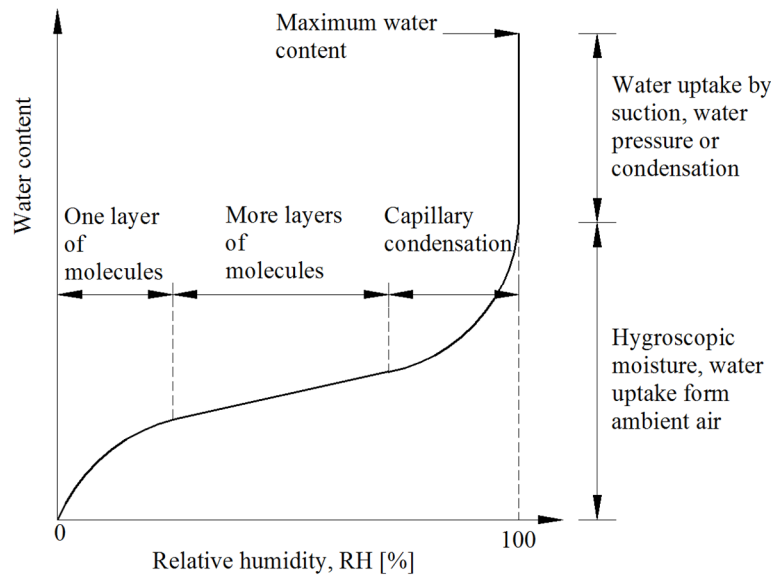


Fig. 2.6 Typical equilibrium moisture curve or sorption isotherm (Hansen, 1986)

Capillary condensation (see Figs. 2.7) starts when the molecular adsorbed water layers in the finest pores alter to a more stable energy arrangement forming menisci between the liquid water and the gas phase (Mertens, 2009).

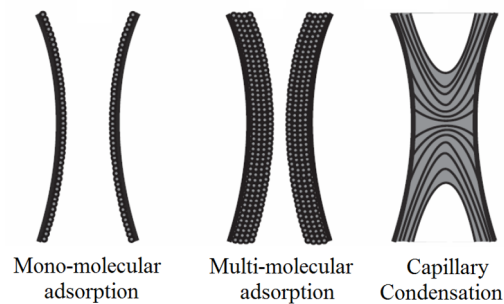


Fig. 2.7 Sorption processes at increasing relative humidity (RH): adsorption and capillary condensation (Van Den Abeele et al., 2002)

The saturation water vapour pressure above curved surfaces decreases depending on the curvature of the meniscus as expressed in Kelvin equation (Broekhoff, 1969). This means that at a given RH all the pores with a certain radius will be filled with water. On the other hand, a high saturated porous media in dry conditions presents fully filled pores at the surface which lose water molecules to the air whose consequence is the development of menisci and the relative decrease of hydrostatic pressure. Correspondingly forming of air

in the pores can then become greater than the volume needed to maintain the minimum critical stable radius. The menisci will break, at lower RH than the value of its forming, when the saturation pressure above the concave pore radius is less than the actual vapor pressure (Åhs, 2007).

The difference in terms of interface between liquid – vapour interface in capillary condensation and capillary evaporation yield to the conclusion that the hysteretic behaviour of concrete is directly related to the “ink-bottle effect” which is the reason of the pronounced hysteresis which can be noted between the phase of capillary condensation and capillary evaporation, as can be seen in Fig. 2.5a,b. Interpretation on the base of this effect is the assumption that moisture trapped in “ink-bottle” shaped pores brings higher water content in the drying phase than that in wetting and that this effect disappear ad temperature rises or as humidity decreases because of the stability of moisture trapped in the “ink-bottle” shaped pores related to the chemical potential of internal water molecules (Maekawa et al., 2008).

As pointed out by Bazant & Bažant (2012), at low vapor pressures (below the saturation pressure) very little bulk liquid exists in the larger pores, therefore the observed hysteresis cannot be attributed to the classical “ink-bottle effect” of capillarity from continuum fluid mechanics. Furthermore, insisting on the validity of any reversible adsorption isotherm (not only BET), then the only way to explain the observed hysteresis is to invoke changes in the accessible internal surface area, e.g. due to chemical transformations or structural damage (Feldman and Sereda, 1968, Thomas et al., 2008, Rarick et al., 1995 and Espinosa and Franke, 2006). Although, the nanopores collapse hypothesis in cement paste and concrete is still an open question and no mathematical theory was until now developed to justify this hypothesis. The theory proposed by Bazant & Bažant (2012) is based on the fact that the mechanism which causes sorption hysteresis at low vapor pressure is a series of snap-through instabilities causing path-dependent non-uniqueness of adsorbate content and dynamic jumps of water content of nanopores at constant vapor pressure. The snap-through instabilities are a consequence of the discreteness of the adsorbate, which leads to non-uniqueness of mass content and to misfit disjoining (transverse) pressures due to a difference between the pore width and an integer multiple of the thickness of a transversely unstressed monomolecular layer of the adsorbate. The hysteresis is explained by the fact that the snap-through instabilities for sorption and desorption follow different paths.

2.2.2 Electrolytic resistivity of concrete

Electrolytic resistivity of concrete can be considered as one of the most important factors responsible for the development in time of steel corrosion in RC structures. Current density and consequently corrosion rate are directly related to its value. However, the impact of this factor is highly dependent on the moisture content, presence of chlorides,

carbonation of the concrete cover, chemical composition of concrete and pore water, w/c ratio and temperature. The value of electrolytic resistivity is also generally useful to estimate the risk of corrosion in case of depassivation of the reinforcement. In this regard, Polder et al. (1998) gave an interpretation of resistivity values with regard to corrosion risk for concrete (see Table 2.1).

Table 2.1 Risk of corrosion of reinforcement associated with concrete resistivity (Polder et al., 1998)

| Relationship of corrosion reinforcement risk and concrete resistivity | |
|---|-------------------|
| Concrete resistivity (Ωm) | Risk of corrosion |
| < 100 | High |
| 100-500 | Moderate |
| 500-1000 | Low |
| > 1000 | Negligible |

2.2.2.1 Experimental determination of electrolytic resistivity of concrete

Electrolytic resistivity is critical parameter in corrosion modelling but is used often also as design parameter. Because of this, several test methods were developed in order to measure and experimentally specify the electrolytic resistivity of concrete, especially on site in the engineering practice. Even though all of them are based on a comparable principle, these different test methods can lead to considerable differences in the results (Weydert & Gehlen, 1999). As described in Weydert & Gehlen (1999), the “Two Electrodes Method” (TEM) method can be considered as the most elemental measuring method, determining the alternating current resulting from an implied alternating voltage between two flat steel electrodes. The TEM with flat steel electrodes, as shown in Fig. 2.8, can easily be applied under laboratory conditions for concrete specimens like cubes or cylinders.

The measuring is performed with an LCR-meter (alternating current at 120 Hz), two electric cables with two steel plates in contact with the concrete surface through a wet sponge. The experiments can be carried out on concrete cubes 150x150x150 mm make sure that the contact surface of the stainless steel plates and sponges has always at least the dimension of the cross-sectional area in order to allow a straight course of the flow lines through the specimen and avoid additional propagation and concentration resistors. Furthermore, to assure the contact a second concrete cube is placed on the steel plate of the tested concrete specimen.

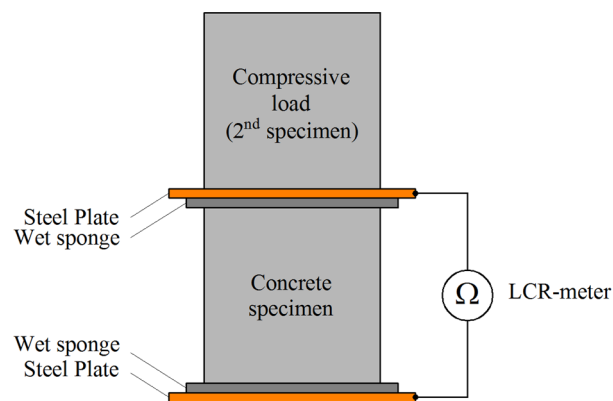


Fig. 2.8 Two-electrode external measurement (Osterminski, 2013)

2.2.2.2 Influence of moisture and w/c ratio on concrete resistivity

As pointed out by Martín-Pérez (1999), electrical current resulting from the corrosion of reinforcing steel is conducted predominantly by the movement of ions in the pore water (Elkey & Sellevold, 1995). Thus the pore structure characteristics of the concrete, the degree of water saturation, and the total ionic concentration of the pore solution are relevant factors affecting the electrical resistivity of concrete. In Fig. 2.9 the change of electrical resistivity as function of RH for concrete with different w/c ratio is illustrated (Gjørsv et al., 1977).

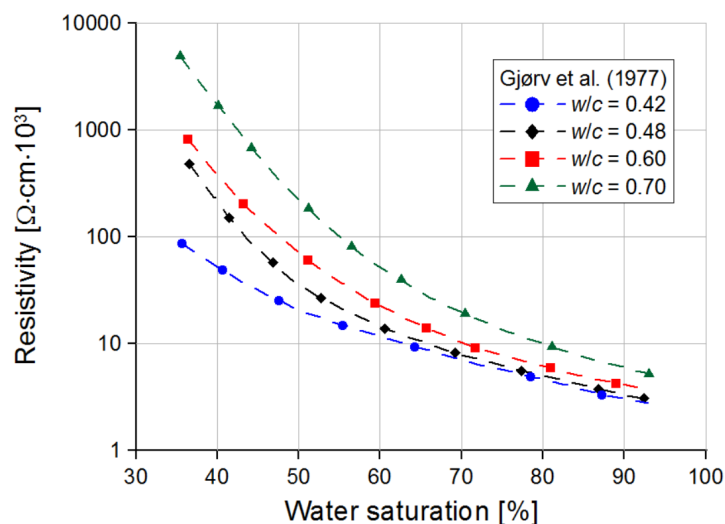


Fig. 2.9 Influence of water saturation on electrical resistivity for concrete with different w/c ratio (Gjørsv et al., 1977)

The w/c ratio influences the capillary porosity therefore water saturation, with increasing of the w/c ratio, has a higher impact on concrete resistivity. For high level of saturation the

values of resistivity decreases slightly but on the other hand at values of approximately 50% of water content (probably when the continuity of the pore water is not more possible) the resistivity is increasing brusquely, especially for high w/c ratios. Furthermore, as can be seen in Fig. 2.9, a change of water content from 40% to 90% induces a reduction of almost three orders of magnitude in terms of concrete resistivity. Therefore the parameter has to be considered of particular relevance in corrosion modelling and in the engineering practice. Values in tabular way of the electrical conductivity, reciprocal value of concrete resistivity, are given in Table 2.2.

Table 2.2 Values of electrical conductivity for concrete as function of water content for different w/c ratio (Gjørsv et al., 1977)

| Electrical conductivity of concrete σ ($10^{-3}\Omega^{-1}\text{m}^{-1}$) | | | | | | | | | |
|--|------|------|------|------|------|------|------|-------|------|
| Saturation(%) | 50 | 55 | 60 | 65 | 70 | 75 | 80 | 85 | 90 |
| $w/c = 0.40$ | 0.20 | 0.25 | 0.53 | 0.75 | 1.00 | 2.00 | 6.00 | 10.00 | 11.2 |
| $w/c = 0.70$ | 2.75 | 3.00 | 4.28 | 8.70 | 9.52 | 10.5 | 11.5 | 12.5 | 13.5 |

2.2.2.3 Influence of chlorides and cement type on concrete resistivity

Chlorides, dissolved in pore water, play an important role in transport of charge through the concrete cover. The specific electrolytic resistivity of mortar as function of the chloride content added to the mix water (see Fig. 2.10) was investigated by Gjørsv et al. (1977).

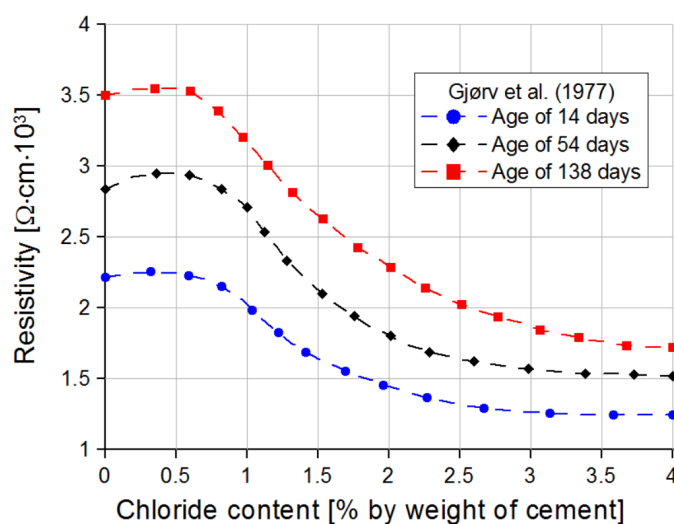


Fig. 2.10 Electrolytic resistivity of mortar samples as function of chloride content (Gjørsv et al., 1977)

As can be seen, contamination of mortar with chlorides affects the electrical conductivity at different level depending on the chloride content. The decrease is very low up to 1.0% of chloride content by weight of cement, but the effect becomes stronger with higher percentage. Especially at approximately 2.5% of chloride content a reduction of about 50% of the original concrete resistivity value can be noted.

Experiments carried out by Polder et al. (1992) confirmed the reduction of resistivity caused by adding of chlorides. Particularly, concrete specimen with 2.0 % of chloride ions (to cement mass) added as fresh concrete mix have shown a resistivity which was about 30% lower than the specimens without chloride. Osterminski (2013) quantified the influence of chlorides on the specific resistivity concrete by contamination of the mixing water with de-icing salts. Fig. 2.11 shows that the results of Gjørv et al. (1977), which were obtained on mortars, could be reproduced also for concrete.

Moreover, the cement type strongly influences the resistivity. This effect is deeply investigated by Osterminski (2013).

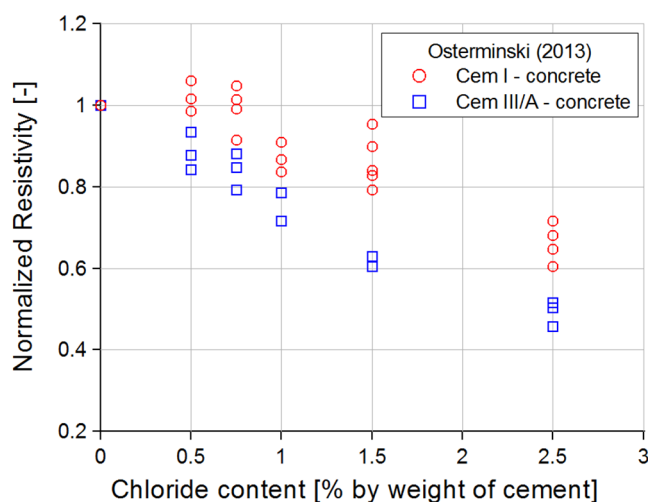


Fig. 2.11 Normalized concrete resistivity of concrete (with respect to non-contaminated concrete) as function of chloride content (Osterminski, 2013)

2.2.3 Influence of oxygen on corrosion of steel in concrete

As mentioned in Section 2.1, free electrons are consumed by oxygen at the cathodic site in presence of water and form hydroxyl ions. Therefore, the supply of oxygen in concrete is essential for the progress of corrosion and in comparison with concrete conductivity, oxygen has an opposite effect on corrosion rate. The cathodic reaction is possible if oxygen, as driving force of the corrosion process, is available at the interface of the reinforcement in a reasonable amount and in concrete with high moisture content the diffusion of oxygen is very low since it has to diffuse through the water in pores which is a much slower process than in air filled pores. On the other hand is well known that in constantly dry concrete (high resistivity) almost no reinforcement corrosion takes place

(Böhni, 2005). In particular, in case of high water content the corrosion process, as mentioned in Section 2.1.1, is considered as a cathodically controlled (Broomfield, 2002) and the cathodic sites on the steel surface can polarize through concentration polarization because oxygen cannot be replaced adequately in order to sustain the oxygen reduction process. In this situation the electrochemical process is controlled by oxygen diffusion. As discussed in Ožbolt et al. (2011) and experimentally demonstrated by Lopez & Gonzalez (1993), the diffusion controlled process takes place at a critical degree of water saturation of 70% and 85% for good ($w/c = 0.4$) and poor ($w/c = 0.7$) concrete quality, respectively.

It is therefore, very important to characterize the oxygen diffusivity in concrete. As demonstrated also experimentally (Kobayashi & Shuttoh, 1991), diffusion rate of oxygen in concrete is dependent on the w/c ratio of concrete and moisture content (Tuutti, 1982) and assumes particular relevance in corrosion modelling. Values of the diffusivity coefficient of oxygen were determined by Tuutti (1982) in function of the level of saturation and concrete quality (see Table 2.3).

Table 2.3 Values of oxygen diffusivity for concrete as function of water content for different w/c ratio (Tuutti, 1982)

| | | Oxygen diffusivity of concrete D_o ($10^{-8}m^2/s$) | | | | | | | | |
|---------------|--|---|------|------|------|------|------|------|------|------|
| Saturation(%) | | 50 | 55 | 60 | 65 | 70 | 75 | 80 | 85 | 90 |
| $w/c = 0.40$ | | 1.55 | 1.30 | 1.20 | 1.00 | 0.75 | 0.45 | 0.30 | 0.20 | 0.13 |
| $w/c = 0.70$ | | 9.30 | 9.00 | 8.00 | 7.50 | 6.00 | 5.00 | 3.50 | 2.50 | 1.50 |

Furthermore, low level of oxygen influences also the formation of the corrosion products. If the anode and cathode are well separated and the concrete has a high level of saturation (being underwater), the ferrous ions Fe^{2+} stay in solution and no expansive forces will be generated. In this kind of environment, for instance in damaged waterproof membranes or some underwater condition, different types of corrosion products are found. This kind of corrosion is potentially dangerous as there is no indication of corrosion by cracking and spalling of concrete and the reinforcing steel may be severely weakened before that corrosion is detected (Broomfield, 2002).

2.2.4 Corrosion products characterization

Corrosion of reinforcement in concrete has different negative effect on RC structure. One of the most important effects is the integrity degradation of the surrounding concrete (cracking and spalling) due to the fact that corrosion products of iron are expansive and their formation causes concrete damage. As mentioned in Section 2.1, in Eq. (2.4), the reaction and production of corrosion products are highly dependent on the environmental conditions and available chemical reactants. One possible occurring reaction is the production of red rust but several studies have shown different kind of corrosion products.

In particular, Suda et al. (1993) detected, for reinforced concrete containing carbon steel and exposed to marine environments for five years, magnetite, goethite and lepidocrocite; Aligizaki et al. (2000) observed that corrosion products could diffuse into the aggregate–paste interface in concrete and that, at the interface, the corrosion product adjacent to the aggregate was magnetite while that close to cement paste was hematite (Jaffer & Hansson, 2009). Vera et al. (2009), tested concrete cylinders exposed to three different environments (natural marine atmosphere, immersion in a simulated marine environment and simulated industrial environment) finding the presence of lepidocrocite, goethite and magnetite in all the environmental conditions under study and akaganite in chloride-rich environments. Poupard et al. (2006) investigated the nature of corrosion products in prestressed concrete beam stored during about 40 years in a tidal marine zone, where goethite, magnetite or maghemite were identified. Furthermore Duffó et al. (2004) concluded that two layers of corrosion products are present around the steel rebar, an inner one composed mainly of magnetite and an outer one composed of goethite and lepidocrocite.

However, the study of chloride-induced corrosion products of steel in concrete is the topic of recent investigation. However, the possible iron compounds which are formed during the corrosion reactions can be found in literature data (Foerst, 1955; Cornell & Schwertmann, 2003; Fischer, 2012) and are summarized in Fig. 2.12.

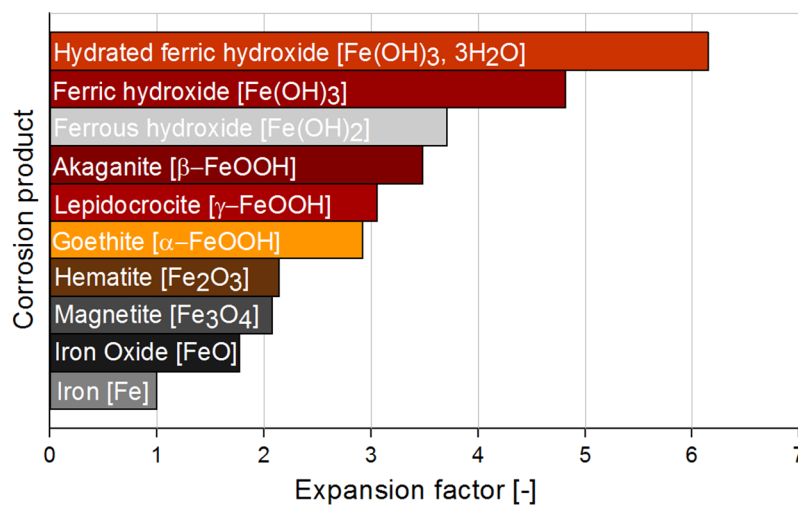


Fig. 2.12 Corrosion products with the relative colour and expansion factor

Furthermore, depending on the environmental conditions such as pH, moisture content and oxygen supply, different corrosion products can be formed. As can be seen from the above presented previous results, the specific reaction kinetics is a very complex process which takes place in a certain number of intermediate reaction steps and can be strongly dependent on the local conditions. Moreover, it is often asked whether corrosion products formed under anodic polarization are the same of the products produced under natural

conditions. For this reason, Fischer (2012) examined by means of the Raman spectroscopy the corrosion products obtained under accelerated corrosion conditions and compared them with the corrosion products formed under natural corrosion.

2.2.5 Corrosion products distribution

2.2.5.1 Penetration of corrosion products in pores and voids

Most of the studies carried out on corrosion of reinforcing steel bars assume that corrosion products accumulate at the rebar/ concrete interface and that cracking is initiated from this interface because of pressure from the corrosion products. However, some scientists made the same assumption considering the possibility of corrosion products to initially diffuse into the concrete without cracking it (Jaffer & Hansson, 2009). They suggested that the time to cracking in concrete is affected from different factors because concrete, as porous media, can contains voids which can act as storage locations for corrosion products and protract the cracking time. Therefore, it is very difficult to estimate the critical amount of corrosion products inducing cracks, which depends on many factors, such as the kind of corrosion products produced, site in which they are eventually deposited, accessible place for deposition (concrete porosity), the possibility to be transported in concrete and cracks as well as material properties, for example concrete tensile strength (Jamali et al., 2013).

Molina et al. (1993) were the first to hypothesize the effect on the cracking phenomenon of voids in the concrete surrounding the reinforcing bars. They stated that part of the corrosion products diffuse into these voids, without exerting any pressure on the concrete. Allan (1995) carried out some experiments simulating corrosion induced cracking of concrete with hydraulic pressurization at the reinforcement/concrete interface in order to determine the quantitative effects of several variables on the pressure required for cracking and spalling of concrete. The phenomenon was confirmed also recently by Michel et al. (2011), who tested reinforced mortar samples under accelerated corrosion conditions analyzing corrosion products formation and propagation of cracks with X-ray attenuation measurements. Furthermore, Angst et al. (2012) pointed out that in chloride induced corrosion the presence of high chlorides quantity strongly increase the solubility of Fe^{2+} and Fe^{3+} . Hence further away from pits, higher will be the macrocell current, flowing from anode to cathode, carried by other ions and less will be the part of current carried by chloride ions. In this way, ferrous ions react with hydroxide and precipitate forming the previous cited products, as final point, over a relatively large area. Furthermore, the location of corrosion product precipitation is highly influenced from the water content. In a concrete with a high degree of saturation, the corrosion products can more easily diffuse to distant places, in which they can precipitate, than in dry concrete (Andrade et al., 1989).

Recent analytical and numerical models take in account the effect of such voids by simply allowing the pores to be occupied in a cylindrical zone of defined width regularly located around the reinforcing bar (Liu & Weyers, 1998; El Maaddawy & Soudki, 2007; Bhargava

et al., 2005; Lu et al., 2011; Chernin & Val, 2011). This region is generally denoted as “diffusion zone”. Liu & Weyers (1998) estimated the thickness of this zone by adjusting their own model (a thick-cylinder model) to their test results as 12.5 μm . Similarly, El Maaddawy & Soudki (2007), Lu (2011) and Thoft-Christensen (2000) proposed a width of 10-20 μm .

This approach was criticized by scientists, who determined experimentally the thickness of this zone. Michel et al. (2011) denoted this zone as “corrosion accommodating region”, whose thickness was experimentally detected in the range of 90-180 μm , as mentioned above, by X-ray attenuation measurements on specimens under accelerated corrosion conditions. On the other hand, Wong et al. (2010) performed some tests on reinforced concrete samples that have been subjected to salt spray on one exposed surface. In order to objectively describe the formation and distribution of the corrosion products, the investigations were carried out without adding chlorides to the concrete mix, without presence of artificial cracks or imposed electrical current to accelerate the corrosion. Their results have shown that the diffusion zone (see Fig. 2.13) was not regular and not more than 100 μm thick.

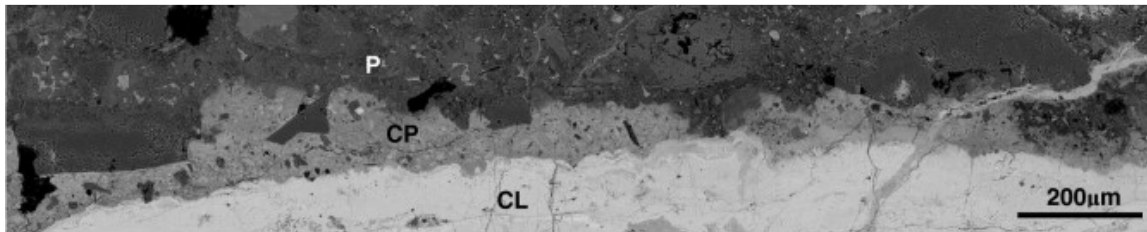


Fig. 2.13 Example of corrosion products diffusion into the cement paste (CL, corrosion layer; CP, corrosion-filled paste, P, unaltered paste) from the experiment of Wong et al. (2010).

Furthermore, Jamali et al. (2013) objected to this assumption, since the eventual equivalent cylinder does not really exist because the interface between rebar and concrete is not exactly delineated as an evidently demarcated edge. Moreover, concrete can be defined as a porous media that allows transport of ions and its porosity in the interface zone between concrete and steel cannot be considered uniform. Additionally, the ideally “porous zone model” has to be also linked to the corrosion kinetics. The rate at which the pores are filled depends strongly on the corrosion rate, the transport phenomena and the pore solution chemistry. At high value of current density, corrosion products have no time to move away, especially if the level of saturation is low. This aspect assumes particular relevance in case of imposed current density. On the contrary, at low current density levels, corrosion products have more time to migrate and precipitate in pores sited far away from the reinforcement bar.

2.2.5.2 Ingress of corrosion products in cracks

Experimental evidences (Wong et al., 2010; Fischer, 2012) have shown that corrosion products diffuse in concrete pores and voids and, as soon as cracking is started, part of them migrate in the corrosion induced cracks (see Fig. 2.14). The first effect is already well documented (see Section 2.2.5.1) but the second process is still an open question and especially few data is available in the literature.

By evaluation of corrosion damage of the performed experimental test on concrete blocks with an embedded rebar Andrade et al. (1993) noted a slowing of the corrosion damage in time attributed to the fact that corrosion products could easily migrate through cracks and its appearance on the external surface of the specimen was clearly observed during the performed tests. The corrosion product migration was also verified by Toongoenthong & Maekawa (2005) by evaluating experimental results of corroded RC specimen under accelerated corrosion conditions before occurrence of cover cracking. The investigation of the corrosion gel penetration front inside the tested specimens revealed the existence of corrosion gel migration into crack spaces around the corroded steel.

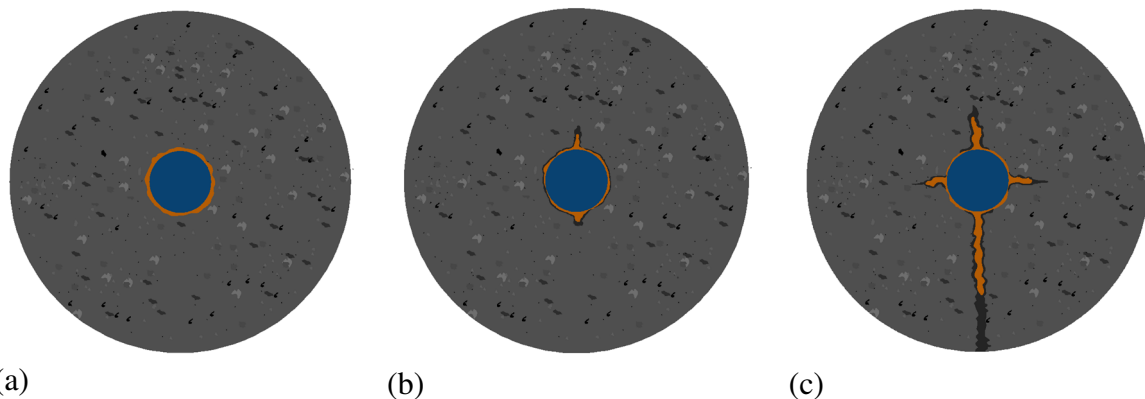


Fig. 2.14 Diffusion in concrete pores and voids (a); migration in corrosion induced cracks (b) and (c)

As mentioned before, Wong et al. (2010) investigated the distribution of the corrosion products in pores and voids but also in cracks. By visual inspection it was noted that in every slice of the specimen, the corrosion products at the steel/concrete interface were not regularly distributed around the steel reinforcement probably due to pitting corrosion and distance from the exposed external surface. Moreover, most of the cracks near the steel/concrete interface were completely filled with corrosion products, on the other hand cracks distant from the rebar were partially filled or had faces noticeable because of the corrosion products. The work presented also useful observations on the corrosion products accumulated around the rebar, penetration in concrete pores, voids and cement paste as well as the role of microcracks. In particular, the dense film of corrosion products resulted structured in different layer and bands related to a different grade of oxidation depending on the environmental circumstances. The extent of penetrated cement paste appeared

wider in specimens at higher corrosion stage and presence of microcracks pattern were also detected around the steel reinforcement bar making available privileged ways for corrosion products to diffuse deeper into the cement paste. Furthermore, it was noted that the transport is impeded by aggregates but promoted by microcracks (see Fig. 2.15).

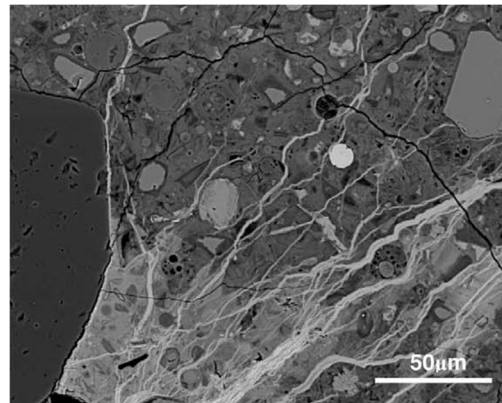


Fig. 2.15 *Microcracks detected close to the concrete-rebar interface from the experiment of Wong et al. (2010).*

Recently, similar considerations were taken in account also by Fischer (2012) in testing RC concrete beam-end specimens. Particularly, it was found out that near to the corrosion layer, small and medium cracks were mostly filled with corrosion products and that larger was the crack more the products diffused far away into it. However, the cracks were mostly not completely filled with products which were deposited on the borders of the cracks and penetrated deeply into the concrete pore structure. Furthermore, it was noted that the corrosion products have penetrated less into the concrete structure at the interface with the reinforced bar than in crack. Furthermore, Zhao et al. (2012a), investigated the crack widths at different locations and the related distribution of corrosion products on concrete specimens subjected to natural simulated conditions. By observation of the specimens with digital microscope, it was noted that the corrosion products do not migrate directly in corrosion induced cracks, but they fill them much faster in case of external cracks. In this case, the rust deposits on the surface of the cracks due to the circulation of the outer solution.

2.3 Experimental tests

Effect of reinforcement corrosion in RC structures is usually studied through both experimental and numerical investigations. Generally, empirical and more complex analytical models are partly created by regression of experimental results developed in the past years. Corrosion tests can be carried out on site, under controlled laboratory conditions, on full-scale damaged elements from existing RC structures or even particular samples exposed to natural conditions for long time corrosion. Unfortunately, in natural corrosion conditions it is quite difficult to separate the effect of corrosion from the other influences, such as weather conditions, degradation of material properties or service loads, factors which can also influence the concrete structure performance. Furthermore, corrosion tests in natural conditions are time consuming. Therefore, numerous scientists have dedicated their effort to study the concrete cracking and the related consequences by means of accelerated corrosion tests. In the following is provided an overview of the research conducted until now.

2.3.1 Accelerated corrosion tests

As mentioned above, impressed current or potential technique is in engineering frequently used to induce reinforcement corrosion in order to obtain a certain corrosion stage, for previous defined research aims, in an acceptable time. In order to accelerate the corrosion, it is normally impressed a direct current to the reinforcement promoting the dissolution of iron. In addition, the specimens are often exposed to splash aggressive conditions. Moreover, to further activate the corrosion process a certain percentage of chlorides is added to the concrete mix. The entity of impressed current, addition of chlorides or exposure conditions can vary depending on the aim of the authors.

2.3.1.1 Corrosion current density influence

Andrade & Alonso (2004) estimated, by means of the Polarization Resistance technique, the current density in large size concrete structures finding a direct relation with resistivity and therefore water content. In Fig. 2.16, the relation between concrete resistivity and corrosion current density is shown. Values under $0.1 \mu\text{A}/\text{cm}^2$ denote negligible corrosion and the reinforcement can be considered as in passive state. On the other hand, the range $0.1\text{-}0.2 \mu\text{A}/\text{cm}^2$ can be classified as a transition zone to active corrosion. Values of $1 \mu\text{A}/\text{cm}^2$ were rarely recorded and current density higher than $10 \mu\text{A}/\text{cm}^2$ was never measured except than in laboratory condition, where a value of $100 \mu\text{A}/\text{cm}^2$ was measured (Alonso et al., 1998). On the other hand, a maximum value of $18 \mu\text{A}/\text{cm}^2$ at 85% of saturation was predicted by modelling a reinforced concrete beam exposed to splash conditions with w/c ratio of 0.7 (Ožbolt et al., 2011).

In accelerated corrosion test performed imposing an impressed current or potential, the value of current density is often much higher than that found in natural corrosion. An

excessive level of current density can influence the corrosion effect such as the corrosion induced damage, bond behaviour, formation and migration of corrosion products as well as their nature. Unfortunately, there is no unique agreement about the threshold level which can be used. In any case, influence of current density can be examined by previous research studies carried out to investigate the corrosion cracking initiation, the bond strength in function of the corrosion level or the effect of concrete quality and cover.

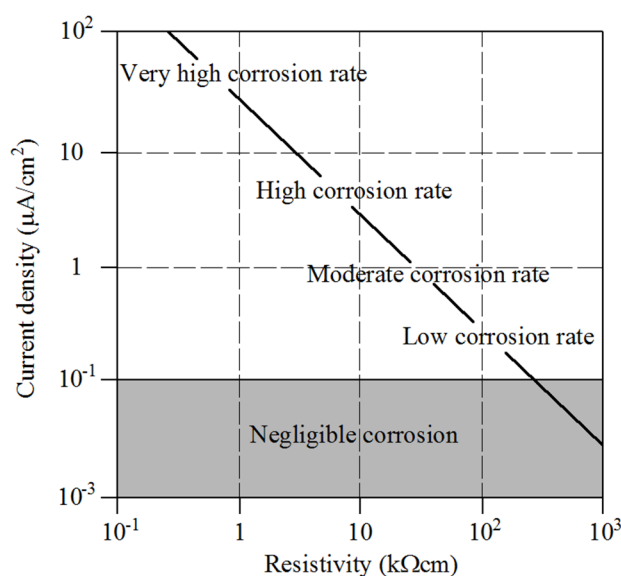


Fig. 2.16 Values of corrosion current density as function of concrete resistivity (Andrade & Alonso, 2004).

Andrade et al. (1993) studied the effect of current density on corrosion cracking of reinforced concrete beam with values very close to the maximum found in real conditions. The experimental results have shown that the same level of crack width is reached at different amount of mass loss under a relatively high current density, $100 \mu\text{A}/\text{cm}^2$, and at a lower value of $10 \mu\text{A}/\text{cm}^2$. In particular, a higher corrosion penetration of approximately $100 \mu\text{m}$ is reached at $100 \mu\text{A}/\text{cm}^2$ in comparison with $50 \mu\text{m}$ at $10 \mu\text{A}/\text{cm}^2$ for a corrosion induced crack width of about 0.3 - 0.4 mm (see Fig. 2.17a).

Similar considerations has been found by Alonso et al. (1998), in which it was demonstrated that a higher attack penetration is necessary at a current density of $100 \mu\text{A}/\text{cm}^2$ in comparison with a value of $10 \mu\text{A}/\text{cm}^2$ (see Fig. 2.17b), confirming the previous results of Andrade et al. (1993). Furthermore, it can be noted that at relatively high level of current density and corrosion penetration there is a pronounced slowing of the crack width increase because of the corrosion products diffusion which cause a reduction of the corrosion pressure (see Section 2.2.5.2) or as hypothesized by Alonso et al. (1998) a slower load application induces higher deformation. On the other hand, it was pointed out that the difference in terms of imposed current density does not have a very strong influence on the first crack appearance.

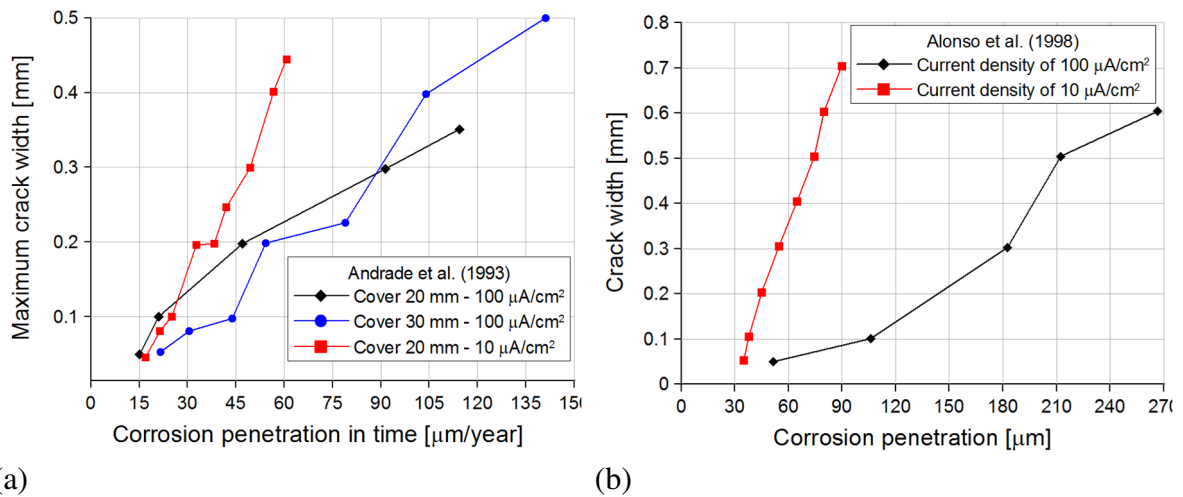


Fig. 2.17 Maximum crack width measured on the surface of the concrete specimen as a function of the corrosion attack penetration (Andrade et al., 1993) (a) and crack width as function of corrosion penetration for two different level of applied current density (Alonso et al., 1998) (b)

The effect of varying the impressed current density was also investigated by other scientists. In particular El Maaddawy & Soudki (2003) studied the effect of current density on different intensity range in comparison with Andrade et al. (1993) and Alonso et al. (1998). It was demonstrated, by experimentally measuring the maximum strain response in time, that at higher level of current density, strains were significantly higher. Specifically, four level of current density were impressed: 100, 200, 350 and 500 $\mu\text{A}/\text{cm}^2$. As can be seen in Fig. 2.18a, the specimens subjected to 350 and 500 $\mu\text{A}/\text{cm}^2$ have shown much higher strain in comparison with the case of 100 and 200 $\mu\text{A}/\text{cm}^2$.

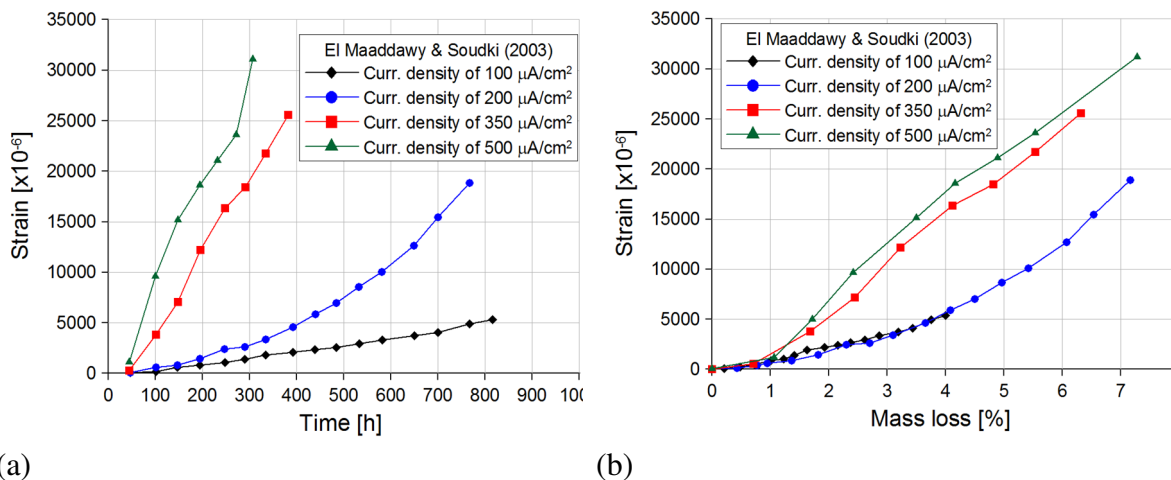


Fig. 2.18 Concrete strain versus time (a) and mass loss (b) at different level of impressed current density (El Maaddawy & Soudki, 2003)

Furthermore, the experiments have shown that at lower level of current density the relationship between strains and percentage of mass loss is nonlinear and concrete strain

rate increases. On the other hand at higher current density almost a linear relationship is observed (see Fig. 2.18b). It was also shown that impressed current density has a strong influence on maximum crack width observed experimentally. In particular, considering the same degree of reinforcement corrosion, an increase of current density results in an increase of maximum crack width.

Upon exposure to impressed current density, concrete response is different and the corrosion induced damage is differently affected depending on the current density level. The reason for such behaviour has to be addressed to the corrosion products produced in time and to their dissipation into the surrounding concrete pores and voids (see Section 2.2.5.1). Taking in account the previous results, it can be hypothesized that the relationship between the development of strain and crack in concrete and corrosion attack penetration is nonlinear. At low current density (about $10 \mu\text{A}/\text{cm}^2$) the amount of corrosion products can be considered too low to be spread through the concrete pores and can accumulate in the vicinity of the rebar despite they have more time to diffuse in accessible place for deposition. Therefore, the increase of strain with the corrosion penetration is higher in comparison with a higher current density level of $100 \mu\text{A}/\text{cm}^2$. On the other hand, when the impressed current exceeds a certain threshold ($100 \mu\text{A}/\text{cm}^2$) corrosion products produced in time is too high to be deposited in pores and the strain due to the expansion pressure around the reinforcement at the same level of attack penetration is higher in comparison with lower impressed current.

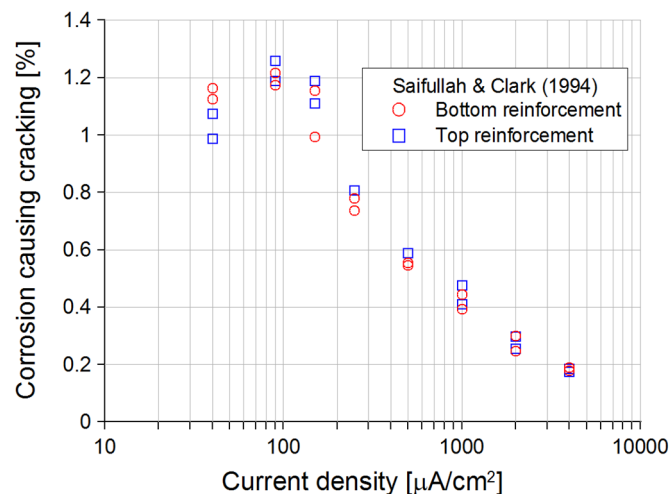


Fig. 2.19 Corrosion percentage responsible of cracking initiation as a function of the current density

The previous observations are also confirmed by laboratory investigations carried out by Saifullah & Clark (1994) in terms of cracking initiation. They performed several test on beam-end test specimens ($w/c = 0.65$) with different constant current densities, specifically 4000, 2000, 1000, 500, 250, 150, 90, and $40 \mu\text{A}/\text{cm}^2$. The appearance of the first crack, and the relative time, was monitored carefully. On the base of the results, variation of the

corrosion amount causing cracking with current density could be investigated (see Fig. 2.19).

As can be seen, an increase of corrosion penetration in function of the current density is observed till a threshold value of $90 \mu\text{A}/\text{cm}^2$. On the other hand at higher imposed current there is a progressive reduction of the corrosion penetration needed to induce cracking initiation.

Table 2.4 Accelerated corrosion experimental test using an impressed current density less than $200 \mu\text{A}/\text{cm}^2$ (Andrade et al., 2016)

| Accelerated corrosion experimental tests | | |
|--|---|------------------------|
| Researchers | Impressed current density ($\mu\text{A}/\text{cm}^2$) | Cover/diameter ratio |
| Andrade et al. 1993 | 10, 100 | 1.25, 1.9 |
| Rodriguez et al. (2004) | 100 | 1.9, 2.0, 2.1, 2.9 |
| El Maaddawy et al. | 165 | 2.2 |
| Torres Acosta et al. (2007) | 80 | 2 |
| Cairns et al. (2008) | 60 | 1.6, 2.6 |
| Al-Harthy et al. (2010) | 59, 100, 169 | 0.37, 0.63, 0.74, 1.25 |
| Coronelli et al. (2011) | 143 | 1.5 |
| Giordano et al. (2011) | 200 | 2.7 |
| Richard et al. (2012) | 100 | 1.25 |
| Prieto (2014) | 100, 150, 200 | 2.1 |

In any case, it has to be noted that frequently accelerated corrosion tests are used to investigate the decrease of the bond strength in relation to the corrosion penetration. Particularly, at high level of corrosion and increasing of the crack width, the ribs of the rebar look completely degraded and the loss of bond strength becomes significant (Cabrera & Ghoddoussi, 1992). Furthermore, it was supposed that the effect of the imposed corrosion current density and the relative value could directly influence the bond behaviour. Namely, Coronelli (1997) pointed out that current density higher than $50 \mu\text{A}/\text{cm}^2$ could damage, by mechanical effect, the cohesion between steel and concrete increasing the effect of corrosion induced damage and consequently also the related bond strength. On the other hand, Andrade et al. (2016), based on recent experimental data available in literature (see Table 2.4), suggested a maximum current density of $200 \mu\text{A}/\text{cm}^2$. Despite many scientists used current densities much higher, the recent experimental tests show the tendency to respect a limit of 100 - $200 \mu\text{A}/\text{cm}^2$.

2.3.1.2 Relationship between corrosion penetration and corrosion induced damage

As previous discussed, the influence of current density can strongly influence the behaviour of RC concrete in terms of induced strain, crack initiation and corrosion induced cracks. Furthermore, as described in Section 2.2.5, the effect of corrosion products expansion can be affected by diffusion in pores and migration in cracks. Adding the irregular distribution of the corrosion products and their different nature depending on the exposure and environmental conditions, it can be concluded that corrosion induced damage, in terms of crack pattern and width, is highly dependent on many factors. However, several researchers tried to find out a relationship between the corrosion penetration and the relative corrosion induced damage, which is generally expressed in terms of crack width. In particular, by modelling the cover cracking as a function of reinforcement corrosion, Molina et al. (1993) proposed a linear relationship between the crack width sum and the corrosion penetration directly related to the expansion factor of the corresponding corrosion product:

$$\sum \frac{w_i}{x_{corr}} = 2\pi(V_{r/s} - 1) \quad (2.13)$$

where w_i is the crack width of the generic crack on the external surface, x_{corr} is the corresponding corrosion penetration and $V_{r/s}$ is the expansion factor related to the nature of the formed corrosion products. Nevertheless, as pointed out by Fischer (2012), the previous mentioned relationship does not take into account the diffusion in the pore structure and migration in cracks as well as the presence of stirrups, which can strongly influence the crack development.

In order to consider the previous mentioned effects, the relationship between crack width and corrosion penetration (Eq. 2.13) was recently revised by Fischer (2012). Specifically, the expansion factor $V_{r/s}$ was replaced by an effective volume factor that takes in account the dependence on environmental condition and especially the diffusion in pores and voids as well as the migration in corrosion induced cracks. Furthermore, an additional factor was introduced to account for the influence of the stirrups. Rearranging the Eq. (2.13), it can be written:

$$\sum \frac{w_i}{x_{corr}} = 2\pi(V_{eff} - 1) \cdot k_{st} \quad (2.14)$$

where V_{eff} is the effective expansion factor which takes into consideration the corrosion products nature and their diffusion and k_{st} is the factor introduced to consider the effect of transverse reinforcement.

Moreover, a relationship between corrosion penetration and the maximum crack width observed experimentally was investigated by Torres-Acosta & Martinez-Madrid (2003).

By regression of the available data an interpolation curve was proposed and it was found out that at low corrosion rate, cracks appear and evolve in length and width more quickly than in case of accelerated corrosion tests (as described in Section 2.6.1.1). Similarly, Andrade et al. (2016) improved the correlation between maximum crack opening and the attack penetration considering the cover/diameter ratio, the concrete tensile strength and the imposed current density level. In particular, it was pointed out that a lower cover/diameter ratio induces a large crack opening and that a higher concrete strength prevents the formation of cracks but at the same time its width remain stable in comparison with a low strength concrete. Additionally, the authors concluded that wider cracks are generally found for lower corrosion rate. Based on the previous consideration a new interpolation function, for applied current density lower than $200 \mu\text{A}/\text{cm}^2$ was suggested:

$$w_{\max} = 15.863 \cdot \left(\frac{x_{\text{aver}}}{r_0} \cdot CT \right)^{0.928} \quad (2.15)$$

$$CT = \left(\alpha_f \cdot \frac{c}{d} \right)^{\frac{\beta_f}{f_{ct}}} \quad (2.16)$$

where w_{\max} is the value of the maximum surface crack width in mm, x_{aver} is the average attack penetration, r_0 is the initial steel bar radius, α_f and β_f are parameters (dimensionless) determined by fitting the experimental data, c is the concrete cover, d is the reinforcement diameter and f_{ct} is the average tensile strength of concrete in MPa.

2.4 Modelling corrosion of reinforcement in concrete

The most known analytical and numerical models for the calculation of corrosion in reinforced concrete are based on the concept proposed by Tuutti (1982). According to this concept (see Fig. 2.20), the modeling of corrosion of reinforcement in concrete can be divided into two phases: the (i) initial phase in which the steel is depassivated because of carbonation of the concrete cover or through the entry of chlorides and the (ii) second phase of the corrosion in which concrete is damaged due to the expansion of the corrosion products.

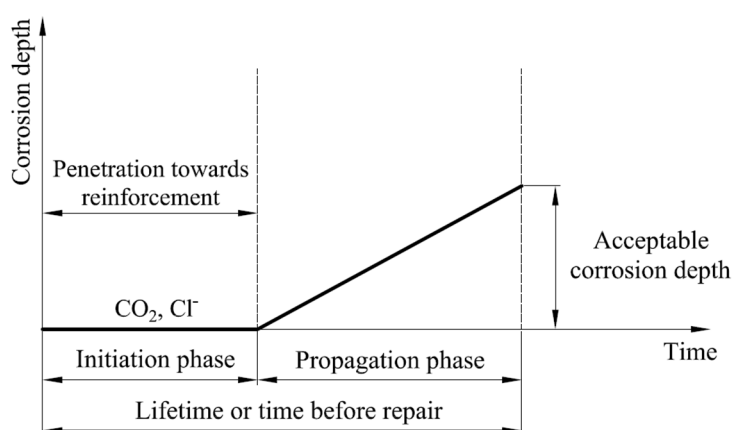


Fig. 2.20 Modelling of corrosion in concrete (Tuutti, 1982)

In chloride induced corrosion, topic of this work and already studied with different mathematical models (Browne, 1982; Funahashi, 1990; Maage et al., 1995; Tang & Nilsson, 1996), the duration of the initial phase is highly dependent on several factors: (i) the penetration rate of chlorides in concrete, (ii) the thickness of the concrete cover, the properties of the concrete and the level of damage as well as (iii) the critical concentration of chlorides in the concrete itself (Tuutti, 1993). After the depassivation, corrosion rate is responsible for the damage of the steel structural elements and it is influenced from several processes such as the oxygen distribution, the transport of water and heat transfer (Tuutti, 1982; Lopez & Gonzalez, 1993). Normally it is assumed that the useful life of a reinforced concrete structure is achieved when a high degree of damage in concrete cover is reached as a result of cracks due to corrosion.

Because of the complexity of the chemo-hygro-thermo processes, and their interaction with the mechanical properties of concrete, so far there is no recognized mathematical models (deterministic) able to calculate the service life of structural elements in reinforced concrete. The main models in fact consider only the first phase. Therefore it is assumed that the useful life of a structural component is reached when a certain part of the reinforcement area is depassivated. This is justified by the fact that normally the initial phase is essentially longer than the second phase which leads to damage of the concrete

cover (Collins & Grace, 1997). In any case, these models can be considered relatively simple because only the transport of water, moisture, oxygen and chlorides are simulated.

However it has been stated by many scientists that the structural safety of the reinforced concrete elements can be significantly influenced by the reduction of the reinforcement cross section or bond resistance due to the corrosion of the reinforcement (Rasheeduzzafar et al., 1992). In order to demonstrate the importance of these effects, it is necessary to simulate the processes of corrosion even after depassivation of steel. Therefore in those models next to the above mentioned transport processes, it is also carried out the calculation of the current density and consequently the corrosion rate as well as their effects on the mechanical properties of concrete.

In the last 30 years, various two-dimensional numerical models, based on various assumptions, have been proposed (Bažant, 1979a, b; Page et al., 1981; Harker et al., 1987; Walton & Sagar, 1987; Walton et al., 1990; Bear & Bachmat, 1991; Andrade et al., 1997; Cairns, 1998; Thomas & Bamforth, 1999; Martin-Perez, 1999; Glass & Buenfeld, 2000), in which was established a critical level for the safety of reinforced concrete structures linked to the reduction of the reinforcement bond resistance and cross section.

The most important aspect of modeling durability of reinforced concrete elements is simulating the damage due to corrosion (Wang et al., 1997; Schießl & Raupach, 1994; Aldea et al., 2000; Marsavina et al., 2008; Tetsuya et al., 2009). This means calculate the loss of cross-sectional area of reinforcement and the decrease in ductility, the cracking and the local spalling of the concrete cover as well as the decrease of the bond strength. Currently, different analytical and empirical models can be found in literature (Andrade et al., 1993; Andrade & Alonso, 1996; Bažant, 1979b; Newhouse & Weyers, 1996; Rodriguez et al., 1996) which can be used to calculate the induced damage in function of the corrosion rate, the material properties of concrete and geometry. Moreover, there are numerical models (Dagher & Kulendran, 1992; Molina et al., 1993; Yokozeki et al., 1997; Isgor et al., 2004, 2006a; Nakamura et al., 2012), based on crack band approach, which are able to calculate the induced damage and the corresponding crack pattern. However, the corrosion rate is prescribed in advance, i.e. it is independent of the mechanical part of the model.

Another additional problem of the existing models is the assumption that the corrosion products are considered uniformly distributed across the reinforcement steel surface. In the case of chloride-induced corrosion this assumption cannot be considered as valid. Performing microscopic analyses it was demonstrated that the distribution of corrosion products on the individual anodic areas over reinforcement surface is not uniform. Furthermore, the migration of corrosion products in concrete pores and cracks is also generally neglected (Fischer, 2012). The amount of products that are transported over the

cracks influence not only their distribution but also the mechanical action due to their expansion and consequently the induced damage in concrete.

2.4.1. Empirical models

The relationship between corrosion rate and induced concrete damage was widely investigated by a certain number of empirical models by interpreting the available literature data and observed experimental results. If, on the one hand, such kind of models have a limited number of parameters and can be easily applied, on the other hand their application is restricted to certain environmental conditions and material properties. In particular, the theoretical corrosion mechanism and the related corrosion processes are not taken into account leading to inaccurate evaluation of corrosion induced damage. Some examples of empirical model are described below.

In this specific field, particular attention is focused explicitly on the development of models able to define the corrosion current density and the cracking time. Liu & Weyers (1998), by multiple non-linear regression of experimental data on specimens simulating concrete bridge decks, developed a model in order to estimate the corrosion current density in function of the chloride content, temperature, ohmic resistance of concrete and corrosion time:

$$\ln i = 8.37 + 0.618 \ln Cl - \frac{3034}{T} - \frac{0.000105}{R_{\epsilon}} + 2.32t^{-0.215} \quad (2.17)$$

where Cl is the free chloride content (kg/m^3 of cement), T is the temperature (in K), R_{ϵ} is the ohmic resistance of concrete (Ω) and t is the corrosion time (years). The experimental data was provided by measuring the current density and electrical resistance of the specimens by employing the linear polarization method and the temperature was recorded by means of thermocouples at the rebar surface. As can be seen, the model is directly dependent on concrete resistance, which can be different for different cover/reinforcement diameter ratio, instead of resistivity (see Section 2.2.2). Furthermore, the model does not take into account the oxygen availability and its interaction with moisture content that is particularly important in case of concentration polarization (See Section 2.1.1).

Similarly, Morinaga (1990) proposed an empirical model for chloride-induced corrosion model, by regression of chloride contaminated specimens exposed to natural environmental conditions. Corrosion rate is, in this specific case, expressed as a function of the w/c ratio, chloride content, concrete cover and reinforcement diameter:

$$i_{rate} = \left[-0.51 - 7.60C_{cl} + 44.97(w/c)^2 + 67.95C_{cl}(w/c)^2 \right] \cdot (d/c^2) \quad (2.18)$$

where C_{Cl} is the chloride content (in % by weight of mixing water), d is the reinforcement diameter (in mm) and c is the concrete cover (mm), w/c is the water cement ratio. The

corrosion rate (in $\text{g/cm}^2\cdot\text{years}$) is resulting from different range of parameters. Specifically, three different w/c ratios (0.40, 0.55, 0.70), various percentage of chloride content (0, 0.1, 0.5, 1.0, 1.5, 3.0), two different reinforcement diameter (9 and 25 mm) as well as several concrete covers (from 4 to 37 mm). Furthermore, in the empirical model the author proposed also an equation for prediction of corrosion cracking, expressed in terms of critical amount of corrosion products to induce concrete damage and cracking time:

$$Q_{cr} = 0.602d \left(1 + \frac{2c}{d} \right)^{0.85} \quad (2.19)$$

$$t_{cr} = \frac{Q_{cr}}{i_{rate}} \quad (2.20)$$

where concrete cover c and reinforcement diameter d are in mm, the critical amount of corrosion products in 10^{-4}g/cm^2 and the cracking time t_{cr} in years. As can be seen, despite the elaboration of a large amount of experimental data the above presented model has a limited application. Namely, the environmental conditions are not included and a second formulation was proposed by the author in order to account for the relative humidity level and oxygen concentration, which unfortunately does not include the concrete quality (w/c). Moreover, the model estimates the cracking time only in terms of corrosion rate.

2.4.2 Mathematical models

Mathematical models, differently from empirical models, represent the electrochemical processes behind the corrosion mechanism, trying to include the influence of several factors such as environmental conditions, concrete properties and quality, geometrical parameters, temperature, concrete resistivity as well as their interaction. Most of the research work is focused on the development of mathematical models, which can be implemented into a finite element code. In the following an overview of the most important mathematical model is presented.

One of the most important models was proposed by Bažant (1979a) which presented a complete mathematical formulation in order to describe the corrosion process in reinforced concrete as well as calculate the corrosion rate and time to cracking in several basic cases. In particular, presence of oxygen, chlorides are considered as diffusion processes and the electrode potential is determined by means of the Nernst equation depending on the concentration of oxygen and ferrous hydroxide. The electric current passing through electrolyte in the concrete pores is supposed governed by Maxwell equations of electrostatics, i.e. Ohm's law, and the corrosion products production is based on the Faraday's law.

The theoretical formulation is also applied to a simplified problem in order to predict corrosion rate and the cracking time. Specifically, the critical time at which the reinforcement corrosion induces cracks (t_{cr}) is supposed to be the sum of the time for depassivation of reinforcement (t_p) related to the diffusion of chlorides and the time needed to damage the concrete cover due to the expansion of the corrosion products (t_{cor}):

$$t_{cr} = t_p + t_{cor} \quad (2.21)$$

where t_{cor} is expressed as:

$$t_{cor} = \rho_{cor} \frac{d\Delta d}{sj_r} \quad (2.22)$$

in which d is the reinforcement diameter, Δd is the increase of diameter due to rust production, j_r is the rate of rust production per unit of area and s is the spacing between the bars. Furthermore, various steady state corrosion processes are analyzed in order to simplify the application of the mathematical model in order to predict the corrosion rate.

Raupach and Gulikers proposed another approach to model the reinforcement corrosion. The macro-cell current flow is calculate by using an equivalent circuit in which the resistance is taken into account as sum of the anodic and cathodic polarization resistance (R_{pa} and R_{ca}) in addition to the steel and concrete resistance (R_s and R_c). The difference of potential is expressed as difference between the anodic and cathodic equilibrium potential. Corrosion current is therefore calculated by applying the Ohm's law:

$$i = \frac{\Phi_{eq,c} - \Phi_{eq,a}}{R_{pc} + R_{con} + R_{pa} + R_s} \quad (2.23)$$

in which the resistances are expressed in Ω and the anodic ($\Phi_{eq,a}$) and cathodic equilibrium ($\Phi_{eq,c}$) are expressed in V.

Differently, Isgor et al. (2006b) developed a model able to predict the corrosion current density and consequently the corrosion rate by calculation of the potential (Φ) distribution around the reinforcement through the Laplace's equation:

$$\nabla^2 \Phi = 0 \quad (2.24)$$

in which the boundary conditions are expressed from the value of potential at the anodic and cathodic site (see section 2.1.1). Once that the potential distribution along the reinforcement is known, current density on the steel surface can be calculated as:

$$i = -\frac{1}{r} \frac{\partial \Phi}{\partial n_{el}} \quad (2.25)$$

in which r is the resistivity of the pore solution and n_{el} is the direction normal to the equipotential lines.

2.4.3 Probabilistic models

The probabilistic models were also developed because of the strong scattering properties in the corrosion processes. In particular in chloride induced corrosion that often presents strong localization of the corrosion penetration. This kind of models is based on the concept that external loads and RC structures resistance cannot be compared in a deterministic way. Specifically, the failure probability is determined as the situation in which the resistance R_{struct} is lower than a load S_{struct} . In case of reinforcement corrosion in concrete, during the propagation phase, the expansion action of the corrosion products can be considered as the load S_{struct} and the concrete strength as the resistance R_{struct} (Gehlen & Banholzer, 2000).

The model proposed by Gehlen & Banholzer (2000), consider the failure probability by comparing the corrosion induce load (S-model) with the resistance (R-model). The S-model is described as (Alisa et al., 1998):

$$\Delta r_s = x_{corr} \cdot t \cdot V_{r/s} = \frac{M}{\rho} \cdot F_{Cl} \cdot F_{Galv} \cdot F_{O_2} \cdot t \cdot V_{r/s} \quad (2.26)$$

in which Δr_s is the increase of steel radius due to the expansion of the corrosion products (mm), V_{Corr} is the corrosion penetration depth, M is a model factor, ρ is the electrolytical resistivity of concrete, F_{Cl} , F_{Galv} and F_{O_2} are the correction factors taking in account the chloride concentration the macro-galvanic effects and the oxygen availability, t is the time and $V_{r/s}$ is the expansion factor. The R-model, on the other hand, is derived by introducing a certain model factors to the analytical resistance, which consider non-linear material properties of concrete and the induced damage (K_C), time dependent material properties and the consequent relaxation (K_R), the spacing of the rebars (K_S):

$$\Delta r_r = \Delta r_{r,A} \cdot K_C \cdot K_R \cdot K_S \quad (2.27)$$

in which $\Delta r_{r,A}$ is the resistance which results from the analytical model. Based on the above consideration the failure (cracks of 0.005 mm from steel to the external surface) occurs when the resistance is lower than the load:

$$p_f = p\{R - S < 0\} = p\{\Delta r_r - \Delta r_s < 0\} \quad (2.28)$$

3. EXPERIMENTAL INVESTIGATIONS

3.1 Objectives of the experimental program

Purpose of the experimental work is the improvement, calibration and validation of the existing CHTM model, with particular reference to the transport of corrosion products into concrete pores and cracks as well as chloride-corrosion induced damage under various environmental conditions and for different geometries.

With the help of experimental investigations it was possible to quantify the induced damage (crack width) and the distribution of the corrosion products in concrete for different corrosion stages of reinforcement bar. Furthermore, influence of water content and concrete conductivity on current density and crack pattern was studied.

Other aim of the tests is to have a better insight into the impressed current or potential technique, which is in engineering frequently used to induce reinforcement corrosion. Based on the results of the experiments, it could be shown in which range of the imposed electric potential the resulting corrosion can be taken as realistic and comparable with the natural case. Moreover, considerations on the type of the corrosion products and relative effect on the induced damage could be evaluated in order to better understand how to use the accelerated corrosion technique in the correct way by understanding its limits and field of application. In effect, it has to be noted that corrosion tests under natural conditions are time consuming, therefore experimental tests are frequently carried out under accelerated conditions with 100 times higher corrosion rate or even more than observed in nature (see Section 2.3.1.1), which can possibly lead to incorrect conclusions.

Particular attention was paid to the characterization of the corrosion products formed under different applied potential and exposure conditions. The relative volume increase, in comparison with steel, differs depending on the corrosion product type and varies from 2 up to the value of approximately 7 (see Section 2.2.4). In order to properly evaluate the results in case of anodic polarization and make them comparable with the natural conditions, formed corrosion products and their distribution around the reinforcement in the described experiments were object of examination.

Moreover, part of the experimental tests under natural conditions is also underway in order to give an objective overview and comparison between environmental and laboratory controlled conditions.

3.1.1 Description of the specimens

Samples used in the experimental tests are cylinders with cast-in reinforcement bars of different sizes and covers. All the samples have a uniform height of 150 mm as shown in Fig. 3.1.

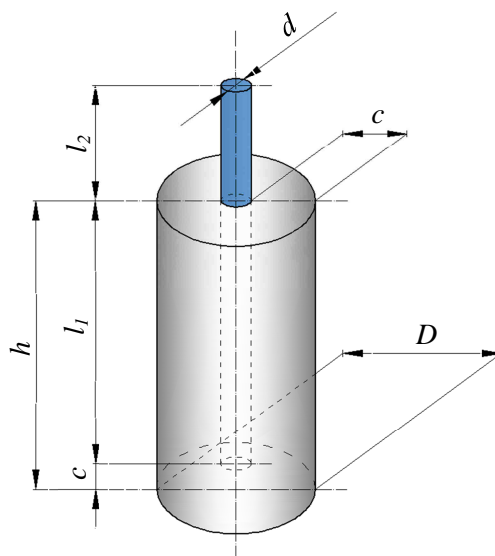


Fig. 3.1 Typical geometry of the specimens

Diameter of the samples, diameter of the reinforcement bar and the respective cover as well as the corresponding embedded length are summarized in Table 3.1.

Table 3.1 Type of the investigated concrete specimens and relative dimensions

| Specimen dimensions | | | | | | | |
|---------------------|----------|--------------|-------|-----------------|--------|-----------------|-----------------|
| Type | Diameter | Bar diameter | Cover | Geometric ratio | Height | Embedded length | External length |
| | D | d | c | c/d | h | l_1 | l_2 |
| | (mm) | (mm) | (mm) | (-) | (mm) | (mm) | (mm) |
| A/8 | 100 | 8 | 46 | 5.75 | 150 | 104 | 60 |
| A/12 | 100 | 12 | 44 | 3.67 | 150 | 106 | 60 |
| A/16 | 100 | 16 | 42 | 2.63 | 150 | 108 | 60 |
| B/8 | 70 | 8 | 31 | 3.88 | 150 | 119 | 60 |
| B/12 | 70 | 12 | 29 | 2.42 | 150 | 121 | 60 |
| B/16 | 70 | 16 | 27 | 1.69 | 150 | 123 | 60 |
| C/8 | 50 | 8 | 21 | 2.63 | 150 | 129 | 60 |
| C/12 | 50 | 12 | 19 | 1.58 | 150 | 131 | 60 |
| C/16 | 50 | 16 | 17 | 1.06 | 150 | 133 | 60 |

3.1.2 Casting and concrete properties

Concrete was manufactured at the Material Testing Institute (MPA) of Stuttgart – concrete department, using Portland cement CEM I 42.5 N and water/cement ratio of 0.6. Siliceous sand and aggregates were used with a maximum aggregate size of 8 mm. Approximately

2.5 % of NaCl by weight of cement was added to the mixture to accelerate depassivation of steel and improve the electrical conductivity of concrete. The mix proportions are summarized in Table 3.2.

Table 3.2 Composition of the concrete mix

| Concrete mix | | | | | | | | |
|-----------------|---|-----------------|----------------------|--------|--------|--------------------------|---------------------------|-------|
| Cement | w/c | Aggregates (mm) | | | | Chlorides ⁽¹⁾ | Stabilizer ⁽²⁾ | |
| | | 4-8 | 2-4 | 1.2-2 | 0-1.2 | | | |
| Type | (kg/m ³) | (-) | (kg/m ³) | | | (-) | (kg/m ³) | |
| CEM I 42.5 N | 360 | 0.6 | 673.78 | 235.83 | 252.67 | 522.19 | 2.5% mass of cement | 0.021 |
| Notes: | ⁽¹⁾ Sodium chloride (NaCl) ⁽²⁾ KELCO-CRETE DG biopolymer | | | | | | | |

Respecting the mix proportions, the quantities of cement, aggregates, water and sodium chloride were weighed employing a platform scale and the sodium chloride was dissolved in the mix in order to distribute it evenly in the concrete mix. Then the aggregates and the cement were poured into the electro-mechanical mixer and mixed for approximately three minutes before adding the chloride contaminated mixing water. Before casting all the concrete mix were kept in the mixer for about five minutes until it looked of the correct workability. PVC moulds of different sizes were used for casting the entire set of samples. An assembly of two wooden units, made of Ply-boards sheets, was used to hold a specific number of moulds firmly. Before casting PVC moulds as well as wooden assembly were cleaned with water and dried to remove any dirty particles. An appropriate hole was drilled in the assembly to fix position of the steel bar and assuring the designed embedment length of the reinforcement. The insides of the PVC mould were oiled and wax was applied on the supporting base of the wooden assembly in order to avoid water loss. On the interface region (concrete – reinforcement) of the sample, a small cone of wax was applied to act as a water tight seal and also to shape the sample for the epoxy coating (see Fig. 3.2).

Steel BSt 500 S in ribbed bars of diameter 8, 12 and 16 mm was used as reinforcement bar. The bars were manufactured by cutting mechanically 3.0 m long standard ribbed steel bar. Before casting, they were cleaned and degreased with acetone. The rods designed for the accelerated corrosion test were preventively drilled on one side in order to create the proper seat for the insertion of an electrical plug. The holes were immediately air sealed to prevent any further corrosion and after this entire procedure, each reinforcement bar was weighed with a precision of 0.01 g on a scale. All the bars were later numbered and the weight of each bar was recorded.

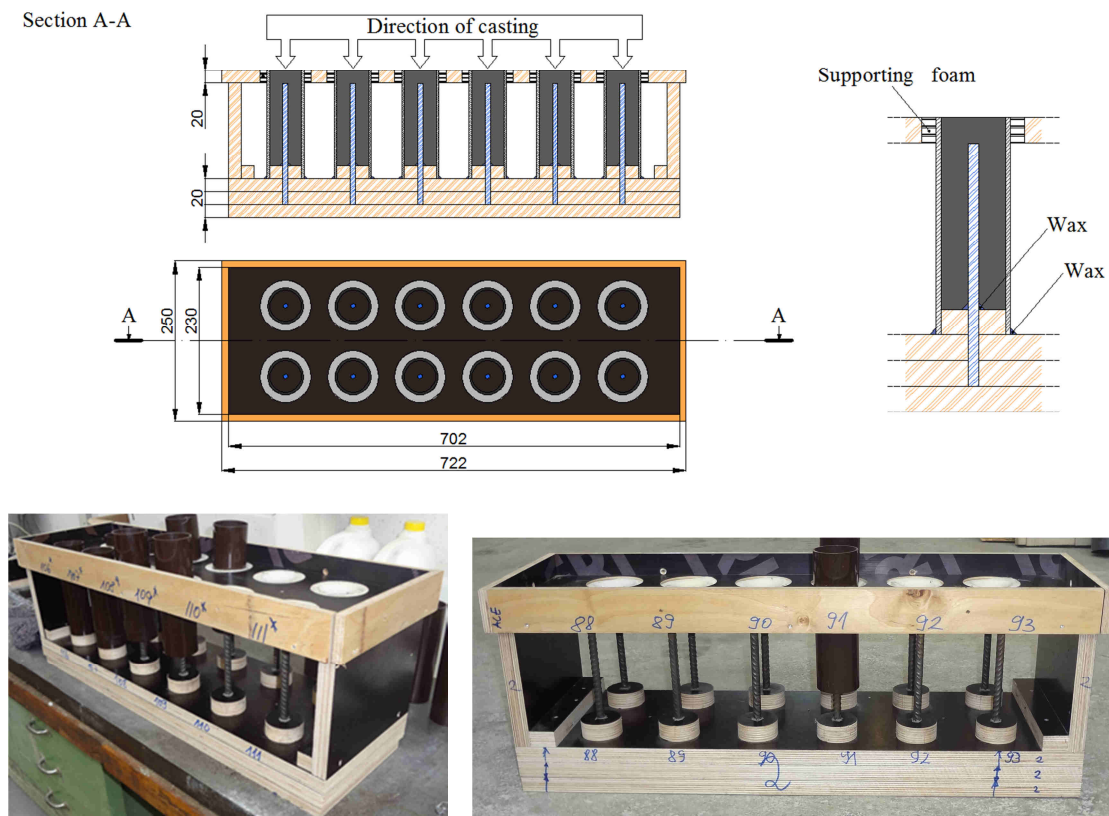


Fig. 3.2 Example of formwork for specimens C/8 and detail of the water sealing

After positioning of the reinforcement bars the concrete was poured into the moulds in two layers. After the pouring of a single layer, the concrete mix of all the moulds were shaken on a vibrating table. The entire assembly was later again vibrated for the third time for few seconds. Afterwards, the samples with their formwork were cured 7 days under constant temperature of 20°C and relative humidity (RH) of 100%. The specimens were demoulded after 24 hours after casting and placed again in the fog room (100% RH). A layer of hot glue was applied on the exposed part of the rebar to prevent any further corrosion. Subsequently, they were stored in a temperature controlled chamber at 20°C with RH of 60%.

The uni-axial concrete compressive strength was tested, before and during testing, on cubic samples 150x150x150mm. Particularly, a total number of 15 cubes were tested after 28 days and 15 after 1 year. Based on the measured cubic strength, the concrete properties, such as cylindrical strength f_c , Young's modulus E_c , Poisson's ratio ν , tensile strength f_t and fracture energy G_F , could be estimated. The average strength and the relative concrete properties are listed in Table 3.3. As can be seen comparing the average compressive strength, an increment of approximately 16% is noted after 1 year. This information assumes particular relevance especially in case of natural corrosion, in which the time plays an important role.

Table 3.3 Concrete properties

| Concrete properties | | | | | | | |
|---------------------|--------------------------|-------------------------|----------------|--------------|----------------|------------------------------|----------------------------------|
| | f_c (28 days) (MPa) | f_c (1 year) (MPa) | E_c (MPa) | ν (-) | f_t (MPa) | G_F (J/m ²) | ρ_c (kg/m ³) |
| Value | 38.47 | 44.65 | 33000.00 | 0.18 | 2.90 | 53.0 | 2236.0 |

3.1.3 Epoxy coating

After the curing, the samples were dried and if some minor superficial corrosion was found on the reinforcement bars, as well as at the end surface of the concrete sample, it was carefully removed using steel brush followed by acetone. The specimens were later coated to prevent undesired corrosion.

The objective of the coating was to permanently cover the exposed area of the steel bars from any environmental actions leading to corrosion. Prior to the coating of the bare bar, a layer of epoxy resin was used to cover the end surface of the concrete cylinder in order to prevent crevice corrosion attack and further corrosion on the discontinuity between bare bar and outer concrete surface (see Lambert, 1983; Lambert et al. 1991). Different kinds of coating and epoxy resin were tested in order to find the best solution suitable for the experiments. In this regard, the exposed bar was coated with direct application of epoxy of different brands or with a combination of grout and epoxy. Based on the results of preliminary experiments performed on 9 differently coated specimens, a primer coating of grout with $w/c=0.4$ followed by application of three layers of epoxy was chosen (see Fig. 3.3a).

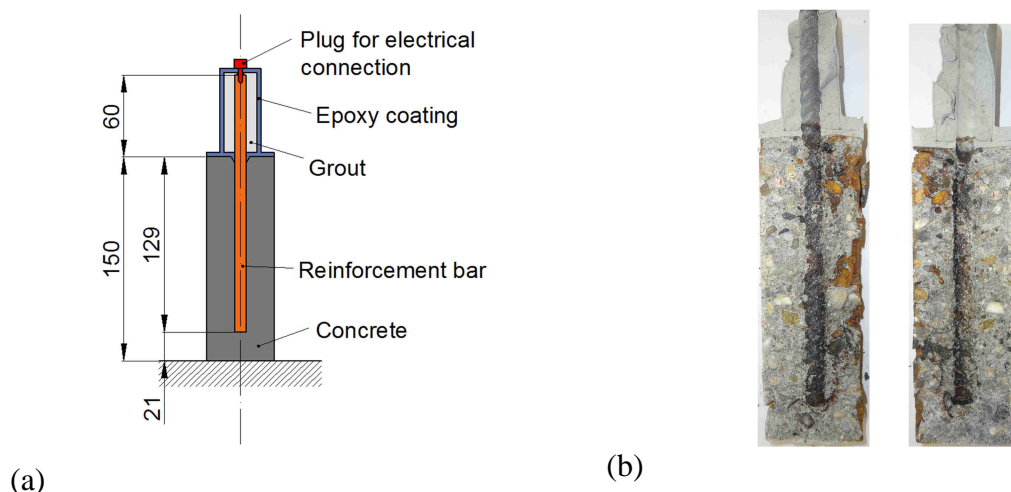


Fig. 3.3 Example of specimen geometry (A/8) and coating (measures in mm) (a) and experimental results after corrosion (b)

The painted coating over the grout is CDS-Pouring Concrete UW which was prepared by mixing epoxy resin with the corresponding hardener. Particular care was also dedicated to the reinforcement bar holes which were kept, during the manufacturing, constantly air sealed such that any epoxy could be poured inside. After the three epoxy layers had fully set, the holes were again checked and cleaned with a diamond head whose diameter was chosen to be close enough to the reinforcement hole diameter in order to prevent any undesired scraping of the non-corroded metal. As can be seen in Fig. 3.3b, after testing the coated part of the reinforcement presented no visible corrosion and no other traces of corrosion could be found on the adjacent grout.

3.2 Performed accelerated corrosion tests

In order to calibrate and verify numerical models, experimental tests are required. However, corrosion tests under natural conditions are time consuming. Therefore, tests are frequently carried out under accelerated conditions with corrosion rates that can be 100 or even more times faster than corrosion rates under natural conditions. Typical accelerated corrosion tests of reinforced concrete include current generation, evaluation of the mass loss due to corrosion and monitoring of the crack pattern and width.

In order to accelerate the corrosion process, an imposed constant potential was applied between the rebar (anode) and a cylindrical shell of platinized titanium mesh (cathode), located around the lateral surface of the specimen. Differently from other authors, the imposed potential was kept constant during the test leading to changes of current intensity and consequently of current density. Motivation on the base of this choice is the purpose of calibrating controlling parameters of the above mentioned 3D CHTM model, i.e. the hysteretic property of concrete in wetting and drying cycles as well as concrete conductivity.

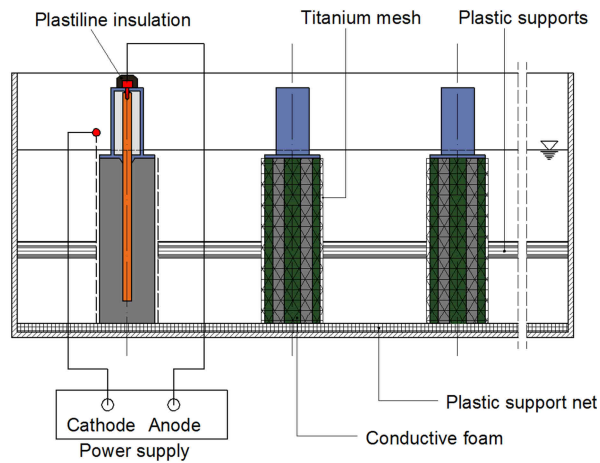
To electrically connect the external titanium mesh with the concrete surface (see Fig. 3.4), four stripes of conductive foam 1.5 cm wide, at 90° to each other, were used. Name of the foam is “Polyolefine foam with nickel-copper (NiCu) metallization” generally used for transmitting and receiving modules, produced by Würth Elektronik. The advantage of this arrangement was that the concrete surfaces were always inspectionable leading to observation of the crack development. During the experiment readings of current were continuously recorded every 30 minutes measuring the drop of voltage, over a resistance unit of 10 Ω , and were performed by a digital multimeter data acquisition and data logging system, KEITHLEY 2701.



(a)



(b)



(c)

Fig. 3.4 Overview (a),(b) and details (c) of the accelerated corrosion test-setup

3.2.1 Environmental exposure

A total number of approximately 170 specimens were tested under laboratory controlled conditions. For each combination (see Table 3.4) three identical specimens were exposed to cyclic wetting/drying regime, 1 day of wetting by 2.5 % NaCl solution, followed by 6 days of drying at relative humidity of approximately 60%. Another batch of samples, same types and amount, were kept under water throughout the experiment. A third batch of specimens (approximately 180 specimens) were exposed to natural conditions which correspond to Stuttgart climate, i.e. variation of air relative humidity in the range from 63% (May) up to maximum 80% (December).

Table 3.4 Combination of the environmental exposure conditions and relative investigated corrosion stage

| Environmental exposure and investigated corrosion stage | | | | | | | | | |
|---|--|------|------|--|------|------|-------------------|------|------|
| Parameter | Combination | | | | | | | | |
| | Accelerated corrosion wetting/drying regime | | | Accelerated corrosion constantly under water | | | Natural corrosion | | |
| Specimen type | A/8 | A/12 | A/16 | A/8 | A/12 | A/16 | A/8 | A/12 | A/16 |
| | B/8 | B/12 | B/16 | B/8 | B/12 | B/16 | B/8 | B/12 | B/16 |
| | C/8 | C/12 | C/16 | C/8 | C/12 | C/16 | C/8 | C/12 | C/16 |
| Corrosion stage | 1 st stage = Low level of damage (Crack width between 0.1 and 0.3 mm) | | | | | | | | |
| | 2 nd stage = Medium level of damage (Crack width between 0.3 and 0.6 mm) | | | | | | | | |
| | 3 rd stage = High level of damage (Crack width wider than 0.6 mm) | | | | | | | | |

3.2.2 Cracks evolution monitoring

During the tests the samples were checked continuously to record the crack width involving three different stages of the cracks evolution, i.e. sum of the crack widths between 0.1 mm and 0.3 mm for the first stage, 0.3 mm and 0.6 mm for the second stage and wider than 0.6 mm for the third stage. Namely, after removing the titanium mesh and conductive foam, the crack width were checked in different locations, every 10-15 mm, over the length of the crack using a measuring magnifier.

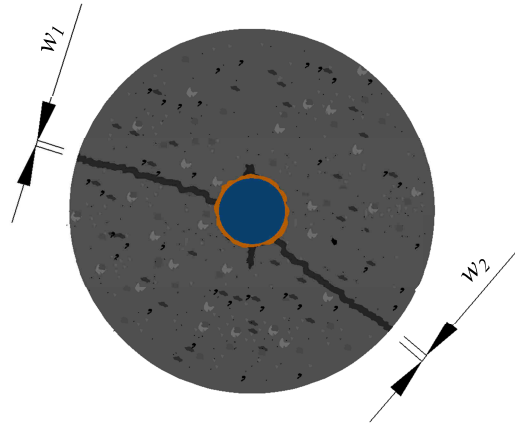


Fig. 3.5 Example of the possible cracks and the relative measuring

The final value of the crack width was evaluated as the sum of the average value of all the measures along the crack. An example of the used criteria is shown in Fig. 3.5, in which the crack width is expressed as:

$$w = \sum_{i=1}^n w_i \quad (3.1)$$

where w_i is the average crack width of the single crack.

3.2.3 Mass and cross-sectional loss

The mass and cross-sectional loss was determined gravimetrically after the splitting of the specimens and the extraction of the steel bar. The reinforcement bars were later cleaned from the corrosion products by pickling in an ultrasonic bath (see Fig. 3.6).

Following this procedure, taking in account that all the reinforcement bars were previously weighed and numbered, the exact mass loss could be determined. Consequently, also the average value of the corrosion penetration, according to Fischer (2012) was calculated as:

$$x_{corr} = \sqrt{\frac{m_0}{\pi \cdot L \cdot \rho}} - \sqrt{\frac{m_0 - \Delta m}{\pi \cdot L \cdot \rho}} \quad (3.2)$$

where m_0 is the initial weight of the reinforcement (g), Δm is the mass loss after corrosion (g), L is the corroded length (cm) and ρ is the density of the steel (7.85 g/cm^3).



(a)



(b)



(c)

Fig. 3.6 Ultrasonic bath: some of the specimens during the cleaning bath (a); reinforcement bar before the accelerated corrosion tests (b) and after (c)

3.3 Preliminary experimental test results at different level of applied potential

In order to test the rate of rust production for different level of potential applied and all the physical, electrochemical and mechanical processes related, preliminary tests were carried out. Considering the high level of applied current density generally used in accelerated corrosion tests (see Section 2.3.1.1) it is questionable whether such high values can influence the test results and the relative conceptual conclusions. To bring more light into the effect of accelerated corrosion and the related influence, such as corrosion induced damage of concrete, a limited number of experimental tests under accelerated condition, with different applied potential, were carried out. A series of 6 (see Table 3.5) cylindrical specimens with reinforcement bar of 8 mm and concrete cover of 21 mm (C/8) were investigated. They were exposed to wetting/drying cycles (1 day wetting, 6 days drying) with two imposed potentials, 100 mV (specimen P1-100, P2-100, P3-100) and 500 mV (specimen P1-500, P2-500, P3-500).

Table 3.5 Preliminary tests: investigated specimens, exposure and applied potential

| Experimental tests at different applied potential | | | |
|---|----------------------|---------------------------|-----------------|
| Specimen (-) | Specimen type (-) | Applied potential (mV) | Exposure (-) |
| P1-100 | C/8 | 100 | Wetting/drying |
| P2-100 | C/8 | 100 | Wetting/drying |
| P3-100 | C/8 | 100 | Wetting/drying |
| P1-500 | C/8 | 500 | Wetting/drying |
| P2-500 | C/8 | 500 | Wetting/drying |
| P3-500 | C/8 | 500 | Wetting/drying |

The average value of anodic current density-time curves of three different specimens for imposed potential of 100 mV (specimen P1-, P2-, P3-100) and 500 mV (specimen P1-, P2-, P3-500) are plotted in Fig. 3.7. However it should be noted that the showed current density is the average value on the anodic area calculated on the base of the measured current intensity.

In both cases (100 mV and 500 mV) the experimental results exhibit sudden increase of current density that is related with sudden wetting of concrete cylinder (1 day wetting). Subsequently, the water is removed and current density gradually decreases (6 days drying). As expected, with the increase of imposed electric potential from 100 mV to 500 mV, average current density increases approximately proportionally with imposed electric potential, i.e. with the factor of five.

Furthermore, the moisture content and anodic current density are strongly influenced by the corrosion induced cracks, which leads to ingress of water into specimen and increase

of saturation in un-cracked concrete. Consequently with increment of wetting-drying cycles, current density tends to increase especially in case of higher imposed potential (500 mV). Moreover, once the crack is generated the water content gradually increases in time. This accelerates the transport of rust from the reinforcement surface through the cracks into direction of concrete specimen surface. The protracted wetting period (1 day) of the specimens under water induces the migration of the corrosion products in the cracks and the precipitation in zones sited far away from the reinforcement.

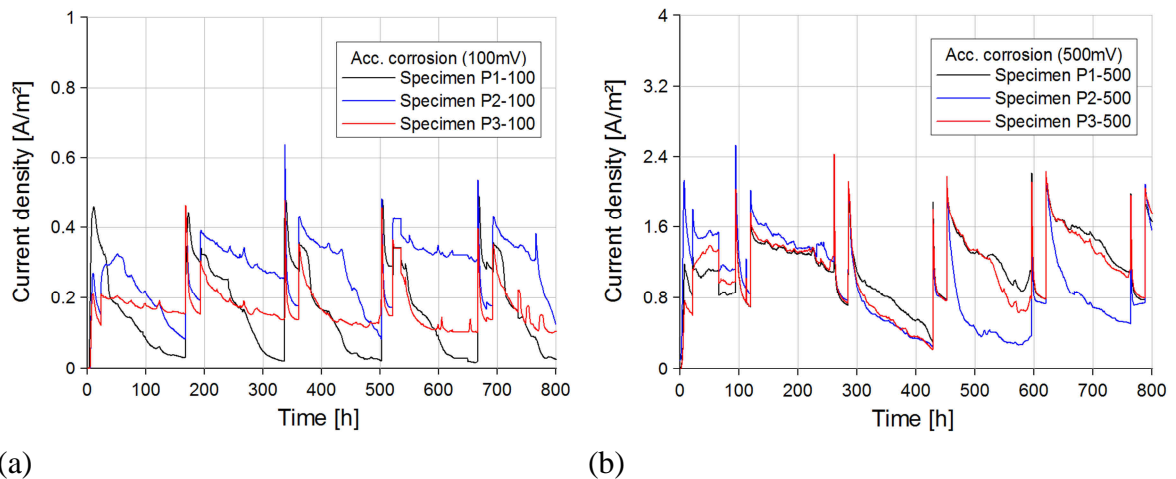


Fig. 3.7 Preliminary tests: average anodic current density as a function of time for an imposed electric potential of 100 mV (a) and 500 mV (b)

It has to be noticed that during wetting periods, in which the specimens are completely under water, the experimental results show a very steep current density increase and a subsequently progressive decrease to a constant value, attributed to the low dissolved oxygen concentration. During the application of the electric potential, the impressed current density contributes to the progressive decrease of the dissolved oxygen concentration since oxygen itself is continuously consumed at the cathodic area (Morikawa et al., 1987). Hence, a decrease of current density is observed.

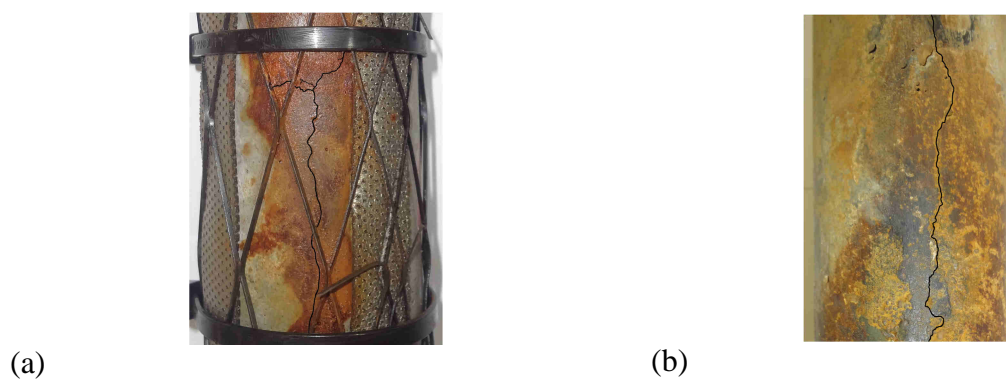


Fig. 3.8 Preliminary tests: crack patterns for potential of 100 mV (a) and 500 mV (b)

Fig. 3.8 shows the experimentally observed crack patterns (crack initiation). For lower and higher imposed potential, the first crack on the external surface of the cylinder (crack width = 0.05 mm) appeared after 20 and 6 days, respectively. In both experimental cases one dominant vertical crack is observed and in case of 500 mV a small secondary crack is observed. Moreover, as can be seen, there is a large amount of rust at the concrete surface. This indicates that a lot of corrosion products are transported from the reinforcement through cracks onto the surface of concrete cylinder. The importance of understanding and investigating this phenomenon is already described from other authors (see Section 2.2.5.2) and it is, later on, in detail investigated for the previous mentioned experimental tests.

3.3.1 Conclusions

The effect of two different applied potential, namely 100 mV and 500 mV, on cylindrical concrete specimens with 50 mm diameter is experimentally investigated. A comparison of the experiments provides more insight into the effect of the potential applied and moisture content. As observed, the imposed current density is directly proportional to the value of the electric potential and linked to the oxygen concentration on the external cathodic surface.

On the other hand the observed time for corrosion cracking is not proportional with the electrical potential. This means that at higher potential the internal radial pressure, due to amount of the corrosion products, is slightly lower. In this case the corrosion products produced in time are higher but part of them can be accommodated in the surrounding concrete pores and voids.

3.4 Accelerated corrosion tests on concrete cylinders with different dimensions

Corrosion induce damage of existing concrete structures and considerable research work brought to light the influence on corrosion of several factors: quality of concrete, cement type, thickness of concrete cover, salinity of water, moisture content, oxygen supply etc. The results of the previous mentioned experimental program, here presented, confirmed the importance of these factors by considering different imposed current density, concrete cover, environmental condition, reinforcement bar diameter as well as the effect of the corrosion induced damage.

Experimental investigations available in literature (see Section 2.2.5.2) have shown that the penetration of the corrosion products into corrosion induced cracks largely influences the crack pattern and the crack development in time. However, nowadays no systematic experimental tests were done to evaluate and quantify the effect of rust transport, especially useful for the calibration of numerical models in which this influence is generally largely neglected. In order to realistically predict the distribution of the corrosion products, by means of a numerical model, it is important to measure and later compare different factors: the current density, the boundary conditions (relative humidity, temperature, etc.) as well as crack width and mass loss at different corrosion levels.

Hence, the purpose of the following presented experiments is to combine and evaluate the effect of the mentioned parameters in order to investigate numerically and validate the non-mechanical and mechanical processes of the 3D CHTM model.

3.4.1 Imposed electric potential and environmental exposure

The value of the imposed potential applied between the reinforcement bar and the platinized titanium mesh was taken such that all the specimen series, A, B and C (see Table 3.1), would start to crack at the same time showing similar crack propagation.

Table 3.6 Values of the imposed potential for the investigated specimens

| Specimen type (-) | Imposed potential | |
|----------------------|---------------------------|------------------------|
| | Applied potential (mV) | Exposure (-) |
| A/8, A/12, A/16 | 700 | Wetting/drying |
| B/8, B/12, B/16 | 150 | Wetting/drying |
| C/8, C/12, C/16 | 100 | Wetting/drying |
| A/8, A/12, A/16 | 700 | Constantly under water |
| B/8, B/12, B/16 | 150 | Constantly under water |
| C/8, C/12, C/16 | 100 | Constantly under water |

Considering the wide range of geometric ratio (c/d), from 1.06 up to 5.75, and a reasonable number of external voltage sources, three different values of imposed potential were chosen (see Table 3.6).

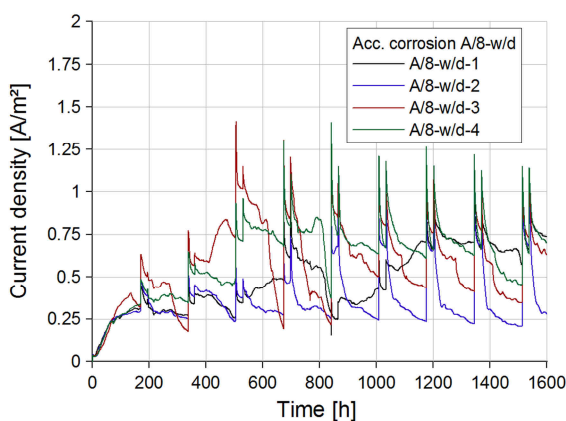
3.4.2 Results of the experimental tests

In this section are described and summarized the results of the experimental tests for each specimen type and exposure condition. Particularly, the influence of the environment and geometric ratio on the imposed current density was investigated. Furthermore, the crack development in time was examined in order to evaluate the effect of the transport of corrosion products. Three specimens for each corrosion stage (see Table 3.4) were investigated in order to find a relationship between the corrosion penetration and the corresponding induced damage for each geometry.

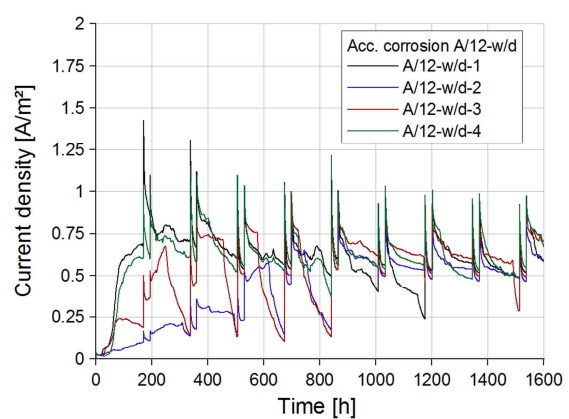
3.4.2.1 Test results for the specimen type A: A/8, A/12 and A/16 – wetting/drying exposure

In order to correctly evaluate the experimental tests, readings of the current intensity throughout the experiment were recorded. Considering the extensive experimental program only part of the specimens were monitored. In particular an average number of four specimens for each type and environmental condition were observed. As already pointed out, the showed current density is the average value on the anodic area calculated on the base of the measured current intensity.

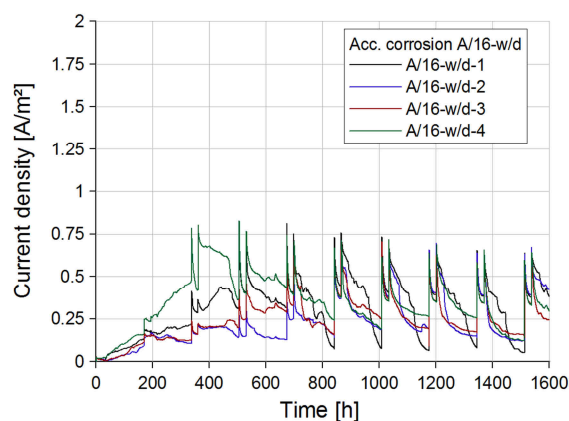
The experimentally recorded average current density-time curves for the series A/8, A/12 and A/16, under an imposed potential of 700 mV exposed to wetting/drying conditions, are plotted for each geometric ratio (c/d) in Fig. 3.9.



(a)



(b)



(c)

Fig. 3.9 Average anodic current density as a function of time under an imposed electric potential of 700 mV for the series A/8 (a), A/12 (b) and A/16 (c)

It can be noted that the current density, for all the presented geometric ratio (c/d), increases in time very slowly in the initial wetting/drying cycles. This behaviour can be attributed to the progressive penetration of water because of the large concrete cover. Furthermore, the total charge of the mass water content is increasing during the wetting/drying cycles leading to a higher conductivity and consequently higher value of current density. This can be clearly seen in the drying phase after a certain number of cycles, depending on the concrete cover, in which the decreasing of current density looks less progressive compared with the previous wetting/drying cycles.

Moreover, reducing the geometric ratio (c/d) the value of the average current density decreases. This can be considered to be a consequence of the different extent of anodic area. In particular, considering that the applied potential for the specimen types A/8, A/12 and A/16 is the same and that the concrete cover ranges from 46 mm and 42 mm, it can be concluded that the reinforcement bar diameter is the governing factor in determining the value of the average current density which decreases with the increasing of the bar diameter.

In any case, the maximum current density reached during the experiments is approximately 1.40 A/m^2 , in the peaks at the beginning and end of the wetting phase, for the specimen A/8. Anyway, most of the time the applied current density is kept at lower level and generally the measured value is much below 1.00 A/m^2 , which can be considered the maximum value found in laboratory conditions simulating a natural environment (Alonso et al., 1998). This value can be considered the maximum acceptable current density to perform accelerated corrosion tests, because a higher level can affect the corrosion induced damage and all the related consequences. However, at the moment no unique agreement about the highest conventional value was found (see Section 2.3.1.1).

The specimens were exposed to wetting/drying cycles for different duration time depending on the corrosion stage (see Table 3.4). The total duration of the experiment for the specimen A/8, A/12 and A/16 was approximately 8 months, during which measuring of the average crack width was taken (see section 3.2.2). As previously described, approximately three specimens for each corrosion stage and type were analysed. The typical failure mode observed during the test is characterized by two or three vertical cracks, more or less inclined, in addition to a singular horizontal crack which in general case connects the vertical ones (see Fig. 3.10).

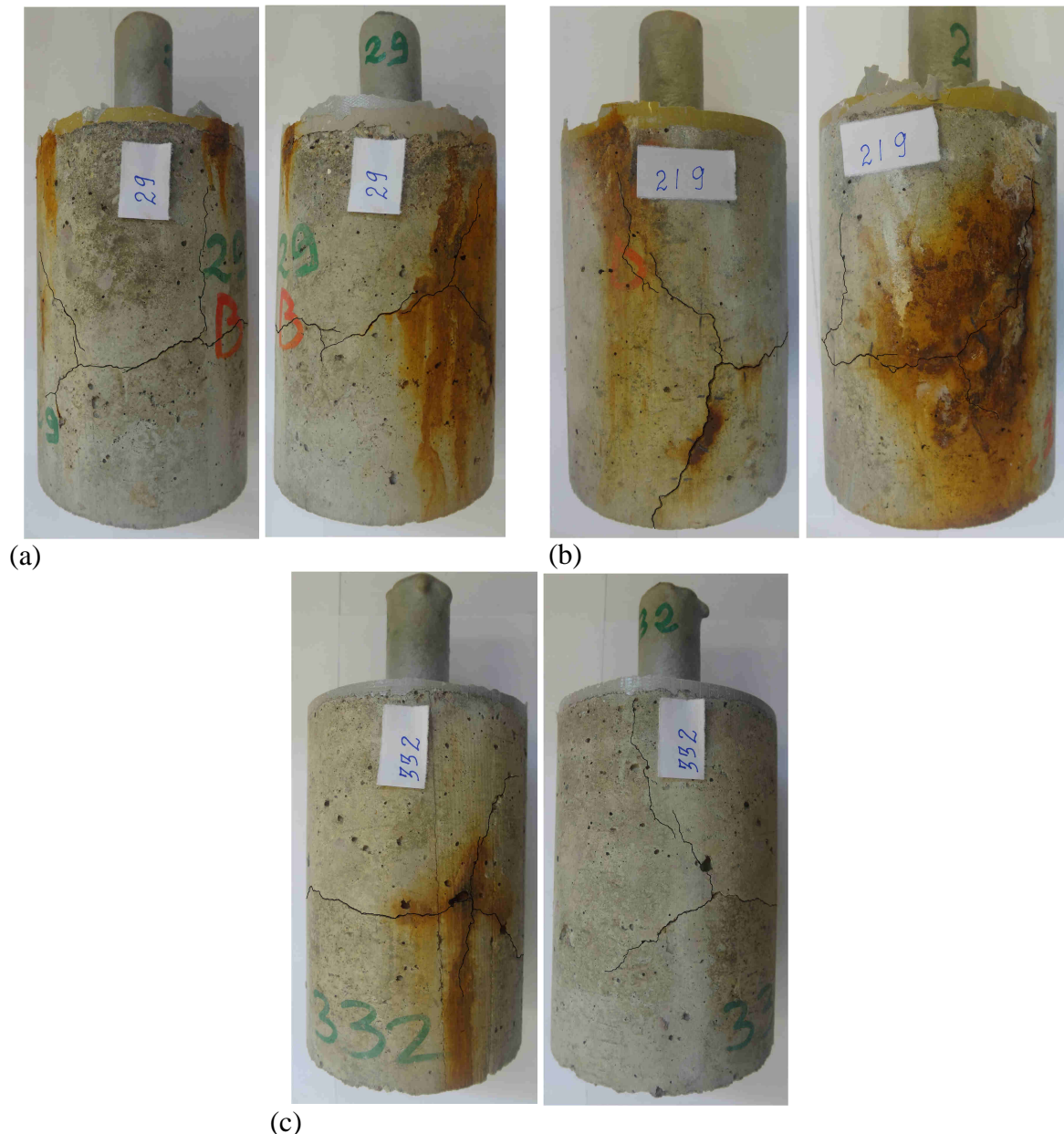


Fig. 3.10 Experimentally observed crack pattern (3rd stage) for the specimen series A/8 (a), A/12 (b) and A/16 (c) under wetting/drying conditions

As shown in Section 3.3, a large area of the external concrete surface exhibits presence of corrosion products, which leads to the conclusion that a part of the corrosion products are transported through cracks, reducing the expansion pressure around the reinforcement bar. The distribution of the products and their progressive penetration in the cracks can be observed in Fig. 3.11.

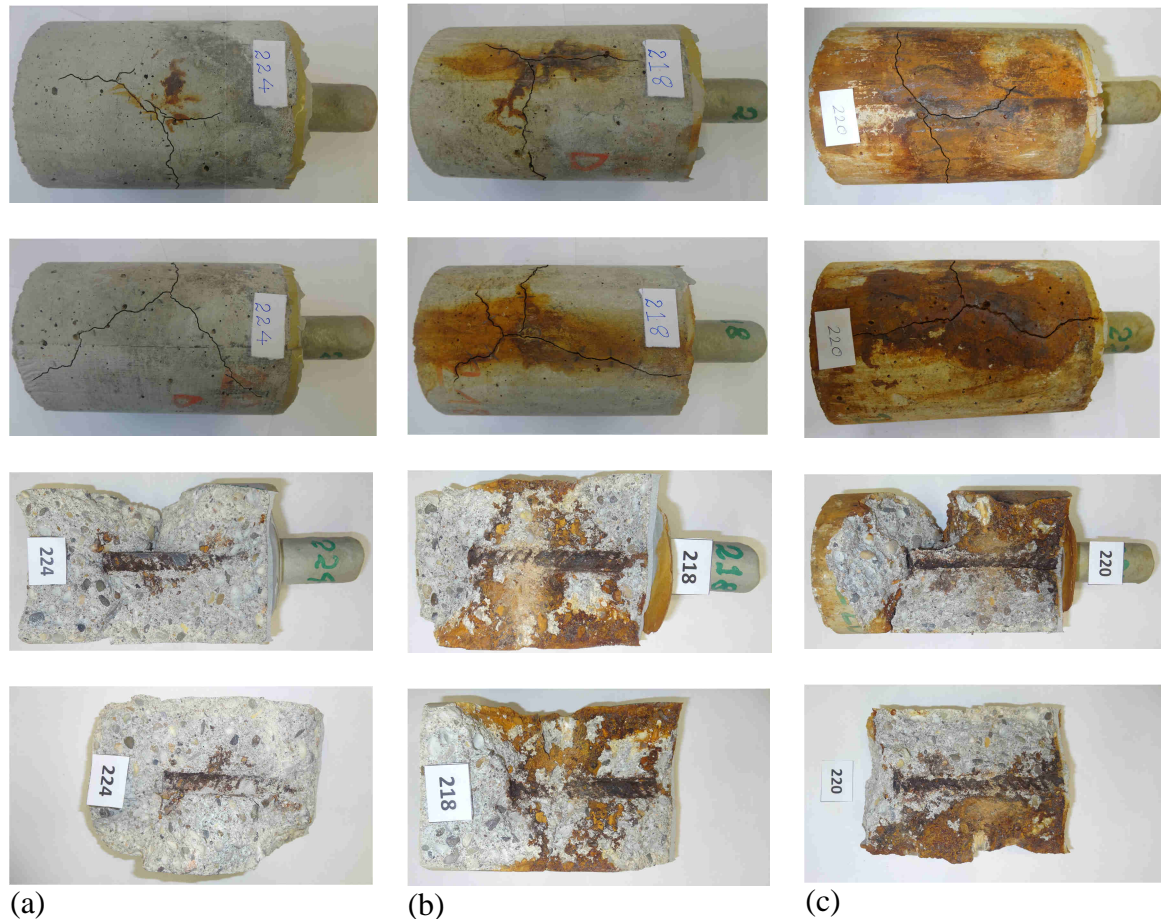


Fig. 3.11 Transport of corrosion products through cracks at different corrosion stages for the specimen type A/12 under an imposed electric potential of 700 mV: 1st stage (a), 2nd stage (b) and 3rd stage (c)

It can be seen that for all the investigated stages, ingress of corrosion products in cracks was observed. After the first stage, which corresponds to 35 days for the specific case, only a small amount of rust in cracks can be noted but already in the second stage, approximately 67 days, a large quantity of products transported through them can be detected. Moreover, the specimen in the third stage, 233 days, shows clearly a high quantity of rust on the external surface of the specimens as well as complete filled cracks. This progressive penetration during the repeated wetting/drying cycles clearly point out the importance of both crack width and circulation of outer solution. Particularly, these results indicate that presence of cracks, with the subsequently ingress of water, leads to the

transport of corrosion products contributing to decrease the level of pressure around the reinforcement bar.

It has to be noted that not all the cracks significantly contribute to the transport process. At the beginning of the corrosion induced damage, cracking of the specimen in vertical direction was observed. These cracks are attributed to the initial high corrosion products pressure (penetration in pores and voids near the reinforcement bar) which tends to increase the induced stresses on the external surface of the specimen in horizontal direction. After that, the cracking is further enhanced by a horizontal crack because the bottom part of the specimen is a plain concrete section and consequently is not subjected to any corrosion induced stress. However, these cracks are not sufficiently interconnected with the vertical ones and cannot contribute directly to the transport of corrosion products.

The previously described behaviour can be observed by visual inspection of the horizontal cracks after splitting of the specimen along them. As can be seen in Fig 3.12, the same specimen A/12 (Fig. 3.11) at the second stage was split along the horizontal crack showing no presence of corrosion products. This demonstrates that the investigated type of cracks, even though in some cases wider than the vertical ones, have no influence on the distribution of rust in concrete but in any case they contribute to increase the saturation of the specimen and the time development of the induced damage.

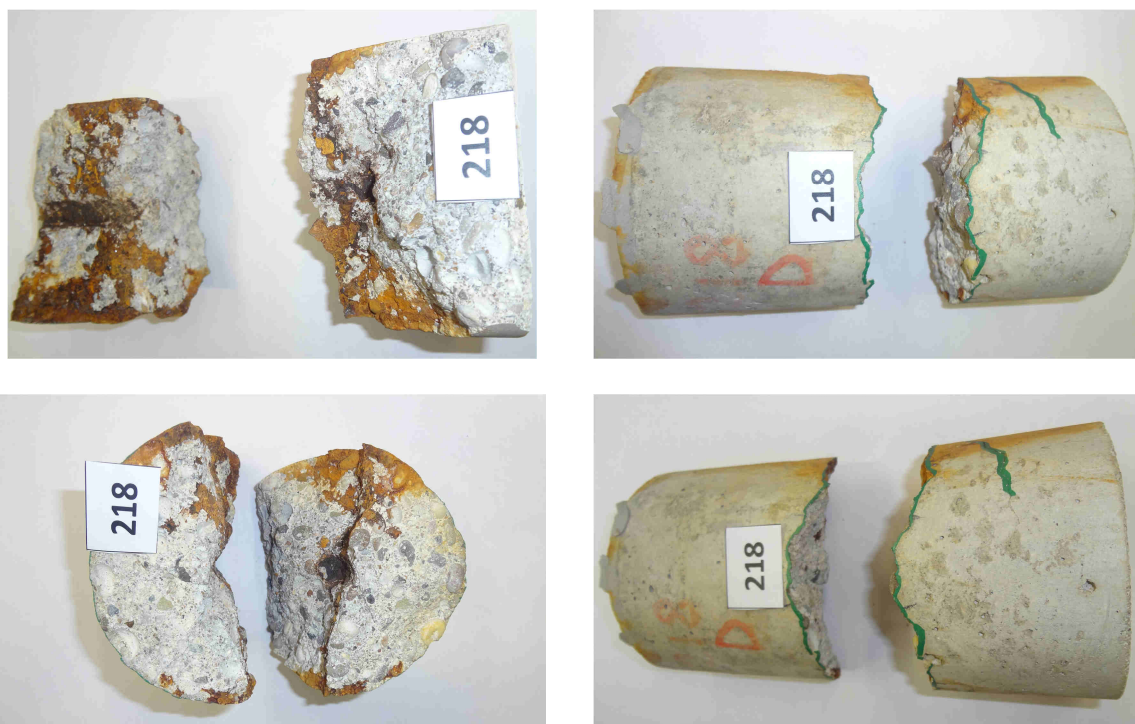


Fig. 3.12 Distribution of corrosion products through cracks at the 2nd corrosion stage for the specimen type A/12 under an imposed electric potential of 700 mV

Since the object of the experiment was to evaluate the effect of the transport of corrosion products through cracks and their penetration in pores and voids in the neighborhood of the reinforcement bar, the cracking initiation and the relative development of the crack width in time was monitored throughout the experiment. Therefore, prior splitting of the specimens, the average width of all the single cracks was measured as described in Section 3.2.2. Moreover, the corrosion penetration was evaluated by means of the measured mass loss after corrosion, as explained in Section 3.2.3.

In order to focus the attention on the crack propagation phase and evaluate the influence of the transport of corrosion products, no measurements of the mass loss was planned before the cracking of the specimens. On the other hand, the time of cracking initiation was constantly checked during the tests (see Table 3.7). Therefore, the critical mass loss and the relative calculated corrosion penetration have to be considered as results of the application of the Faraday's law, assuming 100% current efficiency. In particular, the mass loss at cracking initiation time was computed on the base of the recorded current density in time (see Fig. 3.9).

Table 3.7 Values of the experimentally observed average cracking time and corresponding average computed corrosion penetration on the base of the recorded current density for specimens type A exposed to wetting/drying cycles

| Experimentally observed cracking time and corresponding computed corrosion penetration for specimens type A exposed to wetting/drying cycles | | | |
|--|-----------------------|---|---|
| Specimen type | Average cracking time | Average corrosion penetration, x_{corr} | Average standard deviation, $\sigma_{x_{corr}}$ |
| (-) | (days) | (μm) | (μm) |
| A/8 | 20 | 26.7 | 3.4 |
| A/12 | 23 | 25.2 | 4.8 |
| A/16 | 27 | 22.1 | 2.9 |

As can be seen the cracking time ranges between 20 and 27 days and increases with the decrease of the geometric ratio (c/d). This is possible only because the value of the applied current density is lower when the diameter of the reinforcement bar increases. In particular, this is a consequence of a constant imposed potential of 700 mV, equal for each specimen types, and a small cover range (42 to 46 mm).

For each corrosion stages approximately three specimens were evaluated in terms of mass loss and crack widths. The propagation of the corrosion induced cracks for different levels of corrosion penetration is plotted for the specimen types A/8, A/12 and A/16 in Fig. 3.13.

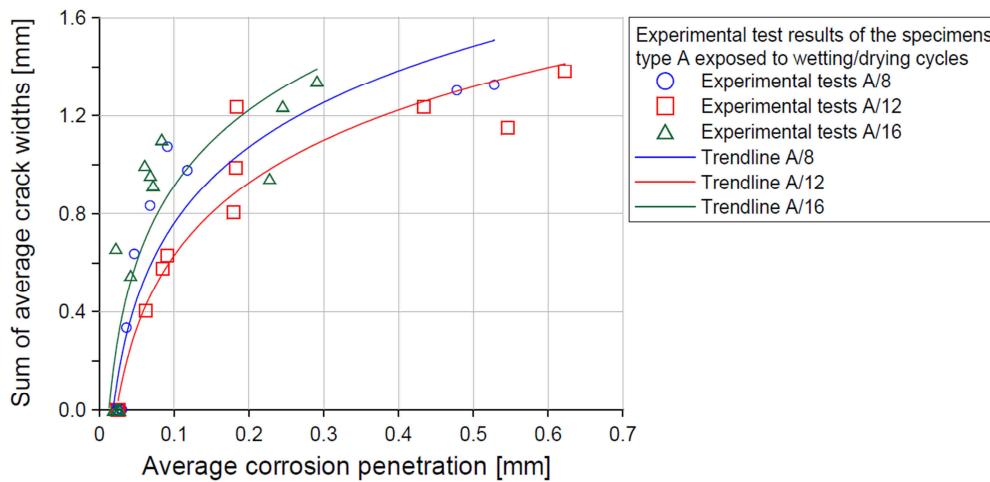


Fig. 3.13 Sum of the average crack widths on the concrete surfaces as a function of the average corrosion penetration for the specimen type A/8, A/12 and A/16 exposed to wetting/drying cycles under an imposed electric potential of 700 mV

As can be noted, for all the investigated geometries the sum of the average crack widths grew very fast for small corrosion penetration, but then the crack growth slows down and the slopes decreases, indicating a reduction of the pressure due to the expansion of the corrosion products. Therefore, it is reasonable to assume that when the crack widths increase, the transport of rust plays the most significant role controlling the corrosion-induced damage of the concrete cover.

The maximum crack width observed is approximately 1.4 mm for all the investigated cases. On the other hand, it can be seen that in case of smaller concrete cover (A/16) the increase of the crack widths is relatively steep in comparison with the other two cases. This behaviour can be attributed to the value of the imposed current density, which is lower because of the large reinforcement area that can significantly influence the development of the corrosion induced damage, as explained in Section 2.3.1.1. The results show also slight differences between the specimens type A/8 and A/12, especially at the beginning of the cracking propagation. In any case a similar logarithmic trend was observed for all geometric ratios.

Comparing the cases of all the investigated geometries, it can be concluded that the results slightly differ in terms of maximum induced damage and trend, except for the specimens type A/16. Namely, the specimen type A/16 show a faster increase of corrosion induced damage at the same level of corrosion depth. This can be attributed to the influence of the imposed corrosion current density and of the diffusion of corrosion products in pores and voids in the vicinity of the reinforcement bar.

3.4.2.2 Test results for the specimen type A: A/8, A/12 and A/16 – submerged specimens

Similar experimental tests, under accelerated corrosion, were carried out keeping the specimens constantly under water throughout the exposure. The resulting current density, except at initial stage, was in this case constant. As already mentioned, this result can be attributed to the low dissolved oxygen concentration. In particular, throughout the application of the imposed potential, the applied current density leads to the reduction of the dissolved oxygen concentration since oxygen itself is continuously consumed at the cathodic area.

Purpose of the described experimental investigations is to investigate the type of corrosion products produced in case of lack of oxygen and impressed electric potential and especially quantify their penetration in pores and voids as well as their transport into corrosion induced cracks. However, nowadays experimental studies of corrosion induced damage are frequently performed by keeping the specimens constantly under water, since currently there is no generally accepted testing method. Some of the tests under laboratory controlled conditions are performed simulating splash conditions and other considering submerged reinforced concrete structures. In general, accelerated corrosion experiments under wetting/drying conditions yields to more realistic results and comparable type of corrosion products with the natural conditions, since corrosion of submerged structures is generally inhibited by the low concentration of dissolved oxygen in immersed parts located far away from the sea level.

The vast majority of the experimental studies also do not consider the nature of the corrosion products formed in submerged concrete specimens. Nevertheless, it is important to characterize corrosion compounds properties and their ability to migrate in pores and cracks to understand the behaviour of immersed structures.

The resulting average current density for the specimen type A/8 was approximately 0.70 A/m^2 , for the specimen type A/12 approximately 0.42 A/m^2 and for the specimen type A/16 an average value of 0.27 A/m^2 was obtained. As under wetting/drying exposure, reducing the geometric ratio (c/d) the values of the average current density decrease because of the different extent of anodic area at the same level of imposed potential confirming that the reinforcement bar diameter is the governing factor in determining the value of the average current density.

The specimens were kept immersed for different duration time, depending on the corrosion stage (see Table 3.4) and specifically 89 days, 175 days and 235 days.

The total duration of the experiment also for the submerged specimens A/8, A12 and A/16 was approximately 8 months. The typical failure mode detected is similar to that obtained

for wetting/drying exposure, although with a higher scatter, and is characterized by two vertical cracks connected by a singular horizontal crack (see Fig. 3.14).

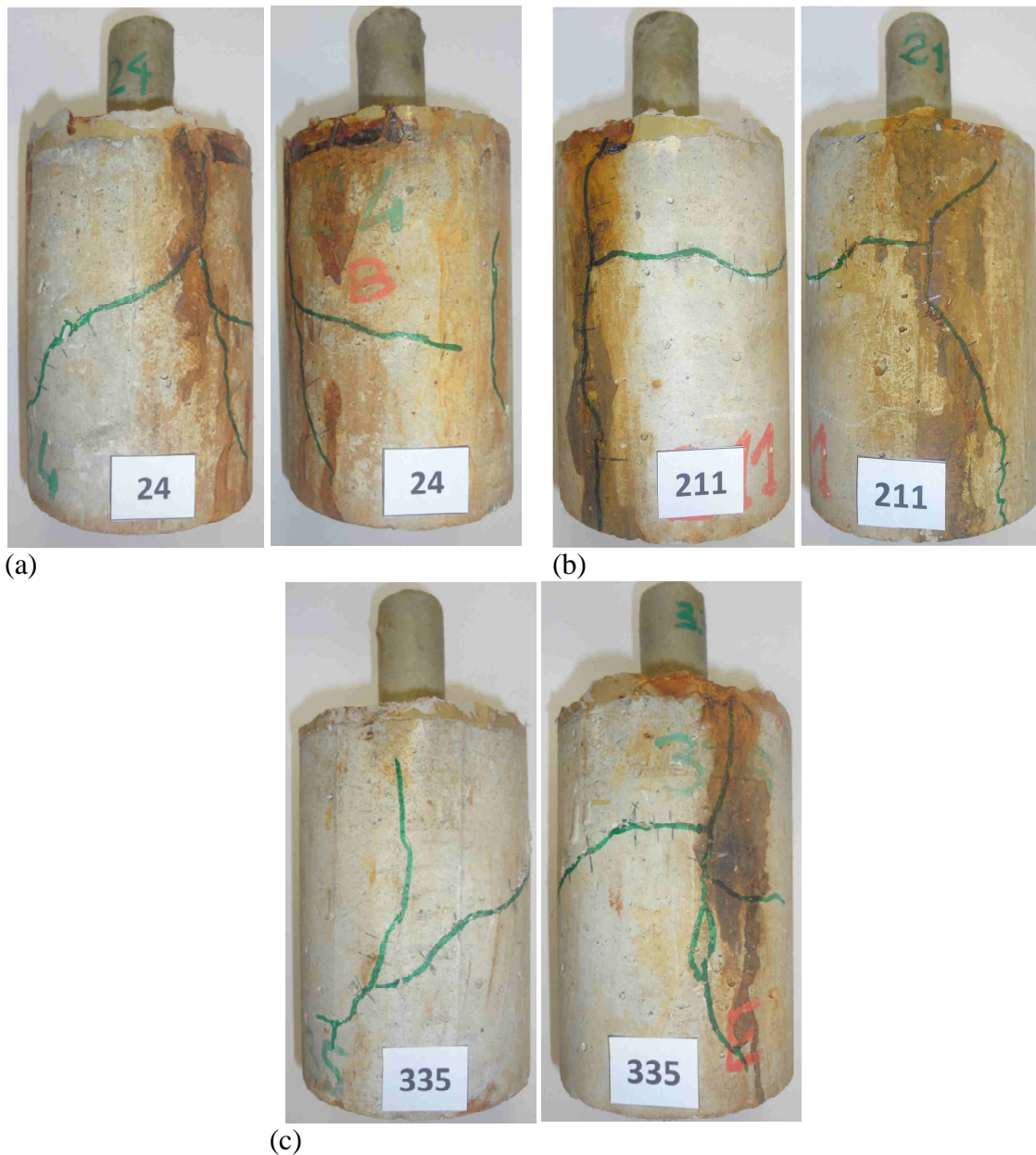


Fig. 3.14 Experimentally observed crack pattern (3rd stage) for the specimen series A/8 (a), A/12 (b) and A/16 (c) constantly submerged in water

Similar to the specimens exposed to wetting/drying conditions, a large ingress of corrosion products in cracks is noted. Differently from the previous case, no circulation of outer solution was possible, since the specimens were constantly submerged in water. Therefore, concentration of corrosion products in cracks and on the adjacent external surface of the specimens was observed. Furthermore, by visual inspection complete different colour of the products was detected, as can be seen in Fig. 3.15. This leads to the conclusion that the compound produced in submerged specimens is magnetite, considering the environmental

conditions poor of dissolved oxygen. In any case, a more accurate examination is needed in order confirm the nature of the products.



Fig. 3.15 Experimentally observed corrosion products (2nd stage), for the specimen type A/16, constantly submerged, some minute after the end of the experiment (approximately 5 months)

To compare the results between the specimens tested under wetting/drying conditions and submerged in water, in terms of cracking initiation and propagation, critical corrosion depth was computed on the base of the current density time history and evaluation of the crack widths on the concrete surfaces as a function of the average corrosion penetration. The values of the average cracking time and resultant average corrosion penetration for submerged specimens are given in Table 3.8.

Table 3.8 Values of the experimentally observed average cracking time and corresponding average computed corrosion penetration on the base of the recorded current density for submerged specimens type A

| Experimentally observed cracking time and corresponding computed corrosion penetration for submerged specimens type A | | | |
|---|-----------------------|---|---|
| Specimen type | Average cracking time | Average corrosion penetration, x_{corr} | Average standard deviation, $\sigma_{x_{corr}}$ |
| (-) | (days) | (μm) | (μm) |
| A/8 | 43 | 82.8 | 11.8 |
| A/12 | 40 | 43.1 | 5.9 |
| A/16 | 56 | 34.1 | 7.0 |

By comparing the exposure conditions, it can be noticed that the results differ both in terms of average cracking time and critical average corrosion. In particular, the submerged specimens show a cracking time characterized by a higher critical corrosion penetration. This indicates that the corrosion products could more easily migrate into pores and voids in the vicinity of the reinforcement bar, considering that in concrete with high water content, rust can more easily diffuse to distant places, as discussed in Section 2.2.5.1.

Furthermore, the difference in terms of corrosion products, which can have a lower expansion factor than in case of splash conditions, would also influence the timing of the corrosion induced damage and the relative corrosion penetration.

The sum of the averaged crack widths on the concrete surface as a function of the average corrosion penetration for submerged specimens, type A/8, A/12 and A/16, is plotted in Fig. 3.16.

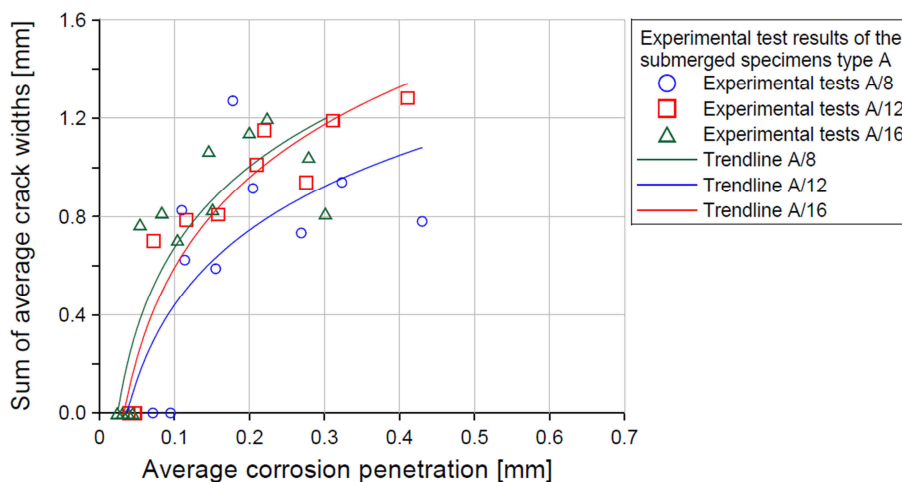


Fig. 3.16 Sum of the average crack widths on the concrete surfaces as a function of the average corrosion penetration for the specimen type A/8, A/12 and A/16 under an imposed electric potential of 700 mV and constantly submerged

The experimentally obtained results show logarithmic trend, as for splash conditions, in terms of crack growing up to maximum average widths of approximately 1.2 mm. With the increase of the corrosion depth, the crack propagation gets slower probably because of the transport of corrosion products. No particular differences can be noted between the types A/12 and A/16 in terms of crack growing. On the other hand, a different response was observed for the specimen type A/8 which shows a less pronounced initial slope and a lower crack width, as average value, at the 3rd corrosion stage.

It can be seen that due to the higher diffusion of corrosion products into pores and voids around the rebar, the crack growth for submerged concrete specimens is slightly slower than in case of wetting/drying exposure. A minor difference can be also found in terms of maximum crack width as well as maximum average corrosion penetration. In particular, the corrosion depth is lower due to the lower value of imposed current density obtained in case of lack of oxygen.

Comparing the investigated exposure with the wetting/drying conditions, it can be concluded that immersed specimens show similar trend (logarithmic) and differ in terms of cracking time and critical corrosion penetration. Slight difference was found comparing crack pattern, crack propagation and maximum induced damage.

3.4.2.3 Test results for the specimen type B: B/8, B/12 and B/16 – wetting/drying exposure

Considering that the main aim of the performed experiments is to calibrate and validate the proposed 3D Chemo-Hygro-Thermo-Mechanical (CHTM) model, investigation of different geometries presents valuable data to verify the model behaviour under different situations. In the following, series of specimen types B/8, B/12 and B/16 are examined under wetting/drying conditions.

The recorded average current density as a function of time for series B/8, B/12 and B/16, exposed to dynamic moisture loading and under an imposed potential of 150 mV, can be found in Fig. 3.17.

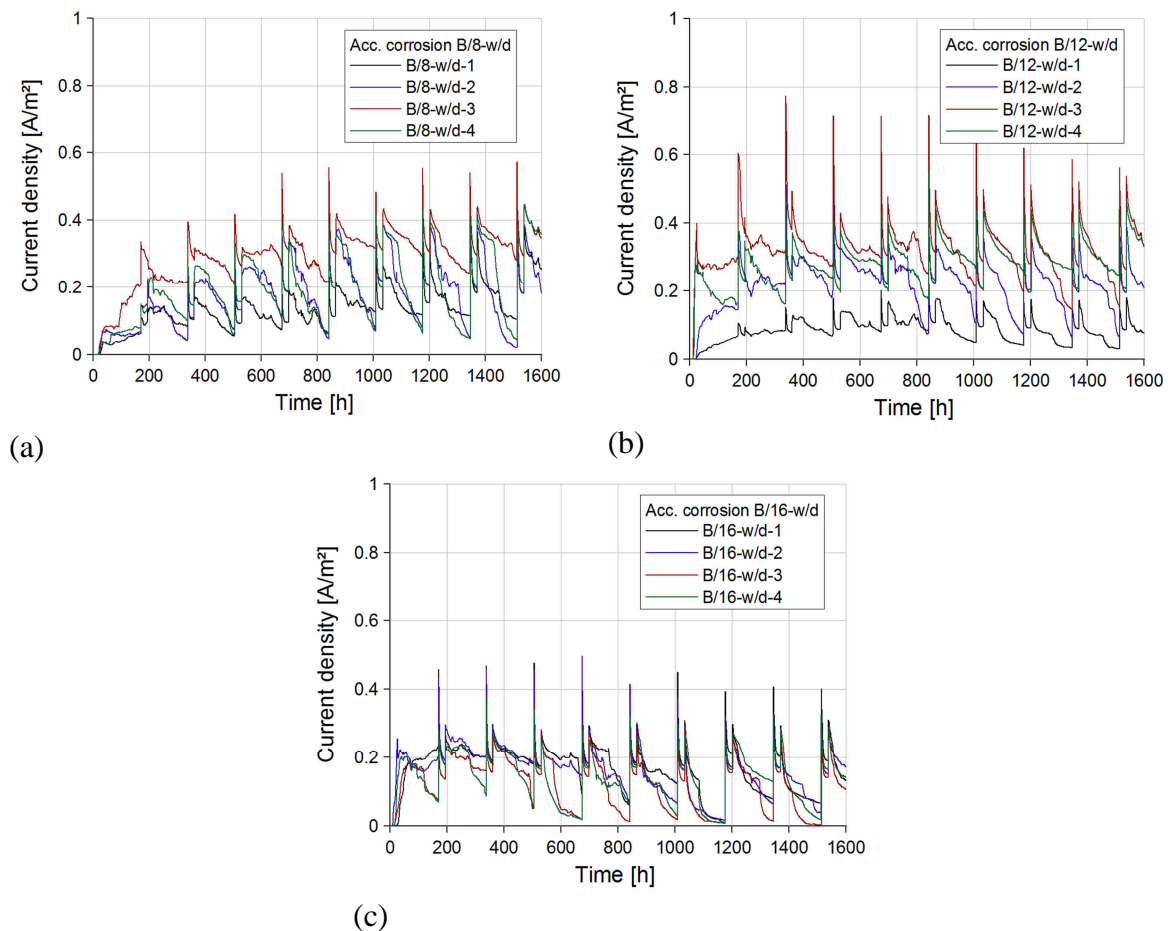


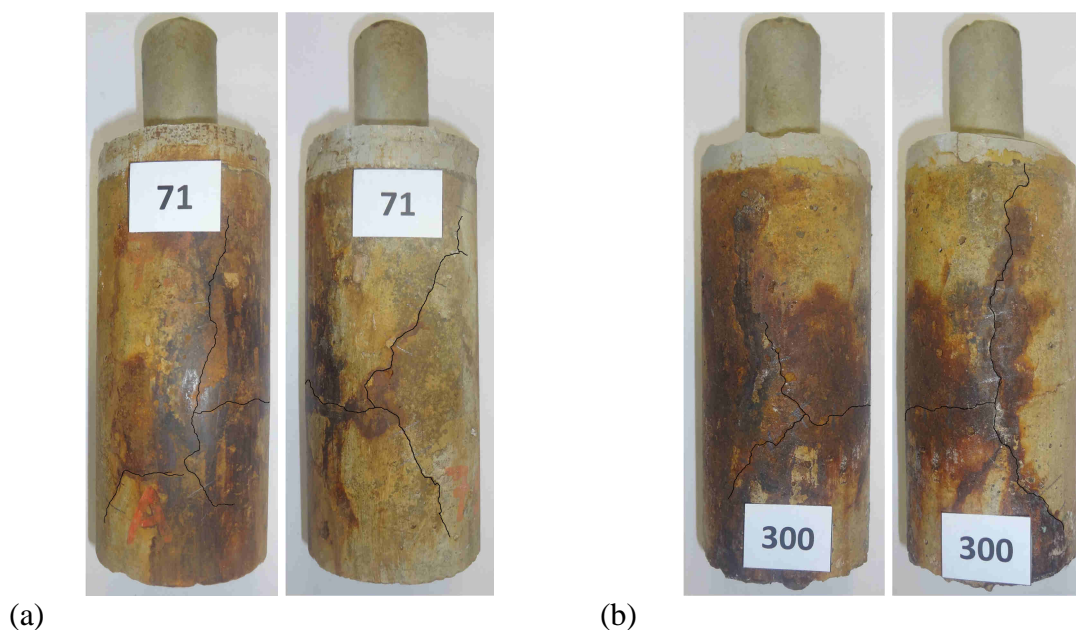
Fig. 3.17 Average anodic current density as a function of time under an imposed electric potential of 150 mV for the series B/8 (a), B/12 (b) and B/16 (c)

The values of current density demonstrate, same as for the specimens of type A, the significant effect of the rebar diameter under constant imposed potential. Similar trend of specimen series A was observed under the wetting and drying phases except for the initial cycles in which a sudden high level of impressed current density is observed for the sample types B/12 and B/16. This can be explained by the thinner concrete cover, which causes a faster increase of water saturation. Furthermore, the results show that with decrease of the concrete cover, lower values of current density during the drying phase can be observed. This means that the moisture content slow decreases, with the ongoing drying, in case of thicker concrete cover leading to the conclusion that for higher geometrical ratio (c/d) cyclic change of moisture has a stronger influence during this period.

Maximum current density observed throughout the experiments is approximately 0.75 A/m^2 , in the peaks of the wetting phase, for the specimen B/12. For the rest of the testing duration current density level is always lower than 0.40 A/m^2 , which is a realistic value if compared with the natural corrosion conditions for concrete manufactured with w/c ratio of 0.7.

As expected, applying a lower electric potential an increase of test duration was observed. The specimens reached the 3rd corrosion stage after approximately 12 months during which the induced damaged was accurately monitored. In particular the crack pattern for each type B/8, B/12 and B/16 are shown in Fig. 3.18.

Similar crack pattern as for the specimen type A is observed. Transport of corrosion products can be noted by visual inspection of the external surface of the samples. As for the previous investigated geometry, it can be stated that the generated cracks in horizontal direction do not directly influence the rust transport.





(c)

Fig. 3.18 Experimentally observed crack pattern (3rd stage) for the specimen series B/8 (a), B/12 (b) and B/16 (c) under wetting/drying conditions

Even though the rust transport in cracks was already deeply investigated for the specimen series A, the study of samples with different geometries is fundamental to demonstrate the influence of the concrete cover on cracking initiation and propagation as well as to describe high complex transport processes, such as moisture behaviour of concrete and diffusion of products into pores and voids. Therefore, average cracking time and critical corrosion depth were examined during the exposure time. Results for the described specimens are summarized in Table 3.9.

Table 3.9 Values of the experimentally observed average cracking time and corresponding average computed corrosion penetration on the base of the recorded current density for specimen types B exposed to wetting/drying cycles

| Experimentally observed cracking time and corresponding computed corrosion penetration for specimens type B exposed to wetting/drying cycles | | | |
|--|-----------------------|---|---|
| Specimen type | Average cracking time | Average corrosion penetration, x_{corr} | Average standard deviation, $\sigma_{x_{corr}}$ |
| (-) | (days) | (μm) | (μm) |
| B/8 | 27 | 13.7 | 3.6 |
| B/12 | 25 | 13.2 | 4.5 |
| B/16 | 26 | 10.8 | 1.4 |

The results indicate similar values of cracking time and a small range of values in terms of critical corrosion depth. This is a consequence of the applied current density which does not differ very much between the three cases, as can be seen in Fig. 3.17. Furthermore,

the results show similar cracking time compared to the samples type A tested under the same exposure. This is a consequence of the lower imposed potential applied to achieve similar cracking time between the considered geometries.

As in the previous analysed cases, crack growing for three different corrosion stages was evaluated. The planned corrosion levels were reached after approximately 80, 240 and 340 days, respectively. The sum of the average crack as function of the corrosion depth is shown in Fig. 3.19.

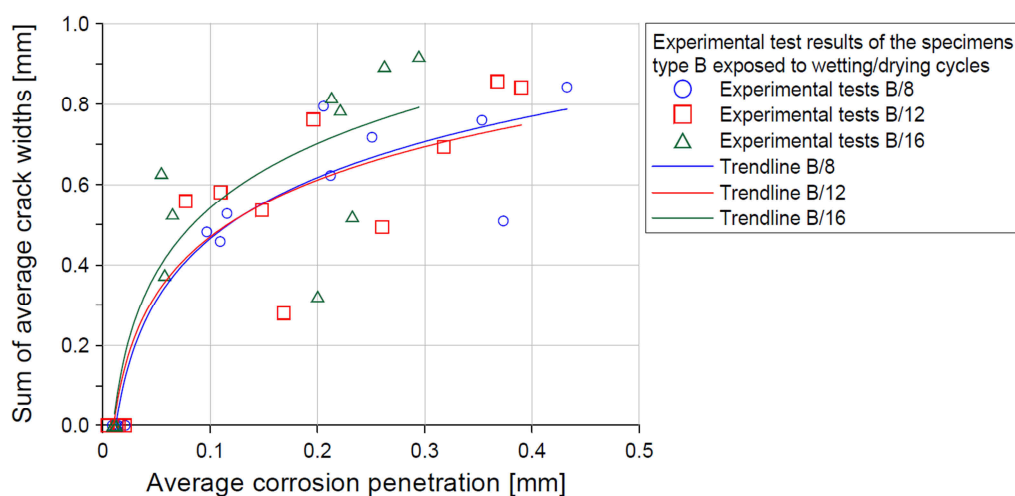


Fig. 3.19 Sum of the average crack widths on the concrete surfaces as a function of the average corrosion penetration for the specimen type B/8, B/12 and B/16 exposed to wetting/drying cycles under an imposed electric potential of 150 mV

It can be noted that the sum of the averaged crack widths, as function of the corrosion penetration, shows logarithmic trend and reaches a maximum value of approximately 0.9 mm, which is much lower compared with the cases of larger concrete cover. Furthermore, increasing of the crack widths as function of the corrosion penetration is lower than in specimens of type A. This indicates a significant influence of the rust distribution on the corrosion induced damage. In particular, reducing the concrete cover, corrosion products can be easily transported in cracks due to the enhanced circulation of outer solution through a shorter crack length. However, it is reasonable to suppose that lower value of imposed current density could also have an influence on the development of the corrosion induced damage. Therefore, it is of great importance to use a numerical model to investigate the progression of damage and evaluate the interaction between different effects, as in this case.

3.4.2.4 Test results for the specimen type B: B/8, B/12 and B/16 – submerged specimens

In the following, experimental results for specimens type B, constantly immersed in water, are shown. Considering the lower electric potential imposed (150 mV), the lower resulting current density due to lack of oxygen and the lower expansion factor of the corrosion products formed in this case, longer test duration was observed.

Crack pattern obtained presented two vertical cracks connected by a singular horizontal crack (see Fig. 3.20).

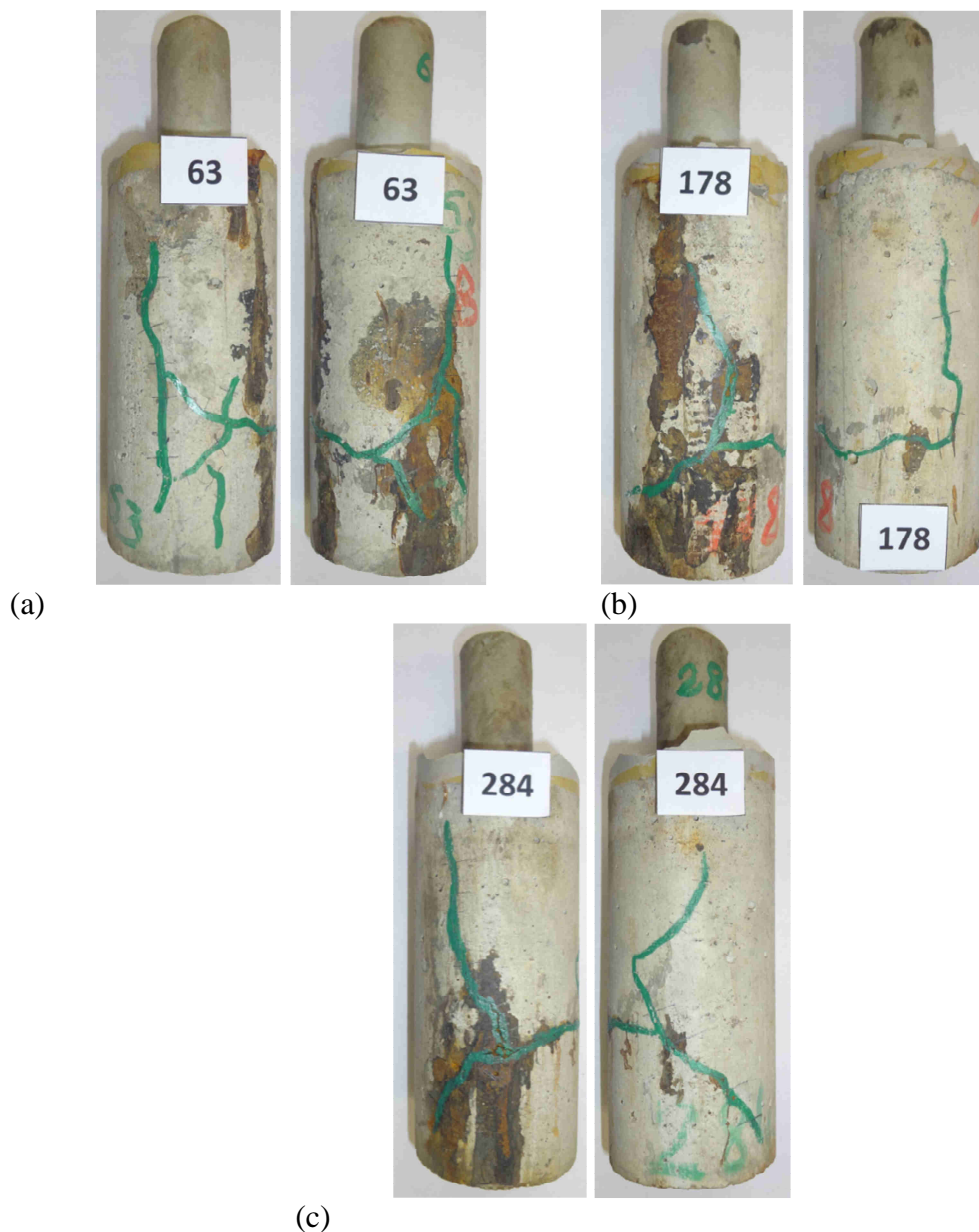


Fig. 3.20 Experimentally observed crack pattern (3rd stage) for the specimen series B/8 (a), B/12 (b) and B/16 (c) constantly submerged

The resulting average current density for the specimen type B/8 was approximately 0.20 A/m^2 , for the specimen type B/12 approximately 0.11 A/m^2 and for the specimen type B/16 an average value of 0.09 A/m^2 was obtained.

The values of the average cracking time and resultant average corrosion penetration for submerged specimens type B can be found in Table 3.10.

Table 3.10 Values of the experimentally observed average cracking time and corresponding average computed corrosion penetration on the base of the recorded current density for submerged specimens type B

| Experimentally observed cracking time and corresponding computed corrosion penetration for submerged specimens type B | | | |
|---|-----------------------|---|---|
| Specimen type | Average cracking time | Average corrosion penetration, x_{corr} | Average standard deviation, $\sigma_{x_{corr}}$ |
| (-) | (days) | (μm) | (μm) |
| B/8 | 77 | 37.3 | 2.9 |
| B/12 | 94 | 32.5 | 5.3 |
| B/16 | 112 | 22.3 | 2.6 |

A large difference can be noted between the average cracking times of the investigated specimens due to the difference in terms of imposed current density. However, a decrease of the critical corrosion depth with the decrease of the concrete cover can be noted. Comparing the values of average corrosion penetration and cracking time for the same specimen type (type B) under two exposure conditions (wetting/drying; constantly submerging), it can be seen that the experimental results confirm the tendency of the corrosion products to easily migrate into pores and voids close to the reinforcement bar, as for the specimens type A.

Total testing period was approximately 15 months. The 1st corrosion stage was reached after approximately 233 days, while the 2nd and the 3rd stages after 358 and 450 days, respectively.

The development of the corrosion induced damage as a function of the average corrosion penetration for submerged specimens, type B/8, B/12 and B/16, is plotted in Fig. 3.21. As for the previous described cases a logarithmic trend can be observed, characterized by a slower increase of the crack width compared with the specimens exposed to wetting drying conditions. However, high data scatter can be noted. A maximum corrosion induced damage of 0.7 mm was detected. Similar response can be noted between the types B/8 and B/12 in terms of crack growing while type B/16 shows a more pronounced initial slope. Comparing with the wetting/drying conditions, it can be concluded that immersed

specimens show similar trend but differ in cracking propagation and time as well as in terms of critical corrosion penetration.

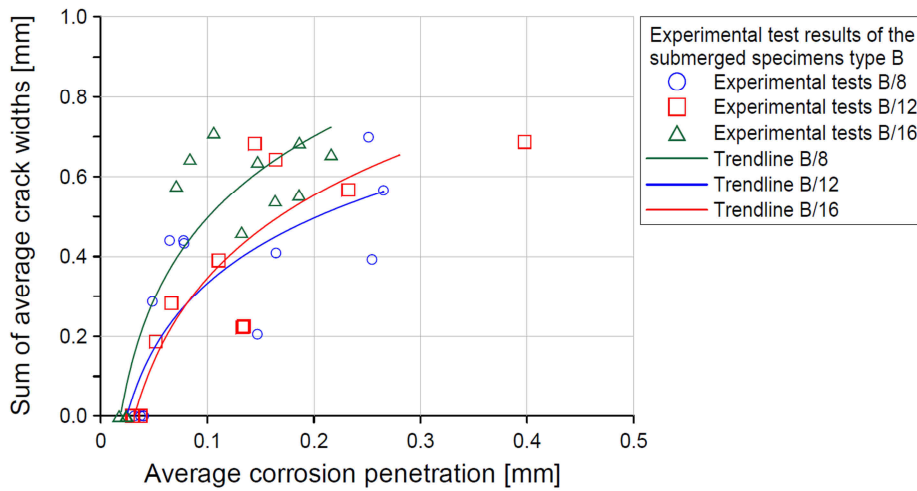
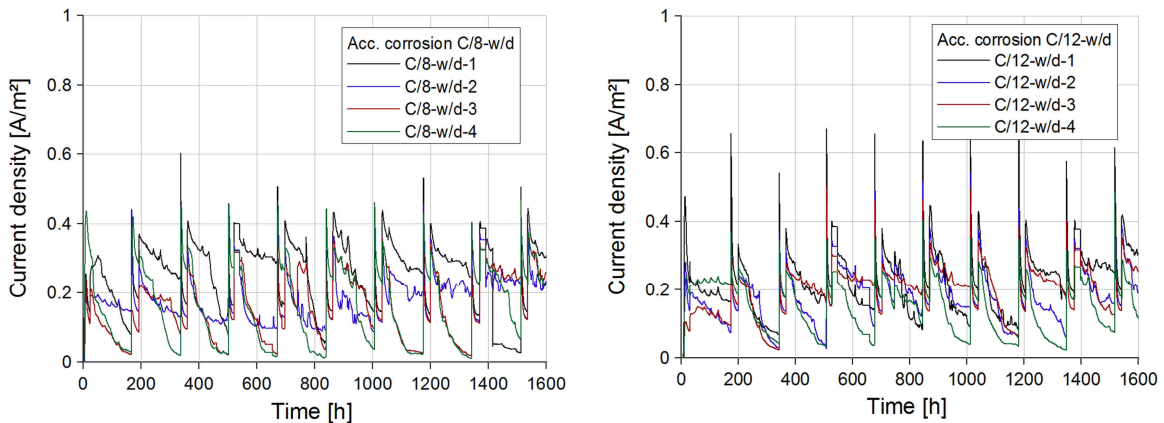


Fig. 3.21 Sum of the average crack widths on the concrete surfaces as a function of the average corrosion penetration for the specimen type B/8, B/12 and B/16 under an imposed electric potential of 150 mV and constantly submerged

3.4.2.5 Test results for the specimen type C: C/8, C/12 and C/16 – wetting/drying exposure

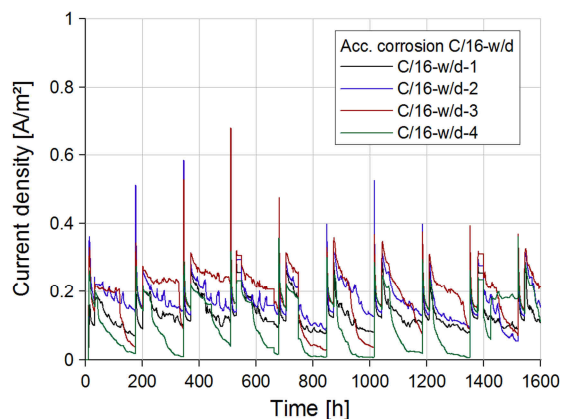
The last batch of samples investigated is composed by the specimens type C/8, C/12 and C/16. In the following, the experimental results for the specimens under wetting/drying conditions are examined. Considering a concrete cover which ranges between 17 and 21 mm, a lower imposed potential than the previous cases was applied (100 mV).

The recorded average current density as a function of time for series C/8, C/12 and C/16, exposed to dynamic moisture loading can be found in Fig. 3.22.



(a)

(b)



(c)

Fig. 3.22 Average anodic current density as a function of time under an imposed electric potential of 100 mV for the series C/8 (a), C/12 (b) and C/16 (c)

As can be seen, values of the resulting current density are very similar to those measured for the specimens type B under the same environmental exposure. Due to the very thin concrete cover, a sudden increase of the current density was recorded during the wetting phase of the first cycle. However, maximum current density in the peaks was approximately 0.60 A/m^2 . Decrease of the current density with increase of the reinforcement diameter can be noted.

Crack pattern was characterized by two vertical and at least one horizontal crack as can be seen in Fig. 3.23.

The duration of the experiments was approximately 13 months during which the 1st stage was reached after 143 days, the 2nd after 269 days and the 3rd after 390 days.



(a)

(b)



(c)

Fig. 3.23 Experimentally observed crack pattern (3rd stage) for the specimen series C/8 (a), C/12 (b) and C/16 (c) under wetting/drying conditions

During the described exposure time, average cracking time was examined and critical corrosion depth could be evaluated on the base of the measured current intensity. Results for the specimens in object are summarized in Table 3.11.

Table 3.11 Values of the experimentally observed average cracking time and corresponding average computed corrosion penetration on the base of the recorded current density for specimen types C exposed to wetting/drying cycles

| Experimentally observed cracking time and corresponding computed corrosion penetration for specimens type C exposed to wetting/drying cycles | | | |
|--|-----------------------|---|---|
| Specimen type | Average cracking time | Average corrosion penetration, x_{corr} | Average standard deviation, $\sigma_{x_{corr}}$ |
| (-) | (days) | (μm) | (μm) |
| C/8 | 22 | 9.8 | 3.2 |
| C/12 | 21 | 7.6 | 2.3 |
| C/16 | 28 | 7.8 | 1.4 |

Due to the thinner concrete cover, the critical corrosion penetration results lower than for the other specimen type. In spite of the very small cover, specimens type C/16 present longer time to crack compared with C/8 and C/12 because of the lower resulting current density.

The effect of a very thin concrete cover on the crack development in time is shown in Fig. 3.24, where the sum of the average cracks as function of the corrosion depth is plotted.

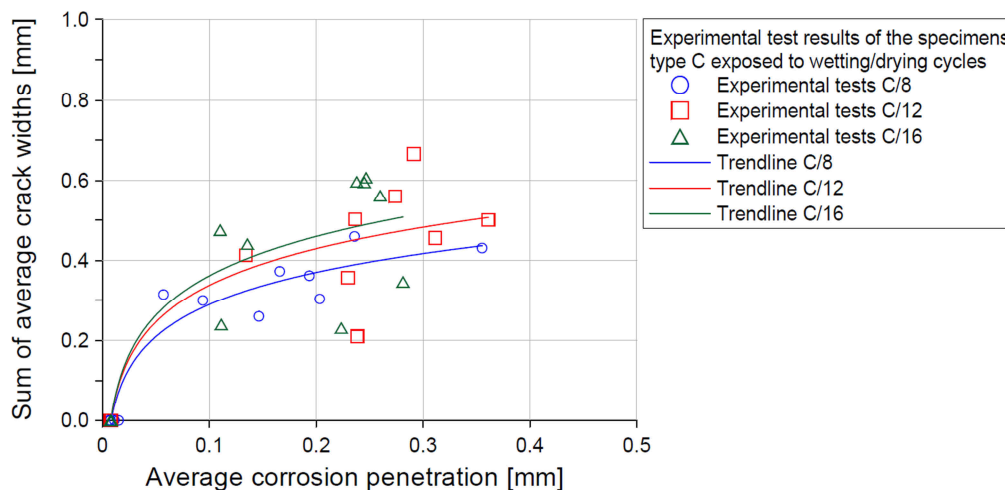


Fig. 3.24 Sum of the average crack widths on the concrete surfaces as a function of the average corrosion penetration for the specimen type C/8, C/12 and C/16 exposed to wetting/drying cycles under an imposed electric potential of 100 mV

As can be seen, the logarithmic trend is much more pronounced than the previous analysed cases and the maximum corrosion damage observed is approximately 0.6 mm. This clearly indicates the influence of the concrete cover on the rust distribution. With the decrease of the concrete cover the outer solution is entering through the cracks in much larger extent leading to a large ingress of corrosion products. This tendency can be confirmed, based on the results obtained for all the specimen types. Specifically, in terms of the maximum corrosion induced crack widths, whose sum is 1.4, 0.9 and 0.6 mm for the specimen type A, B and C, respectively.

3.4.2.6 Test results for the specimen type C: C/8, C/12 and C/16 – submerged specimens

The last case investigated involves the specimen type C constantly immersed in water. As consequence of the very low imposed potential in addition to the lack of oxygen, the duration of the experimental test was longer than in the other proposed cases, i.e. approximately 570 days.

In Fig. 3.25, the corrosion induced damage at the 3rd stage is shown. Considering an applied potential of 100 mV, the measured average current density for the specimen type C/8 was approximately 0.12 A/m², for the specimen type C/12 approximately 0.08 A/m² and for the specimen type C/16 0.07 A/m².

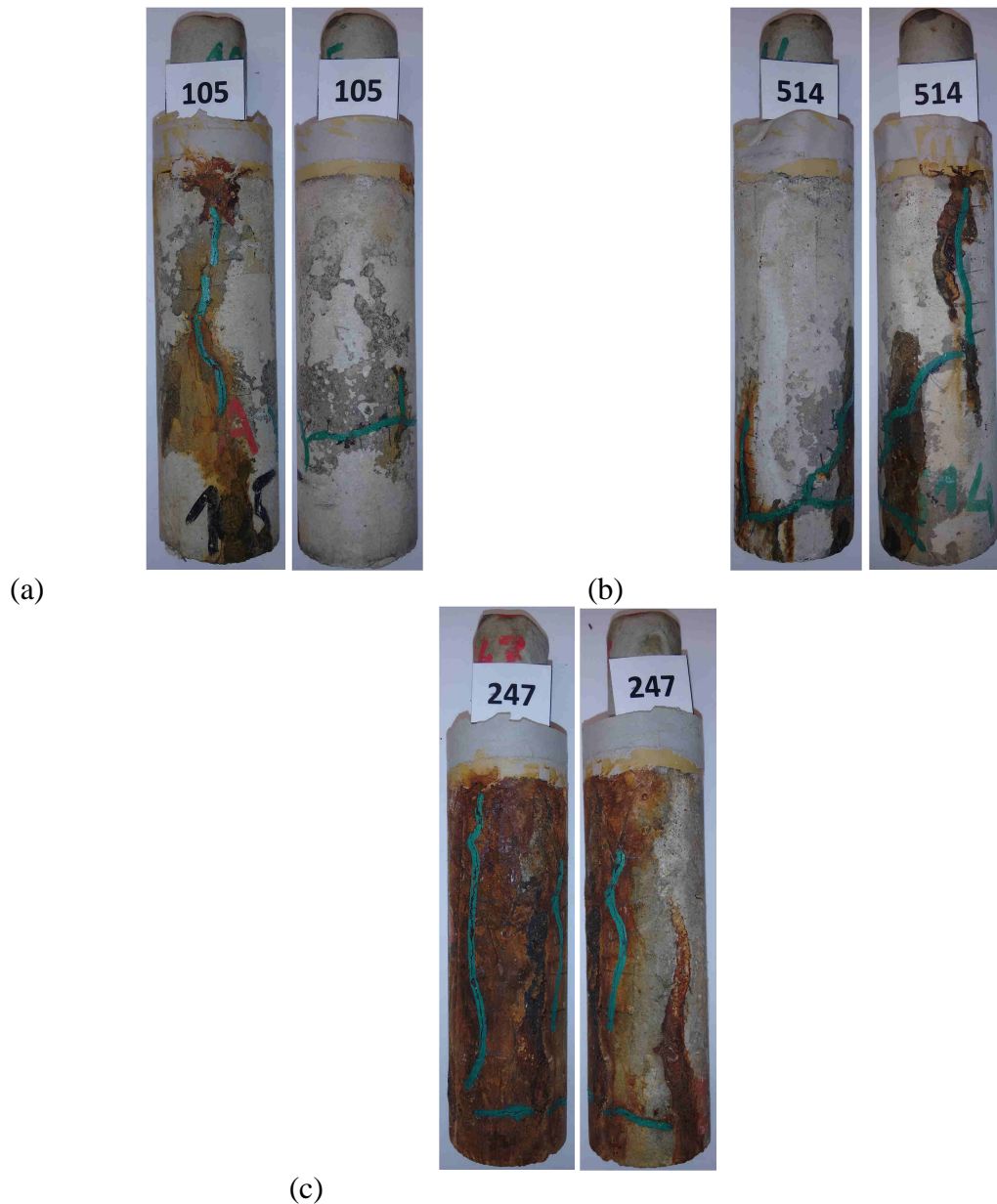


Fig. 3.25 Experimentally observed crack pattern (3rd stage) for the specimen series C/8 (a), C/12 (b) and C/16 (c) constantly submerged

In Table 3.12 are listed the observed values of the average cracking time as well as the average corrosion penetration calculated on the base of the recorded current density.

The detected corrosion penetration resulted higher than in case of wetting/drying exposure, confirming the strong influence of water on the migration of corrosion products in pores and voids before cracking. However, the corrosion penetration which induces damage presented a higher scatter in comparison with the other geometries.

Total testing period was approximately 19 months. The 1st corrosion stage was reached after approximately 300 days, while the 2nd and the 3rd stage after 463 and 547 days, respectively.

Table 3.12 Values of the experimentally observed average cracking time and corresponding average computed corrosion penetration on the base of the recorded current density for submerged specimens type C

| Experimentally observed cracking time and corresponding computed corrosion penetration for submerged specimens type C | | | |
|---|-----------------------|---|---|
| Specimen type | Average cracking time | Average corrosion penetration, x_{corr} | Average standard deviation, $\sigma_{x_{corr}}$ |
| (-) | (days) | (μm) | (μm) |
| C/8 | 83 | 17.1 | 5.9 |
| C/12 | 98 | 20.3 | 5.2 |
| C/16 | 116 | 25.4 | 6.3 |

The crack growth as a function of corrosion depth is shown in Fig. 3.26. As can be seen, the experimental data presents a high scatter even though the logarithmic trend can be captured. Especially type C/12 has shown a large crack width also at medium level of corrosion penetration.

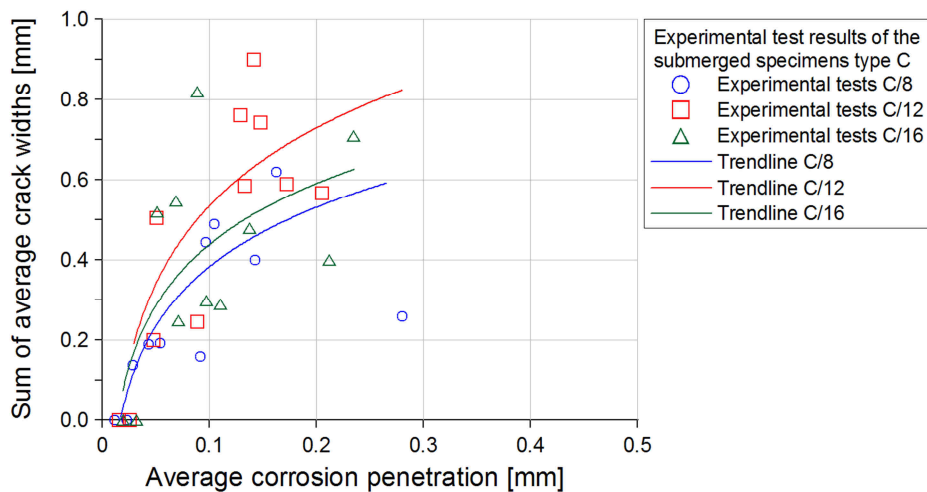


Fig. 3.26 Sum of the average crack widths on the concrete surfaces as a function of the average corrosion penetration for the specimen type C/8, C/12 and C/16 under an imposed electric potential of 100 mV and constantly submerged

3.5 Characterization and distribution of corrosion products in pores and cracks

In previous experimental results (see Section 2.2.4), it was obtained that the reaction and production of corrosion compounds are strongly dependent on the environmental circumstances and presence of chemical reactants. Furthermore, the nature of the corrosion products can differently influence the initiation and development of cracks in concrete. In particular, the experimental results of the present work (see Section 3.4) confirmed the influence, on the corrosion induced damage, on the product types as well as their diffusion in concrete pores and transport through cracks.

However, the study of chloride-induced corrosion products of steel in concrete is a recent topic, especially in case of accelerated corrosion. Even though impressed current or potential technique is in engineering frequently used to induce reinforcement corrosion, the characterization of corrosion products is largely neglected.

In order to correctly interpret the results in case of anodic polarization and make them comparable with the natural conditions, corrosion products formed in the presented experimental tests are examined with Raman spectroscopy. Furthermore, distribution of the corrosion products in the vicinity of the reinforcement and in the neighborhood of the cracks is investigated by means of microscope analysis.

Both, nature of corrosion products and distribution in pores and cracks, are essential to correctly calibrate the corresponding governing parameters of the CHTM model, which are inputs for the numerical model and strongly influence the predicted crack pattern and crack width. Pressure due to their expansion can be interpreted in a wrong way if the type of compounds is not accurately determined as well as their distribution over the concrete domain.

As mentioned by Fischer (2012) the relative volume increase (see Section 2.2.4) has to be considered as a theoretical value, calculated from the molar volumes which results from the quotient of the molar mass and density of the respective compounds. Furthermore, these values are based on analysis of iron minerals under laboratory controlled conditions which can differ from the current morphology of corrosion products and their layered structure.

3.5.1 Microscope analysis and Raman spectroscopy

Microscope analysis and Raman spectroscopy were carried out on different samples (see Table 3.13) to investigate the influence of concrete cover, environmental conditions, and imposed electric potential, on the nature and distribution of the corrosion products. Specifically, to evaluate the migration of the corrosion compounds into concrete pores and cracks at different corrosion levels (1st and 3rd stage), two specimens A/8, under

wetting/drying conditions, were examined. Furthermore, to investigate the effect of different impressed current density, two specimens C/8 under an imposed electric potential of 100 mV and 500 mV, exposed to wetting/drying cycles, were analysed. Finally, a comparison between the corrosion compounds formed in submerged specimens and samples exposed to dynamic moisture loading was possible by inspection of one specimen A/8 kept immersed throughout the experiment.

Table 3.13 Description of the investigated samples, exposure and applied potential for microscope analysis and Raman spectroscopy

| Investigated samples for microscope analysis and Raman spectroscopy | | | | |
|---|---------------|-----------------|-------------------|----------------|
| Specimen | Specimen type | Corrosion stage | Applied potential | Exposure |
| (-) | (-) | (-) | (mV) | (-) |
| MR-1 | C/8 | 1 st | 100 | Wetting/drying |
| MR-2 | C/8 | 1 st | 500 | Wetting/drying |
| MR-3 | A/8 | 1 st | 700 | Wetting/drying |
| MR-4 | A/8 | 1 st | 700 | Submerged |
| MR-5 | A/8 | 3 rd | 700 | Wetting/drying |

The type of corrosion products and the corresponding distribution in space and time were investigated on concrete thin section. The preparation and the relative analyses were performed at the Institute of mineralogy and crystal chemistry, University of Stuttgart. In particular, the selected section were first impregnated, under vacuum, with epoxy resin and later mounted on a glass slide with a curing adhesive. After hardening, the pieces were lapped and polished on a rotary polishing machine equipped with a metal bound diamond grinding wheel. Because of the thickness of the thin section, the steel reinforcement was removed taking care not to damage the corrosion product layer.

The microscope pictures, with different magnification, were taken using a polarizing microscope Zeiss Axioplan with digital photo device Jenoptik ProgRes C10 (see Fig. 3.27a), which can be used for observation of the sample in transmitted light and in reflected light.

For the analysis of the corrosion products Raman spectroscopy was employed. The investigations were carried out with a Raman microscope (Fig. 3.27b) coupled with a confocal polarization microscope, Olympus BX51. Using this equipment, Raman spectra of solids, liquids and gases in very small sample area can be measured (up to 1 μm resolution in diameter). The Raman spectrum is determined by the type of atoms present and strength of their chemical bonding, therefore compounds properties can be identified.

Furthermore, Raman spectra can be also used specifically to identify specimens in microscopic range with a high spatial resolution. Various informations can be obtained from Raman spectra. For instance, the directional change of chemical bond lengths in compressive stress of test specimens can be examined.

The measures were performed on thin sections with a Raman microscope of the company Horiba, model XploRa. Firstly, they were visually examined with 10x magnification and compared with the microscope photos of the samples. Later, after selecting the measuring ranges, specific points were investigated spectroscopically at 50X magnification. The measurements were always carried out starting from the steel area and then following the concrete cracks filled with iron minerals. The adjustment of the measuring points was performed with an electronically controlled table at XYZ-axis control. The input parameters for the Raman spectra were set in the appropriate software. In addition, the spectra were stored electronically and then evaluated with a Data-Processing Software.

Microscope images in the neighborhood of the measuring points were taken as examples to illustrate the distribution of mineral substances. The measurements were taken setting the laser emitting to 532 nm with a power of approximately 2.5 mW, using a 1200 gr/mm grating.

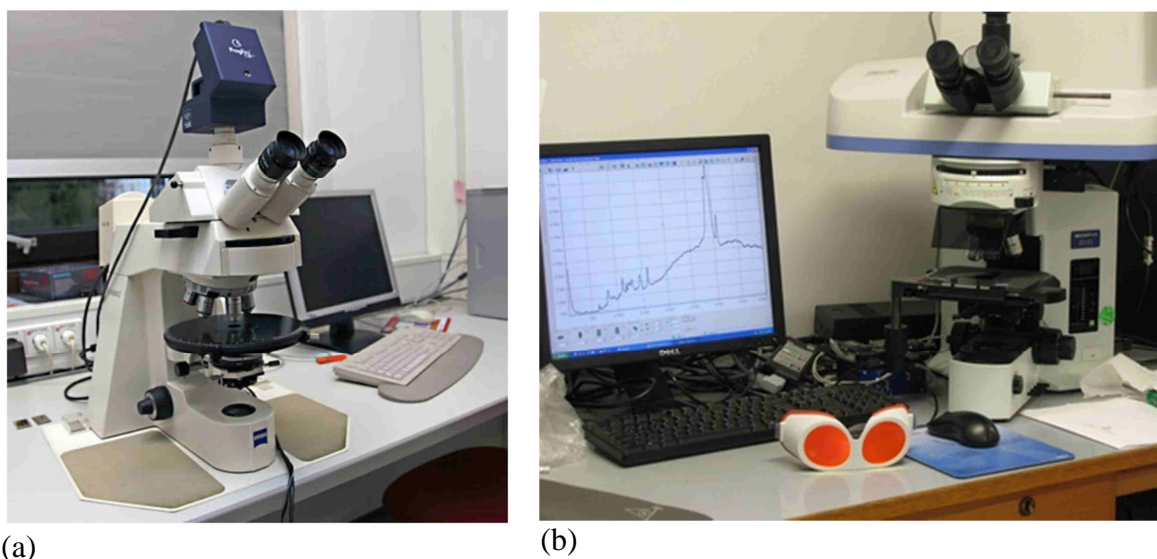


Fig. 3.27 Microscope analysis and Raman spectroscopy: polarizing microscope Zeiss Axioplan with digital photo device Jenoptik ProgRes C10 (a) and Raman microscope of the company Horiba, model XploRa (b)

3.5.1.1 Microscope analysis and Raman spectroscopy results: specimens MR-1 and MR-2

In the following, the results of the microscope analysis and Raman spectroscopy for the cases MR-1 and MR-2 are described.

Figs. 3.28-3.29 and 3.30-3.31 show the microscope photos as well as the determined Raman spectrum in the corresponding measuring point for the sample MR-1 and MR-2, respectively.

By splitting of the corroded specimens and visual observation, the rebar showed corrosion mostly on the entire surface of the rebar. However, non-uniform corrosion depth was observed on the reinforcement, along its length and circumference, with a deeper penetration on the bottom half of the rebar. This can be explained by the heterogeneous nature of concrete, presence of cracks as well as dissimilar distribution of moisture and impressed potential. Furthermore, from the thin sections shown in the following figures, it can be seen that in addition to a circumferentially irregular corrosion penetration also a local uneven corrosion penetration was detected. This is typical for chloride-induced corrosion and can be attributed to presence of pitting corrosion as can be clearly seen in Figs. 3.28 and 3.30.

Moreover, in the cracked region the supply of chlorides and moisture could be increased leading to a strong localization of the corrosion region (see Figs. 3.28 and 3.30) as well as an increase of the concrete conductivity. Similar results can be also found in Poupard et al. (2006). In any case, it has to be noted that both occurrence of corrosion and its distribution over the reinforcement surface are strongly influenced by the environmental conditions (Cairns et al., 2005).

The Raman spectroscopy revealed mostly presence of Goethite and Akaganeite in the layer of corrosion products accumulated at the steel-concrete interface, for the specimen MR-1 and MR-2, respectively.

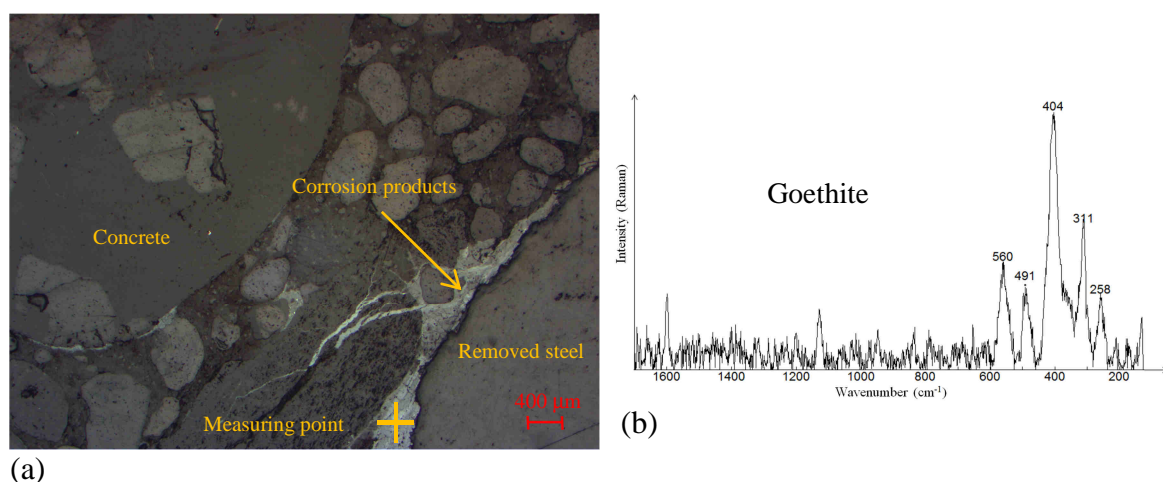


Fig. 3.28 Specimen MR-1: microscope image of the concrete-rebar interface (a) and the corresponding Raman spectrum determined in the measuring point (b)

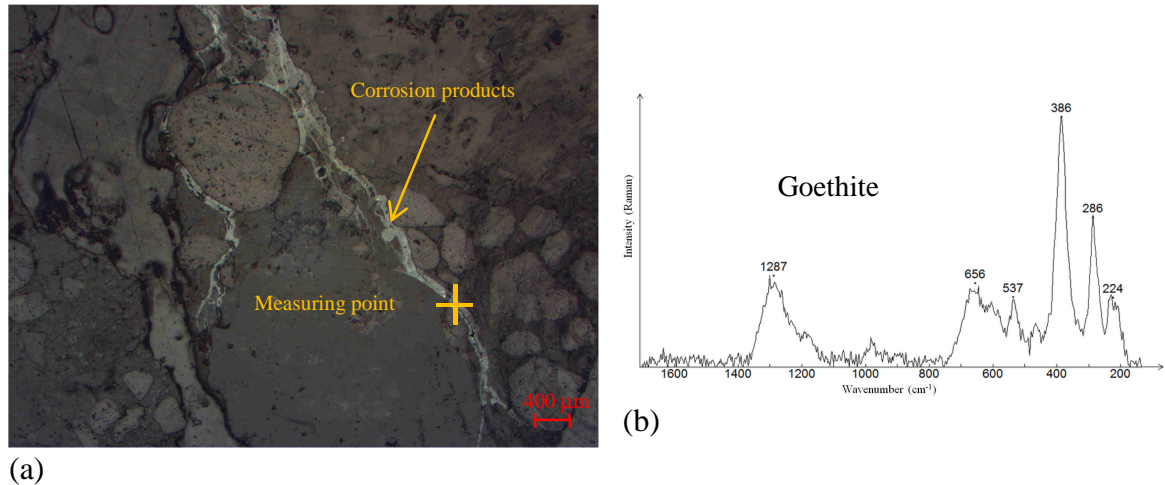


Fig. 3.29 Specimen MR-1: microscope image of a detected corrosion induced crack (a) and the corresponding Raman spectrum determined in the measuring point (b)

A layered structure of products was observed in cracks. This was particularly pronounced in sample MR-2, in which additionally to Akaganeite inclusions of Hematite were found. On the other hand, sample MR-1 exhibited mostly presence of Goethite also in cracks. Moreover, by comparing Figs. 3.29 and 3.31, an accumulation of products on the edge of the cracks can be noted. As can be seen, smaller cracks were completely filled with products especially in the neighborhood of the reinforcement (see Fig. 3.29a).

It can be concluded that a higher imposed current density does not have a strong influence on the expansion factor related to the nature of the corrosion compounds, considering that Goethite and Akaganeite have similar behaviour.

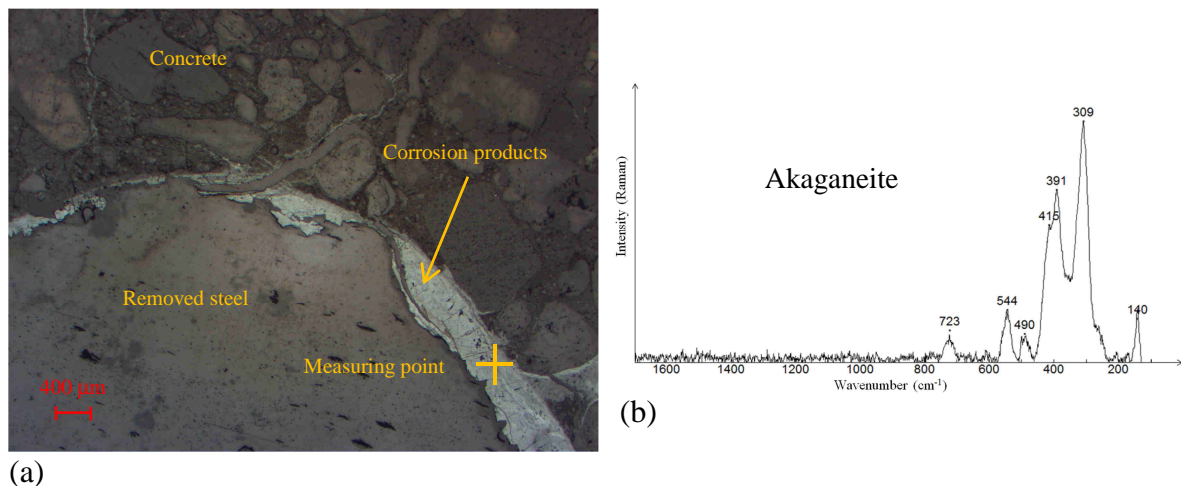


Fig. 3.30 Specimen MR-2: microscope image of the concrete-rebar interface (a) and the corresponding Raman spectrum determined in the measuring point (b)

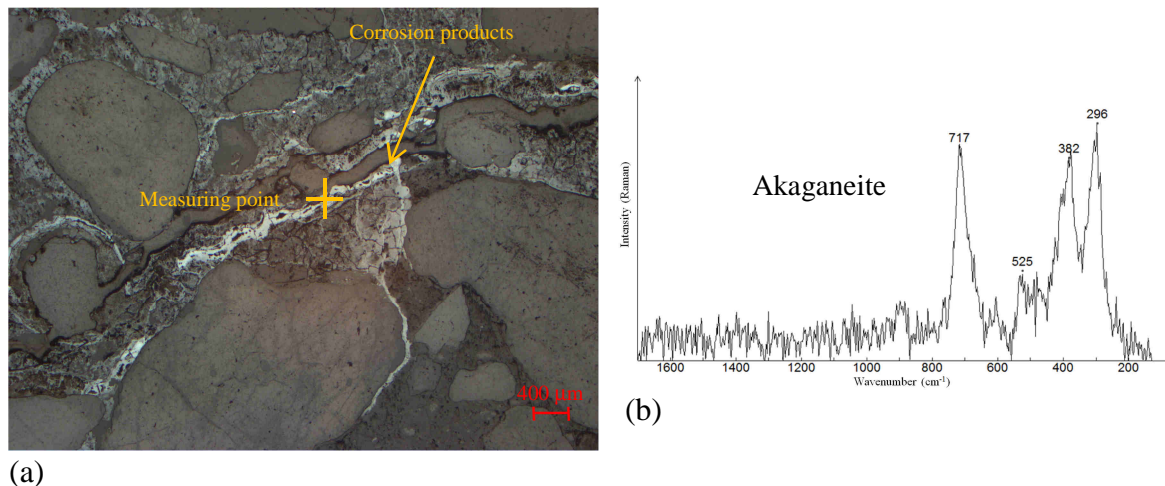


Fig. 3.31 Specimen MR-2: microscope image of a detected corrosion induced crack (a) and the corresponding Raman spectrum determined in the measuring point (b)

3.5.1.2 Microscope analysis and Raman spectroscopy results: specimens MR-3, MR-4 and MR-5

It is well known that presence of chloride ions strongly influences the mechanism and kinetic of the corrosion process involving an intermediate soluble species called “green complexes” (see Wong et al., 2010; Sagoe-Crentsil & Glasser, 1993). These ions dissolve in the concrete pore solution improving their mobility in pores and voids. Therefore, the location of their precipitation is highly influenced from the water content.

The objective of the following microscope analyses is to investigate the influence of the water saturation on the diffusion of corrosion products into pores and voids near the reinforcement bar, by comparing the results between a specimen exposed to wetting/drying cycles and a sample constantly submerged in water. Furthermore, characterization of corrosion products is performed in order to establish the nature of the compounds formed under low oxygen concentration.

In the following, the results of the microscope analysis and Raman spectroscopy for the cases MR-3 and MR-4 are discussed. As can be seen from Fig. 3.32, the products found in the neighborhood of the reinforcement in the sample MR-3 are the same observed in the specimen MR-1. On the other hand, Lepidocrocite and Maghemite were detected in cracks (Fig. 3.33). In general, the presence of Maghemite can be explained by oxidation of magnetite due to the diffusion of oxygen through the pores within concrete and in the oxide layer during the wetting/drying cycle (Poupard et al., 2006). This can be explained by the higher permeability of cracks compared with un-cracked concrete. In particular, it can be supposed that higher level of water content for a protracted wetting period induces the production of Magnetite, further oxidized in short drying stages. These results emphasize the influence of the concrete cover, i.e. the effect of the wetting/drying

exposure on corrosion products in cracks is dependent on the crack length and presumably changes along the depth.

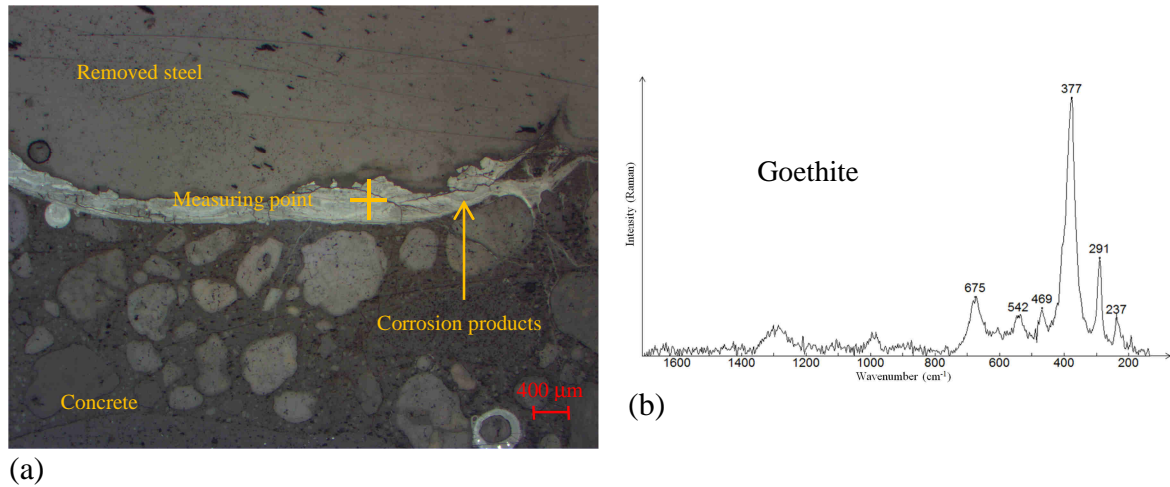


Fig. 3.32 Specimen MR-3: microscope image of the concrete-rebar interface (a) and the corresponding Raman spectrum determined in the measuring point (b)

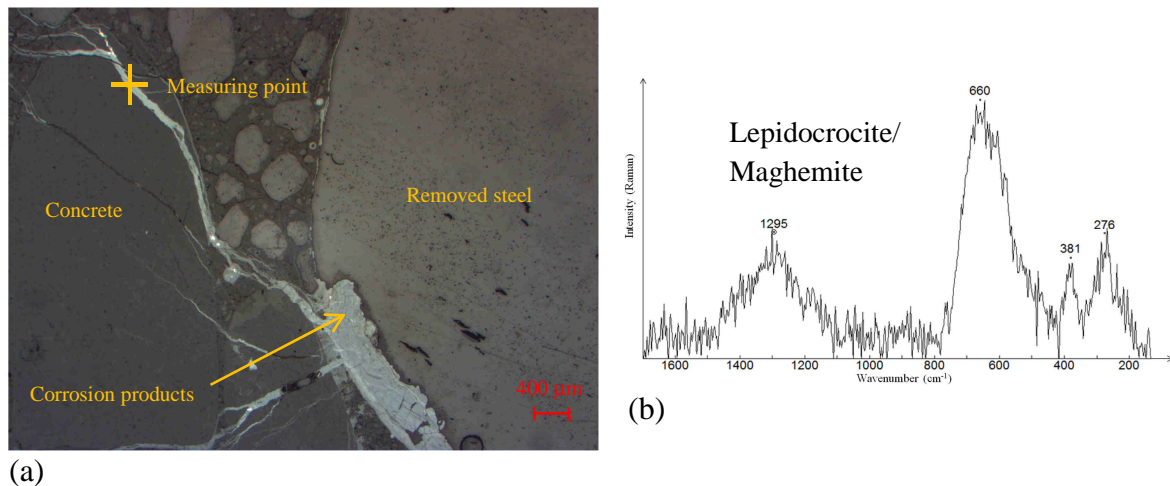


Fig. 3.33 Specimen MR-3: microscope image of a detected corrosion induced crack (a) and the corresponding Raman spectrum determined in the measuring point (b)

In case of submerged specimens MR-4 (Figs. 3.34 and 3.35), principally Magnetite was detected at the concrete/steel interface. As already mentioned, this kind of products is often observed in environment with low concentration of dissolved oxygen.

Furthermore, it can be assumed that specimens constantly immersed in water are subjected to stationary environmental exposure, except for an initial period in which the water content increases up to the complete saturation of concrete. This probably explains why the corrosion products in cracks do not differ from the compounds in the vicinity of the rebar.

Further on, Fig. 3.34 illustrates the penetration in the cement paste for high level of saturation. As can be seen, a more extensive penetration occurred compared with specimen MR-3 (Fig. 3.32), confirming the higher mobility of the intermediate species before precipitation.

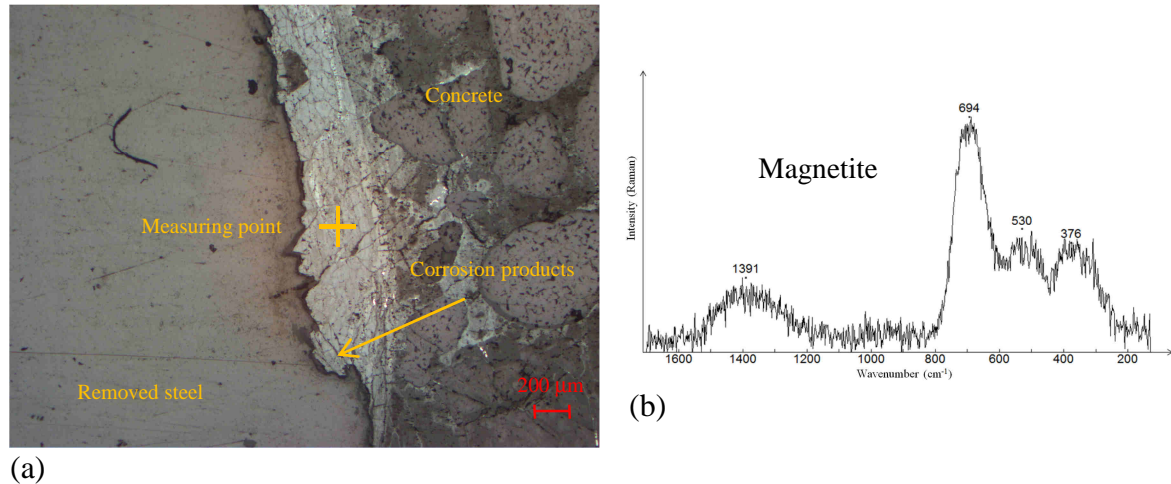


Fig. 3.34 Specimen MR-4: microscope image of the concrete-rebar interface (a) and the corresponding Raman spectrum determined in the measuring point (b)

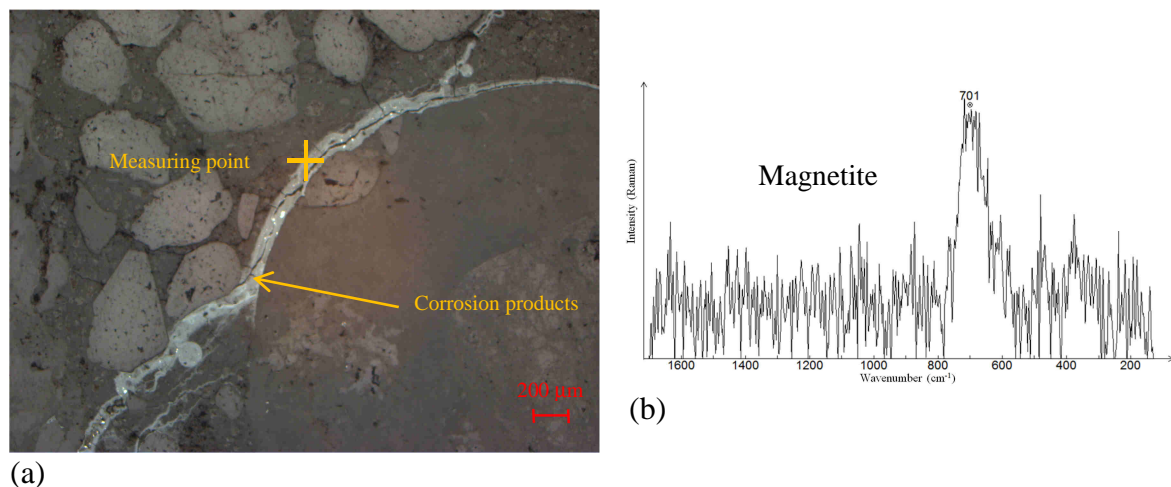


Fig. 3.35 Specimen MR-4: microscope image of a detected corrosion induced crack (a) and the corresponding Raman spectrum determined in the measuring point (b)

Finally, the penetration and distribution of the corrosion products in time were investigated. To highlight the difference between the 1st and the 3rd corrosion stage, a comparison between specimen MR-3 and MR-5 is illustrated. Comparing Fig. 3.36 with 3.32, it can be seen that a thick layer of corrosion products has been accumulated. Furthermore, a high penetration of products in pores is noted confirming the tendency that higher levels of corrosion increase the affected cement paste area (Wong et al., 2010).

Moreover, the cracks can be considered a favorite direction for transport of corrosion products. In particular, after the cover cracking the circulation of the outer solution is much more pronounced at high level of corrosion, in which wider cracks can be noted. This can explain the difference between cracks at the 1st stage (Fig. 3.33a), which are partially filled with products, and cracks at the 3rd stage which result almost empty (Fig. 3.36b).

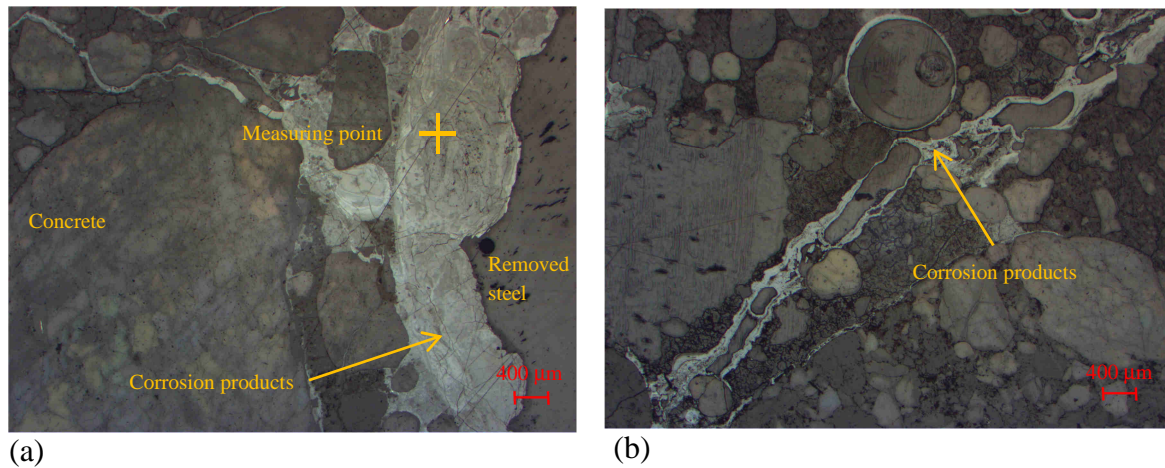


Fig. 3.36 Specimen MR-5: microscope image of the concrete-rebar interface (a) and of the corresponding induced crack (b)

3.6 Summary of the experimental results

Table 3.14 gives an overview of the investigated case, corresponding maximum current density detected and critical cracking time. It has to be noted that the maximum current density has to be considered as the average value of the highest recorded values.

Table 3.14 Type of the investigated specimens, corresponding maximum measured current density and critical cracking time

| Overview of the experimental results | | | | | | |
|--------------------------------------|--------------------|----------------------------------|--------------------------|------------------------|----------------------------------|--------------------------|
| Type | Wetting/drying | | | Constantly under water | | |
| | t_{cr} (days) | i_{max} (A/m ²) | x_{corr} (μ m) | t_{cr} (days) | i_{max} (A/m ²) | x_{corr} (μ m) |
| A/8 | 20 | 1.26 | 26.7 | 43 | 0.70 | 82.8 |
| A/12 | 23 | 1.14 | 25.2 | 40 | 0.42 | 43.1 |
| A/16 | 27 | 0.77 | 22.1 | 56 | 0.27 | 34.1 |
| B/8 | 27 | 0.58 | 13.7 | 77 | 0.20 | 37.3 |
| B/12 | 25 | 0.57 | 13.2 | 94 | 0.11 | 32.5 |
| B/16 | 26 | 0.46 | 10.8 | 112 | 0.09 | 22.3 |
| C/8 | 22 | 0.61 | 9.8 | 83 | 0.11 | 17.1 |
| C/12 | 21 | 0.56 | 7.6 | 98 | 0.08 | 20.3 |
| C/16 | 28 | 0.54 | 7.8 | 116 | 0.07 | 25.4 |

Considering that different imposed potential were used to induce cracking at the same time (100, 150 and 700 mV), no direct comparison can be proposed on the base of the cracking time. On the other hand, it is possible to directly compare the critical corrosion penetration as a function of the geometric ratio c/d (see Fig. 3.37).

As can be seen, an increase of the geometric ratio induces a deeper corrosion penetration due to the higher expansion pressure needed for the cover cracking. However, two different linear trends can be observed. Namely, the submerged specimens show a larger corrosion depth at the same level of geometric ratio. This can be explained on the base of the enhanced diffusivity of the corrosion products at high degree of saturation compared with dry concrete. Furthermore, it has to be considered that different kind of corrosion products were detected for submerged specimens. These results bring to light the importance of the environmental settings in laboratory controlled conditions.

In specimens subjected to wetting/drying cycles mainly Goethite was detected in the dense corrosion layer around the reinforcement rebar. In submerged specimens, presence of Magnetite was observed.

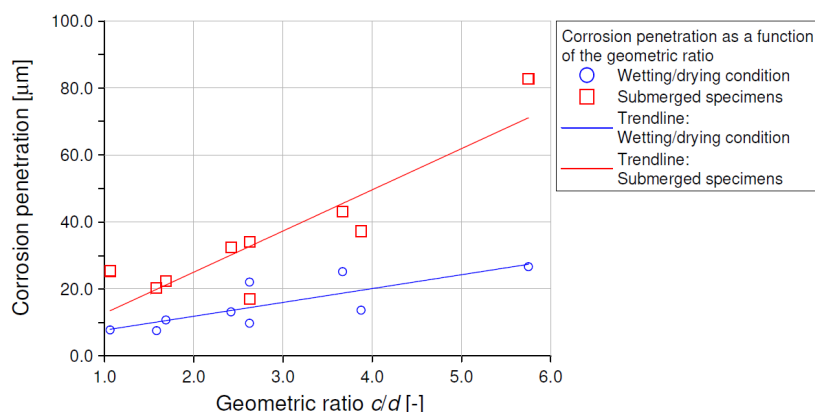


Fig. 3.37 Overview of the experimental tests: corrosion penetration as a function of the geometric ratio c/d

Similar behaviour and crack pattern was obtained for all the tested specimens in terms of crack width as a function of the corrosion penetration. The development of the corrosion induced damage as function of the corrosion depth has shown a logarithmic shape. However, reduction of the maximum crack width was observed with the decrease of the concrete cover. This leads to the conclusion that the circulation of the outer solution has stronger effect on the transport of corrosion products in thinner concrete cover. Furthermore, the crack growth in immersed specimens is marginally slower than in case of wetting/drying conditions.

In terms of impressed current density, a reduction with the increasing of the reinforcement diameter was noticed at same level of imposed potential. This can be explained on the base of the different extent of anodic area. Furthermore, the values are always under the maximum value of 1.00 A/m^2 found in laboratory conditions by Alonso et al., 1998, except for the types A/8 and A/12 exposed to wetting/drying cycles. However, also in the latter cases the current density is most of the time under the proposed threshold.

4. CHEMO-HYGRO-THERMO-MECHANICAL MODEL (CHTM MODEL)

The 3D Chemo-Hygro-Thermo-Mechanical (CHTM) model for concrete used in the present work was developed by Ožbolt et al. (2010, 2011, 2012a,b and 2014) and further improved by Oršanić (2015). The model is able to realistically predict the processes before and after depassivation of steel reinforcement in concrete and it can nicely simulate the hysteretic moisture behaviour of concrete and distribution of chlorides in concrete (Ožbolt et al., 2016).

It is well known that corrosion can be caused by reaching a certain critical threshold of chloride ions in the vicinity of the reinforcement or by concrete carbonation (Tuutti, 1993; Glass & Buenfeld, 1995; Sandberg et al., 1995). As soon as the surface layer of ferric oxide that covers and protects the steel is damaged, corrosion is activated. It has to be noted that in the present work only chloride induced corrosion is investigated.

Corrosion of steel after depassivation can be considered as an electrochemical process with two half-cell reactions which is dependent on electrical conductivity, oxygen concentration dissolved in pore water and saturation level (Bažant, 1979a; Page & Treadaway, 1982). The proposed model couples the physical and electrochemical processes with the mechanical behaviour described by microplane model for concrete with relaxed kinematic constraint (Ožbolt et al., 2001).

Moreover, a further development of the model to bring more light into the effect of different anode/cathode surface positions is discussed in Section 7.

In the presented work, the model is used to predict the corrosion induced damage after depassivation of the reinforcement in natural conditions and under accelerated corrosion. However, a short overview of the simulated processes before and after depassivation can be found in the following. More details on the CHTM model are available in Ožbolt et al. (2010, 2011, 2012a,b, 2014) and Oršanić (2015).

4.1 Non-mechanical processes before depassivation of reinforcement

4.1.1 Transport of capillary water

Due to the fact that concrete is in practice rarely saturated, permeability is not a suitable parameter to describe the transport of capillary water through the concrete. At complete saturation, the suction exerted by concrete is reduced to zero therefore “extended” Darcy equation to formulate unsaturated flow is employed (Bear & Bachmat, 1991):

$$\mathbf{j}_w = K_w(\theta_w)\mathbf{F}_c(\theta_w) \quad (4.1)$$

where $\mathbf{j}_w = \theta_w \mathbf{v}_w$ is the specific water discharge, \mathbf{v}_w is the mean water velocity (m/s), K_w is the unsaturated hydraulic conductivity (m/s), \mathbf{F}_c is the capillary force and θ_w is the volume fraction of pore water ($\text{m}^3_{\text{H}_2\text{O}}/\text{m}^3_{\text{con}}$). Capillary force can be expressed as the gradient of capillary potential:

$$\mathbf{F}_c(\theta_w) = -\nabla\Psi(\theta_w) \quad (4.2)$$

so that the “extended” Darcy equation can be written as

$$\mathbf{j}_w = -K_w(\theta_w)\nabla\Psi(\theta_w) \quad (4.3)$$

As the capillary potential depends on the volumetric moisture content, equation 4.3 reads:

$$\mathbf{j}_w = -D_w(\theta_w)\nabla\theta_w \quad (4.4)$$

where

$$D_w(\theta_w) = K_w(\theta_w)\frac{\partial\Psi}{\partial\theta_w} \quad (4.5)$$

is the water diffusivity (m^2/s).

The mass balance equation for pore water, without source or sink terms, becomes:

$$\frac{\partial(\theta_w\rho_w)}{\partial t} = -\nabla\cdot(\theta_w\rho_w\mathbf{v}_w) = \nabla\cdot(\rho_w\mathbf{j}_w) \quad (4.6)$$

where ρ_w is the density of water. Substituting (4.4) into (4.6), under assumption that $\rho_w = \text{const}$, it follows:

$$\frac{\partial\theta_w}{\partial t} = \nabla\cdot[D_w(\theta_w)\nabla\theta_w] \quad (4.7)$$

Equation (4.7) describes transport of capillary water in terms of volume fraction of pore water in aged concrete. Capillary water diffusivity is a function of moisture content (Leech et al., 2003):

$$D_w(\theta_w) = D_{lm} e^{n\bar{\theta}_w} \quad (4.8)$$

Where $D_{lm}=2.2 \times 10^{-4} \text{ m}^2/\text{s}$ is the limiting magnitude term, $\bar{\theta}_w = (\theta_w - \theta_{wi}) / (\theta_{wd} - \theta_{wi})$ is reduced water content, θ_{wi} and θ_{wd} are initial and saturated water content, respectively, and $n = 6.4$ is the shape term.

4.1.2 Transport of oxygen

Transport of oxygen through concrete will be considered as convective diffusion problem. Oxygen dissolved in the pore water is transported through concrete by molecular diffusion and convection as a consequence of capillary suction and moisture diffusion.

The macroscopic flux $\mathbf{j}_{o,diff}$, due to molecular diffusion of oxygen is expressed as:

$$\mathbf{j}_{o,diff} = -D_o(\theta_w) \nabla C_o \quad (4.9)$$

Where C_o is the oxygen concentration in pore solution ($\text{kg}_{\text{oxygen}} / \text{m}^3_{\text{pore solution}}$) and $D_o(\theta_w)$ is the effective oxygen diffusion coefficient (m^2/s). The macroscopic $\mathbf{j}_{o,conv}$, due to capillary suction and moisture diffusion is expressed as:

$$\mathbf{j}_{o,conv} = C_o \mathbf{v}_w \quad (4.10)$$

The total mass flux of oxygen, \mathbf{j}_o takes the form:

$$\mathbf{j}_o = C_o \mathbf{v}_w - D_o(\theta_w) \nabla C_o \quad (4.11)$$

The mass balance for oxygen in the pore water is given as (Bear & Bachmat, 1991):

$$\frac{\partial(\theta_w C_o)}{\partial t} = -\nabla \cdot (\theta_w \mathbf{j}_o) \quad (4.12)$$

and inserting expression (4.11) into the balance equation (4.12), it follows:

$$\frac{\partial(\theta_w C_o)}{\partial t} = -\nabla \cdot \theta_w (C_o \mathbf{v}_w - D_o(\theta_w) \nabla C_o) \quad (4.13)$$

By combining (4.13) and volume balance equation (4.6), under assumption that $\rho_w = \text{const}$, the equation which describes transport of oxygen through concrete before depassivation of reinforcement is obtained as:

$$\theta_w \frac{\partial C_o}{\partial t} = D_w(\theta_w) \nabla \theta_w \nabla C_o + \nabla \cdot [\theta_w D_o(\theta_w) \nabla C_o] \quad (4.14)$$

The effective oxygen diffusion coefficient (m^2/s) is dependent on pore relative humidity h (Isgor & Razaqpur, 2006a), as indicated in the following expression:

$$D_o(h) = 1.92 \times 10^{-6} p_{cp} (1-h)^{2.2} \quad (4.15)$$

in which p_{cp} is the porosity of hardened cement paste and is expressed as (Isgor & Razaqpur, 2004):

$$p_{cp} = p_c \left(1 + \frac{\frac{a \rho_c}{c \rho_a}}{1 + \frac{w \rho_c}{c \rho_w}} \right) \quad (4.16)$$

Where p_c is the concrete porosity, a/c = aggregate/cement ratio, w/c = water/cement ratio, ρ_c , ρ_a and ρ_w are the densities of cement, aggregate and water, respectively.

4.1.3 Transport of chloride ions

Transport of chloride ions through concrete, before steel depassivation, is also considered as a convective diffusion problem and the total mass flux of chloride ions, \mathbf{j}_c analogous to expression (4.11) may be written as:

$$\mathbf{j}_c = C_c \mathbf{v}_w - D_c(\theta_w, T) \nabla C_c \quad (4.17)$$

where C_c is the concentration of free chloride dissolved in pore solution ($\text{kg}_{\text{Cl}^-}/\text{m}^3_{\text{pore solution}}$), T is temperature and $D_c(\theta_w, T)$ is the effective chloride diffusion coefficient (m^2/s). Due to the fact that part of the chlorides can be bound into cement hydration products, the balance equation for chloride ions in concrete is given by:

$$\frac{\partial(\theta_w C_c)}{\partial t} = -\nabla \cdot (\theta_w \mathbf{j}_c) - \frac{\partial C_{cb}}{\partial t} \quad (4.18)$$

where C_{cb} is the concentration of bound chlorides ($\text{kg}_{\text{Cl}^-}/\text{m}^3$ of concrete).

By combining (4.18) and volume balance equation (4.6), under assumption that $\rho_w = \text{const}$, the equation that describes transport of chloride ions through concrete before depassivation of reinforcement is:

$$\theta_w \frac{\partial C_c}{\partial t} = D_w(\theta_w) \nabla \theta_w \nabla C_o + \nabla \cdot [\theta_w D_c(\theta_w, T) \nabla C_c] - \frac{\partial C_{cb}}{\partial t} \quad (4.29)$$

Mathematical model of chloride binding mechanism by hardened cement paste is given as:

$$\frac{\partial C_{cb}}{\partial t} = k_r (\alpha_b C_c - C_{cb}) \quad (4.20)$$

where k_r is the binding rate coefficient (s^{-1}), $\alpha_b = 0.7$ is constant and shows that there exists a linear relation between concentration of bound and free chloride and also that there is a limit value for bound chloride (Saetta et al., 1993). The dependence of chloride diffusion coefficient on water content and temperature is expressed as:

$$D_c(\theta_w, T) = D_{c,ref} \left[1 + \frac{(1-h(\theta_w))^4}{(1-h_c)^4} \right]^{-1} \cdot \exp \left[\frac{U}{R} \left(\frac{1}{T_{ref}} - \frac{1}{T} \right) \right] \quad (4.21)$$

where, $D_{c,ref}$ is a reference value of D_c evaluated at standard conditions, $h_c = 0.75$, $h(\theta_w)$ expresses dependence of relative humidity on pore water content in concrete according to the adsorption isotherm of a BSB model (Saetta et al., 1993), U is the activation energy of chloride diffusion process (44.6 kJ/mol for $w/c = 0.5$), R is universal gas constant and $T_{ref} = 296$ K.

4.1.4 Heat transfer in concrete

The equation which describes temperature distribution in solid reads:

$$\lambda \Delta T + W(T) - c \rho_{con} \frac{\partial T}{\partial t} = 0 \quad (4.22)$$

where λ is thermal conductivity ($\text{W}/(\text{mK})$), c is heat capacity per unit mass of concrete ($\text{J}/(\text{K}\cdot\text{kg})$), ρ_{con} is mass density of concrete (kg/m^3) and W is internal source of heating (W/m^3).

4.2 Non-mechanical processes after depassivation of reinforcement

The corrosion of steel is activated with the depassivation of reinforcement in concrete. The non-mechanical processes important for the propagation stage of steel corrosion are: (1) Mass sinks of oxygen at steel surface due to cathodic and anodic reaction, (2) The flow of electric current through pore solution and (3) The cathodic and anodic potential.

4.2.1 Oxygen consumption

The oxygen molecules approaching the cathode surface are being reduced to OH⁻ ions which carry the electric current through the pore solution. The number of ions produced per unit surface of cathode and per unit time (electric current density i_c (A/m²)) is equal to:

$$i_c = -FzQ \quad (4.35)$$

where $F = 96486.7$ C/mol is Faraday's constant, $z = 4$ is the number of hydroxyl ions in the oxygen reduction reaction and Q is the number of oxygen molecules reduced per unit surface of cathode and per unit time (mol/m²s). The oxygen diffusion flux at the cathode surface, j_o^c (kg/m²s) can be calculated as follows:

$$j_o^c = -D_o(S_w, p_c) \left. \frac{\partial C_o}{\partial n} \right|_{cathode} \quad (4.26)$$

where n is the outward normal to the cathode surface. A balanced condition is established between the approaching and reacting oxygen molecules, that is:

$$j_o^c = -D_o(S_w, p_c) \left. \frac{\partial C_o}{\partial n} \right|_{cathode} = Q \quad (4.27)$$

or

$$D_o(S_w, p_c) \left. \frac{\partial C_o}{\partial n} \right|_{cathode} = -\frac{1}{Fz} i_c = k_c i_c \quad (4.28)$$

where after converting moles into kg, $k_c = 8.29 \times 10^{-8}$ kg/C.

Similar analogy is applied to the anodic sites, so it can be written:

$$i_a = j_{fn} Fz \quad (4.49)$$

where i_a (A/m²) is the current density at the anode surface, j_{fh} (mol/m²s) is the rate of Fe(OH)₂ production and $z = 2$. The rate of oxygen consumption on the anode is given as follows:

$$j_o^a = -\frac{32}{359.4} j_{fh} = -0.089 j_{fh} \quad (4.30)$$

or

$$D_o(S_w, P_c) \left. \frac{\partial C_o}{\partial n} \right|_{cathode} = -0.089 \frac{1}{Fz} i_c = -k_a i_a \quad (4.315)$$

where after converting moles into kg, $k_a = 4.14 \times 10^{-8}$ kg/C.

4.2.2 Flow of electric current through electrolyte

The mechanism of the ionic transport in solution can be described by the Nernst - Planck equation (Bertolini et al., 2004). In the here presented model, a simplified version of the Nernst-Planck equation is used in which the chemical activity effects are neglected. This is assumed in order to keep the mathematical derivation of equations governing the electric current passing through the electrolyte in the concrete pores as simple as possible. The flux of various ions, \mathbf{j}_i (mol/m²s) through electrolyte in the concrete pores can be described by the following equation (Newman & Thomas-Alyea, 2004):

$$\mathbf{j}_i = -z_i \gamma_i F C_i \nabla \Phi - D_i \nabla C_i + C_i \mathbf{v} \quad (4.36)$$

where index i refers to various ions, γ is mobility of ions, C is concentration of ions, Φ is electric potential, D is diffusivity of ions and \mathbf{v} is flow velocity of electrolyte. The first term in Eq. 4.32 is related to migration of ions in electric field and the second and the third terms are related to diffusion and convection, respectively. The electric current through the electrolyte is a result of motion of charged particles and it can be written as:

$$\mathbf{i}_i = F \sum_i z_i \mathbf{j}_i \quad (4.33)$$

or taking into account the Eq. 4.32:

$$\mathbf{i}_i = -F^2 \nabla \Phi \sum_i z_i^2 \gamma_i C_i - F \sum_i z_i D_i \nabla C_i + F \mathbf{v} \sum_i z_i C_i \quad (4.34)$$

With the assumptions of the electrical neutrality of the system and the uniform ions concentration, the second and the third term are equal to zero and Eq. 4.34 can be rewritten as follows:

$$\mathbf{i} = -\sigma(S_w, p_c) \nabla \Phi \quad \text{with: } \sigma(S_w, p_c) = F^2 \sum_i z_i^2 \gamma_i C_i \quad (4.75)$$

Where \mathbf{i} (A/m²) is vector of the electric current density, σ is electrical conductivity of concrete dependent on degree of water saturation of concrete and concrete porosity.

If the electrical neutrality is accounted for and the electrical conductivity of concrete is assumed as uniformly distributed, the equation of electrical charge conservation (Newman & Thomas-Alyea, 2004) reads:

$$\nabla \cdot \mathbf{i} = 0 \quad (4.36)$$

By substituting Eq. 4.35 into Eq. 4.36 and by assuming that the electrical conductivity is uniformly distributed, the following equation is given:

$$\nabla^2 \Phi = 0 \quad (4.37)$$

For a given boundary conditions, the solution of the Laplace's equation (Eq. 4.37) determines the distribution of electric potential and by using Eq. 4.35 the corrosion current density can be calculated.

4.2.3 Polarization of anode and cathode

In the present model the kinetics of reaction at the anode surface can be estimated according to Butler-Volmer kinetics as follows (Martin-Perez, 1999):

$$i_a = i_{0a} e^{2.3(\Phi - \Phi_{0a})/\beta_a} \quad (4.38)$$

where i_a is the anodic current density (A/m²), i_{0a} is the exchange current density of the anodic reaction (A/m²), Φ is electric potential in pore solution near reinforcement surface (V), Φ_{0a} is the anodic equilibrium potential (V) and β_a is the Tafel slope for anodic reaction (V/dec). Equation 4.38 assumes that the reaction at the anode is only influenced by activation polarization. For the cathodic reaction it is assumed that it is subjected to both activation and concentration polarization. Hence, the kinetics at the cathode site are given by:

$$i_c = i_{0c} \frac{C_0}{C_{ob}} e^{2.3(\Phi_{0c} - \Phi)/\beta_c} \quad (4.39)$$

where i_c is the cathodic current density (A/m²), i_{0c} is the exchange current density of the cathodic reaction (A/m²), C_{ob} is oxygen concentration at the boundary surface of the investigated concrete specimen (kg/m³), Φ_{0c} is the cathodic equilibrium potential (V) and β_c is the Tafel slope for cathodic reaction (V/dec).

4.2.4 Rate of rust production and distribution of corrosion products

Rate of rust production J_r (kg/m²s) and mass of hydrated red rust per related surface (A_r) of rebar m_r (kg), respectively, are calculated as (Martin-Perez, 1999):

$$\begin{aligned} j_r &= 5.536 \times 10^{-7} i_a \\ m_r &= J_r \Delta t A_r \end{aligned} \quad (4.40)$$

where Δt is time interval in which the corrosion is taking place and A_r is the corresponding surface of the steel reinforcement. The coefficient of proportionality between the anodic current density i_a and rate of rust production J_r is calculated using the stoichiometry of chemical reactions and Faraday's law (Martin-Perez, 1999; Ožbolt et al., 2011, 2012a, 2012b).

Recent experimental investigations (Wong et al., 2010; Fischer, 2012) have shown that the penetration of corrosion products into the pores and their relatively large ingress through the corrosion induced cracks around the bar, has a significant effect on the development of corrosion induced damage. The influence can be summarized as: (1) The distribution of rust and radial pressure over the anodic surface is not uniform and (2) Damage due to expansion of products is less pronounced.

The distribution of corrosion product (red rust) R into the pores and through the cracks in concrete has been mathematically formulated as a convective diffusion problem:

$$\theta_w \frac{\partial R}{\partial t} = \nabla \cdot [\theta_w D_r \nabla R] + D_w (\theta_w) \nabla \theta_w \nabla R \quad (4.41)$$

in which D_r is the diffusion coefficient (m²/s) of corrosion product. It is important to note that Equation 4.41 does not directly describe the transport of red rust, but rather the distribution of the rust formed in the concrete pores and cracks as a consequence of soluble species (which can dissolve in concrete pore solution and subsequently migrate in the pores and cracks) reacting with oxygen in the pore water (Wong et al., 2010).

4.3 Hysteretic moisture model for concrete

Concrete elements exposed to natural climate conditions are subjected to periodic changes of the ambient relative humidity (RH), which is defined as the ratio of the partial vapour pressure to the saturated vapour pressure of air at a certain temperature. As the air humidity rises, the corresponding relative humidity in concrete is getting higher and the moisture content is subsequently rising. Similarly, with decreasing RH, concrete is getting drier. The amount of moisture content in concrete for the corresponding RH and temperature of the ambient air, can be obtained from the isotherm curves, which are not same for drying and wetting conditions.

The moisture content can be described as: the water to dry mass ratio, u , the moisture content per m^3 of concrete, w , or as the degree of saturation, S_w (Hansen, 1986). In the case of water to dry mass ratio, water content is determined by weighing a concrete specimen, m_{wet} , and then subsequently drying it at 105°C until the mass is constant, m_{dry} . The water to dry mass ratio or mass water content in $\text{kg}_{water}/\text{kg}_{concrete}$ is determined as follows:

$$u = \frac{m_{wet} - m_{dry}}{m_{dry}} \quad (4.42)$$

The moisture content w per m^3 of concrete ($\text{kg}_{water}/\text{m}^3_{concrete}$) can be calculated from the water to dry mass ratio, u , by knowing the mass density of the concrete specimen, ρ_{con} (Hansen, 1986):

$$w = \rho_{con} u \quad (4.43)$$

The degree of saturation S_w is defined as the ratio of the moisture content to the maximal amount of moisture which material can contain after spontaneous water suction.

4.3.1 Moisture transport

During wetting and drying cycles is assumed that concrete is exposed only to changes in relative humidity, so the macroscopic liquid flow is not included. Transport of moisture through the concrete is described as a vapour transport, which means that for nonsaturated concrete at uniform temperature, moisture flux $\mathbf{j}_{w,mass}$ ($\text{kg}/\text{m}^2\text{s}$) may be expressed as (Kwiatkowski et al., 2009):

$$\mathbf{j}_{w,mass} = -\delta_v(h) p_{v,sat} \nabla h \quad (4.44)$$

where h is relative humidity (dimensionless), $\delta_v(h)$ is water vapour permeability (s) and $p_{v,sat}$ is water vapour saturation pressure (Pa). The mass conservation condition is

$$\frac{\partial w(h)}{\partial t} = \frac{\partial w(h)}{\partial t} \frac{\partial h}{\partial t} = \nabla \cdot (\delta_v(h) p_{v,sat} \nabla h) \quad (4.45)$$

where t is time (s), w is moisture content ($\text{kg}_{\text{H}_2\text{O}} / \text{m}^3_{\text{con}}$) and $\partial w / \partial h \equiv \xi$ is the moisture capacity (derivative of the sorption isotherm).

The main adsorption and desorption isotherms for the investigated concrete are taken as model input data from the experimentally obtained results. If the water content from the input isotherm data is defined in terms of mass water content, u ($\text{kg}_{\text{water}} / \text{kg}_{\text{concrete}}$), the moisture capacity can be introduced into Eq. (4.45) by accounting for the density of concrete in kg/m^3 , ρ_{con} :

$$\frac{\partial w(h)}{\partial t} = \rho_{con} \frac{\partial u(h)}{\partial h} \quad (4.46)$$

and the Eq. 4.45 can be rewritten in the following form:

$$\rho_{con} \frac{\partial u(h)}{\partial h} \frac{\partial h}{\partial t} = \nabla \cdot (\delta_v(h) p_{v,sat} \nabla h) \quad (4.47)$$

The boundary conditions are defined on the exposed surface as follows:

$$\mathbf{n} \mathbf{j}_{w,mass} = \beta_{hum} (h_s - h_{env}) \quad (4.48)$$

where \mathbf{n} is the unit vector normal to the exposed surface, β_{hum} is the surface humidity transfer coefficient (m/s), h_s is the value of the relative humidity at the exposed concrete surface and h_{env} is the given relative humidity of the ambient air.

4.3.2 Water vapour permeability

Values of water vapour permeability $\delta_v(h)$ for unsaturated concrete are taken from Bažant & Kaplan (1996) according to the following expression:

$$\delta_v(h) = a_o f_1(h) \quad (4.49)$$

where a_o is the reference permeability at the temperature of 25 °C. For a mature paste, values range from 10^{-10} to 10^{-14} (s) (Neville, 1973; Bažant, 1975). Function $f_1(h)$ reflects

the moisture transfer within the adsorbed water layers and according to Bažant & Najjar (1972) it is estimated as follows:

$$f_1(h) = \alpha + \frac{1 - \alpha}{1 + \left(\frac{1-h}{1-h_c}\right)^4} \quad (4.50)$$

where $h_c \approx 0.75$ and $\alpha \approx 0.05$ at 25°C.

According to Ochs et al. (2008) the saturation pressure $p_{v,sat}$ can be calculated in a temperature range from 0 °C to 109.9 °C with the following expression:

$$p_{sat,v} = 610.8 \cdot e^{\frac{17.08085 - \vartheta}{234.175 + \vartheta}} \quad (4.51)$$

where ϑ is the temperature in °C.

4.3.3 Empirical model for determining the scanning curves

The solution of differential equation (4.45), i.e. (4.47), gives the distribution of relative humidity, not the content of water in the capillary pores. As the transport of moisture in concrete is a slow process, the different phases of water in the pores of concrete remain almost in thermodynamic equilibrium at any time (Bažant & Najjar, 1972), and the content of free water can be determined using sorption isotherms that relate the relative humidity and content of evaporable water at a constant temperature. However, it is known that for materials such as concrete, there are different curves that relate the relative humidity and free water in the pores during adsorption (wetting) and desorption (drying). In other words, the hysteresis loops are observed during wetting and drying cycles. Thus, for the more accurate calculation of the moisture distribution in the concrete a proper mathematical model of hysteresis phenomenon in cycles of wetting and drying is required.

For hysteretic material, such as concrete, the moisture capacity is determined by the slope of the scanning curves which are located between the main adsorption and desorption isotherms. A simple empirical model, proposed by Pedersen (1990), is used to determine the slope of the scanning curve for the adsorption conditions:

$$\xi_{hys,a} = \frac{0.1(w - w_a)^2 \xi_d + (w - w_d)^2 \xi_a}{(w_d - w_a)^2} \quad (4.52)$$

and for the desorption conditions:

$$\xi_{hys,d} = \frac{(w-w_a)^2 \xi_d + 0.1(w-w_d)^2 \xi_a}{(w_d-w_a)^2} \quad (4.53)$$

where ξ_{hys} is the moisture capacity, i.e. the slope of the scanning curve at a given relative humidity, $\xi_a = \partial w_a / \partial h$ is the moisture capacity at a given relative humidity calculated from the main adsorption isotherm, $\xi_d = \partial w_d / \partial h$ is the moisture capacity at a given relative humidity calculated from the main desorption isotherm, w is the current moisture content, w_a and w_d are moisture contents calculated from main adsorption and desorption curves corresponding to the current relative humidity.

Equation (4.52) is used in (4.45), (4.47) when the water content is rising compared to two previous time steps. Correspondingly, Equation (4.53) is employed when the water content is decreasing compared to the two previous time steps.

The water content during scanning between the main adsorption and desorption isotherms is determined by the following relation:

$$w = w_0 + \xi_{hys} \cdot \Delta h \quad (4.54)$$

where w_0 is the initial moisture content and Δh is the change in the relative humidity which equals the difference between the humidity at time $j+1$ and j , at a spatial point i .

4.3.4 Chloride convective diffusion

The transport of chlorides is formulated here same as in Section 4.1.3, except that the convective flux of chloride ions needs to be expressed in terms of relative vapour pressure. When the concrete surface is exposed to drying and wetting, besides the diffusion contribution to the transport of chloride, the contribution due to water ingress (convection) must be taken into account. Therefore, transport of chloride ions through concrete, before steel depassivation, will be considered as convective diffusion. Free chloride ions in pore water are transported through concrete by diffusion and convection as consequence of moisture transport. The macroscopic flux of chloride $\mathbf{j}_{c,diff}$, due to diffusion is expressed as:

$$\mathbf{j}_{c,diff} = -D_c(\theta_w, T) \nabla C_c \quad (4.55)$$

where C_c is the concentration of free chloride dissolved in pore water ($\text{kg}_{\text{Cl}^-}/\text{m}^3$ of pore solution), $\theta_w = w/\rho_w$ is the volume fraction of pore water (m^3 of water / m^3 of concrete), ρ_w is density of water, T is temperature and $D_c(\theta_w, T)$ is the effective chloride diffusion coefficient (m^2/s). The macroscopic flux of chloride $\mathbf{j}_{c,conv}$, due to moisture transport is expressed as:

$$\mathbf{j}_{c,conv} = C_c \mathbf{v}_w \quad (4.56)$$

where \mathbf{v}_w is the mean water velocity (m/s). Thus, the total mass flux of chloride ions, \mathbf{j}_c , takes the form:

$$\mathbf{j}_c = C_c \mathbf{v}_w - D_c(\theta_w, T) \nabla C_c \quad (4.57)$$

Due to the fact that part of the chlorides can be bound into cement hydration products, the balance equation for chloride ions in concrete is given by (Bear & Bachmat, 1991):

$$\frac{\partial(\theta_w C_c)}{\partial t} = -\nabla \cdot (\theta_w \mathbf{j}_c) - \frac{\partial C_{cb}}{\partial t} \quad (4.58)$$

where C_{cb} is the concentration of bound chloride ($\text{kg}_{\text{Cl}^-}/\text{m}^3$ of concrete). By inserting expression (4.58) into equation (4.57), it follows:

$$\frac{\partial(\theta_w C_c)}{\partial t} = -\nabla \cdot (\theta_w C_c \mathbf{v}_w - \theta_w D_c(\theta_w, T) \nabla C_c) - \frac{\partial C_{cb}}{\partial t} \quad (4.59a)$$

or

$$\theta_w \frac{\partial C_c}{\partial t} = -\nabla \cdot (C_c \mathbf{j}_{w,vol} - \theta_w D_c(\theta_w, T) \nabla C_c) - \frac{\partial C_{cb}}{\partial t} \quad (4.59b)$$

Where $\mathbf{j}_{w,vol} = \theta_w \mathbf{v}_w = \frac{\delta_v(h)}{\rho_w} p_{v,sat} \nabla h$ denotes specific water discharge (volume of pore water per unit area of concrete per unit time). Under assumption that $\rho_w = const$, the mass balance for pore water, without source or sink terms, can be written as:

$$\frac{\partial \theta_w}{\partial t} = -\nabla \cdot \mathbf{j}_{w,vol} \quad (4.60)$$

By combining (4.59b) and balance equation (4.60) we obtain the equation that describes transport of chloride ions through concrete:

$$\theta_w \frac{\partial C_c}{\partial t} = \left(\frac{\delta_v(h)}{\rho_w} p_{v,sat} \nabla h \cdot \nabla C_c \right) - \nabla \cdot (\theta_w D_c(\theta_w, T) \nabla C_c) - \frac{\partial C_{cb}}{\partial t} \quad (4.61)$$

Mathematical model of chloride binding mechanism by hardened cement paste is given as:

$$\frac{\partial C_{cb}}{\partial t} = k_r (\alpha C_c - C_{cb}) \quad (4.62)$$

where k_r is the binding rate coefficient, $\alpha = 0.7$ is constant and shows that there exists a linear relation between concentration of bound and free chloride and also that there is a limit value for bound chloride (Saetta et al., 1993). The dependence of chloride diffusion coefficient on water content and temperature is expressed as:

$$D_c(\theta_w, T) = D_{c,ref} f_1(h(w)) f_2(T) = D_{c,ref} \left[1 + \frac{(1-h(\theta_w))^4}{(1-h_c)^4} \right]^{-1} \exp \left[\frac{U}{R} \left(\frac{1}{T_{ref}} - \frac{1}{T} \right) \right] \quad (4.63)$$

where $D_{c,ref}$ is a reference value of D_c evaluated at standard conditions, $h_c = 0.75$, $h(w)$ expresses dependence of relative humidity on pore water content in concrete according to the model of sorption isotherms, U is the activation energy of chloride diffusion process (44.6 kJ/mol for $w/c = 0.5$), R is universal gas constant and $T_{ref} = 296$ K.

4.4 Chemo-Hygro-Thermo-Mechanical coupling

The governing equilibrium equation for the mechanical behaviour of a continuous body in the case of static loading condition reads:

$$\nabla[D_m(u, \theta_w, T)\nabla u] + \rho b = 0 \quad (4.64)$$

in which D_m is material stiffness tensor, ρb is specific volume load and u is displacement field. In the mechanical part of the model the total strain tensor ε_{ij} is decomposed into mechanical strain ε_{ij}^m , thermal strain, hygro strain ε_{ij}^w (swelling-shrinking) and strain due to expansion of corrosion products ε_{ij}^{corr} :

$$\varepsilon_{ij} = \varepsilon_{ij}^m + \varepsilon_{ij}^T + \varepsilon_{ij}^w + \varepsilon_{ij}^{corr} \quad (4.65)$$

The mechanical strain component can be decomposed into elastic, plastic and damage parts. It is used to calculate the effective stress increments (stress in the solid phase of concrete matrix) and macroscopic stresses increment from the microplane model for concrete (Ožbolt et al., 2001) as a constitutive law.

4.4.1 Microplane model with relaxed kinematic constraint

The constitutive law employed for concrete in this work is microplane model with relaxed kinematic constraint (Ožbolt et al., 2001). The model utilizes the strength of both macroscopic and microscopic models and therefore is known to provide results in very good agreement with the experiments. The model is able to realistically describe microstructural phenomena such as cohesion, friction and aggregate interlock.

Contrary to classical macroscopic type of constitutive laws, which are based on tensorial invariants of stresses and strains, in the microplane model the material response is calculated based on the monitoring of stresses and strains in a number of predefined directions. Integrating microplane stresses in a thermodynamically consistent way, it is possible to calculate macroscopic stress tensor from a known macroscopic strain tensor. The constitutive framework is similar to discrete type of the models (e.g. random particle model) with the difference that the model is formulated in the framework of continuum. The physical concept behind the microplane model was already discussed at the beginning of last century by Taylor (1938). The microplanes may be imagined to represent damage planes or weak planes in the microstructure, such as those that exist at the contact between aggregate and the cement matrix or slip planes in the theory of plasticity as shown in Fig. 3.1 (Ožbolt et al., 2001).

Generally, in macroscopic models the macroscopic strain tensor is related to a macroscopic stress tensor through a constitutive relationship valid at macro level. In the microplane model the macroscopic strain tensor at each integration point is projected

into a number of microplanes in normal and shear directions, which characterize the material behaviour.

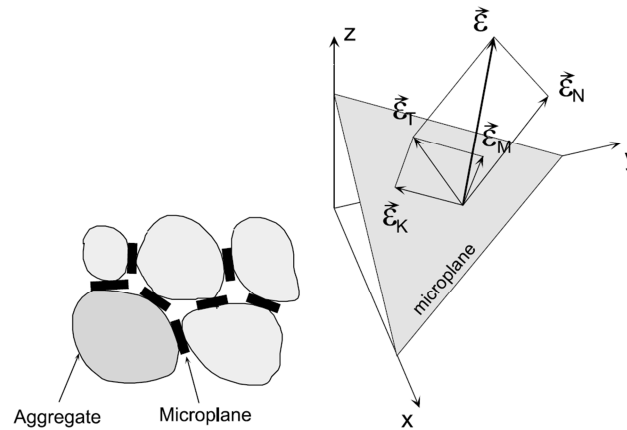


Fig. 4.1 Microplane model: Idealized contact planes (left) and decomposition of the total macroscopic strain tensor on the microplane (Ožbolt et al., 2001) (right)

In the model each microplane is defined by its unit normal vector components n_i . microplane strains are assumed to be the projections of macroscopic strain tensor ε_{ij} (kinematic constraint). Normal (σ_N, ε_N) and two shear stress-strain components ($\sigma_K, \sigma_M, \varepsilon_K, \varepsilon_M$) are considered on the microplane. To realistically model concrete, the normal microplane stress and strain components have to be decomposed into volumetric and deviatoric parts ($\sigma_N = \sigma_V + \sigma_D, \varepsilon_N = \varepsilon_V + \varepsilon_D$). Unlike the most microplane formulations for concrete, which are based on the kinematic constraint approach, to prevent unrealistic model response for dominant tensile load, in this model kinematic constraint is relaxed (Ožbolt et al. 2001).

Fig. 4.2 shows the implementation of the model at the 3D FE level. As shown, for a 3D solid finite element having eight integration points, the macroscopic strain tensor is for each integration point first projected to the microplane and then decomposed into normal and shear microplane directions. Uniaxial stress-strain relations on each microplane are then employed to determine the respective microplane stress components. Finally, using the principle of virtual work, a numerical integration over all microplanes is performed to determine the macroscopic stress tensor.

At the integration point, the number of microplanes considered can have any natural number as a value. Obviously, larger number of microplanes will produce more accurate results but at the same time will need much higher computational effort. A good balance between the computational time and accuracy can be obtained by considering 21 microplanes for the symmetric part of the unit radius sphere, as shown in Fig. 4.2. The major advantage of the model is that, since microplanes with different spatial

orientations have been considered, the tensorial invariant restrictions are automatically fulfilled and they need not be directly enforced.

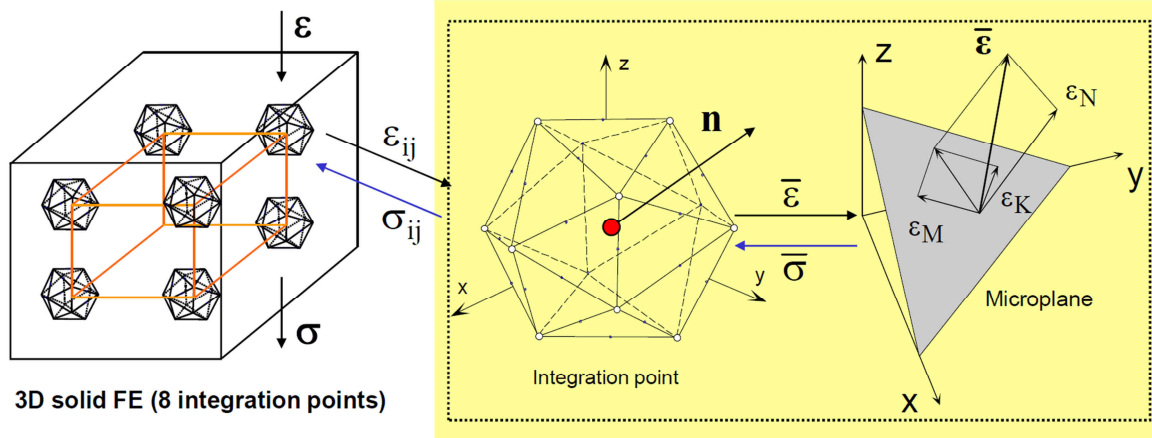


Fig. 4.2 Concept of microplane model: calculation of the macroscopic stress tensor (Ožbolt et al., 2001)

Based on the micro-macro work conjugacy of volumetric-deviatoric split and using in advance defined microplane stress-strain constitutive laws, the macroscopic stress tensor is calculated as an integral over all possible predefined microplane orientations:

$$\sigma_{ij} = \sigma_v \delta_{ij} + \frac{3}{2\pi} \int_s \left[\sigma_D \left(n_i n_j - \frac{\delta_{ij}}{3} \right) + \frac{\sigma_k}{2} (k_i n_j + k_j n_i) + \frac{\sigma_M}{2} (m_i n_j + m_j n_i) \right] dS \quad (4.66)$$

where S = the surface of the unit radius sphere, δ_{ij} = Kronecker delta and k_i and m_i = directions of shear microplane components.

To account for large strains and large displacements, Green-Lagrange finite strain tensor is used. Furthermore, to account for the loading history of concrete, the corotational Cauchy stress tensor is employed. For more detail see Bažant et al. (2000) and Ožbolt et al. (2001).

4.4.2 One-dimensional corrosion contact elements

One-dimensional corrosion contact elements are employed to account for the inelastic strains due to the expansion of corrosion products. They are placed radially around the reinforcement bar surface and their main function is to simulate the contact between reinforcement and the surrounding concrete. These contact elements can take up only shear forces in direction parallel to reinforcement axis and compressive forces perpendicular to the adjacent surface of the reinforcement. The inelastic radial expansion due to corrosion Δl_r is calculated as:

$$\Delta l_r = \frac{m_r}{A_r} \left(\frac{1}{\rho_r} - \frac{r}{\rho_s} \right) \quad (4.67)$$

where $\rho_r = 1.96 \times 10^3$ (kg/m³) and $\rho_s = 7.89 \times 10^3$ (kg/m³) are densities of rust and steel, respectively, r is the ratio between the mass of steel (m_s) and the corresponding mass of rust (m_r) over the related surface of reinforcement A_r that corresponds to the contact element. Note that the ratio between densities of steel and rust is assumed to be 4 in case of red rust (Bažant, 1979a; Cornell & Schwertmann, 1996; Liu, 1996). The stiffness of the rust layer is assumed to be $E_r = 100$ MPa (Zhao et al., 2012b). In the model it is represented by the axial stiffness of the corrosion contact elements. The shear resistance of the contact elements, defined by the bond-slip relationship, is used to model the bond between deformed steel reinforcement and concrete.

4.4.3 Numerical implementation

The equilibrium Equation (Eq. 4.64) is solved by employing the Newton-Raphson iterative scheme. In the finite element analysis cracks are treated in a smeared way, i.e. smeared crack approach is employed. To avoid mesh size dependency the simple crack band approach is employed as a regularization method (Oh & Bažant, 1983). The crack band theory assumes that the crack (damage) is localized in a crack band such that the specific fracture energy consumed by concrete inside the band corresponds to concrete fracture energy. In the finite element analysis the band corresponds to a row of finite elements. The width of the band is equal to the effective element size h . The crack width (opening) is calculated by multiplying maximum principal strain, which is perpendicular to the direction of crack propagation, with the element size h . For more detail see Ožbolt et al. (2001) and (Ožbolt & Reinhardt, 2002).

It should be pointed out that the coupling between mechanical and non-mechanical processes is not performed in explicit sense. It is implicitly accounted for through the incremental finite element analysis and continuous update of mechanical and non-mechanical concrete properties. For instance, the inelastic expansion strains of the corrosion contact elements, calculated from the produced mass of red rust (Eq. 4.67), causes cracking of the surrounding concrete.

On the other hand, the damage (cracks) calculated by using the microplane model (Ožbolt et al., 2001) influences the non-mechanical processes through the continuous update of the model parameters, i.e. the diffusivity coefficients which are formulated as damage dependent. Data related to these dependencies are not available in the literature, due to a challenging task of measuring effects of the cracked concrete on the non-mechanical processes related to the corrosion of the embedded steel reinforcement. Therefore, the shape of the model curve describing the diffusivity dependency on the crack width is based on the experimental results for water permeability in cracked and fully

saturated concrete (Wang et al., 1997; Aldea et al., 2000) shown in Figure 4.3. It can be seen that by reaching a critical crack width ($C_{w,c} = 0.2$), the permeability increases up to its maximum value, that is up to three orders of magnitude greater than its initial value. For further increase of the crack width (open crack), permeability is assumed to be constant due to the numerical reasons. For more detail see Ožbolt et al. (2010).

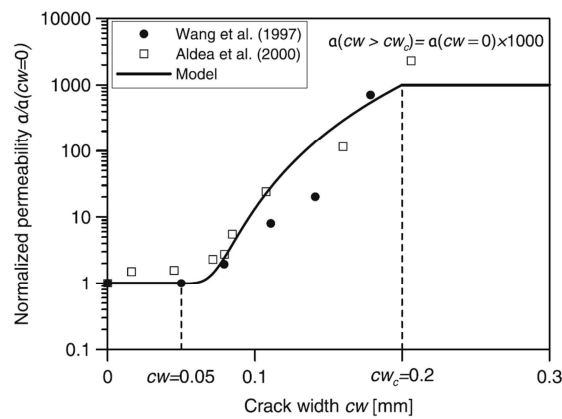


Fig. 4.3 Normalized water permeability of concrete as a function of crack width (Ožbolt et al., 2010)

4.5 Entropy production in corrosion processes of steel reinforcement in concrete

It has been demonstrated that the position and size of anode and cathode strongly influences the crack pattern and the corrosion rate Ožbolt et al. (2012a, 2014). Currently there is no algorithm which can predict the combination between anode and cathode surfaces on reinforcement that results to the highest corrosion induced damage. Therefore, to investigate this influence the expression for maximum entropy production, deduced from irreversible thermodynamics, is formulated. The entropy is produced by dissipative processes, which are in this special case the flow of ions through the electrolyte, the anodic and cathodic polarization and the diffusion oxygen process. Through several numerical examples, in which the size and position of anodic and cathodic surfaces are varied, is demonstrated that maximum entropy leads to maximum corrosion induced damage.

In current computations of corrosion rate of steel in concrete cathodic and anodic areas are determined in advance. If these areas cannot be determined experimentally, the corrosion rate cannot be calculated properly without additional conditions. Such additional conditions could be deduced from irreversible thermodynamics using the principle of maximum entropy production (or the principle of maximum dissipation of energy) generated in the dissipative processes such as mass transfer through porous media, the flow of ions through the electrolyte and cathodic and anodic polarization. Assuming that the temperature of the domain under consideration is uniform over entire domain (isothermal problem), the energy dissipation due to heat transfer through the porous media is not considered. Based on the above assumptions in the following the mathematical formulation of the processes relevant for the propagation stage of steel corrosion in concrete is presented.

4.5.1 Energy dissipation analysis

In order to calculate rate of energy dissipation per unit volume of corrosion cell and energy dissipation per unit surface of anode and cathode, the differential Eqs. (4.14) and (4.37) have to be iteratively solved. Then, knowing the scalar fields for each time step (oxygen concentration and electrical potential) and their gradients, using Eqs. (4.38) and (4.39), the source terms of energy dissipation rate can be evaluated. According to (Naterer et al., 2006; Hansen & Kjelstrup, 1996; Kjelstrup & Bedeaux, 2008), the specific energy dissipation rate in the corrosion cell is composed of energy dissipation rate due to oxygen diffusion, ohmic losses and anodic and cathodic polarization:

$$\dot{Q} = \dot{Q}_{diff} + \dot{Q}_{ohm} + \dot{Q}_{polar,a} + \dot{Q}_{polar,c} \quad (4.68)$$

The first term, which represent volumetric energy dissipation rate due to oxygen diffusion, can be written as follows:

$$\dot{Q}_{diff} = -\mathbf{j}_o \nabla \mu_T \quad (4.69)$$

where $\mathbf{j}_o = -D_o \nabla C_o$ is oxygen flux vector and $\mu_T = RT \ln C_o f + const$ is chemical potential at constant temperature (R is universal gas constant, T is temperature and f activity coefficient) (Kjelstrup & Bedeaux, 2008). The expression for the chemical potential is obtained assuming that the activity is equal to the product of concentration of the solution and the activity coefficient. Furthermore, the solution behaves approximately ideally for low concentration, therefore the activity coefficient $f \approx 1$. After converting moles into kg and short computation, taking into account the above considerations, Eq. (4.69) can be written as:

$$\dot{Q}_{diff} = D_o RT \frac{1000}{32} \frac{(\nabla C_o)^2}{C_o} \quad (4.70)$$

The electrical resistance of the corrosion cells depends on its geometry, electrical conductivity of the electrolyte and electrode. Since the electrical conductivity of metals is significantly higher than the electrical conductivity of the electrolyte and that the electrodes of the corrosion cells are located next to each other, the ohmic resistance through the anode and cathode will be assumed as negligible, i.e. the second term of Eq. (4.68), which is the volumetric energy dissipation rate due to the flow of ions through the electrolyte can be expressed as:

$$\dot{Q}_{ohm} = -\mathbf{i} \nabla \Phi = \sigma (\nabla \Phi)^2 \quad (4.71)$$

A non-equilibrium thermodynamics can be defined for surface where the excess properties of the surface are essential in defining equations governing dissipated energy. For the electric current density \mathbf{i} at the electrode – solution interface, such an excess of the normal component of the electric field may occur and can be identified with overpotential η . In electrochemistry, this phenomenon is known as polarization. The value of the overpotential can be considerably higher than the potential difference over a comparable distance in the bulk regions.

The third and the fourth terms in Eq. (4.68), relating the rate of energy dissipation due to the polarization of the anode and cathode, can be written, using Eqs. (4.38) and (4.39), as (Hansen & Kjelstrup, 1996):

$$\dot{Q}_{polar,a} = i_{na} \eta_a = \frac{\beta_a}{2.3} i_{na} \ln \left(\frac{i_{na}}{i_{0a}} \right) \quad (4.72)$$

$$\dot{Q}_{polar,c} = i_{nc} \eta_c = -\frac{\beta_c}{2.3} i_{nc} \ln \left(\frac{i_{nc}}{i_{0c}} \cdot \frac{C_{ob}}{C_o} \right) \quad (4.73)$$

where i_{na} and i_{nc} is the normal component of the electric current density at the anode and cathode surface, respectively.

The total rate of energy dissipation in a given volume of corrosion cell and electrode surfaces \dot{Q}_v is computed by integrating all contributions (Sciacovelli, 2010):

$$\dot{Q}_v = D_o RT \frac{1000}{32} \int_V \frac{(\nabla C_o)^2}{C_o} dV + \sigma \int_V (\nabla \Phi)^2 dV + \frac{\beta_a}{2.3} \int_{A_a} i_{na} \ln \left(\frac{i_{na}}{i_{0a}} \right) dA - \frac{\beta_c}{2.3} \int_{A_c} i_{nc} \ln \left(\frac{i_{nc}}{i_{0c}} \cdot \frac{C_{ob}}{C_o} \right) dA \quad (4.74)$$

where V is the volume of corrosion cell, A_a and A_c are anodic and cathodic surface, respectively. Note that the expression for the rate of energy dissipation can be written as $\dot{Q} = T\dot{S}$ where \dot{S} is entropy production rate. Therefore the above considerations can also be applied to the production of entropy.

By considering total rate of energy dissipation as objective function, the geometrical parameters such as cathodic and anodic areas and its position, can be generally determined in a way to maximize the objective function, namely:

$$\dot{Q}_v(\xi, A_a, A_c) = \max \quad (4.75)$$

where ξ represents the spatial coordinates. As the procedure of the objective function maximization Eq. (4.75) is mathematically highly demanding, cathodic and anodic areas are defined in different proportion in order to find the one which maximizes the objective function.

5. VALIDATION OF THE 3D CHTM MODEL: ACCELERATED CORROSION AT DIFFERENT LEVEL OF IMPOSED POTENTIAL

5.1 Specimen C/8 at different level of imposed potential

Further extensions of the 3D Chemo-Hygro-Thermo-Mechanical Model, i.e. calculation of moisture content according to the hysteretic behaviour of concrete (Ožbolt et al., 2016) and implementation of the accelerated corrosion conditions, are tested on the base of the experimental tests described in Section 3.3. It has to be noted that distribution of dissolved oxygen is assumed to be constant and uniformly distributed over the specimen. Therefore, the effects related to lack of oxygen or cracking of the concrete cover are not implemented. The specimen geometry and the corresponding environmental conditions are chosen according to the performed experimental tests (see Section 3.1.1 and 3.3). The main aim of the numerical study is to verify and calibrate the above discussed 3D chemo-hygro-thermo-mechanical model for the case of accelerated corrosion. Furthermore, the influence of water content and concrete conductivity on current density and crack pattern is investigated. Moreover, the influence of the imposed electric potential and related current density on the transport of rust and related crack pattern is studied.

5.1.1 Numerical model

The geometry of the FE model is the same as in the preliminary experiments (see Section 3.3) except that only a length of 50 mm is simulated assuming axisymmetric conditions (geometrical, mechanical and environmental). The finite element discretization is performed using solid 8-node finite elements for both concrete and steel (see Fig. 5.1).

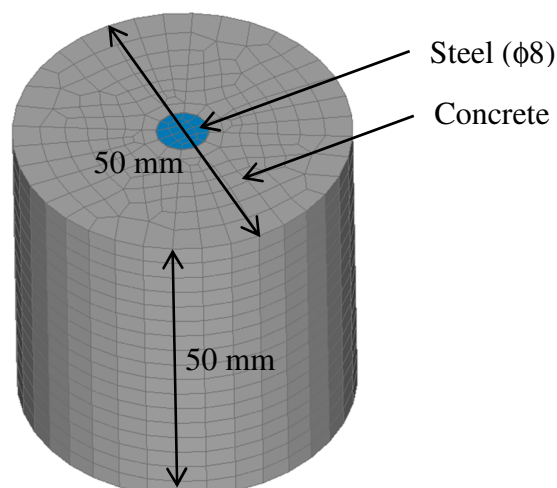


Fig. 5.1 FE discretization of the investigated specimen (type C/8)

Layer of 1D corrosion contact elements are placed radially in the interface layer around the rebar in order to simulate the expansion of the corrosion products.

It is assumed that the entire length of the steel bar is activated as anode (depassivated) at the start of the analysis. Consequently, only water content, electric potential, current density at the surface of reinforcement, transport of rust through concrete pores and cracks are computed. The concrete properties were estimated based on the experimentally determined average strength (see Section 3.1.2). The mechanical properties of concrete, steel and epoxy used in the analysis are summarized in Table 5.1.

Table 5.1 Mechanical parameters used in the Finite Element model

| Mechanical parameters of concrete, steel and epoxy | |
|---|-----------|
| Parameter | Value |
| Modulus of elasticity of concrete, E_c (N/mm ²) | 31600.00 |
| Poisson's ratio of concrete, ν_c (-) | 0.18 |
| Tensile strength of concrete, f_t (N/mm ²) | 3.10 |
| Uniaxial compressive strength of concrete, f_c (N/mm ²) | 40.00 |
| Fracture energy of concrete, G_F (J/m ²) | 55.00 |
| Modulus of elasticity of steel, E_s (N/mm ²) | 210000.00 |
| Poisson's ratio of steel, ν_s (-) | 0.33 |
| Modulus of elasticity of epoxy, E_{ep} (N/mm ²) | 70000.00 |

The analysis is performed for the same concrete quality of the experiment ($w/c=0.6$) and the parameters of the hysteretic moisture model were calibrated from experimental results obtained for the two investigated imposed electric potential: 100 and 500 mV. The used sorption isotherms (concrete $w/c = 0.65$) are plotted in Fig. 5.2.

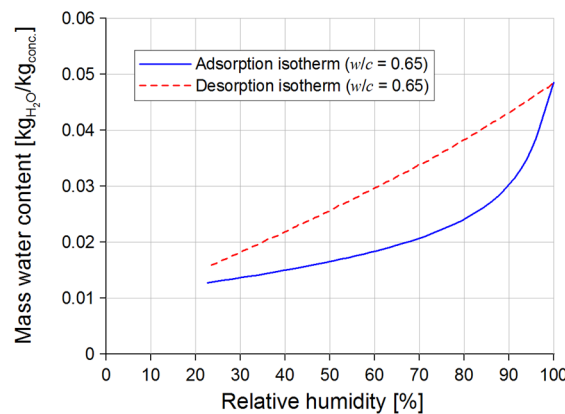


Fig. 5.2 Input main adsorption and desorption curves from the experiments performed by Hansen (1986) for concrete with $w/c=0.65$

The microscope analysis and the Raman spectroscopy, extensively discussed in Section 3.5, showed the presence of a dense layer of products mostly consisting one or several mixed oxy-hydroxides. As described, the major corrosion products of this layer were identified as Goethite (α -FeOOH) in case of 100 mV and Akaganeite (β -FeOOH) in case of 500 mV applied. Considering the investigations on morphology and distribution of corrosion products in the vicinity of the reinforcement surface, the volume expansion factor of the products is assumed to be congruent with $\alpha_v = \rho_s/\rho_r = 1.9$ in case of accelerated corrosion.

5.1.2 Numerical results under accelerated corrosion conditions (preliminary tests)

Change of relative humidity and water content during 7 weekly cycles of wetting and drying as result of the numerical simulation, performed for 100 mV according to the wetting/drying regime exposure of the experimental tests, is shown in Fig. 5.3. Corresponding parameters, needed for the analysis of relative humidity, i.e. moisture distribution, are listed in Table 5.2 (isothermal conditions, temperature = 20°C).

It has to be noted that the water content is expressed in terms of mass water content and the numerical data is taken at the depth of 21 mm from the exposed surface, which corresponds to the interface between the steel reinforcement and concrete. Based on the experimental values of current density (Section 3.3), the analyses are assumed to start at 60% RH from the adsorption curve. As can be seen, in the first wetting phase there is a large increase of water content, following the adsorption isotherm, before showing hysteretic behaviour (scanning loops), which is more pronounced in the presence of concrete damage.

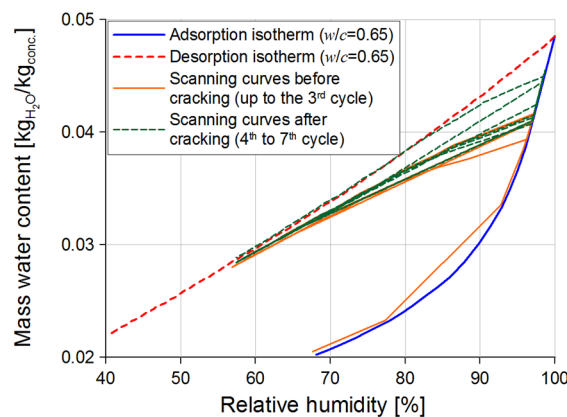


Fig. 5.3 Calculated scanning curves during the 7 weekly cycles of wetting and drying at the depth of 21 mm before and after cracking, under an imposed potential of 100 mV

The predicted damage (crack after 17 days in case of 100 mV, end of the 3rd cycle) influences the non-mechanical processes through the continuous update of the model parameters, such as water vapour permeability, whose dependency on crack width is based

on experimental results for water permeability in cracked concrete (Wang et al., 1997; Aldea et al., 2000). It can be also noted that the scanning curves cover a relatively large RH range. This is due to the high w/c ratio and the fact that the corresponding total mass water content is increasing in time.

Table 5.2 Model parameters relevant for computation of relative humidity for the specimens type C/8

| Hysteretic moisture model for concrete | |
|---|-----------------------|
| Sorption isotherms | $w/c = 0.65$ |
| Water vapour permeability (s) | 5.0×10^{-10} |
| Surface humidity transfer coefficient (m/s) | 4.5×10^{-6} |

Furthermore, electrical conductivity of concrete (see Table 5.3) was calibrated based on the experimentally measured average current density and from the experimentally measured conductivity on fully saturated concrete cube specimens using the “Two Electrodes Method” (TEM). As described in Section 2.2.2.1, the conductivity is relevant for the computation of current density, especially in chloride contaminated concrete.

The experimental value of conductivity was measured on three fully saturated concrete cubes of 150 mm by means of a LCR meter. The average value of the experimental measures is $29.9 \times 10^{-3} \Omega^{-1} m^{-1}$, with an average deviation of $4.3 \times 10^{-3} \Omega^{-1} m^{-1}$. The lowest and the highest values detected are $22.1 \times 10^{-3} \Omega^{-1} m^{-1}$ and $37.5 \times 10^{-3} \Omega^{-1} m^{-1}$.

It has to be noted that the experimental value is considered at 90% of saturation, since the conductivity is measured taking out the concrete cubes from water. Therefore, it can be assumed that the water content decreases to 90%.

Table 5.3 Electrical conductivity of concrete with $w/c=0.6$ ($10^{-3} \Omega^{-1} m^{-1}$), calibrated on the base of the experimental test

| Electrical conductivity of concrete | | | | | | | | | |
|-------------------------------------|------|------|-------|-------|-------|-------|-------|-------|-------|
| Saturation (%) | 50 | 55 | 60 | 65 | 70 | 75 | 80 | 85 | 90 |
| $\sigma_{accelerated}$ | 8.75 | 9.54 | 13.61 | 27.67 | 30.27 | 33.39 | 36.57 | 39.75 | 42.93 |

It is assumed that, due to the insufficient information from the experiments, all the values from 50% to 85% of water saturation are obtained scaling the proposed value of Gjrv et al. (1977) by the calculated factor (numerical value divided experimental value of conductivity) obtained at 90% of saturation. However, the values suggested from Gjrv et al. (1977) are used in natural corrosion conditions and are lower than in the present accelerated experimental tests. Namely, in the present work, 2.5% of NaCl by weight of

cement was added to the concrete mix employed in the manufacture of the samples. For this reason higher concrete conductivity is expected (see Section 2.2.2.3). Same considerations are assumed also in Section 6 for all the other investigated cases.

As can be seen, the value of concrete conductivity at 90% of saturation differs slightly from the average value but it is very close to the detected upper limit. Nonetheless, the difference is relatively small considering the heterogeneous nature of concrete. Furthermore, relatively small concrete cover presents generally a lower amount of aggregates, inducing a lower resistivity due to the higher porosity of the cement paste. Finally, this discrepancy emphasizes the influence of the Finite Element model, i.e. the influence of a different moisture distribution along the reinforcement which cannot be simulated in axisymmetric conditions.

The resulting average experimental and numerical values of anodic current density-history curves for the investigated specimens under an imposed potential of 100 mV (specimen P1-100, P2-100, P3-100) and 500 mV (specimen P1-500, P2-500, P3-500) are plotted in Fig. 5.4. The experimental data are average values on the anodic surface area calculated using measured current intensity. As can be seen, the numerical model is able to realistically simulate anodic current density time history curve. The analysis and the experiment exhibit sudden increase of current density that is related with sudden wetting of concrete cylinder (see hysteretic behaviour of concrete in Fig 5.3). Subsequently the water content decreases and current density gradually decreases as well (6 days drying). As expected, with increase of imposed electric potential from 100 mV to 500 mV, average current density increases approximately proportionally with imposed electric potential, i.e. with the factor of five.

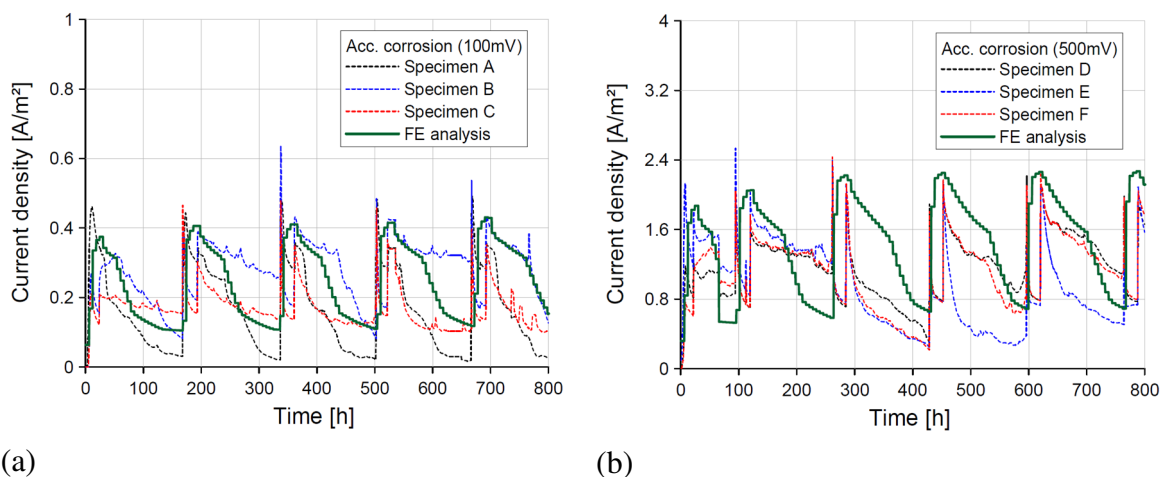


Fig. 5.4 Time dependent distribution of the average anodic current density for an imposed electric potential of 100 mV (a) and 500mV (b)

It can be noted that the moisture content and the anodic current density are strongly influenced by the corrosion induced cracks (Fig. 5.3), which leads to ingress of water into

specimen and increase of saturation in un-cracked concrete. Consequently, with increasing wetting/drying cycles, current density tends to increase, especially in case of higher imposed potential (500 mV). Moreover, as already mentioned, once the crack is generated the water content gradually increases in time. This accelerates the transport of rust from the reinforcement surface through the cracks into direction of concrete specimen surface. It has to be noticed that during wetting periods, in which the specimens are completely under water, the analysis does not indicate significant change in current density, as in experimental tests. This is probably a consequence of the assumption that the accelerated corrosion process is not dependent on the oxygen concentration. Fig. 5.5 shows the observed and calculated crack patterns (crack initiation). For lower and higher imposed potential in the experiment the first crack at the surface of the three investigated cylinders (crack width = 0.05 mm) appeared after 20 and 6 days, respectively, and in the analysis after 17 and 4 days, respectively. Having on mind the complexity of the problem, this is relatively in good agreement and the crack patterns are also similar. There is one dominant vertical crack in the experiment and in the analysis. Furthermore, it can be seen that there is a large amount of rust at the concrete surface. This indicates that a lot of corrosion products are transported from the reinforcement through cracks onto the surface of the concrete cylinder.

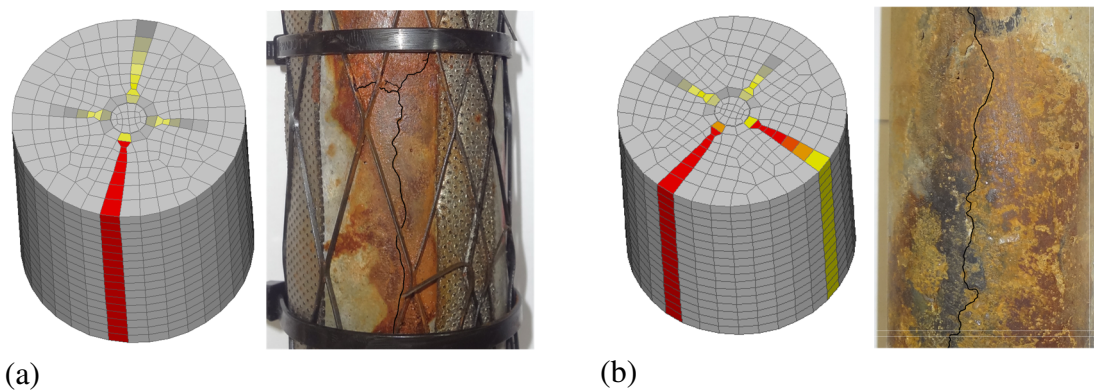


Fig. 5.5 Predicted (crack initiation at surface) and experimentally observed crack patterns for potential of 100 mV (a) and 500 mV (b) (red = crack opening ≥ 0.05 mm).

As discussed in Section 2.2.5.1, the expansion factor of rust and its transport through concrete play an important role in determining the corrosion induced damage. In the used model, transport of rust through pores of concrete and cracks is modeled as diffusion-convection governed process (mathematical interpretation). Note that from the physical point of view the rust is not transported, instead, ions are transported and corrosion products are generated in the pores around the reinforcement bar and in cracks. The relation between diffusivity of rust and crack width is obtained based on the calibration, fitting the experimental data.

The initial diffusion coefficient for un-cracked concrete, obtained by comparing the experimental corrosion time for cracking, is set to $D_r = 32.0 \times 10^{-16}$ m²/s in case of 100 mV

applied and $D_r = 95.0 \times 10^{-16} \text{ m}^2/\text{s}$ in case of 500 mV. The difference can be explained on the base of the amount of corrosion products produced in time, which diffuse in concrete pores and voids. In case of high applied current density more products are accommodated in the neighborhood of the reinforced and thus more of them penetrate into pores of concrete. However, it should be noted that diffusion coefficient does not directly describe the transport of the corrosion products, but the distribution of products formed in pores and cracks as consequence of soluble species reacting with oxygen and pore water. Therefore, the different values of diffusion coefficients at the two levels of corrosion products amount have to be considered valid in the previous described mathematical formulation as consequence of calibration, based on experimental tests.

5.1.3 Numerical results under natural conditions

In order to be able to investigate the difference between corrosion induced damage between natural and accelerated corrosion the above specimen is numerically analyzed assuming natural corrosion conditions. Only active phase of corrosion is computed, i.e. the phase after depassivation of steel.

Table 5.4 Electrical conductivity of concrete ($10^{-3} \Omega^{-1} \text{m}^{-1}$) with $w/c=0.7$, according to Gjrv et al. (1977).

| Electrical conductivity of concrete – natural conditions | | | | | | | | | |
|--|------|------|------|------|------|-------|-------|-------|-------|
| Saturation (%) | 50 | 55 | 60 | 65 | 70 | 75 | 80 | 85 | 90 |
| σ_{natural} | 2.75 | 3.00 | 4.28 | 8.70 | 9.52 | 10.50 | 11.50 | 12.50 | 13.50 |

The parameters relevant for the calculation of electric potential, consumption of oxygen and current density are listed in Table 5.5.

Table 5.5 Parameters used in the numerical simulation of the electrochemical kinetics

| Parameters of the numerical simulation of the corrosion process | |
|---|------------------------|
| Parameter | Value |
| Anodic exchange current density, i_{0a} (A/m ²) | 1.875×10^{-4} |
| Cathodic exchange current density, i_{0c} (A/m ²) | 6.250×10^{-6} |
| Anodic equilibrium potential, Φ_{0a} (V vs. SCE) | -0.780 |
| Cathodic equilibrium potential, Φ_{0c} (V vs. SCE) | 0.160 |
| Tafel slope for anodic reaction, β_a (V/dec) | 0.06 |
| Tafel slope for cathodic reaction, β_c (V/dec) | 0.160 |

It is assumed (see Section 3.2.1) that the concrete cylinder is exposed to the constant air temperature of 20°C with humidity conditions which correspond to Stuttgart, i.e. variation

of air relative humidity in the range from 63% (May) up to maximum 80% (December). To calculate corrosion rate, it is necessary to compute distribution of relative humidity, oxygen and electric potential. Electric potential is computed based on the Butler-Volmer kinetics (see Section 2.1.1) assuming anodic and cathodic surfaces as shown in Fig. 5.6a. The volume expansion factor is assumed to be congruent with $\alpha_v = \rho_s/\rho_r = 4.0$ (red rust) and diffusivity for rust transport is set to $D_r = 2.2 \times 10^{-16} \text{ m}^2/\text{s}$ (Ožbolt et al., 2014). The electrical conductivity of concrete used in the analysis is specified in Table 5.4. It has to be noted that the conductivity in natural conditions, especially considering the climate of Stuttgart, can be considered much lower than in case of accelerated corrosion. In particular, the presence of chlorides in the pore water can significantly increase the mobility of ions compared to a non-aggressive environment (see Section 2.2.2.3). However, in case of natural conditions values of concrete conductivity are defined according to GjØrv et al. (1977).

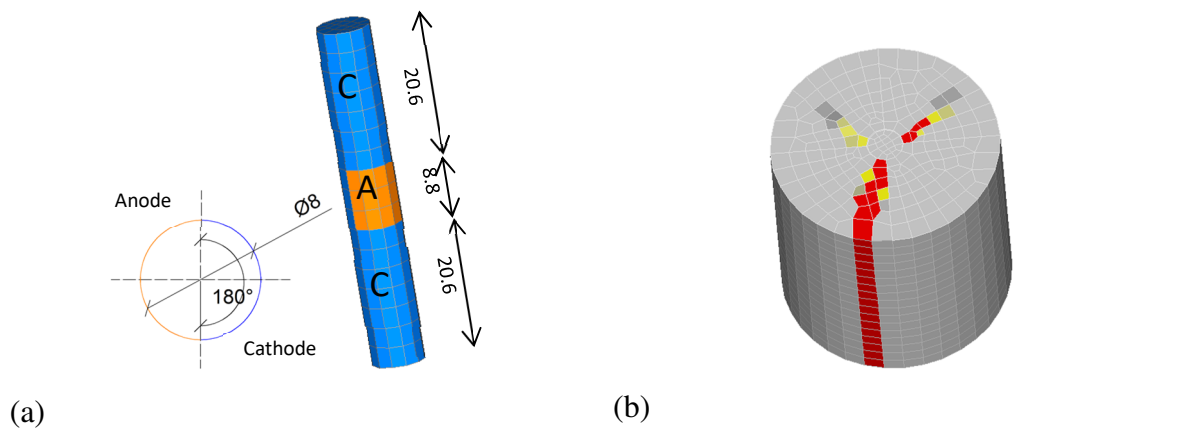


Fig. 5.6 Assumed position of anode and cathode [mm] (a) and first visible crack at concrete surface (180 days, red=0.05 mm crack width) (b)

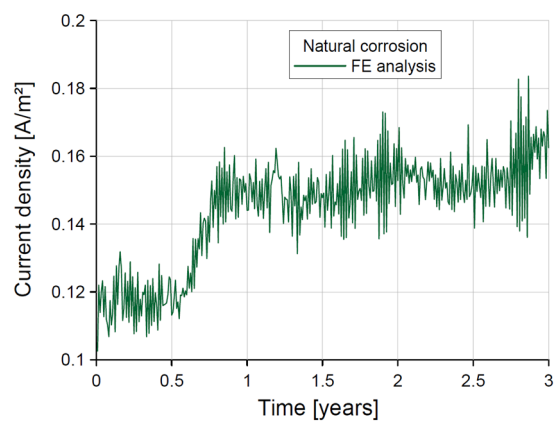


Fig. 5.7 Time history of current density, at the anode-cathode transition zone, in case of natural conditions

Fig. 5.6b shows typical crack pattern at crack initiation, 180 days after depassivation. The time history of average current density at the anodic-cathodic transition zone is plotted in Fig. 5.7.

As can be seen, maximum current density reaches approximately the value of 0.16 A/m^2 , which is, for the assumed concrete quality ($w/c=0.60$) and given environmental conditions, a realistic value. Compared to accelerated corrosion, the computed corrosion rate is approximately 3 (100 mV) and 15 (500 mV) times higher. In spite of this, the computed crack pattern is very similar to that obtained for the accelerated corrosion.

5.1.4 Conclusions

The application of the developed 3D Chemo-Hygro-Thermo-Mechanical Model for concrete in case of accelerated corrosion conditions and dynamic moisture loading is investigated. Experimental tests and numerical analysis of accelerated corrosion of steel reinforcement embedded in concrete cylinders are performed. The results are compared with numerical analysis assuming natural corrosion conditions. Based on the evaluations the following conclusions can be drawn out.

The recently proposed coupled 3D chemo-hygro-thermo-mechanical model is able to realistically simulate experimental tests on accelerated corrosion of steel reinforcement in concrete.

The model can realistically predict the hysteretic moisture behaviour of concrete predicting the scanning curves between the main adsorption and desorption isotherms under dynamic moisture loading conditions. Consequently, computed current density and related time of cracking and crack patterns are very similar to the experimentally observed ones.

In order to better calibrate the concrete conductivity, transport of corrosion products into pores and investigate the crack propagation, a complete model (no symmetry planes) that can predict also the moisture distribution along the rebar, is required. Moreover, study of different geometries is particularly significant for calibration of the rust transport in the corrosion induced cracks.

Although for natural corrosion, current density is up to 20 times lower than in accelerated corrosion (500 mV), the crack patterns are very similar. Therefore it can be concluded that for the present geometry and environmental exposure, accelerated conditions with imposed electric potential up to 500 mV yields to results that are comparable with the results obtained assuming natural corrosion. However, more detailed and systematic studies are needed.

6. VALIDATION OF THE 3D CHTM MODEL: INVESTIGATION OF REINFORCED CONCRETE CYLINDERS WITH DIFFERENT DIMENSIONS

6.1 Validation of the transport of corrosion products against experimental test

Previous section has shown a good agreement of the predicted corrosion induced damage using the 3D CHTM model with the corresponding experimental results. However, the investigation of only one concrete cover and reinforcement bar is not enough to calibrate the controlling parameters of the above mentioned model. Especially the calibration of the transport of corrosion products, into pores and cracks, needs to be verified for different geometric ratio (c/d) and under different environmental conditions. Numerical simulation of nine different geometric ratios and two different exposure conditions is a challenging task not only for analysing the transport of corrosion products, but also for capturing the specific crack pattern of each case. Moreover, the dynamic moisture loading (wetting/drying) has a significant effect on the crack propagation and needs to be accounted and coupled together with the rust transport.

The application of the 3D CHTM model is verified against the performed experimental tests described in Section 3.4 and results are presented in the following. Same as in the previous section, the oxygen is assumed to be constant and uniformly distributed in the investigated specimens.

6.1.1 Objectives of the numerical simulations

Main aim of the experiments described in Section 3 was to investigate the influence of the transport of corrosion products on the corrosion induced damage in reinforced concrete specimens. Therefore, all the cases object of experimental investigation, were simulated to study the effect of distribution of products into pores and through cracks. Simultaneously, validation of the hysteretic moisture model, concrete conductivity and computation of current density could be performed on the base of the experimental results.

It has to be noted that recent analytical and numerical models take in account the effect of migration of corrosion products in pores and voids, considering a corrosion accommodating region (see Section 2.2.5.1). However, there is no unique agreement about the thickness of this zone. In addition, effects of imposed current density and environmental conditions can highly influence the distribution of the corrosion products. Therefore, the study of the experimental tests by means of the CHTM model is useful to find a relationship between the diffusion of products into pores and the corresponding exposure conditions as well as the effect of the imposed current density.

Furthermore, as pointed out in Section 2.2.5.2, ingress of corrosion products in cracks reduces significantly the expansion pressure around the reinforcement bar. In particular,

this effect is directly influenced by the entrance and circulation of the outer solution, dependent on crack width, as explained in Section 3. Consequently, it is reasonable to assume a dependency of the diffusion coefficient of rust on the water content in cracks. At the moment there are no coupled models in the literature capable of predicting the corrosion products distribution, especially in concrete exposed to various environmental exposures (cyclic wetting and drying, immersion in water, natural conditions). However, modelling of transport of products in concrete cracks presents a further challenge due to the dominant moisture effects. In order to confirm the validity of this hypothesis, a parametric study employing the CHTM model was carried out to simulate the experiments described in Section 3. In the following sections, the employed numerical models are presented and the results of the numerical analyses, using the above mentioned approach, are discussed. Moreover, a relationship between diffusion of corrosion products as a function of the crack width and water content is proposed.

6.1.2 Numerical model

The geometries of the FE models for the corresponding specimen A, B and C are the same as in the experiment, also considering the presence of the epoxy layer on the top part of the specimen and the plain concrete on the base of the sample. The finite element discretization is performed using solid 8-node finite elements for both concrete and steel. In Fig. 6.1, the FE element models of the samples with the largest and smallest concrete cover, respectively A/8 and C/16, are shown.

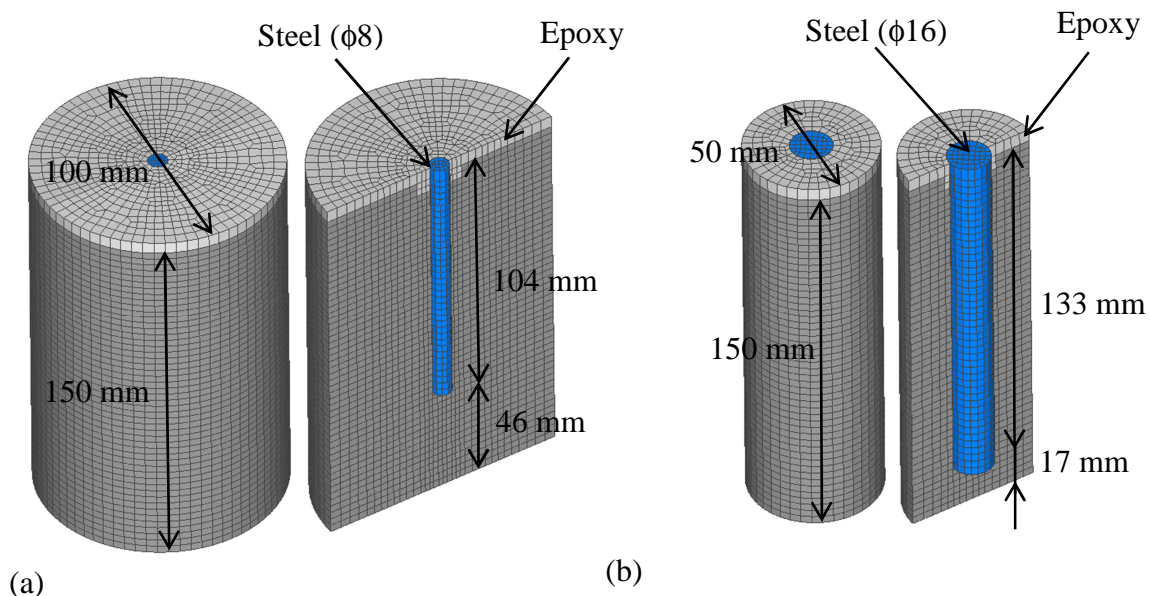


Fig. 6.1 FE discretization of the investigated specimen: type A/8 (a) and type C/16(b)

As already mentioned in the previous section, it is assumed that the entire length of the steel bar is activated as anode (depassivated) at the start of the analysis. Consequently, only water content, electric potential, current density at the surface of reinforcement,

transport of rust through concrete pores and cracks are computed. Concrete properties ($w/c=0.6$) estimated on the base of the experimental tests are the same of the previous section and can be found in Table 5.1 (see Section 5.1.1). Same consideration can be done for the input main adsorption and desorption curves (see Fig. 5.2 in Section 5.1.1). Likewise, the boundary and initial conditions correspond to the conditions defined in Section 5.

It has to be noted that in case of wetting/drying conditions, a weekly cycle of 1 day wetting and 6 days drying was simulated (see Fig. 6.2), while for submerged specimens a constant value of 100% RH was assumed throughout the simulation.

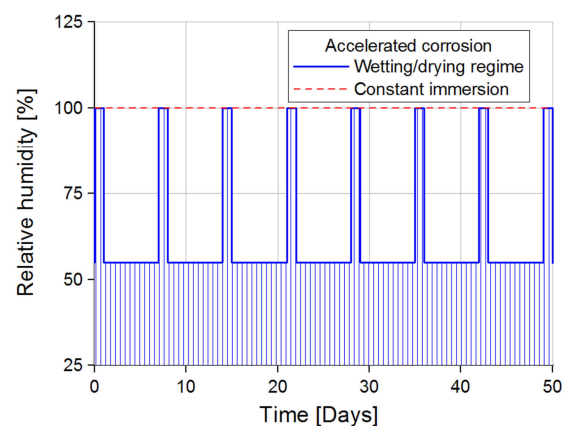


Fig. 6.2 Change of relative humidity at constant temperature of 20 °C during approximately 7 wetting/drying cycles and 7 weeks of constant immersion

The values of the expansion factors used as input in the numerical simulations are based on the characterization of the corrosion products illustrated in Section 3.5, and are listed in Table 6.1.

Table 6.1 Type of corrosion product and corresponding volume expansion factor α_v used in the numerical simulation

| Volume expansion factor of the corrosion products | | |
|---|---------------------|------------------------------|
| Exposure conditions | Corrosion product | $\alpha_v = \rho_s / \rho_r$ |
| Wetting/drying | Goethite/Akaganeite | 1.9 |
| Submerged specimens | Magnetite | 1.5 |

6.1.3 Penetration of the corrosion products in cracks: diffusivity dependency on crack width and water content

As already mentioned, the 3D chemo-hygro-thermo-mechanical model for concrete is able to couple mechanical and non-mechanical processes. In particular, the damage (cracks) calculated by using the microplane model (see Section 4) influences the non-mechanical

processes through the continuous update of the model parameters. The effect of cracks on distribution of oxygen, chlorides and relative humidity are already extensively investigated (see Ožbolt et al., 2010, 2011, 2012, 2014 and Oršanić, 2015). However, data related to the dependencies of transport of corrosion products on crack width and water content are not available in literature, due to the challenging task of measuring the effects of cracked concrete on the distribution of the corrosion compounds. Therefore, the shape and the values of the model curve describing the diffusivity of corrosion products is still an open question.

Considering the wide range of concrete cover and rebar diameter investigated, the systematic experimental test carried out (see Section 3) presented enough data to calibrate the model parameters and validate the effect related to the transport of corrosion products.

Since the distribution of corrosion products in cracks is considered directly dependent on water content, it has to be noted that permeability dependency on crack width is based on experimental tests on fully saturated concrete (Wang et al., 1997; Aldea et al., 2000) and that hysteretic moisture behaviour is assumed.

Based on the results of the performed numerical analyses, discussed in detail in the next sections, it can be concluded that the diffusivity of corrosion products increases with the increase of the crack width, following a logarithmic trend (see Fig. 6.3).

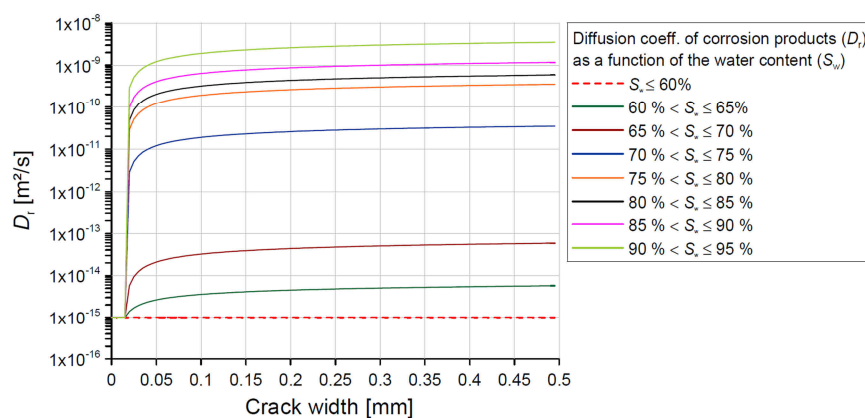


Fig. 6.3 Diffusivity of corrosion products as a function of the crack width and level of water saturation

As can be seen, no change of diffusivity is assumed for water content lower than 60%. At higher level of saturation (between 60% and 70%), a progressive ingress of products is expected. On the other hand, for values of water content between 70 and 100%, the influence of the water content becomes stronger, leading to a large ingress of products in cracks. In this way, the mechanism of transport of corrosion products can be considered as diffusive dominant, hypothesis which make sense considering also the low gradients of relative humidity predicted in the cracks and shown in the following sections.

It has to be noted, that the initial value D_{r0} ($S_w \leq 60\%$) plotted in Fig. 6.3, has to be considered as a qualitative value, since the initial diffusion in pores and voids in the vicinity of the reinforcement can be significantly influenced from water content and imposed current density. More accurate description of the initial corrosion products diffusivity is given in the next sections.

6.2 Results of the numerical simulations

6.2.1 Numerical results for the specimen type A: A/8, A/12 and A/16 – wetting/drying exposure

As mentioned in Section 5.1, the experiments performed in the present work investigated the change of current density related to the dynamic moisture loading, the crack initiation time, the distribution of the corrosion products, the development of the corrosion induced damage as well as the mass loss and corrosion penetration.

6.2.1.1 Prediction of corrosion current density and model parameters

The results from the Section 3.4.2.1 demonstrated that at the same level of imposed potential (700 mV) and similar concrete cover (46 to 42 mm), the reinforcement diameter is the governing factor responsible for the value of the average current density.

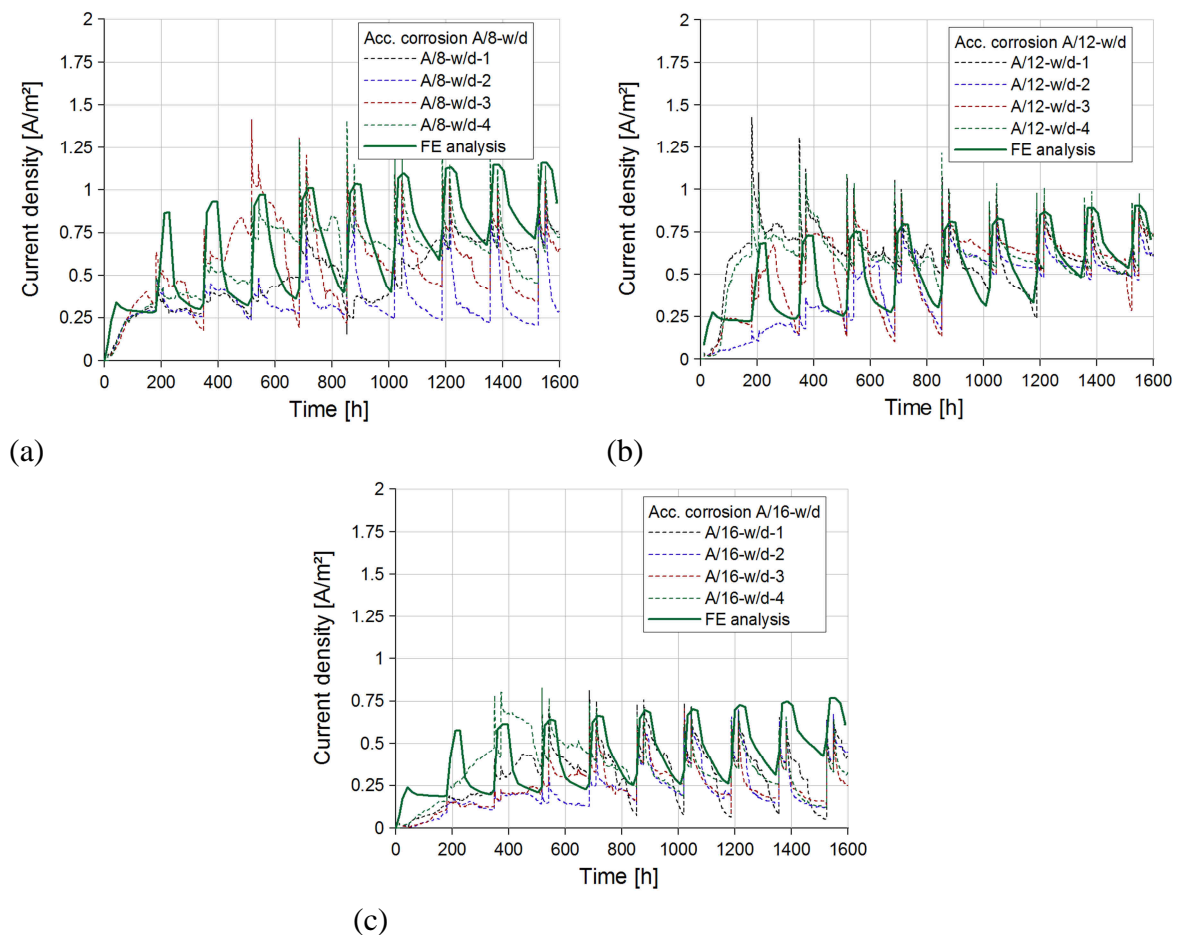


Fig. 6.4 Comparison between numerical and experimental results in terms of average current density in time, for the series A/8 (a), A/12 (b) and A/16 (c) exposed to wetting/drying conditions

Furthermore, a correct prediction of the corrosion current density in time is particularly relevant to calculate the corrosion penetration and distribution of corrosion products. Therefore, to analyse the influence of the bar diameter and verify the correct prediction of the current density, a comparison between experimental and numerical results is needed.

The current density time history of the three specimen types A/8, A/12 and A/16 is shown in Fig. 6.4. It can be seen that the prediction of the average current density in time corresponds nicely with the measured values for the three different specimen types. Same as in the experiment, the samples exhibit a high increase of water in time leading to less pronounced oscillations of the current density during the wetting/drying cycles. This is particularly marked in type A/12 and the same tendency can be recognized in samples type A/8 and A/16. As already mentioned in Section 5, during wetting period, the analyses do not show changes in current density, as in experimental tests, since oxygen is considered constant.

Calibration of the concrete conductivity was performed on the base of the illustrated curves of current density as a function of time (Fig. 6.4) and can be found in tabular representation in Table 6.2.

Table 6.2 Electrical conductivity of concrete with $w/c=0.6$ ($10^{-3}\Omega^{-1}m^{-1}$), calibrated on the base of the experimental test of the specimen series A/8, A/12 and A/16

| Electrical conductivity of concrete | | | | | | | | | |
|-------------------------------------|------|------|------|-------|-------|-------|-------|-------|-------|
| Saturation (%) | 50 | 55 | 60 | 65 | 70 | 75 | 80 | 85 | 90 |
| $\sigma_{accelerated}$ | 3.93 | 4.29 | 6.12 | 12.44 | 13.61 | 15.02 | 16.45 | 17.88 | 19.31 |

Comparing the values of concrete conductivity with the average value determined experimentally on fully saturated cubes (see Section 5.1.2), it can be noted that the used parameters are very close to the lower limit of the average value and very similar to the lowest value measured with the TEM. The reason of these differences can be addressed to a different concrete quality between several castings but also to the quality of the singular specimen type. In particular, better concrete quality is also obtained by calibration of the parameters of the hysteretic moisture model (see Table 6.3), in which the water vapour permeability resulted lower than in specimen C/8 (see Section 5.1.3).

Table 6.3 Model parameters relevant for computation of relative humidity for the specimens type A/8, A/12 and A/16

| Hysteretic moisture model for concrete | |
|---|-----------------------|
| Sorption isotherms | $w/c = 0.65$ |
| Water vapour permeability (s) | 4.5×10^{-10} |
| Surface humidity transfer coefficient (m/s) | 4.5×10^{-6} |

Furthermore, the difference in terms of concrete conductivity can be explained also on the base of the model input data, i.e. the influence of the main isotherm input data which are taken from literature due to lack of material information from the experiment. On the other hand, the inhomogeneous distribution of the chloride content in cement paste can strongly influence the resistivity of concrete. Moreover, the discrepancy between the average value of concrete conductivity between experiments and numerical analysis can be a consequence of the dissimilar distribution of electric potential in the experimental tests.

As mentioned in Section 6.1.3, the initial diffusivity coefficient of corrosion products (D_{r0} at $S_w \leq 60\%$) is highly dependent on water content and imposed current density. The value used in the simulations was determined taking in account the experimental cracking time $t_{cr,exp}$ and by calibrating the model predictions with the experimental results obtained in terms of crack pattern, crack width, crack development in time, corrosion penetration x_{corr} and measured current density. The used parameters and the corresponding results of the numerical analysis are summarized in Table 6.4.

Table 6.4 Comparison between numerical and experimental results for the specimens type A/8, A/12 and A/16 under wetting/drying conditions and the corresponding parameter D_{r0} used in the simulations

| Comparison between numerical and experimental results and values of the corrosion products diffusivity | | | | | |
|--|------------------------|-------------------------------------|------------------------|-------------------------------------|---------------------------------------|
| Specimen type | Experimental tests | | FE analysis | | |
| | $t_{cr,exp}$ (days) | $x_{corr,exp}$ (μm) | $t_{cr,num}$ (days) | $x_{corr,num}$ (μm) | D_{r0} (m^2/s) |
| A/8 | 20 | 26.7 | 23 | 23.7 | 8.0×10^{-16} |
| A/12 | 23 | 25.2 | 25 | 22.9 | 17.0×10^{-16} |
| A/16 | 27 | 22.1 | 25 | 19.1 | 18.0×10^{-16} |

It can be seen that the model prediction, for all the specimen types, exhibits good agreement with experimental data in terms of cracking time and corrosion penetration. Moreover, the calibrated diffusivity coefficient increases with higher values of current density. These results are in contrast with the assumed trend, regarding the diffusivity coefficient, hypothesized in Section 5.1.3. Therefore, a non-linear relationship between the diffusivity of the corrosion products and the current density can be assumed.

6.2.1.2 Crack pattern and development of the corrosion induced damage

The failure mode at the last level of corrosion damage, for the specimens type A/8, A/12 and A/16, is shown in Fig. 6.5. As can be seen, experimentally obtained failure mode due to the cracking of the concrete cover is correctly replicated by the numerical results.

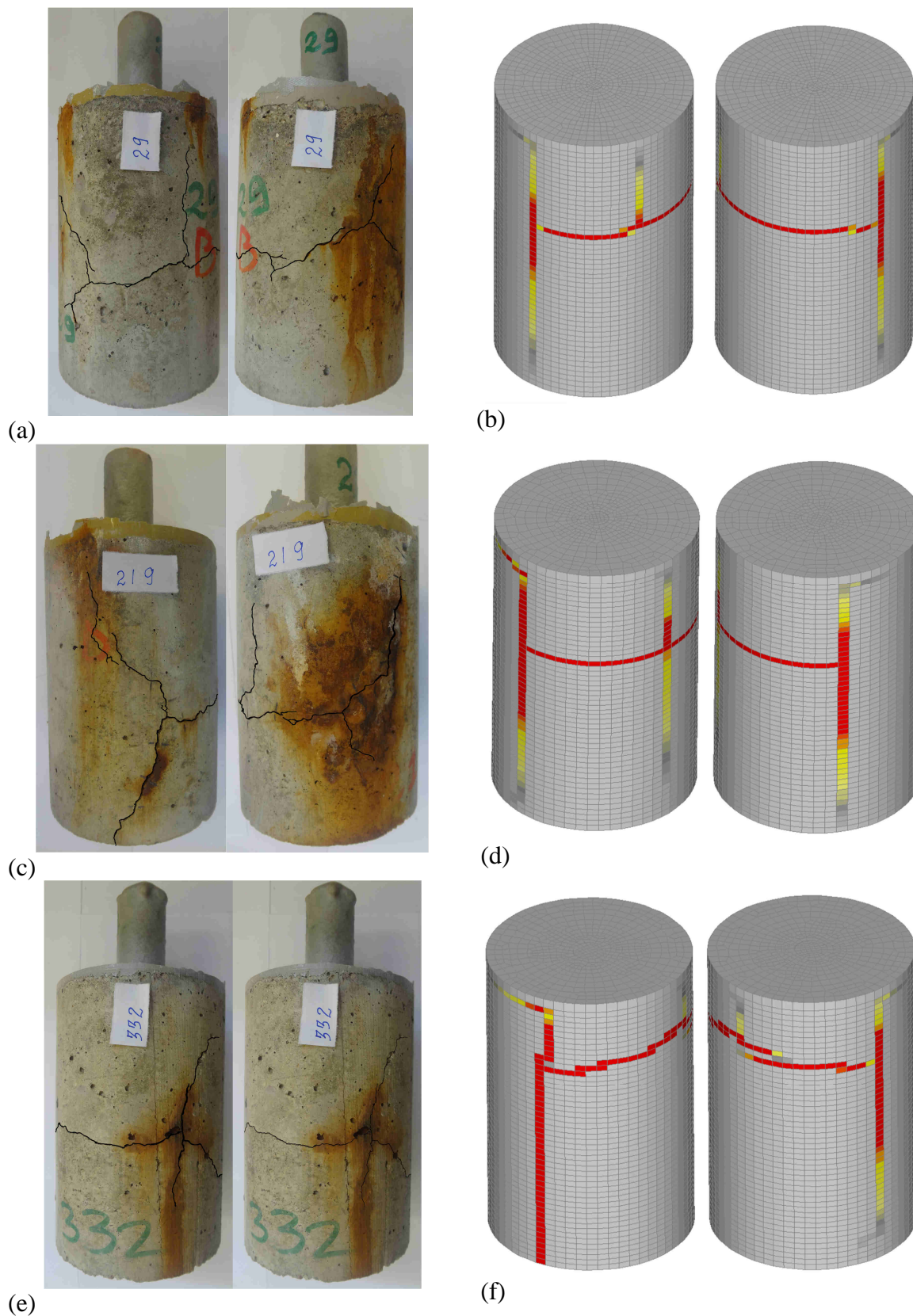


Fig. 6.5 Comparison of the crack pattern between numerical and experimental results (wetting/drying conditions) for the series A/8 (a), (b), A/12 (c), (d) and A/16 (e), (f)

It is relevant to emphasize the importance of modelling the distribution of the corrosion products into pores (see Table 6.4) and cracks (see Section 6.1.3) as well as the calibration of the corresponding parameters. In particular, the simulated corrosion induced damage is strongly influenced by the initial diffusivity coefficient and transport of products through cracks. Therefore, predicted crack pattern can significantly differ from the experimental results if the mentioned effects are not simulated, leading to much higher induced damage.

Another objective of the here presented study is to investigate the effect of transport of corrosion products on the development of the corrosion induced damage throughout the experiments. The predicted and experimentally measured average crack width is plotted in Fig. 6.6 as a function of the average corrosion penetration of the reinforcement bar, x_{corr} . For each specimen types (A/8, A/12, A/16), the crack width is computed from the damaged finite elements on the external surface of the specimens, as the sum of their average crack widths.

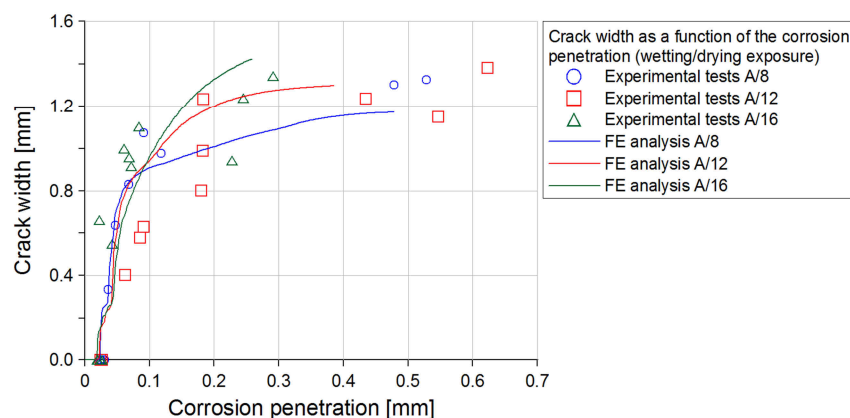


Fig. 6.6 Predicted and measured values of the sum of the average crack widths as a function of the average corrosion penetration for the specimen type A/8, A/12 and A/16 exposed to wetting/drying conditions

It has to be noted that the development of the corrosion induced damage exhibits good agreement with the experimental data, in spite of the high complexity of the problem. Due to the transport of corrosion products the increase of the crack width becomes progressively slower indicating also a significant influence of the water circulation at higher level of the induced damage. Furthermore, the model is able to replicate the faster increase of the crack width experienced for the type A/16, which can be attributed to a higher initial diffusion coefficient and lower geometric ratio c/d .

6.2.1.3 Hysteretic moisture behaviour and distribution of relative humidity

To illustrate the change of water content during the weekly cycles of wetting and drying, the scanning curves for all the three concrete cover, 46 mm (A/8), 44 mm (A/12) and

42 mm (A/16), are plotted in Fig. 6.7. It has to be noted that the analyses are assumed to start at 60% RH from the adsorption curves.

Due to thicker concrete covers, the effect of humidity variations for un-cracked concrete at the interface with reinforcement is lower in comparison with very thin concrete cover (see Section 5.1.2). In particular, the initial increase of water content due to the initial wetting is slower and the increase of water content is less pronounced. As for smaller cover, due to the low concrete quality ($w/c=0.6$), the scanning curves cover a large RH range. However, a progressive accumulation of water content and reduction of the RH range is noted. On the other hand, in cracked concrete a large increase of water content is predicted due to the increase of water permeability in the induced damage (Wang et al., 1997; Aldea et al., 2000). Compared to very thin concrete cover, the exposure conditions (wetting/drying) has a lower influence which becomes stronger with the increase of the crack width.

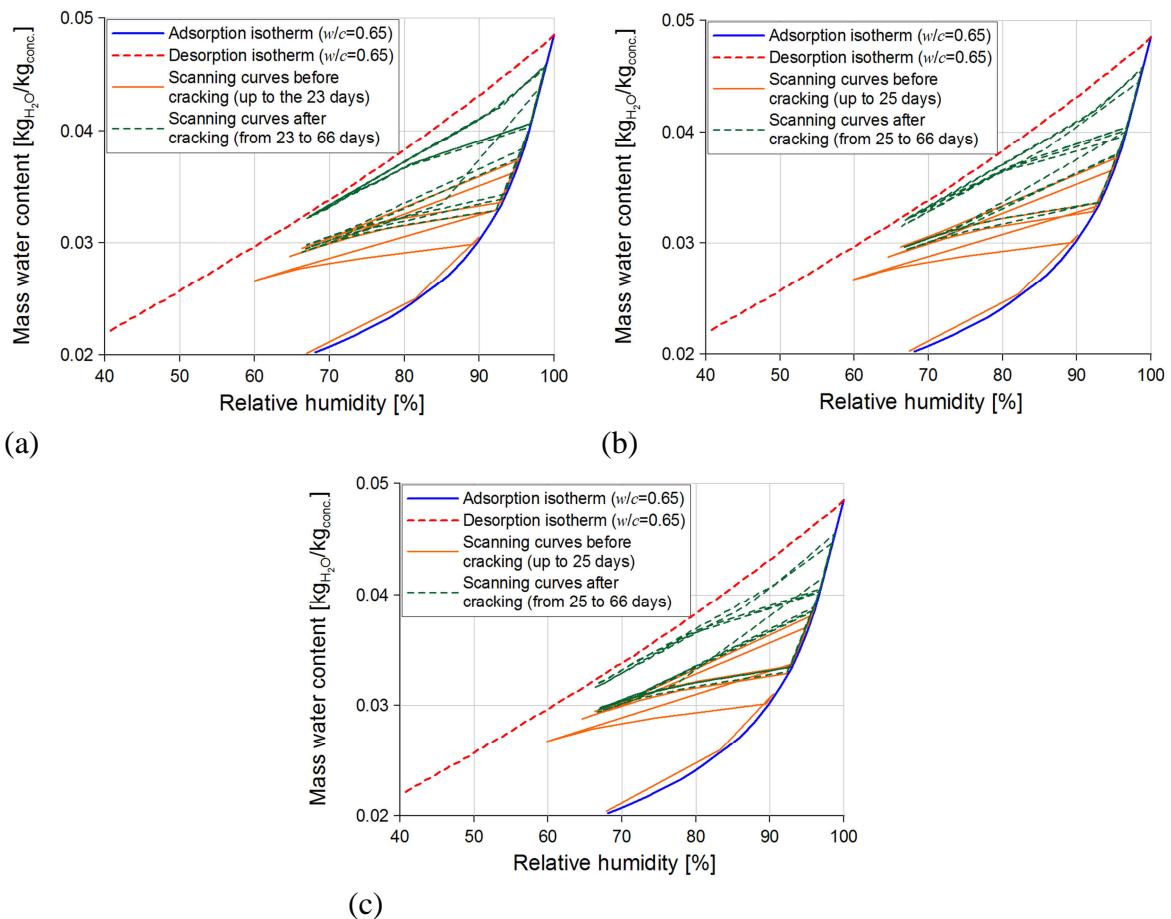
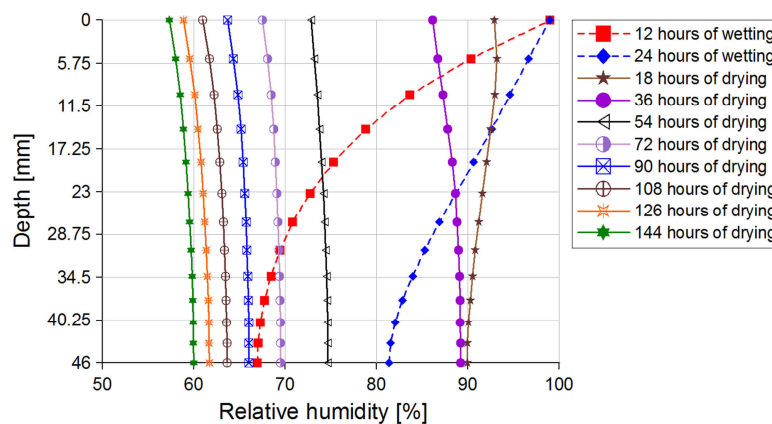


Fig. 6.7 Calculated scanning curves during the 7 weekly cycles of wetting and drying at the depth of 46 mm for the type A/8 (a), of 44 mm for the type A/12 (b) of 42 mm for the type A/16 (c)

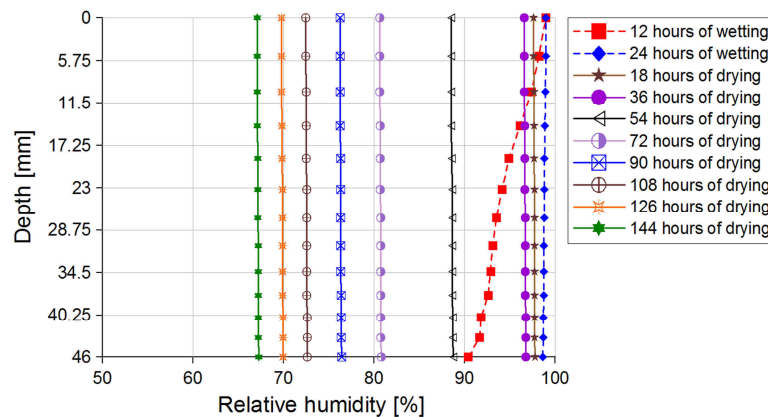
As expected, no particular differences can be noted between the three investigated concrete covers (42, 44 and 46 mm) except for the number of the cycles and the time

needed to reach a most pronounced hysteretic behaviour due to a high corrosion induced damage.

In order to bring more light into the effect of the moisture behaviour in cracked and un-cracked concrete the distribution of the relative humidity during the cyclic humidity changes is in the following investigated. In particular, the relative humidity profiles for the type A/8 are depicted in Fig. 6.8 for two different stages of the wetting phase and eight stages of the drying phase during the 1st and the 7th cycle, before and after cracking, respectively.



(a)



(b)

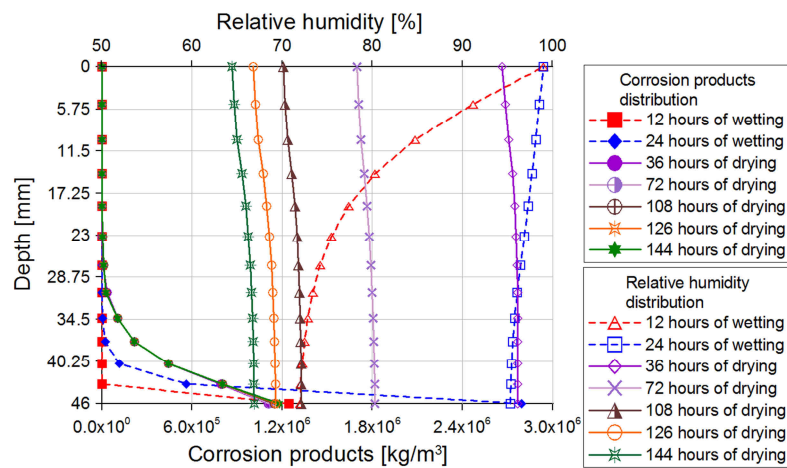
Fig. 6.8 Numerically obtained values of the relative humidity distribution along the depth for different time periods in the case of specimen type A/8: 1st cycle (a) and 7th cycle (b)

As can be seen, during the wetting phase (1 day), the relative humidity suddenly increases on the external concrete surface in both un-cracked (Fig. 6.8a) and cracked concrete (Fig. 6.8b). It has to be noted that increasing value along the depth is dependent on the surface humidity transfer and especially water vapour permeability. Considering that in cracks the water vapour permeability increases exponentially with the crack width, the influence of the wetting exposure is much stronger with the increasing depth, compared with the un-cracked concrete.

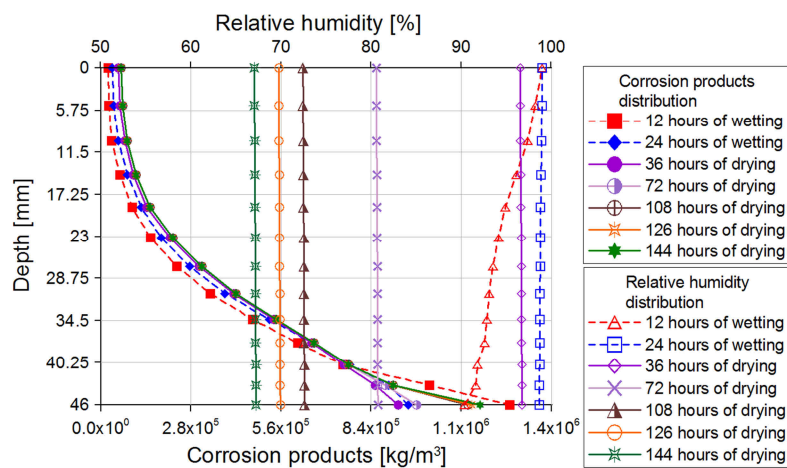
On the other hand, during the drying period (6 days) reduction of the relative humidity on the external surface is predicted. In un-cracked concrete the gradient of relative humidity is oriented towards the surface and is characterized by low values. In cracked concrete, no evident gradients of relative humidity can be observed due to the high permeability. However, the reduction of the relative humidity along the depth during the drying is slower than in un-cracked concrete, as observed by Tuutti (1982).

6.2.1.4 Distribution of the corrosion products

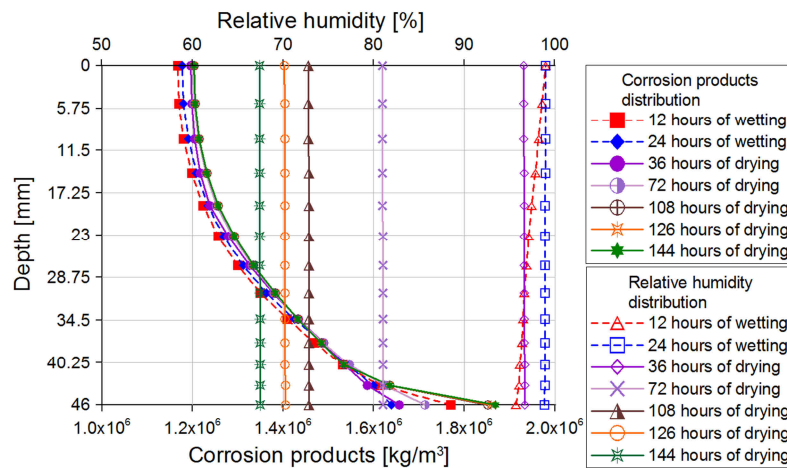
To illustrate the transport of corrosion products through cracks with the ongoing expansion of the corrosion products and circulation of outer solution, distribution of products (kg/m^3) along the crack depth for the specimen type A/8, at different time during the 4th, 7th and the 32nd cycle, is shown in Fig. 6.9.



(a)



(b)



(c)

Fig. 6.9 Numerically obtained values of corrosion products and relative humidity distribution along the depth for different time periods during the 4th cycle (a) 7th cycle (b) and the 32nd cycle (c) of wetting drying exposure for specimen type A/8

As can be seen, depending on the corrosion induced damage, different distribution of the corrosion products is possible on the base of the relative humidity profile. In particular, during the wetting phase of the 4th cycle (Fig. 6.9a) the relative humidity is slowly increasing due to the small crack width. Consequently, the amount of corrosion products for the depth of 46 mm is higher at the end of the wetting phase, because of the increased conductivity, and later they are transported through cracks. After that, no particular changes of the distribution of corrosion products during the drying phase can be noted except a slow accumulation of corrosion products around the rebar.

On the other hand, during the wetting phase of the 7th cycle (Fig. 6.9b) a sudden increase of corrosion products at the depth of 46 mm is noted. However, at the end of the wetting phase a reduction of the corrosion amount is observed due to the presence of outer solution since the crack width is already quite large (crack width of 0.7 mm on the external surface). Furthermore, the products are pushed farther away from the reinforcement and start to accumulate along the crack. During the drying phase, accumulation at the interface between concrete and steel rebar is detected.

With the increasing of crack width (32nd cycle) the effect of the water circulation is much more pronounced and, even though there is an increase of conductivity and corrosion compound production, products are easily transported through cracks during the wetting phase (see Fig. 6.9c). After that, accumulation of products in the vicinity of the reinforcement can be observed during the drying phase. This means that at this stage the production of corrosion products is increased due to the higher conductivity but they are immediately transported in cracks in the wetting periods.

In Fig. 6.9, it can be also noted that the products at the interface between steel and concrete are higher at the 4th cycle and suddenly decreases with the ingress of water (7th cycle). After that there is a slow accumulation during the drying phase.

Further on, it can be observed that the gradient of relative humidity is always relatively small along the depth, especially in the drying phases. This leads to the conclusion that the diffusion contribution to the transport of corrosion products has a stronger influence than the convective part. This result confirms the importance of describing the diffusivity of corrosion products as function of the water content (see Section 6.1.3).

In order to evaluate the amount of corrosion products responsible for the concrete cracking and damage propagation, the total quantity of products around the steel reinforcement is plotted in Fig. 6.10 as a function of time, for specimens A/8, A/12 and A/16. It is important to note that the proposed graphs describe the mass of corrosion products formed in concrete pores and voids as a consequence of soluble species which are dissolved in pore solution.

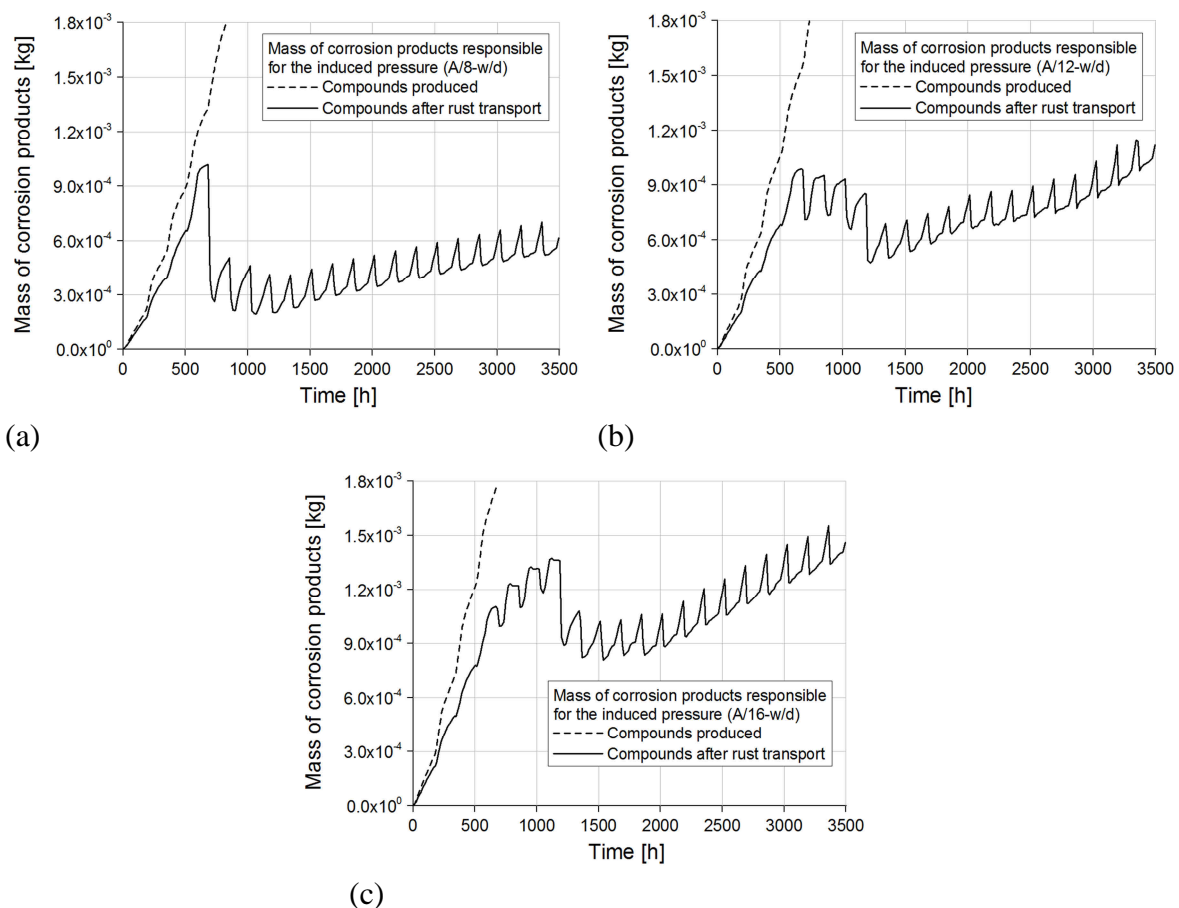


Fig. 6.10 Total mass of corrosion products around the reinforcement bar, responsible for the induced pressure for the type A/8 (a), A/12 (b) and A/16 (c) exposed to wetting/drying conditions

As can be seen, before concrete cracking the increase of mass around the reinforcement bar is almost linear and slows down with the ongoing of the drying phase. On the other hand, there is a fast increase of the compounds production due to the increased conductivity in the wetting phase. It has to be noted that in this case the diffusion in concrete pores and voids is dominant and induce to dissipate part of the induced pressure.

After concrete cracking the mass of products responsible for the corrosion induced stress rapidly decreases due to the higher diffusivity, which is enhanced by the ingress of outer solution. Furthermore, accumulation of products is observed during the drying phases and corresponding transport in cracks during the wetting periods. However, a general increase of products amount is noted also after cracking as mentioned in the comments of Fig. 6.9. Additionally, different behaviour can be noted for the three different cases. In particular, in the case A/8 (Fig. 6.10a) after cracking there is a sudden decrease of corrosion products due to the presence of diffused microcracks (see Wong et al., 2010) and interfacial damage (see Michel et al., 2016). This improves the circulation of water and transport of rust in the interface between concrete and steel. On the other hand, the previous mentioned effect is less pronounced in the cases A/12 and A/16, in which the induced pressure resulted lower due to lower impressed current density and larger diameter of the reinforcement bar. Furthermore, an increase of the critical mass for cracking with the increase of the reinforcement diameter can be noticed because of the larger anodic area.

6.2.2 Numerical results for the specimen type A: A/8, A/12 and A/16 – submerged specimens

As mentioned in Section 3.4.2.2, the simulation of submerged specimens is important to calibrate the diffusivity of corrosion products under high saturation conditions, even though corrosion in submerged structures is generally inhibited by the low concentration of oxygen. In the following, the experimental tests previously described are replicated by means of the Chemo-Hygro-Thermo-Mechanical model and calibration of corrosion products diffusivity is carried out.

6.2.2.1 Corrosion current density and model parameters

Considering that the main aim of the numerical analysis is to calibrate the diffusivity of corrosion products and that no significant change in current density is noted throughout the experiments, the resulting average experimental current density (see Section 3.4.2.2) was used in the numerical calculation. Therefore, only the following is calculated: distribution of water and humidity, corrosion rate, expansion of corrosion products and induced damage as well as transport of corrosion products.

Concrete conductivity and the model parameters for the computation of relative humidity and water content are assumed to be the same as in Section 6.2.1.

Similar as in Section 6.2.1 the initial diffusivity of corrosion products was determined by fitting the experimental cracking time and trying to replicate the experimental results in terms of crack pattern, crack width, crack development in time, corrosion penetration x_{corr} and measured current density. The used parameters and the corresponding results of the numerical analysis are summarized in Table 6.5. As can be seen, the numerical model can nicely replicate the experimental results. As expected, due to the high level of saturation, diffusivity of corrosion products resulted higher than in case of wetting and drying.

Table 6.5 Comparison between numerical and experimental results for the submerged specimen type A/8, A/12 and A/16 and the corresponding parameter D_{r0} used in the simulations

| Comparison between numerical and experimental results and values of the corrosion products diffusivity | | | | | |
|--|------------------------|-------------------------------------|------------------------|-------------------------------------|---------------------------------------|
| Specimen type | Experimental tests | | FE analysis | | |
| | $t_{cr,exp}$ (days) | $x_{corr,exp}$ (μm) | $t_{cr,num}$ (days) | $x_{corr,num}$ (μm) | D_{r0} (m^2/s) |
| A/8 | 43 | 82.8 | 47 | 71.3 | 24.0×10^{-16} |
| A/12 | 40 | 43.1 | 43 | 45.4 | 14.0×10^{-16} |
| A/16 | 56 | 34.1 | 59 | 39.9 | 12.5×10^{-16} |

In spite of the high complexity of the problem, it can be seen that the numerical prediction are very similar to the experimental results in terms of average corrosion penetration and cracking time. As already mentioned, due to the difference of current density applied in types A/8, A/12 and A/16 the initial diffusivity of corrosion products exhibits a non-linear behaviour which will be analysed together with all the other specimens and current densities.

Furthermore, comparing the corrosion penetration and cracking time with the specimens exposed to wetting/drying conditions, it can be seen that the numerical results confirm the higher diffusivity of products in pores and voids in case of submerged specimens. This leads to a higher corrosion depth for cracking that together with a lower volume expansion factor (see Section 6.1.2) induces a longer cracking time.

6.2.2.2 Crack pattern and development of the corrosion induced damage

In order to validate the proposed model also in case of high saturation failure mode and corrosion induced damage in time is compared with the experimental results. In Fig. 6.11 the crack patterns at the 3rd corrosion stage of submerged specimen type A/8, A/12 and A/16, are shown. As for the wetting/drying conditions, the crack pattern is characterized by two vertical cracks connected by a horizontal crack and could be very well reproduced by the numerical simulation.

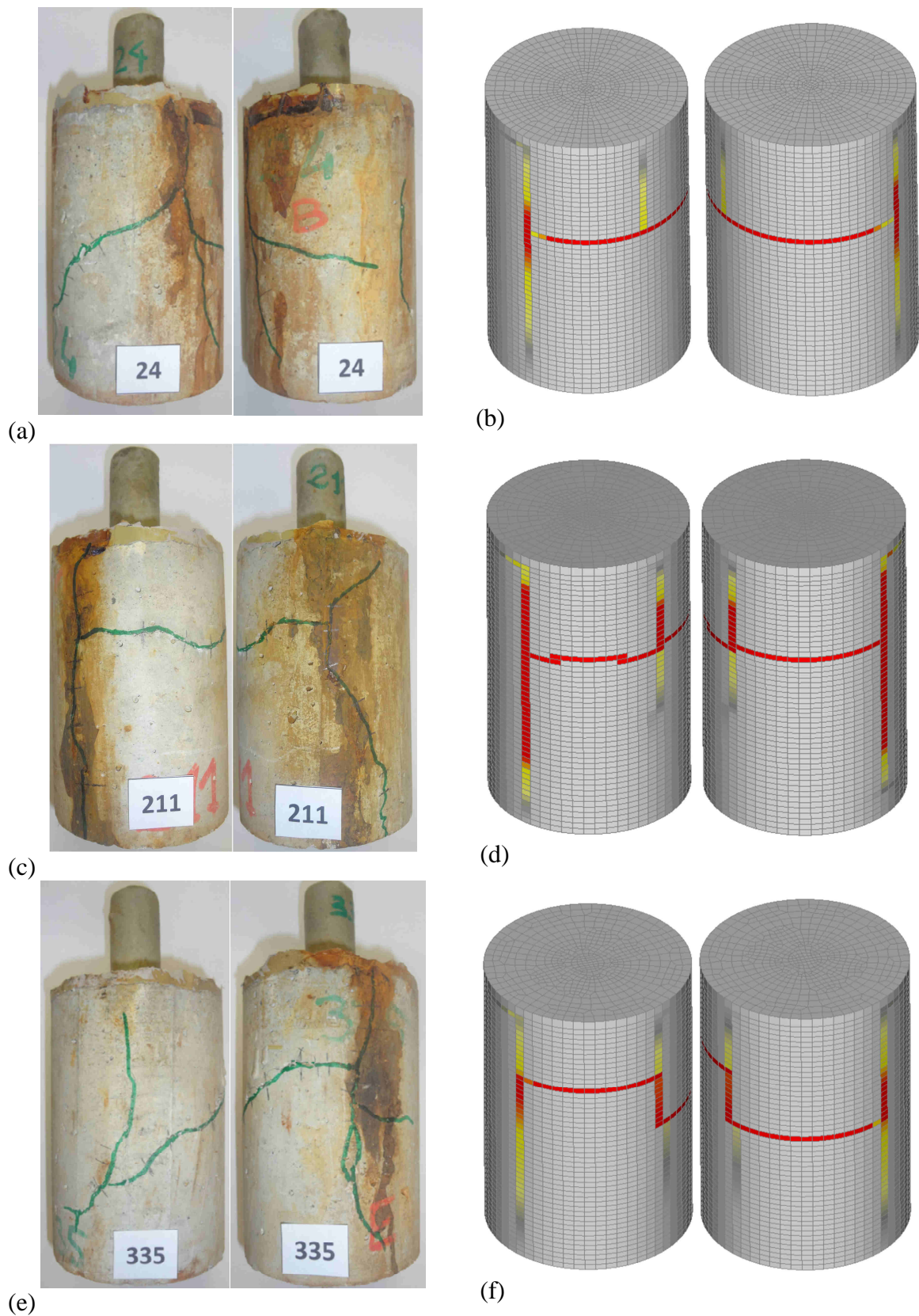


Fig. 6.11 Comparison of the crack pattern between numerical and experimental results of submerged specimens for the series A/8 (a), (b), A/12 (c), (d) and A/16 (e), (f)

In Fig. 6.12 the predicted average crack width is plotted as a function of the average corrosion penetration of the reinforcement bar, x_{corr} , and compared with experimental test results. As can be seen, both crack pattern and development of corrosion induced damage are in agreement with the experimental tests and confirm the ability of the proposed relationship, between diffusivity of corrosion products and crack width (see Section 6.1.3), to correctly evaluate the penetration of rust in cracks at high level of water saturation.

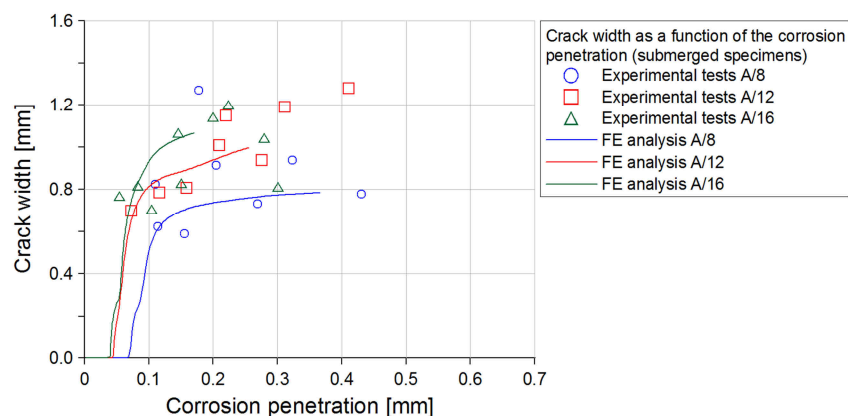


Fig. 6.12 Predicted and measured values of the sum of the average crack widths as a function of the average corrosion penetration for the submerged specimen type A/8, A/12 and A/16

It has to be noted that experimental and numerical average crack width covers a small range of corrosion depth because of the lower impressed current density and its maximum value resulted lower than in case of wetting/drying exposure as consequence of the higher diffusivity.

6.2.2.3 Distribution of the corrosion products

In Fig. 6.13, the distribution of corrosion products along the crack depth is shown. It can be observed, after crack opening, that the products in the vicinity of the reinforcement tend to decrease and there is a progressive redistribution in cracks due to the high diffusivity in saturated specimens. In particular, the rust tends to fill the crack showing a gradual accumulation in cracks.

Due to the previous described behaviour, there is a reduction of the corrosion induced pressure which is responsible for the slower increase of the crack width. The difference with the wetting/drying condition can be highlighted by analysing the amount of corrosion products responsible for the concrete cracking and damage propagation plotted in Fig. 6.14. As can be seen, the corrosion critical mass for all the three types is reached later than in case of wetting/drying exposure. This explains also the higher initial diffusivity of products before cracking. After the crack opening, there is strong reduction of the corrosion products, which are transported in the cracks.

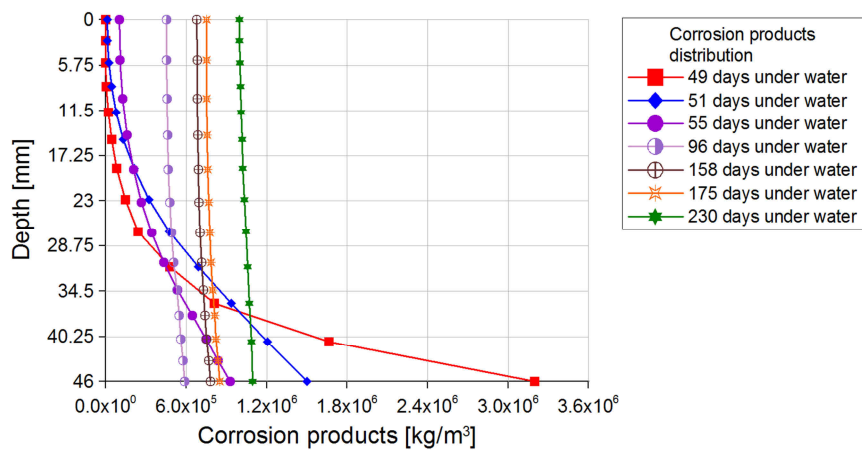


Fig. 6.13 Numerically obtained distribution of corrosion products along the depth for different time periods for the submerged specimen type A/8

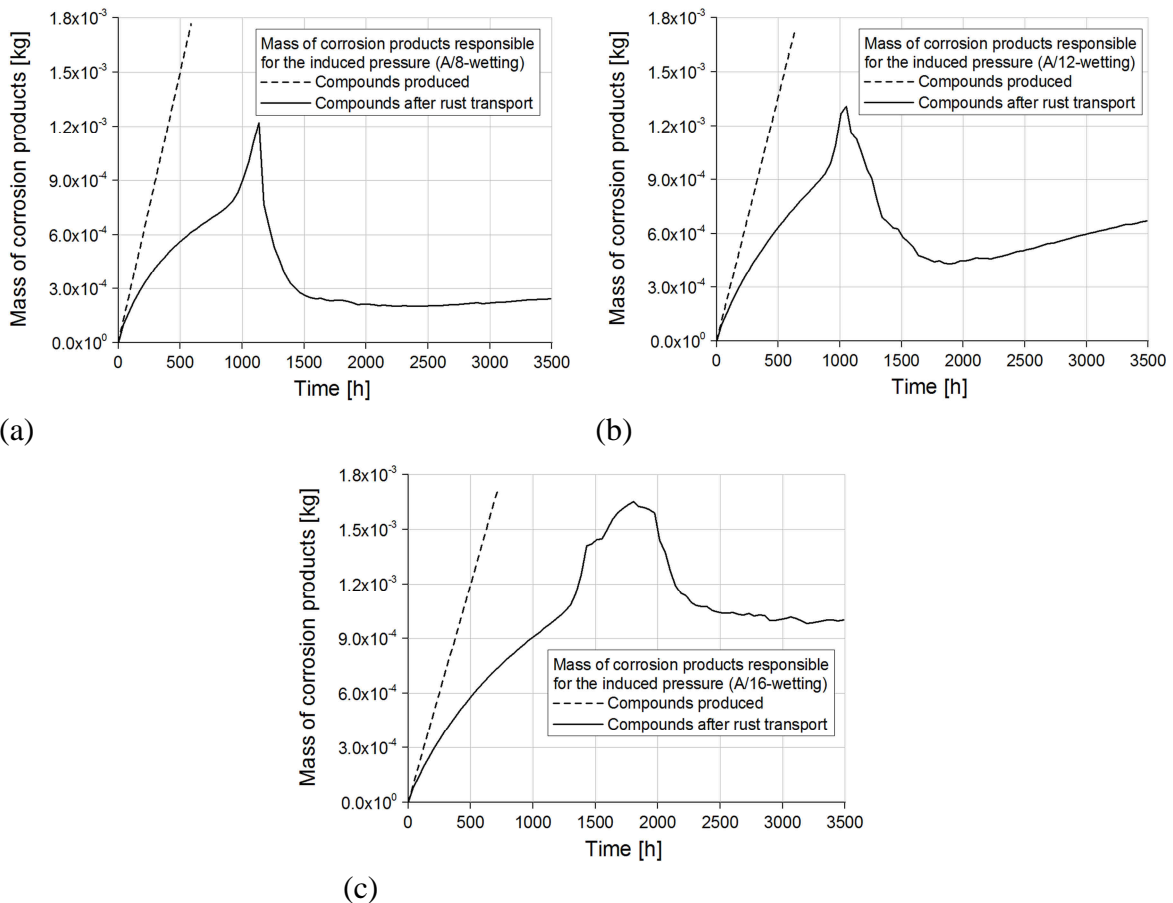


Fig. 6.14 Total mass of corrosion products around the reinforcement bar, responsible for the induced pressure for the submerged specimen A/8 (a), A/12 (b) and A/16 (c)

It can be noted also that after cracking very low accumulation of products around the rebar is observed in comparison with the specimens exposed to wetting/drying conditions, since the high saturation enhance the diffusivity and induce the corrosion products to be transported and formed in cracks. However, due to the different extent of the anodic areas,

an increase of the critical mass for cracking with the increase of the rebar diameter is predicted. Compared with the wetting/drying conditions, the critical mass resulted higher for all the investigated case since the expansion factor of Magnetite (submerged specimens) is lower than that of Goethite (wetting/drying conditions).

6.2.3 Numerical results for the specimen type B: B/8, B/12 and B/16 – wetting/drying exposure

To further demonstrate the applicability of the Chemo-Hygro-Thermo-Mechanical model, numerical simulations of the specimen types B/8, B/12 and B/16 are compared with the experimental tests.

6.2.3.1 Prediction of corrosion current density and model parameters

The comparison of numerically calculated current density with the experimental results is shown in Fig. 6.15. It can be seen that the prediction of the average corrosion current density is in agreement with the measured values during the exposure time.

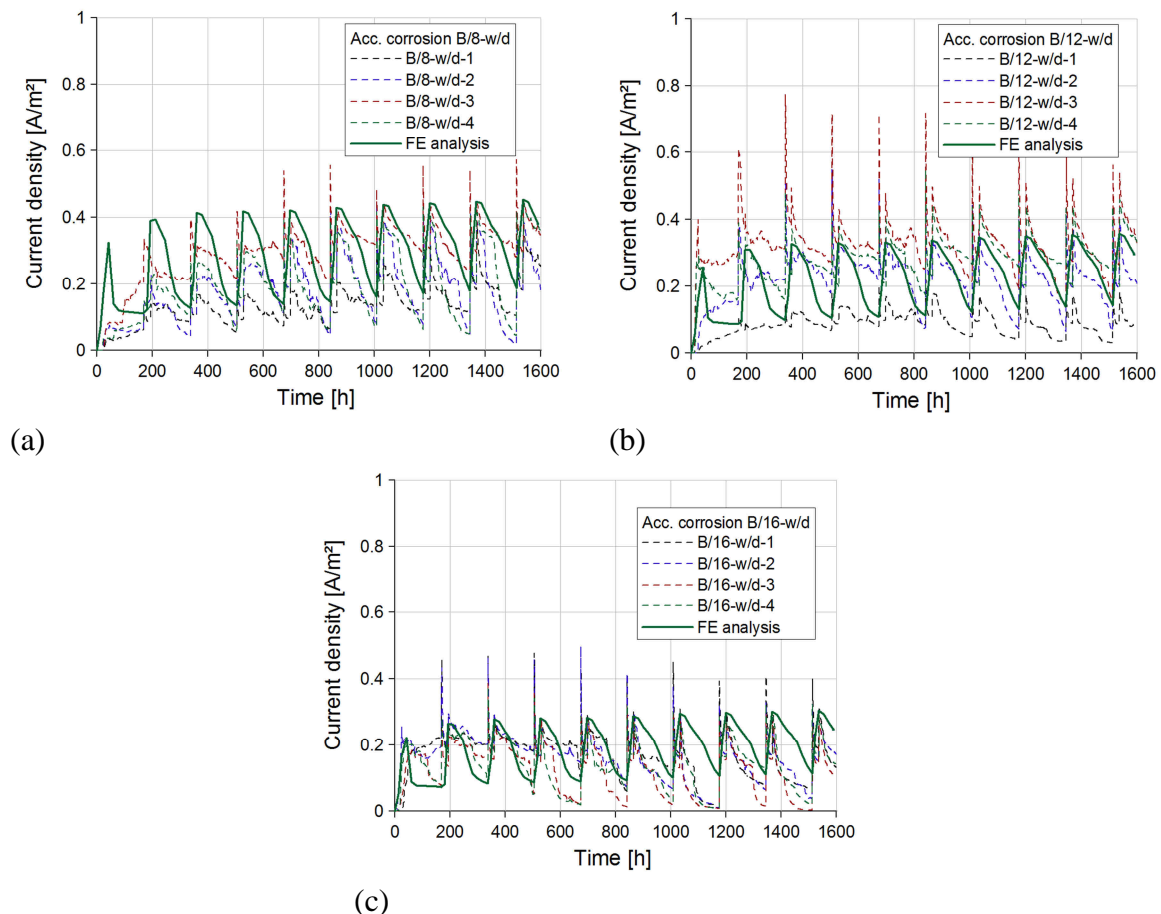


Fig. 6.15 Comparison between numerical and experimental results in terms of average current density in time, for the series B/8 (a), B/12 (b) and B/16 (c) exposed to wetting/drying conditions

As for the type A, at the same level of imposed potential (150 mV) the corrosion current density decreases with the increase of the reinforcement diameter.

As for the type A, concrete conductivity was calibrated on the base of the measured current density as a function of time (Fig. 6.15) and is listed as a function of the water saturation in Table 6.6.

Table 6.6 Electrical conductivity of concrete with $w/c=0.6$ ($10^{-3}\Omega^{-1}m^{-1}$), calibrated on the base of the experimental test of the specimen series B/8, B/12 and B/16

| Electrical conductivity of concrete | | | | | | | | | |
|-------------------------------------|------|------|------|-------|-------|-------|-------|-------|-------|
| Saturation (%) | 50 | 55 | 60 | 65 | 70 | 75 | 80 | 85 | 90 |
| $\sigma_{accelerated}$ | 6.33 | 6.90 | 9.84 | 20.01 | 21.90 | 24.15 | 26.45 | 28.75 | 31.05 |

In this case the concrete conductivity, at high saturation, is very similar to mean value obtained experimentally on fully saturated cubes (see Section 5.1.2). Calibration of the parameters for the hysteretic moisture model can be found in Table 6.7.

Table 6.7 Model parameters relevant for computation of relative humidity for the specimens type B/8, B/12 and B/16

| Hysteretic moisture model for concrete | |
|---|-----------------------|
| Sorption isotherms | $w/c = 0.65$ |
| Water vapour permeability (s) | 5.0×10^{-10} |
| Surface humidity transfer coefficient (m/s) | 4.5×10^{-6} |

Table 6.8 Comparison between numerical and experimental results for the specimens type B/8, B/12 and B/16 under wetting/drying conditions and the corresponding parameter D_{r0} used in the simulations

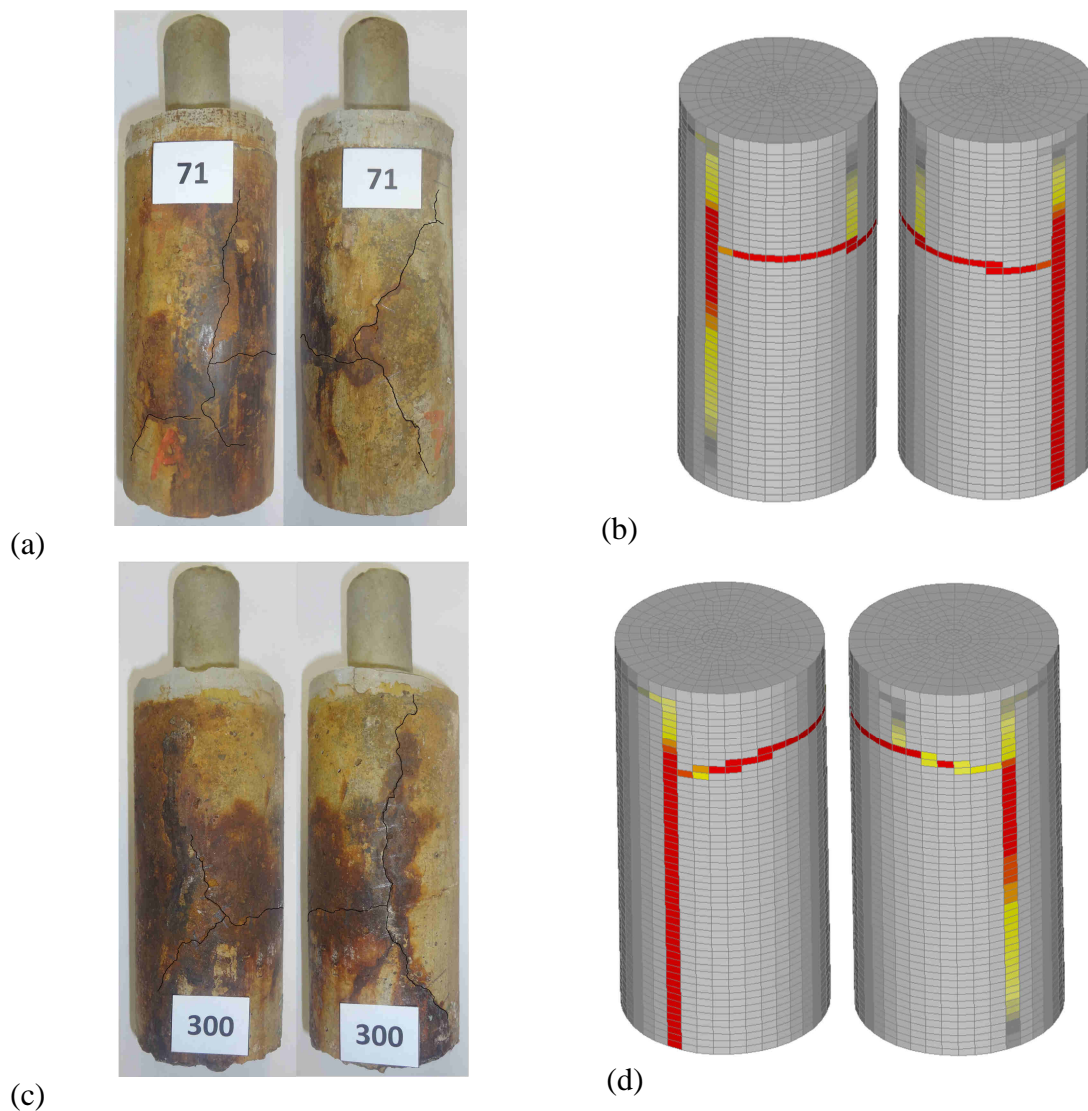
| Comparison between numerical and experimental results and values of the corrosion products diffusivity | | | | | |
|--|------------------------|-------------------------------|------------------------|-------------------------------|-------------------------|
| Specimen type | Experimental tests | | FE analysis | | |
| | $t_{cr,exp}$ (days) | $x_{corr,exp}$ (μm) | $t_{cr,num}$ (days) | $x_{corr,num}$ (μm) | D_{r0} (m^2/s) |
| B/8 | 27 | 13.7 | 29 | 13.7 | 15.0×10^{-16} |
| B/12 | 25 | 13.2 | 27 | 12.6 | 14.0×10^{-16} |
| B/16 | 26 | 10.8 | 28 | 10.9 | 7.5×10^{-16} |

Values of the initial diffusivity of corrosion products (see Table 6.8) were calibrated based on the experimental cracking time, corrosion current density time, development of the crack width in time and corrosion penetration.

It can be seen that the experimental and numerical results are very similar both in terms of corrosion penetration and cracking time for all the specimen types.

6.2.3.2 Crack pattern and development of the corrosion induced damage

Predicted corrosion induced damage, at the third corrosion stage, is shown in Fig. 6.16. The crack is plotted in terms of maximum principal strains on undeformed specimens with the red zone corresponding to the crack opening of 0.20 mm or larger. The simulated corrosion damages are characterized by two vertical cracks connected by a horizontal crack and correspond nicely to the experimental results.



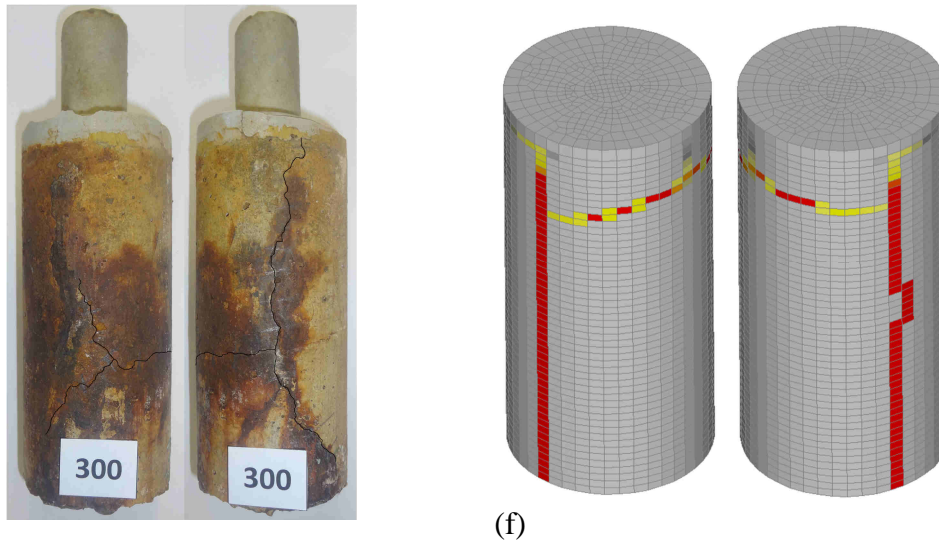


Fig. 6.16 Comparison of the crack pattern between numerical and experimental results (wetting/drying conditions) for the series B/8 (a), (b), B/12 (c), (d) and B/16 (e), (f)

Average calculated widths of the cracks on the external surface of the concrete specimen are plotted in Fig. 6.17 as a function of the average corrosion penetration of the reinforcement bar.

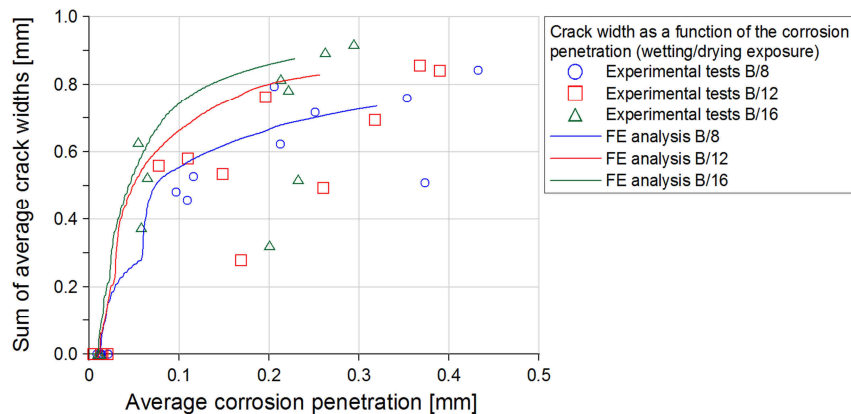


Fig. 6.17 Predicted and measured values of the sum of the average crack widths as a function of the average corrosion penetration for the specimen type B/8, B/12 and B/16 exposed to wetting/drying conditions

As can be seen, the model is able to predict the development of damage (cracks) in the concrete specimens also for the other geometries proposed in the experimental tests. Furthermore, the slower increase of crack width confirms the strong influence of the transport of corrosion products due to the wetting drying exposure.

6.2.3.3 Hysteretic moisture behaviour and distribution of relative humidity

In Fig. 6.18, predicted change of relative humidity and water content during the 7 weekly cycles of wetting and drying is plotted. The water content is expressed in terms of mass water content and the numerical data is taken at the interface between steel and concrete. The analysis is assumed to start at 60% RH from adsorption curves.

Comparing the calculated scanning curves for the three different types B/8, B/12 and B/16, the effect of the changing environment conditions slightly differs. On the other hand, in un-cracked concrete a faster increase of water content is predicted in comparison with the specimen type A due to the thinner concrete cover. Moreover, there is a slow change of water content due to the relatively small cover.

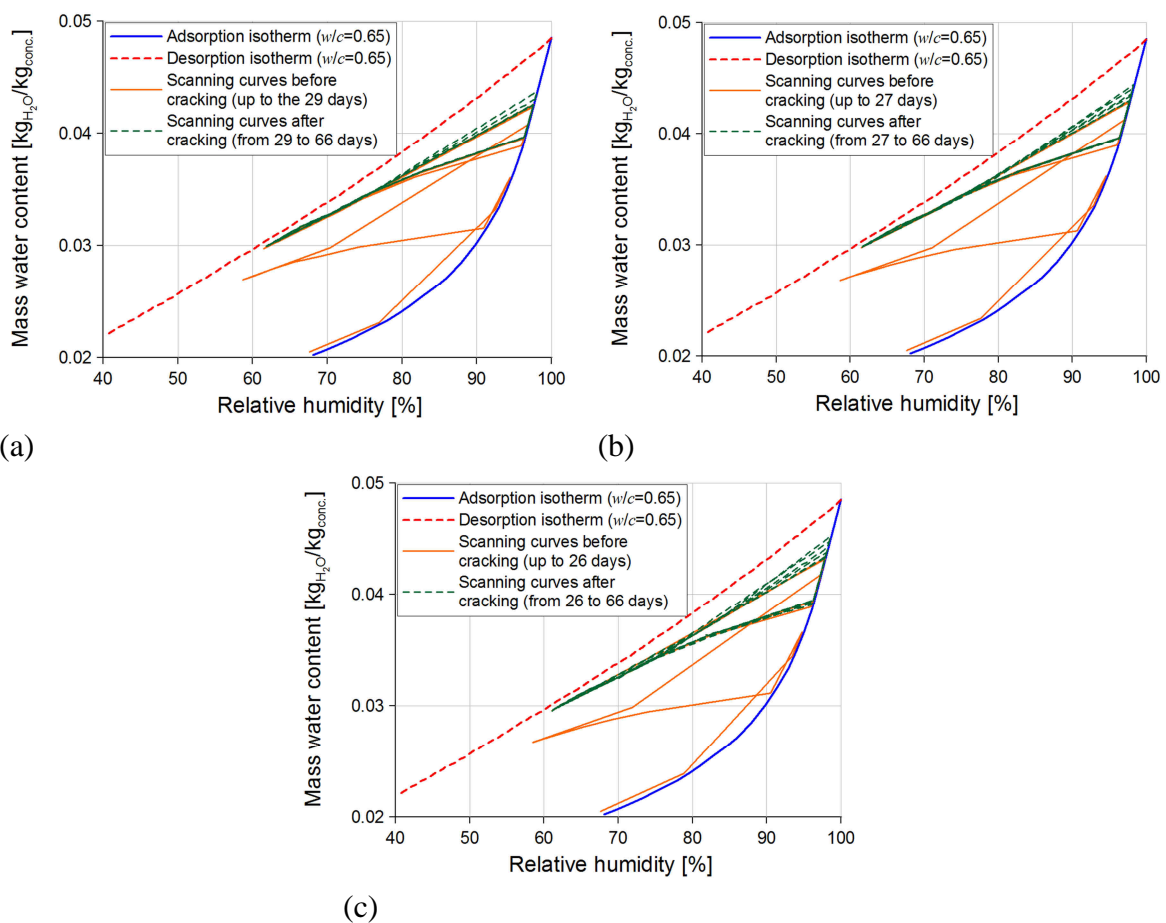
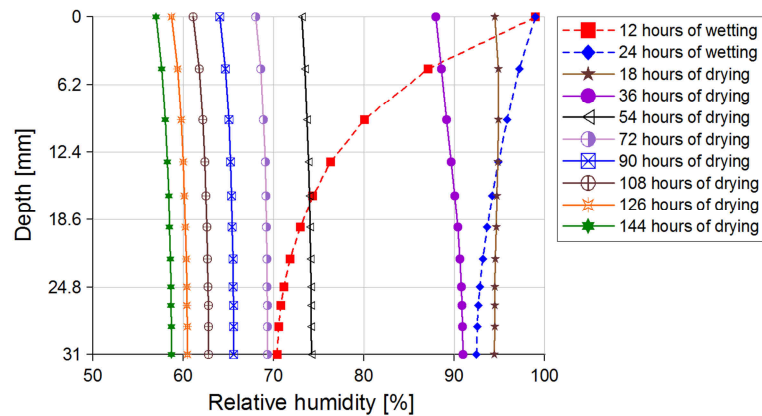
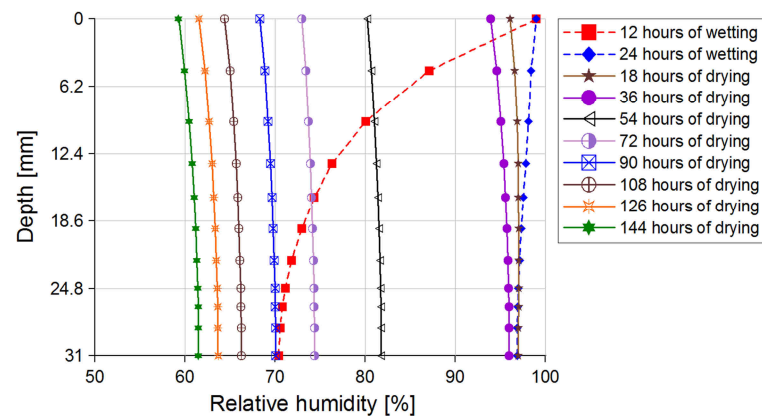


Fig. 6.18 Calculated scanning curves during the 7 weekly cycles of wetting and drying at the depth of 31 mm for the type B/8 (a), of 29 mm for the type B/12 (b) of 27 mm for the type B/16 (c)

As for the geometry A, relative humidity distribution in concrete crack is examined. Specifically, in Fig. 6.19 relative humidity profiles before and after cracking can be found. Two different stages of wetting phase and eight stages of the drying phase are investigated during the 1st and the 7th cycle.



(a)



(b)

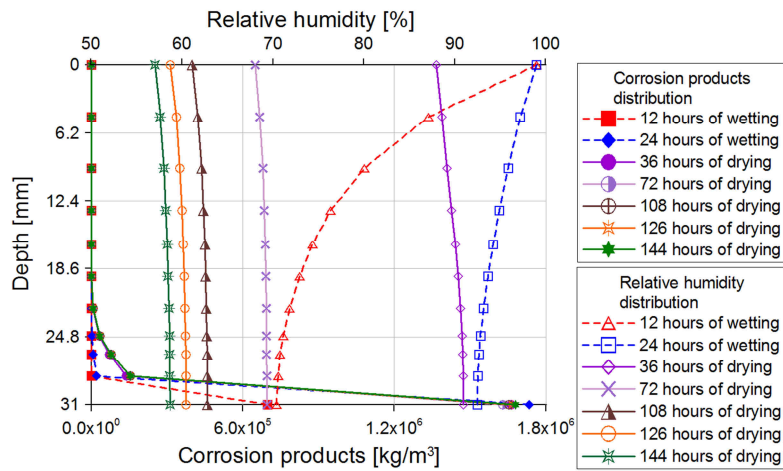
Fig. 6.19 Numerically obtained values of the relative humidity distribution along the depth for different time periods in the case of specimen type B/8: 1st cycle (a) and 7th cycle (b)

As can be noted the numerical results indicate that concrete cover thickness is one of the governing factor for the distribution of relative humidity in cracked and un-cracked concrete. During the wetting phase the increase of relative humidity is relatively faster compared with the specimen type A and the drying phase leads to lower values along the depth. This behaviour is much more pronounced after cracking. Namely, the relative humidity is entering through the concrete cover in larger extent during the wetting phase and during drying the relative humidity is decreasing much faster compared with the specimen type A. As expected, change of external environmental conditions has a stronger influence on the water saturation level in thinner concrete cover.

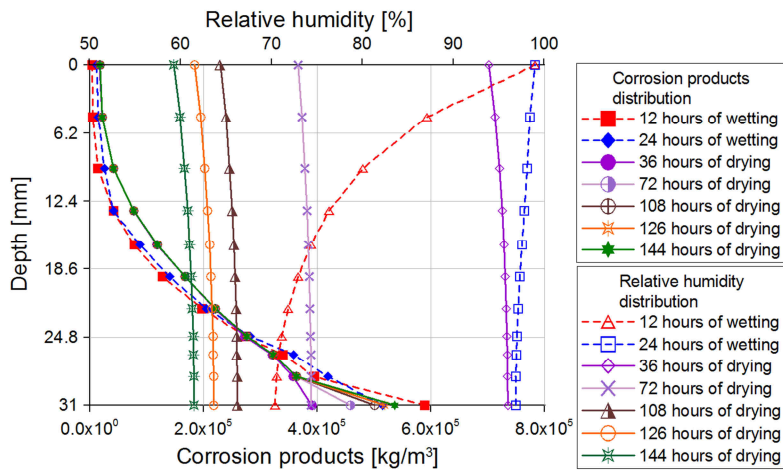
6.2.3.4 Distribution of the corrosion products

In order to investigate the transport of corrosion products through cracks for the described specimen type B, distribution of products along the depth is depicted in Fig. 6.20. As for

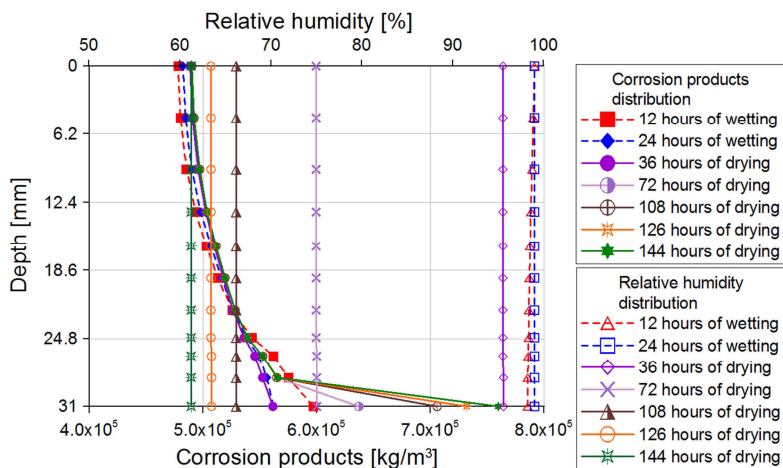
the specimen type A, different time periods were examined throughout the 4th, 7th and the 32nd cycle.



(a)



(b)



(c)

Fig. 6.20 Numerically obtained values of corrosion products and relative humidity distribution along the depth for different time periods during the 4th cycle (a) 7th cycle (b) and the 32nd cycle (c) of wetting drying exposure for specimen type B/8

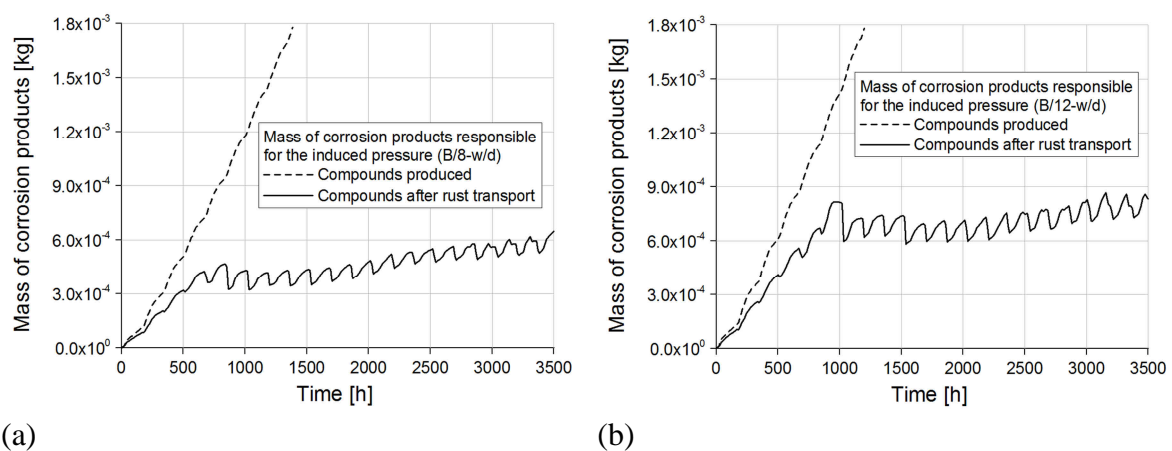
It can be noted that during the wetting phase of the 4th cycle (Fig. 6.20a) due to the slow increase of relative humidity, the amount of corrosion products at the interface with the rebar tends to grow consistently with the concrete conductivity. Later on, due to the persisting high level of relative humidity the products are transported through cracks. However, there is a sudden decrease of relative humidity during the drying phase, compared with the specimen type A. This leads to relatively small reduction of corrosion products in the vicinity of the reinforcement. After that, a very slow accumulation of corrosion products is noted as consequence of the low concrete conductivity.

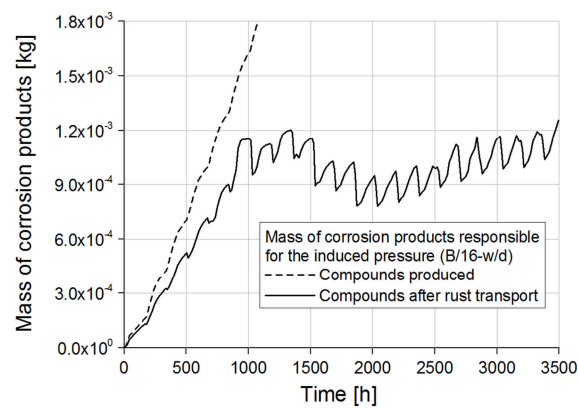
During the 7th cycle (Fig. 6.20b), with the increasing of the crack width, there is a large ingress of the corrosion products in cracks due to the faster increase of relative humidity. Consequently, there is no accumulation of compounds in the vicinity of the reinforcement during the wetting phase but only a progressive reduction, as for the specimen type A. After that, increasing of products near the rebar can be noted especially at low level of relative humidity during the drying.

During the 32nd cycle (Fig. 6.20c), the change of environmental conditions has a stronger influence on both wetting and drying phase. In particular, the transport through cracks is much more pronounced because of the higher level of relative humidity during wetting and in drying conditions there is an accumulation of products along the entire crack length.

It can be concluded that the transport of corrosion products in cracks is very similar in specimen types A and B, except that the effects related to the cyclic wetting and drying are much more pronounced.

To illustrate the change of corrosion products in the vicinity of the reinforcement throughout the simulation, the total quantity of products responsible for the concrete cracking and damage propagation is plotted in Fig. 6.21 as function of time.





(c)

Fig. 6.21 Total mass of corrosion products around the reinforcement bar, responsible for the induced pressure for the type B/8 (a), B/12 (b) and B/16 (c) exposed to wetting/drying conditions

Comparing the total mass of corrosion products around the reinforcement bar for the three different concrete cover, a similar behaviour can be noted. Two phases can be distinguished: an initial phase, before cracking, in which the corrosion products penetrate in concrete pores and voids and a second period in which the compounds are transported through cracks due to the ingress of outer solution.

However, different behaviour can be noted after cracking in comparison with the specimen type A. In particular, the decrease of the corrosion amount due to the crack opening is minor, due to the lower damage of the concrete around the reinforcement bar. This can be physically explained excluding the presence of diffused microcracks and interfacial damage as a consequence of the lower impressed current density, which induces lower pressure on concrete.

6.2.4 Numerical results for the specimen type B: B/8, B/12 and B/16 – submerged specimens

In the following numerical results for specimens type B, constantly immersed in water are compared with the corresponding experimental tests, in order to validate the applicability of the proposed model under high saturation conditions and different geometric ratios.

6.2.4.1 Corrosion current density and model parameters

As for the specimen type A, the resulting average experimental current density (see Section 3.4.2.4) was used in the numerical simulation considering that only the following transport processes are simulated: distribution of water and humidity, corrosion rate, expansion of corrosion products and induced damage as well as transport of corrosion products.

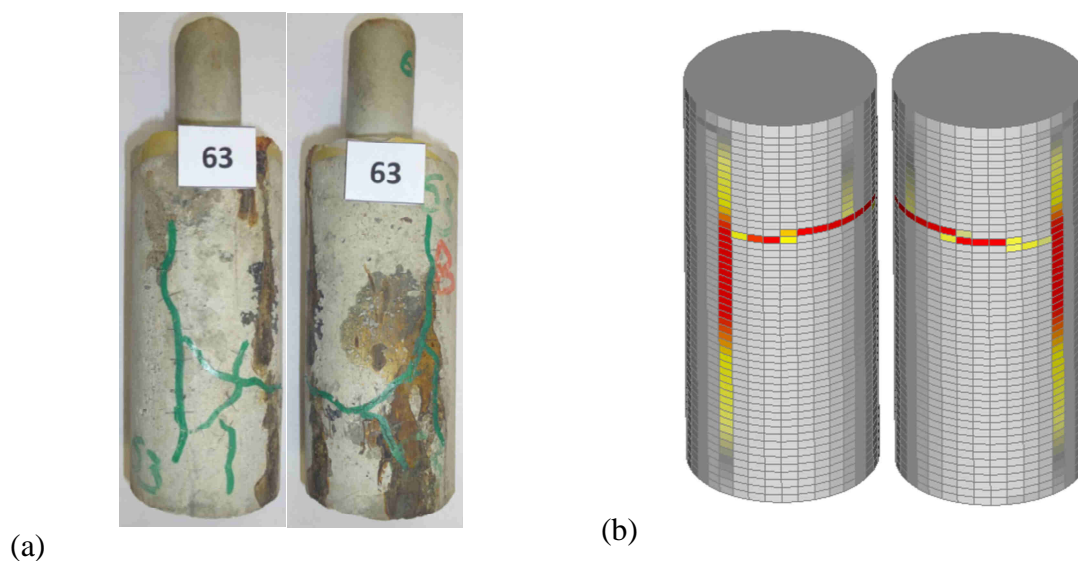
The model parameters can be found in Section 6.2.3.1. On the other hand the initial diffusivity of corrosion products was calibrated on the base of the experimental tests as for the specimen type A. Based on the comparison between experiments and numerical simulation, diffusivity coefficient was determined (see Table 6.9)

Table 6.9 Comparison between numerical and experimental results for the submerged specimen type B/8, B/12 and B/16 and the corresponding parameter D_{r0} used in the simulations

| Comparison between numerical and experimental results and values of the corrosion products diffusivity | | | | | |
|--|------------------------|-------------------------------------|------------------------|-------------------------------------|---------------------------------------|
| Specimen type | Experimental tests | | FE analysis | | |
| | $t_{cr,exp}$ (days) | $x_{corr,exp}$ (μm) | $t_{cr,num}$ (days) | $x_{corr,num}$ (μm) | D_{r0} (m^2/s) |
| B/8 | 77 | 37.3 | 81 | 36.3 | 7.5×10^{-16} |
| B/12 | 94 | 32.5 | 101 | 29.3 | 4.5×10^{-16} |
| B/16 | 112 | 22.3 | 104 | 25.3 | 3.8×10^{-16} |

6.2.4.2 Crack pattern and development of the corrosion induced damage

In Fig. 6.22 the crack patterns at the 3rd corrosion stage of submerged specimen types B/8, B/12 and B/16 are plotted. As can be seen, the numerical simulation can realistically predicted the corrosion induced damage even though the position of the horizontal crack, which connects the two vertical cracks, is not exactly replicated in the presented cases, especially for the types B/12 and B/16.



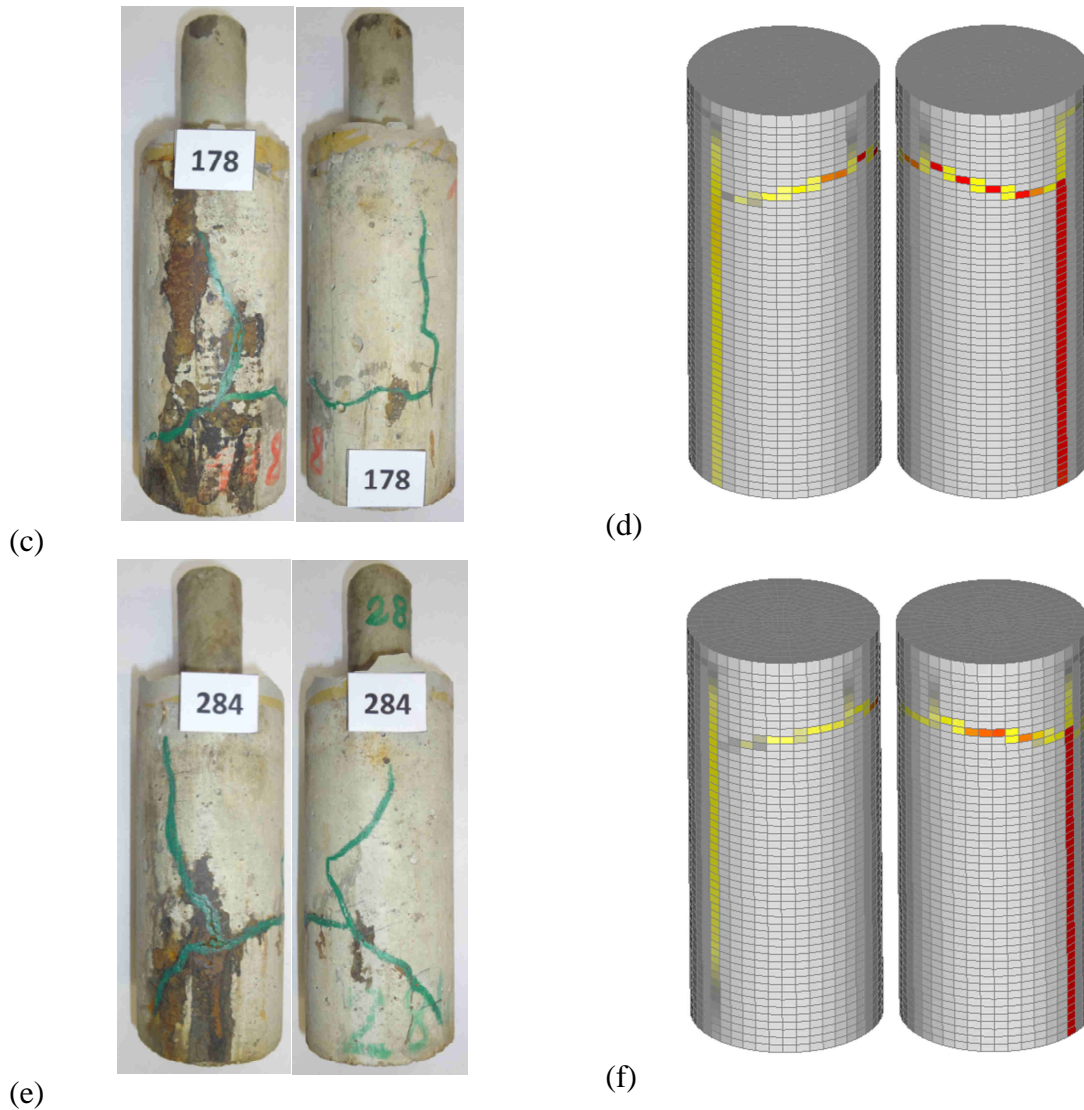


Fig. 6.22 Comparison of the crack pattern between numerical and experimental results of submerged specimens for the series B/8 (a), (b), B/12 (c), (d) and B/16 (e), (f)

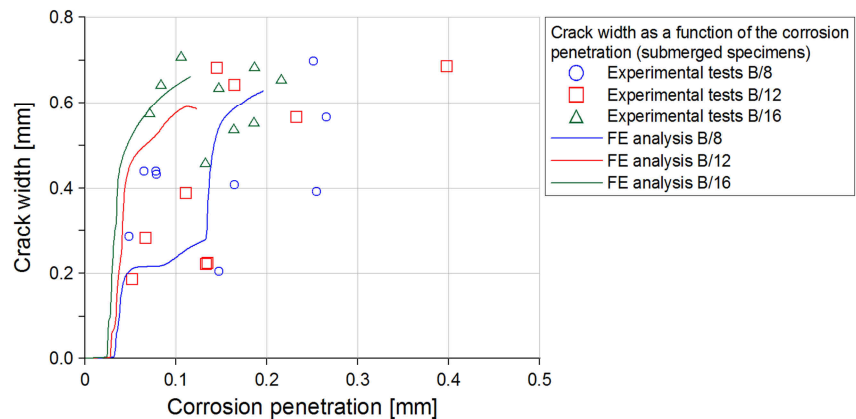


Fig. 6.23 Predicted and measured values of sum of the average crack widths as a function of the average corrosion penetration for the submerged specimen type B/8, B/12 and B/16

In Fig. 6.23 prediction of the average crack width as a function of the average corrosion penetration is shown. Even though the experimental results presented a higher scatter compared with the other tests, the model is able to replicate the development of the corrosion induced damage. However, for the type B/8 the formation of the horizontal crack is delayed in comparison with the experimental evidence. This leads to a sudden increase of the crack width at a high level of corrosion penetration in contrast with the general trend noticed in the experimental results.

6.2.4.3 Distribution of the corrosion products

Distribution of the corrosion products in kg/m^3 in time along the largest radial crack for the specimen type B/8 is illustrated in Fig. 6.24. Similar to type A but with different timing, there is a reduction of corrosion products which migrate in the cracks accumulating along the crack depth due to the enhanced diffusivity in high saturation condition.

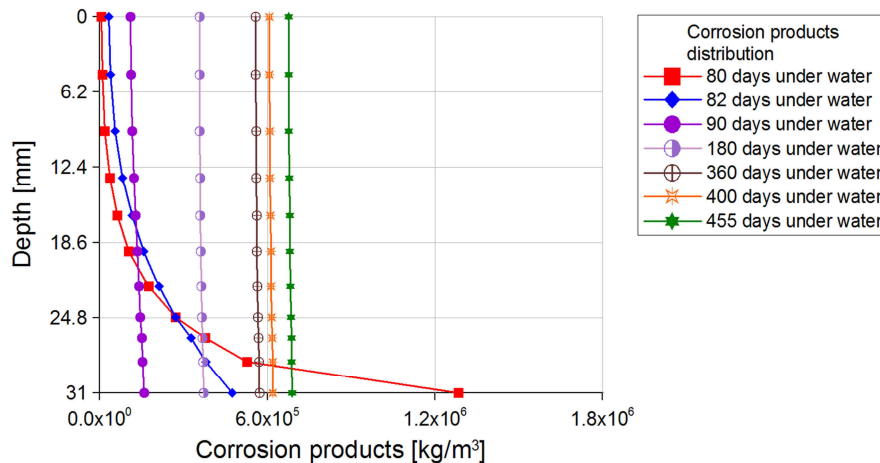
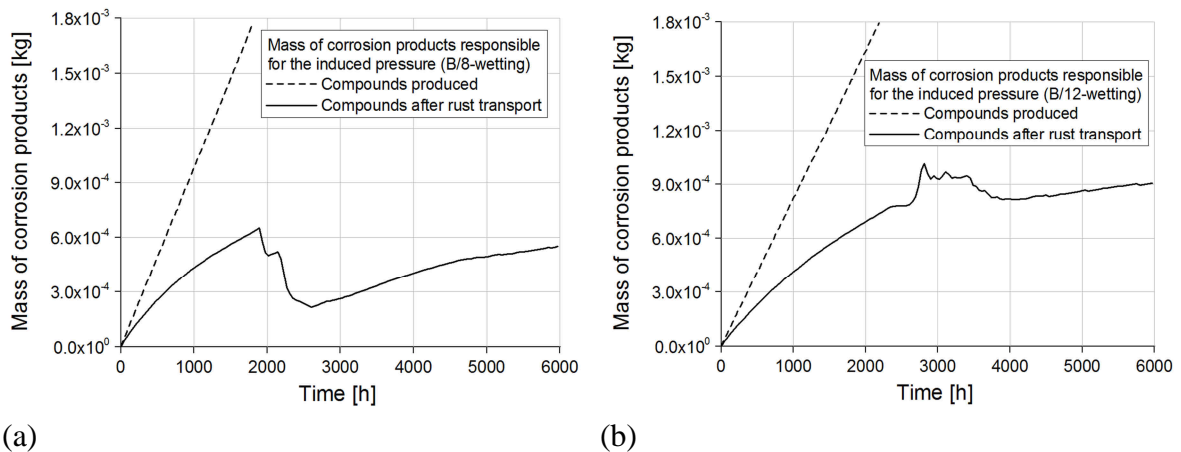
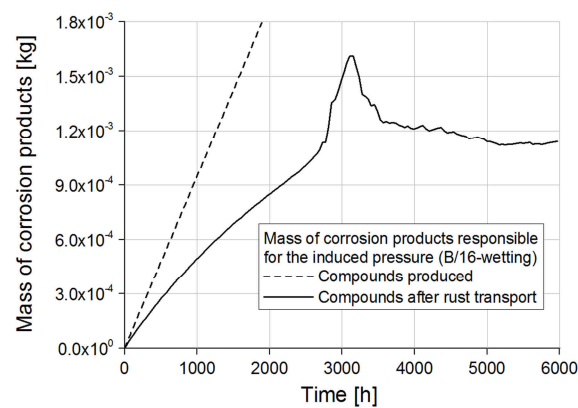


Fig. 6.24 Numerically obtained distribution of corrosion products along the depth for different time periods for the submerged specimen type B/8





(c)

Fig. 6.25 Total mass of corrosion products around the reinforcement bar, responsible for the induced pressure for the submerged specimen B/8 (a), B/12 (b) and B/16 (c)

In Fig. 6.25 the mass of corrosion products responsible for the induced pressure as a function of time is plotted. As can be seen, there is an increase of the critical mass for cracking with the increase of the rebar diameter. Namely, this result confirms the tendency observed in the previous cases. Furthermore, as expected the critical mass around the reinforcement bar, that induces cover cracking, is higher than in case of wetting/drying exposure. The reason on the base of this behaviour is the different nature of the corrosion products detected for the two different environmental conditions (see Sections 3.5 and 6.1.2).

6.2.5 Numerical results for the specimen type C: C/8, C/12 and C/16 – wetting/drying exposure

Previous sections shows good agreement of the predicted corrosion induced damage using the 3D Chemo-Hygro-Thermo-Mechanical model with the results of the performed experimental tests. However, it is also important for the engineering applications to verify and validate the model in case of very thin concrete covers.

6.2.5.1 Prediction of corrosion current density and model parameters

Same as in the previous sections predicted corrosion current density is compared with the experimental results in case of wetting and drying conditions (see Fig. 6.26).

As can be seen, the model is able to realistically predict the corrosion current density in time for all the proposed geometric ratios c/d .

A reduction of the corrosion current density with the increase of rebar diameter is predicted according to the experimental results. Based on the comparison between numerical and experimental data, electrical conductivity of concrete was calibrated (see Table 6.10).

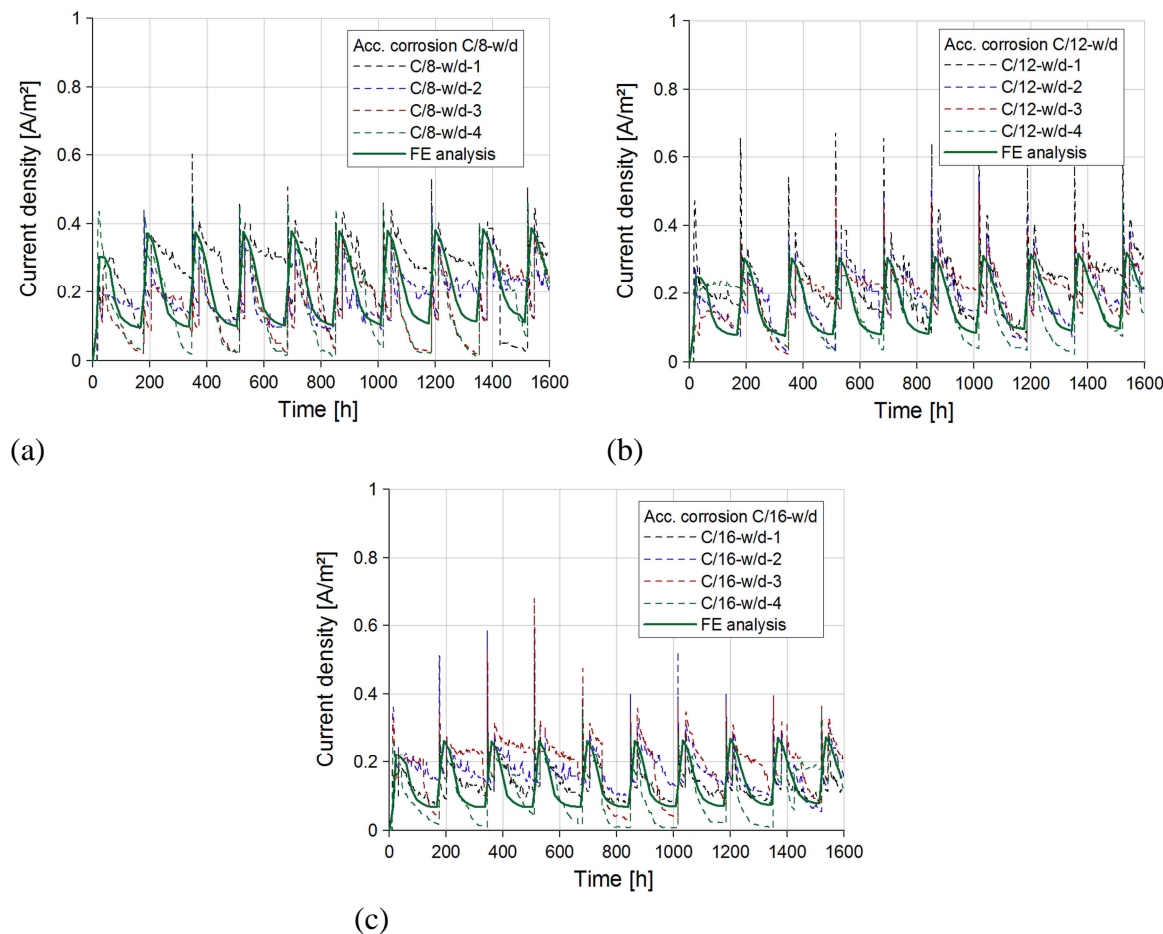


Fig. 6.26 Comparison between numerical and experimental results in terms of average current density in time, for the series C/8 (a), C/12 (b) and C/16 (c) exposed to wetting/drying conditions

Table 6.10 Electrical conductivity of concrete with $w/c=0.6$ ($10^{-3}\Omega^{-1}m^{-1}$), calibrated on the base of the experimental test of the specimen series C/8, C/12 and C/16

| Electrical conductivity of concrete | | | | | | | | | |
|-------------------------------------|------|------|-------|-------|-------|-------|-------|-------|-------|
| Saturation (%) | 50 | 55 | 60 | 65 | 70 | 75 | 80 | 85 | 90 |
| $\sigma_{accelerated}$ | 7.15 | 7.80 | 11.13 | 22.62 | 24.75 | 27.30 | 29.90 | 32.50 | 35.10 |

As can be seen, the calibrated value of conductivity at high level of saturation is very close to that obtained experimentally (see Section 5.1.2). Parameters for the hysteretic moisture model are the same as in Section 5 and 6.2.3.

In Table 6.11 the resulting values of initial diffusivity used in the calculation are listed. Comparison between the experimental and numerical results is also shown in terms of cracking time and critical corrosion depth.

Table 6.11 Comparison between numerical and experimental results for the specimens type C/8, C/12 and C/16 under wetting/drying conditions and the corresponding parameter D_{r0} used in the simulations

| Comparison between numerical and experimental results and values of the corrosion products diffusivity | | | | | |
|--|------------------------|-------------------------------------|------------------------|-------------------------------------|---------------------------------------|
| Specimen type | Experimental tests | | FE analysis | | |
| | $t_{cr,exp}$ (days) | $x_{corr,exp}$ (μm) | $t_{cr,num}$ (days) | $x_{corr,num}$ (μm) | D_{r0} (m^2/s) |
| C/8 | 22 | 9.8 | 24 | 13.7 | 21.0×10^{-16} |
| C/12 | 21 | 7.6 | 22 | 12.6 | 14.0×10^{-16} |
| C/16 | 28 | 7.8 | 29 | 10.9 | 10.9×10^{-16} |

It can be noted that the numerical results nicely agree with the experimental results and that a decrease of the initial diffusivity is predicted due to the lower level of corrosion current density at larger reinforcement diameter.

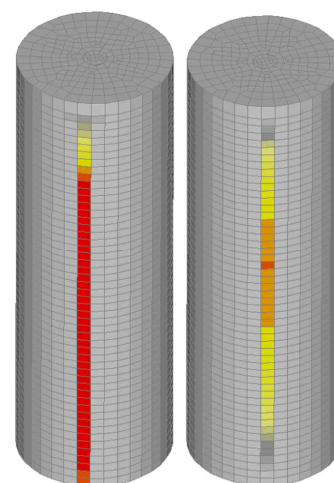
6.2.5.2 Crack pattern and development of the corrosion induced damage

In Fig. 6.27, the illustration of the predicted corrosion induced damage and the experimentally observed crack pattern is shown. The results indicate the ability of the model to replicate the crack pattern also in case of very thin concrete cover, in which the change of environmental conditions plays an important role and has much more influence on the transport of corrosion products.

Additionally, in Fig. 6.28 the sum of the average calculated widths of the cracks on the external surface of the concrete specimen are plotted as a function of the average corrosion penetration of the reinforcement bar.



(a)



(b)

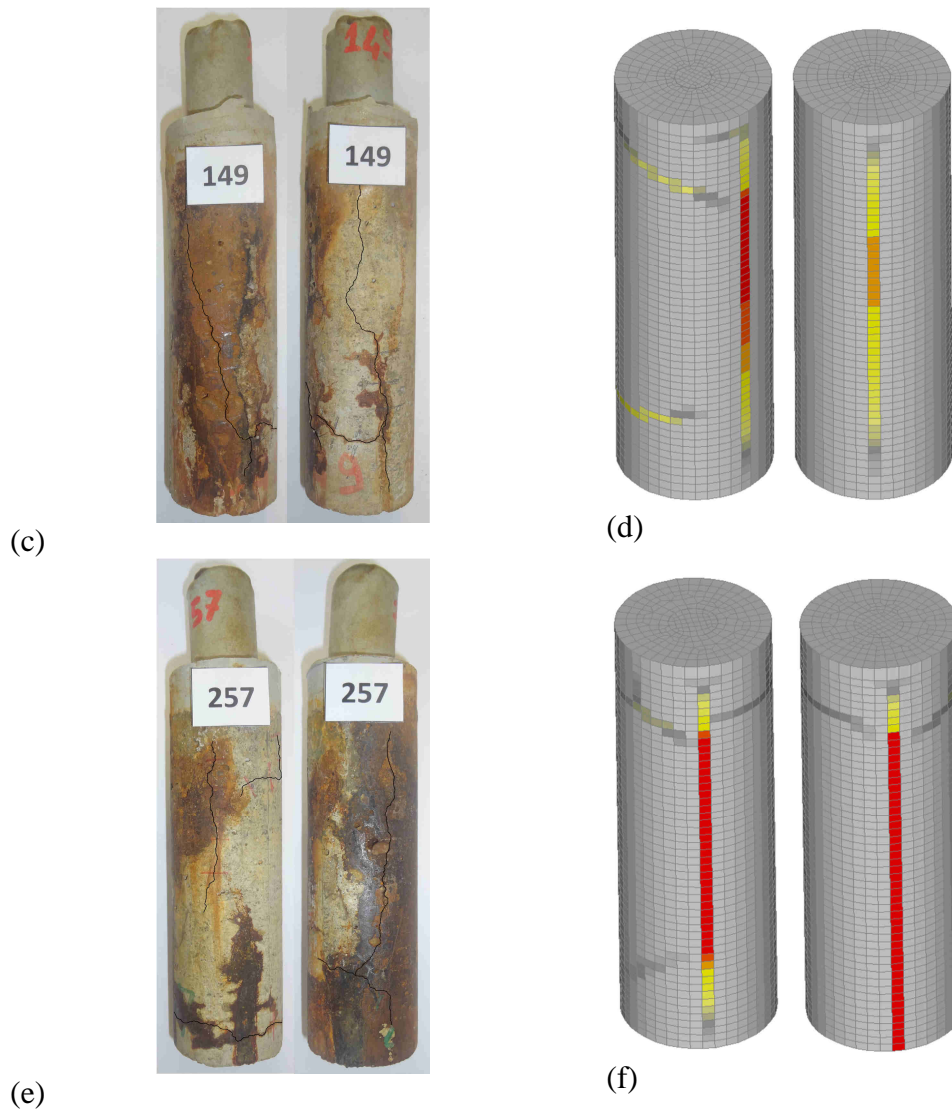


Fig. 6.27 Comparison of the crack pattern between numerical and experimental results (wetting/drying conditions) for the series C/8 (a), (b), C/12 (c), (d) and C/16 (e), (f)

The calculated increase of crack width as a function of the corrosion penetration shows a nice agreement with the experimental obtained data. However, the values of the calculated corrosion depth differ from the measured data and resulted lower. The difference between the numerical and experimental results in terms of corrosion penetration can be explained by different concrete quality, which can be extremely variable in case of small cover. Namely, this effect is especially stronger in cases C/12 and C/16 in which the concrete cover is relatively thin.

Moreover, it has to be noted that maximum value of the sum of the average crack widths is lower than in case of type A and B. This confirms the strong influence of the corrosion transport, which is in the specific case enhanced due to the very short crack length.

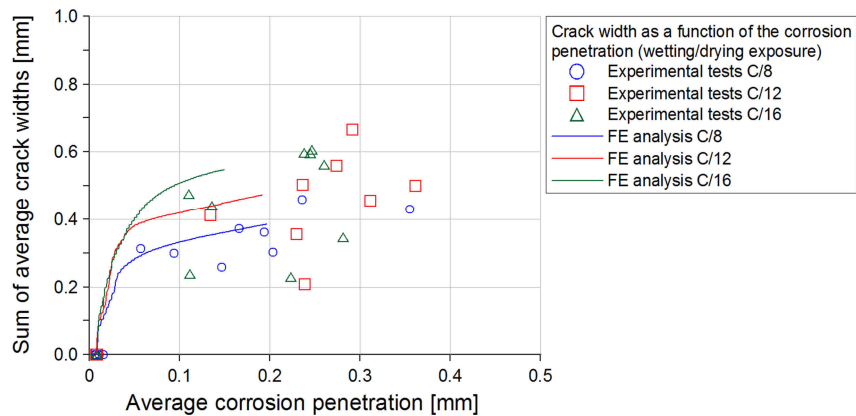


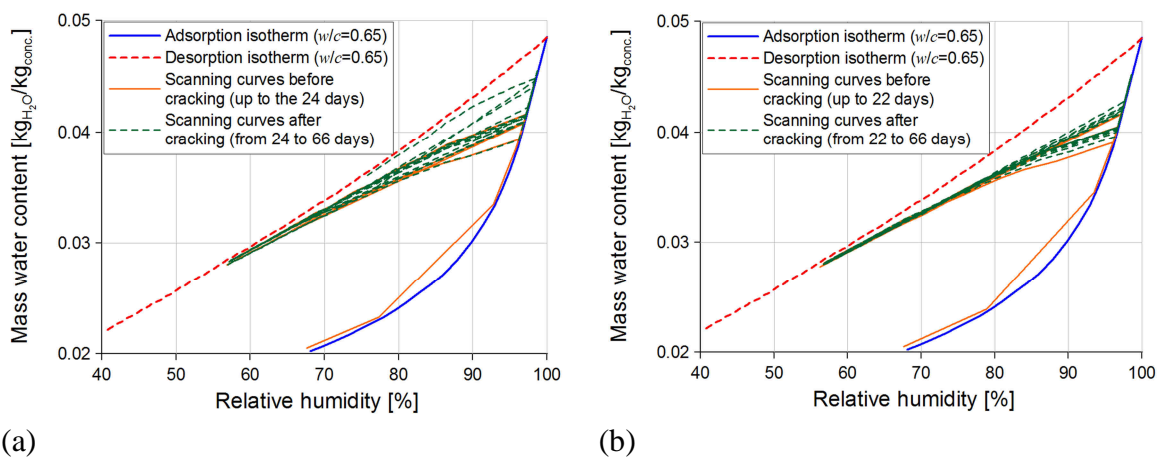
Fig. 6.28 Predicted and measured values of the sum of the average crack widths as a function of the average corrosion penetration for the specimen type C/8, C/12 and C/16 exposed to wetting/drying conditions

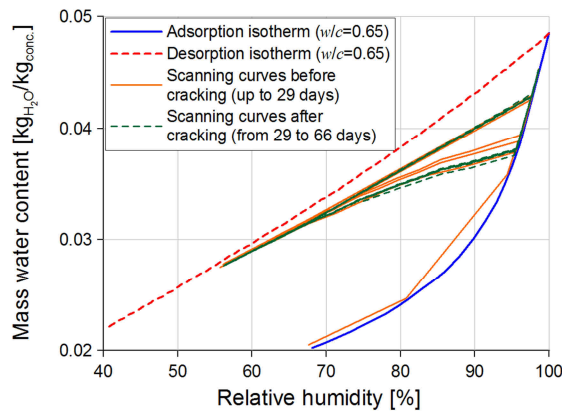
6.2.5.3 Hysteretic moisture behaviour and distribution of relative humidity

Illustration of the numerical results in terms of relative humidity and water content during cyclic wetting and drying is shown in Fig. 6.29. The analysis is assumed to start at 60% RH from adsorption curve.

It can be seen that the results of the changing external exposure with cyclic wetting/drying is different in comparison with specimen types A and B. Specifically, it can be noted that hysteretic behaviour is much more pronounced already before cracking of the concrete as result of the thinner cover. However, an increase in time of the total charge of mass is predicted after the crack opening, even though very slight.

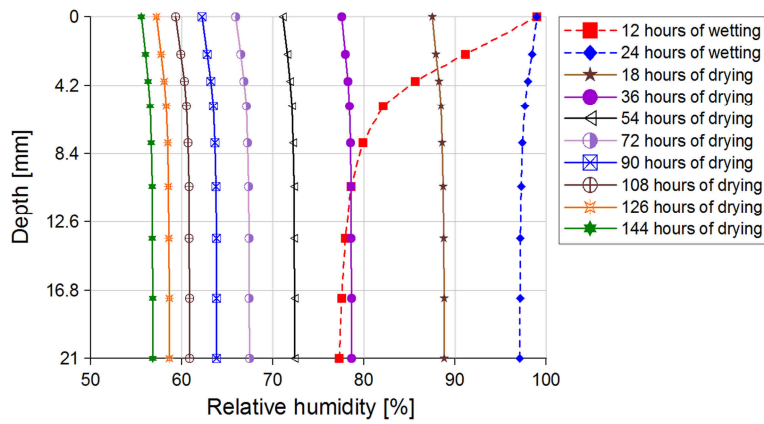
The previous described behaviour can be also detected from the prediction of the relative humidity distribution along the depth of the specimen before and after cracking (see Fig. 6.30). As expected, it can be noted that the smaller concrete exhibits faster wetting as well as drying behaviour.



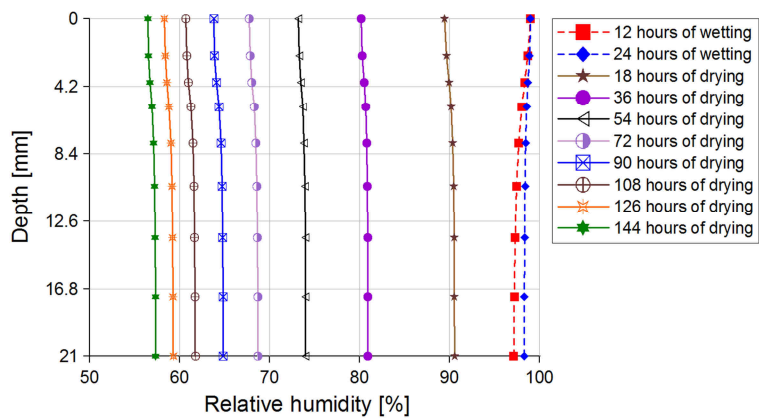


(c)

Fig. 6.29 Calculated scanning curves during the 7 weekly cycles of wetting and drying at the depth of 21 mm for the type C/8 (a), of 19 mm for the type C/12 (b) of 17 mm for the type C/16 (c)



(a)



(b)

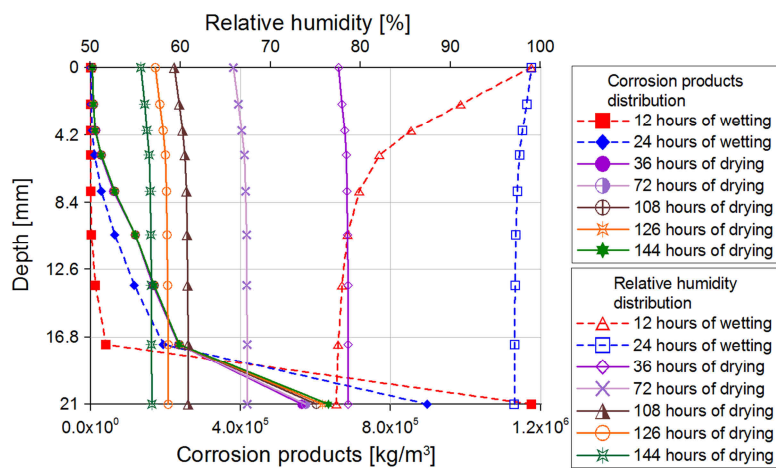
Fig. 6.30 Numerically obtained values of the relative humidity distribution along the depth for different time periods in the case of specimen type C/8: 1st cycle (a) and 7th cycle (b)

6.2.5.4 Distribution of the corrosion products

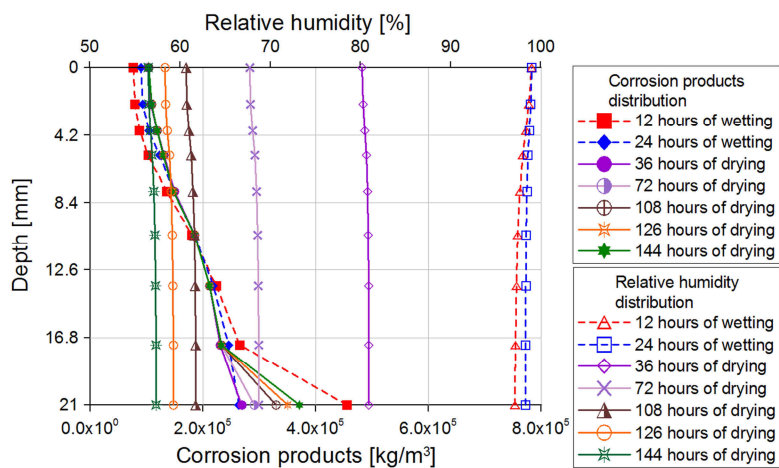
As for the other specimen types, the distribution of the corrosion products along the crack depth, together with the relative humidity distribution, is plotted in Fig. 6.31.

Directly after cracking (4th cycle), a different behaviour in comparison with the specimen types A and B can be noticed. Namely, due to the faster increase of relative humidity, the corrosion products are rapidly transported in cracks and start to accumulate along the crack. Later on, a slow increase of products around the rebar can be noted as consequence of the very low concrete conductivity and relative humidity values.

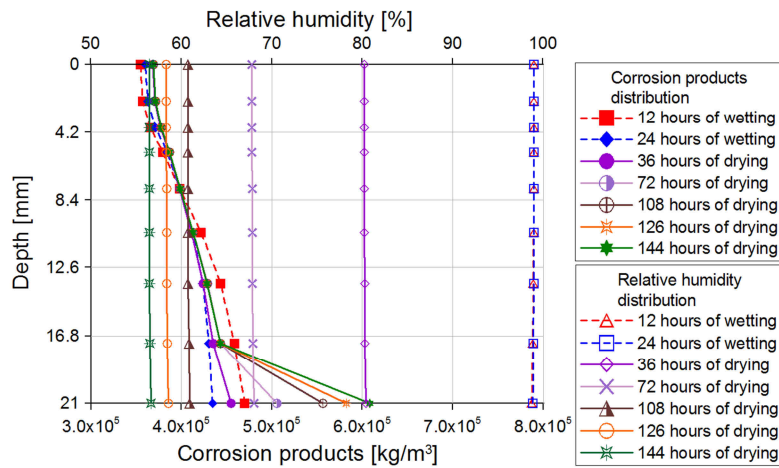
During the 7th and 32nd cycle no particular differences in the distribution of the corrosion products can be noted. However, the effect of wetting and drying, previously described are much more prominent due to the stronger effect of the dynamic moisture loading.



(a)



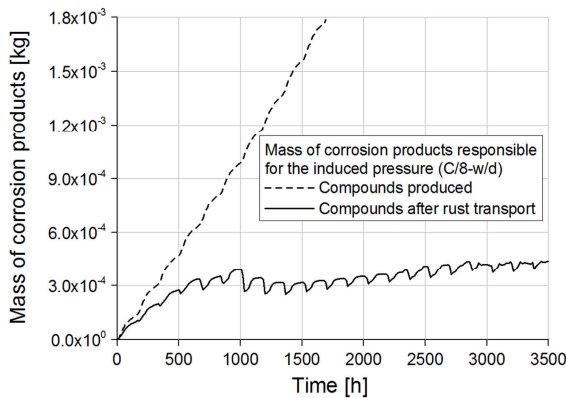
(b)



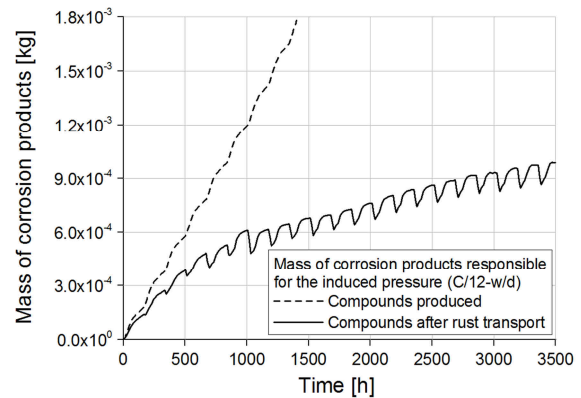
(c)

Fig. 6.31 Numerically obtained values of corrosion products and relative humidity distribution along the depth for different time periods during the 4th cycle (a) 7th cycle (b) and the 32nd cycle (c) of wetting drying exposure for specimen type C/8

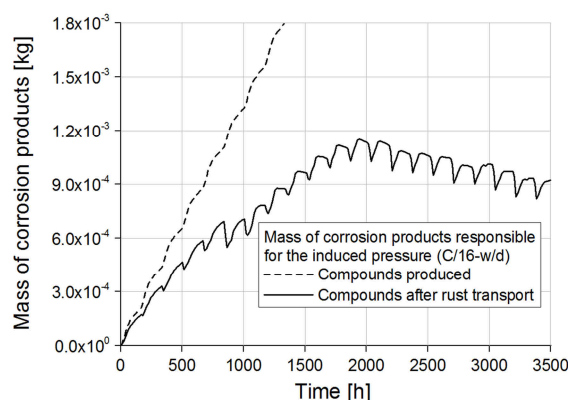
In the following, the amount of corrosion products which cause the cover cracking is plotted as a function of time (see Fig. 6.32). Similar to the specimen types A and B, an increase of the corrosion around the reinforcement bar is predicted before cracking. Due to the diffusion of corrosion products in pores and voids, the initial slope is lower than that of the curve which describes the compounds produced in time. After cover cracking, the behaviour can be considered similar to the specimen type B, since no sudden reduction of the mass is predicted. In case of larger cover (type A) the quick decrease of the products amount can be explained on the base of the higher pressure needed for cracking and higher impressed current density. In particular, the damage is characterized by failed elements around the rebar that physically are represented by microcracks (Wong et al., 2010) and interfacial damage (Michel et al., 2016). This effect is not noticed in types B and C in which no pronounced decreases are predicted, especially for the rebar diameters 8 and 12. However, for the cases B/16 and C/16 a slow decrease after cracking is detected due to the presence of internal cracks, consequence of the larger extent of anodic area.



(a)



(b)



(c)

Fig. 6.32 Total mass of corrosion products around the reinforcement bar, responsible for the induced pressure for the type C/8 (a), C/12 (b) and C/16 (c) exposed to wetting/drying conditions

6.2.6 Numerical results for the specimen type C: C/8, C/12 and C/16 – submerged specimens

The last case investigated is the simulation of the specimen type C continuously submerged. In the subsequent sections, comparison with experimental results and calibration of the initial diffusivity of corrosion products are presented.

6.2.6.1 Corrosion current density and model parameters

As already mentioned in the previous sections, only distribution of water and humidity, corrosion rate, expansion of corrosion products, induced damage and transport of corrosion products are simulated. Experimental average current density is used as input.

Table 6.12 Comparison between numerical and experimental results for the submerged specimen type C/8, C/12 and C/16 and the corresponding parameter D_{r0} used in the simulations

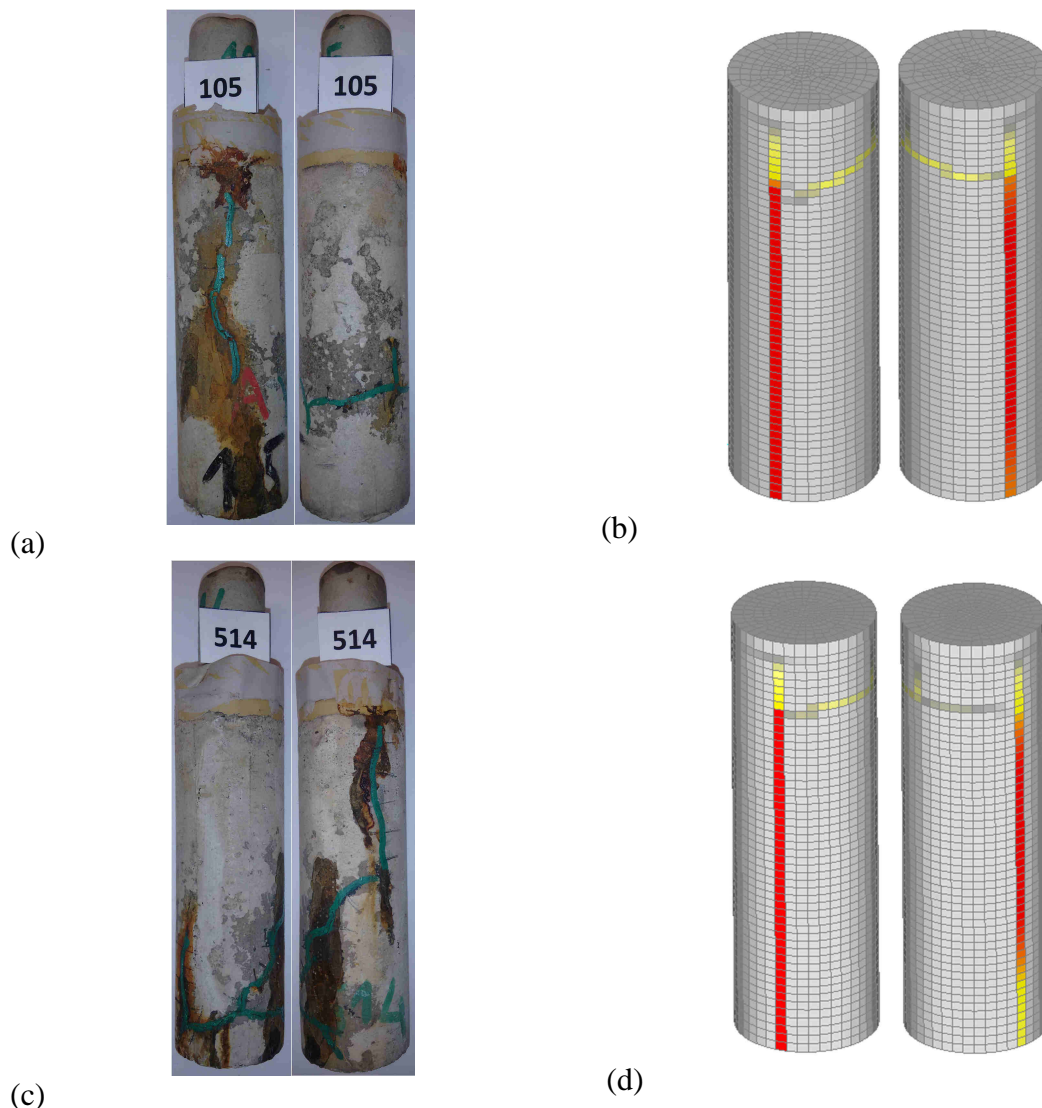
| Comparison between numerical and experimental results and values of the corrosion products diffusivity | | | | | |
|--|------------------------|-------------------------------------|------------------------|-------------------------------------|---------------------------------------|
| Specimen type | Experimental tests | | FE analysis | | |
| | $t_{cr,exp}$ (days) | $x_{corr,exp}$ (μm) | $t_{cr,num}$ (days) | $x_{corr,num}$ (μm) | D_{r0} (m^2/s) |
| C/8 | 83 | 17.1 | 76 | 15.1 | 5.5×10^{-16} |
| C/12 | 98 | 20.3 | 88 | 18.9 | 3.8×10^{-16} |
| C/16 | 116 | 25.4 | 115 | 22.1 | 3.5×10^{-16} |

The model parameters are the same as for the wetting/drying exposure and diffusivity of corrosion products (see Table 6.12) was calibrated on the base of the experimental results even though higher scatter of experimental data was obtained.

6.2.6.2 Crack pattern and development of the corrosion induced damage

Comparison between the experimental and numerical results at the 3rd corrosion stage is shown in Fig. 6.33. The numerical simulation can predicted nicely the presence of the vertical and horizontal cracks, even though the position of the horizontal damage cannot be exactly replicated. However, this can be considered a good result considering the complexity of the problem.

Similarly for the other cases, in Fig. 6.34 the sum of the average crack widths detected experimentally are compared with the experimental results. Even though higher scatter in the experimental data is obtained, the numerical simulation seems to follow the trend.



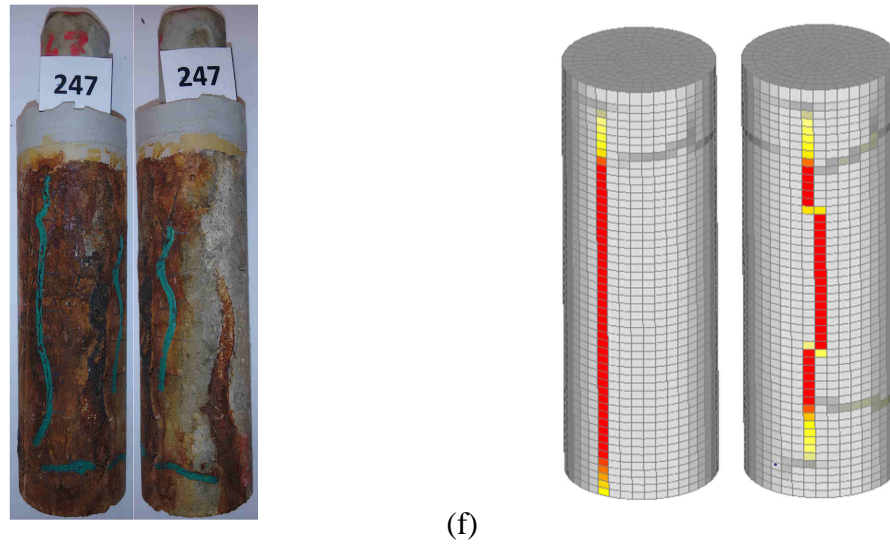


Fig. 6.33 Comparison of the crack pattern between numerical and experimental results of submerged specimens for the series C/8 (a), (b), C/12 (c), (d) and C/16 (e), (f)

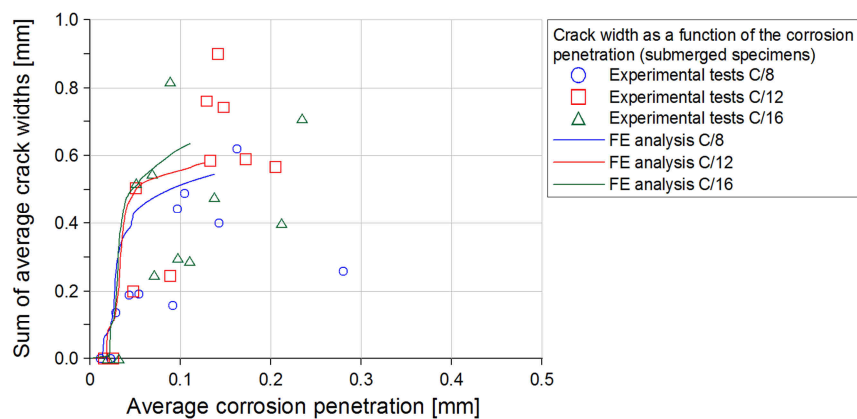


Fig. 6.34 Predicted and measured values of sum of the average crack widths as a function of the average corrosion penetration for the submerged specimen type C/8, C/12 and C/16

6.2.6.3 Distribution of the corrosion products

In Fig. 6.35 distribution of the corrosion products in kg/m^3 after cracking at different periods is shown. As expected, similar behaviour of the types A and B is observed. However, due to smaller concrete cover the redistribution of the corrosion products along the crack length is much faster.

On the other hand in Fig. 6.36 is plotted the mass of corrosion products which controls the cover cracking and the development of the induced damage in time. As can be seen, due to the lower pressure needed to induce concrete cracking, the critical mass is lower than in the cases A and B. Furthermore, a higher amount of products are predicted in comparison with the wetting/drying exposure due to the higher diffusivity detected.

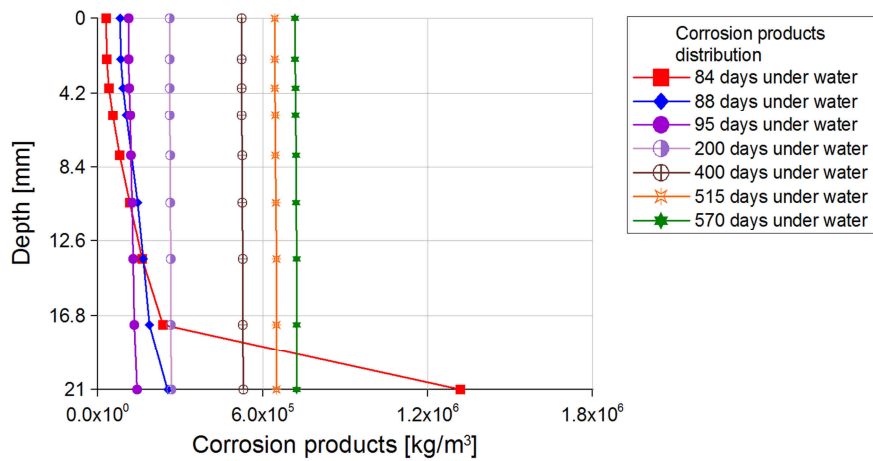


Fig. 6.35 Numerically obtained distribution of corrosion products along the depth for different time periods for the submerged specimen type C/8

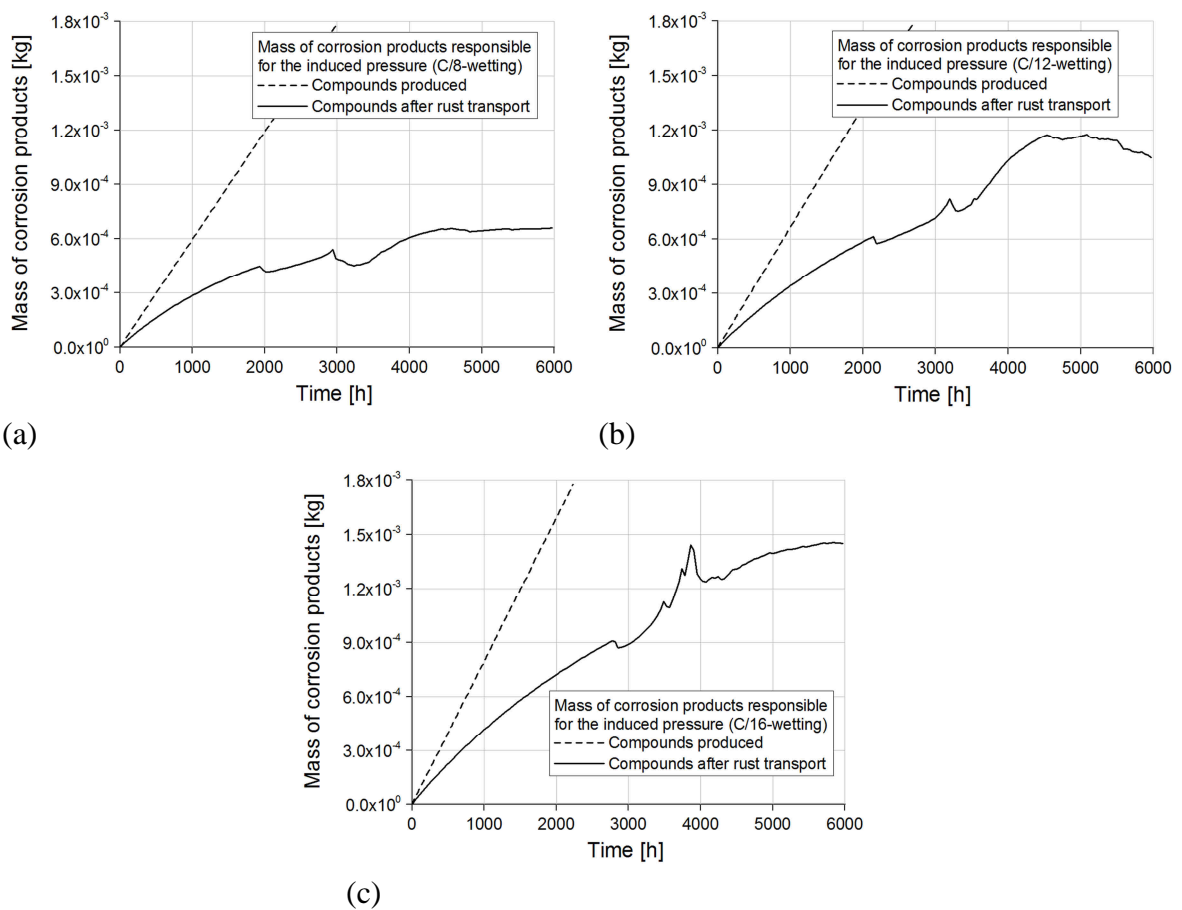


Fig. 6.36 Total mass of corrosion products around the reinforcement bar, responsible for the induced pressure for the submerged specimen C/8 (a), C/12 (b) and C/16 (c)

6.3 Summary of the numerical results

In order to give an overview of the numerical results and better describe the non-linear behaviour of the diffusion coefficient a summary of the calibrated parameter is shown in the following.

In Fig. 6.37, comparison between experimental and numerical results in terms of critical corrosion penetration as a function of the geometric ratio (c/d) is illustrated. As can be seen, the numerical results agree nicely with the experimental tests. Moreover, the different behaviour under wetting/drying conditions and for submerged specimens could be also captured.

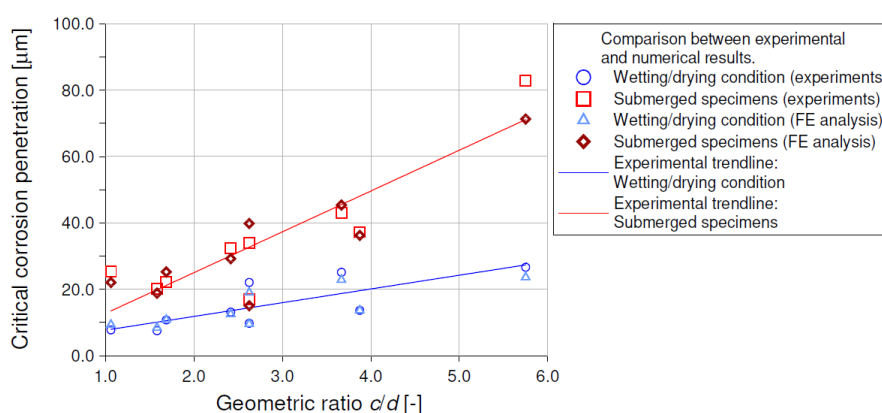


Fig. 6.37 Comparison between numerical and experimental results: critical corrosion penetration as a function of the geometric ratio c/d

Considering that the numerical model is able to reproduce the experimental test in terms of critical corrosion penetration, current density time history, crack pattern and development of induced damage, it can be concluded that the proposed relationship for diffusivity as a function of crack width and water content (described in Section 6.1.3) leads to realistic results.

However, no unique agreement could be found for the initial diffusivity in un-cracked concrete, which describes the penetration of the corrosion products in pores and voids around the reinforcement. Therefore, it can be concluded that the initial diffusivity is highly dependent on the imposed corrosion current density as already pointed out by several authors (see Section 2.3.1.1).

In Fig. 6.38, the resulting initial diffusivity, calibrated on the base of the experimental tests, is plotted as a function of the maximum current density detected in the numerical simulations.

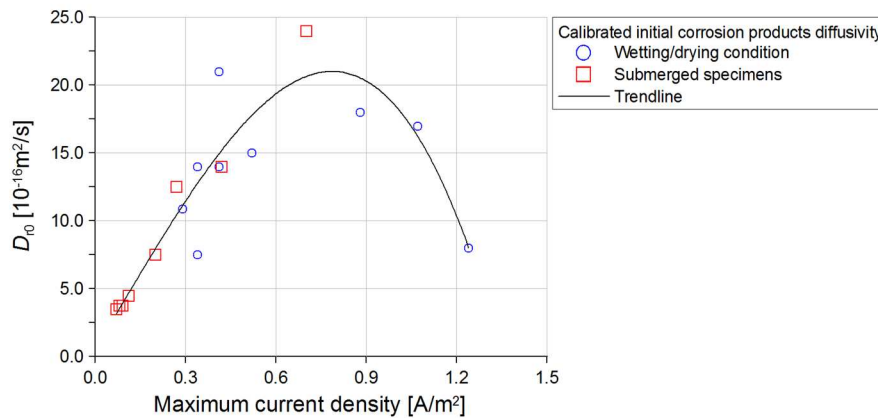


Fig. 6.38 Calibrated initial diffusivity of the corrosion products as a function of the maximum corrosion current density detected

As can be seen, the impressed corrosion current density has a strong influence on the value of the initial diffusivity, which reaches its maximum at approximately $0.80 \text{ A}/\text{m}^2$. However, values of current density much higher than $0.100 \text{ A}/\text{m}^2$ are not taken in consideration since they can significantly influence the formation and migration of the corrosion products. As demonstrated in Section 5, level of current density below $2.50 \text{ A}/\text{m}^2$ leads to reasonable results in terms of initial cracking but the initial diffusivity of products resulted much higher (approximately 4 times) than for lower applied current density.

6.4 Conclusions

The application of the developed 3D Chemo-Hygro-Thermo-Mechanical model for the simulation of the corrosion induced damage is validated against the proposed experimental tests. Different geometric ratios and exposure conditions are investigated. The hysteretic moisture model previously implemented is coupled with the other corrosion processes and it is used to predict the impressed corrosion current density and corrosion products distribution. It is shown that the change of relative humidity significantly influences the development of the corrosion induced damage. Moreover, the cracking of the concrete cover and the consequently transport of the corrosion products in cracks has a strong influence on the induced damage.

The numerical results and their comparison with the experimental tests yield to the following conclusions:

For the assumed concrete quality ($w/c=0.6$) and material properties, the predicted corrosion induced crack pattern correctly replicate the results of the experimental tests which is generally characterized by two vertical cracks connected by a horizontal one.

Computed current density under wetting/drying conditions and related time for cracking is similar to the experimentally observed result. Based on the comparison with the experiments, calibration of hysteretic moisture model and concrete conductivity was carried out.

It is shown that the exposure conditions significantly influence the critical corrosion penetration and cracking time. Higher diffusivity of corrosion products and higher critical corrosion depth are predicted in case of submerged specimens. However, a non-linear dependency of the initial diffusivity in function of the impressed corrosion current density is expected.

Transport of corrosion products in crack plays an important role in the development of the corrosion induced damage. The distribution of the corrosion products in cracks are considered dependent on crack width and level of saturation. Even though the process is modeled as convective diffusion problem, diffusion can be considered dominant in products migration. Furthermore, quantitative calibration of the corrosion products diffusivity on the base of the experimental results is proposed. It is shown that diffusivity increases logarithmically with the crack width following different curves, depending on the water content.

Due to the fact that a relatively large amount of corrosion products is distributed over the cracks, corrosion induced damage slows down at wider cracks due to the circulation of the outer solution which yields to an enhanced products diffusion.

7. ENTROPY PRODUCTION IN CORROSION PROCESSES OF STEEL REINFORCEMENT IN CONCRETE: NUMERICAL EXAMPLE

7.1 Objectives of the numerical applications

In general case, to compute the corrosion rate and the related induced damage it is necessary to assume position of anode and cathode on the reinforcement surface. The influence and the effect of their distribution is a complex aspect of the modelling of corrosion which is still not solved. Therefore, to bring more light into the effect of different anode/cathode surface positions several combinations on a typical RC beam, are numerically simulated. Based on the principle of maximum entropy production, deduced from irreversible thermodynamics, it is possible to find out which anode-cathode combination results to the highest corrosion induced damage. The entropy is produced by dissipative processes which are the flow of ions through electrolyte, the anodic and cathodic polarization and the diffusion oxygen process.

Particularly, in the following several numerical simulations on a multi-rebar RC beam are shown, by changing anodic and cathodic regions along the rebar length and over the circumference.

7.1.1 Numerical case study: Multi-rebar RC beam

As already mentioned, recent applications of the above presented 3D chemo-hygro-thermo-mechanical model (Ožbolt et al., 2010, 2011, 2012a,b and 2014) showed that the model is able to realistically replicate processes before and after depassivation of reinforcement as well as the corrosion induced damage. It has been demonstrated that the position of anodic and cathodic regions over the surface of reinforcement bars influences the corrosion of reinforcement and the crack pattern (Ožbolt et al., 2012a, 2014). In the following numerical parametric study the model is used to investigate the critical combination of the anode/cathode position by employing the principle of maximum entropy production. The parametric study for several different geometric parameters determining the position of the anode and cathode and its area ratio is performed for a multi-rebar reinforced concrete beam (Oršanić, 2015; Dong et al., 2011) which is a typical application from the engineering practice. The study is performed assuming that for the given boundary conditions, oxygen diffusivity and electrical conductivity of concrete, such geometrical relationship between anode and cathode is possible for the selected reinforced concrete element. Because of the complexity of the problem, only a beam segment of 130 mm is discretized (see Fig. 7.1). The three longitudinal reinforcement bars with diameter of 16 mm and spacing of 60 mm are investigated. The lateral and the bottom covers are 52 mm and 32 mm, respectively. Concrete and reinforcement bars are discretized using eight-node solid finite elements. The expansion due to the corrosion

products is simulated by means of one-dimensional (1D) radially oriented corrosion contact finite elements.

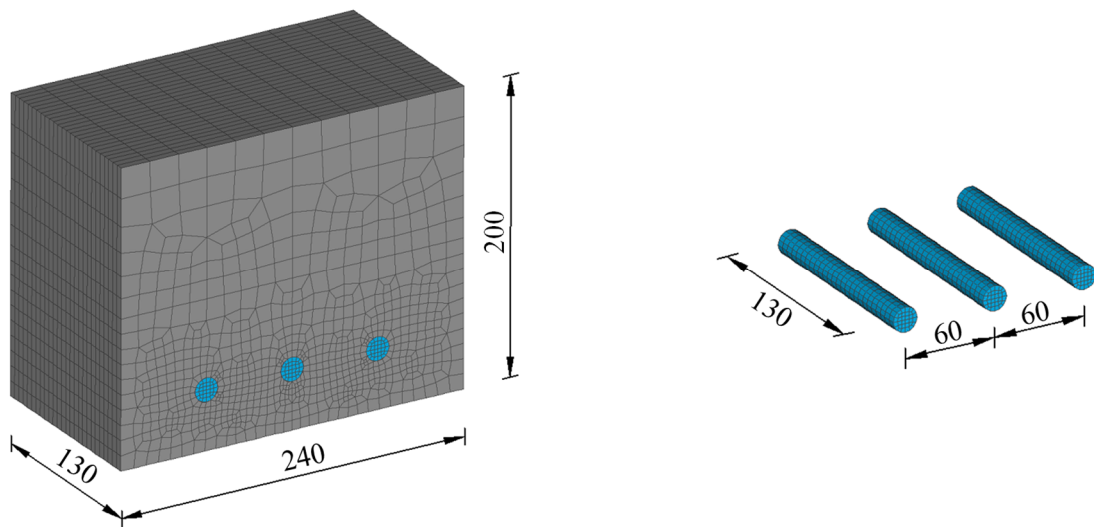
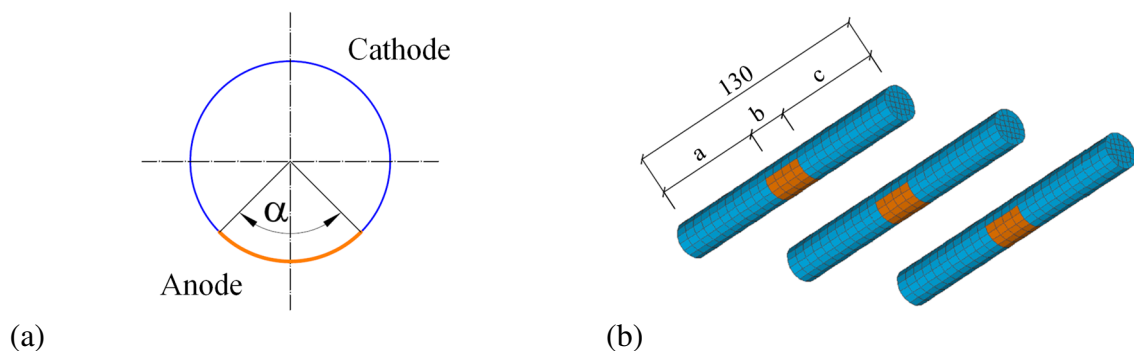


Fig. 7.1 Entropy production in corrosion processes: FE model of the beam section used in the numerical analysis (all in mm)

Since the aim of the parametric study is to investigate the influence of the position of the anodic and cathodic regions along the reinforcement bar length and across the section circumference on the entropy production and corrosion induced damage, different arrangements are examined. Three different longitudinal configurations are assumed (see Fig. 7.2). In the configuration A only one anodic region along the longitudinal direction is assumed and the rest of the reinforcement is considered as cathode. The configuration B and C have multiple anodic regions, subdivided in two and three portions, respectively. As already mentioned, in all of the three configurations different extent of the anodic area along the reinforcement length and over the circumference are investigated. These cases are chosen in order to find out which combination has the highest influence on the energy dissipation (entropy production) and, consequently, on the corrosion induced damage in concrete. The summary of the investigated cases can be found in Table 7.1. In total 26 different combinations are object of study.



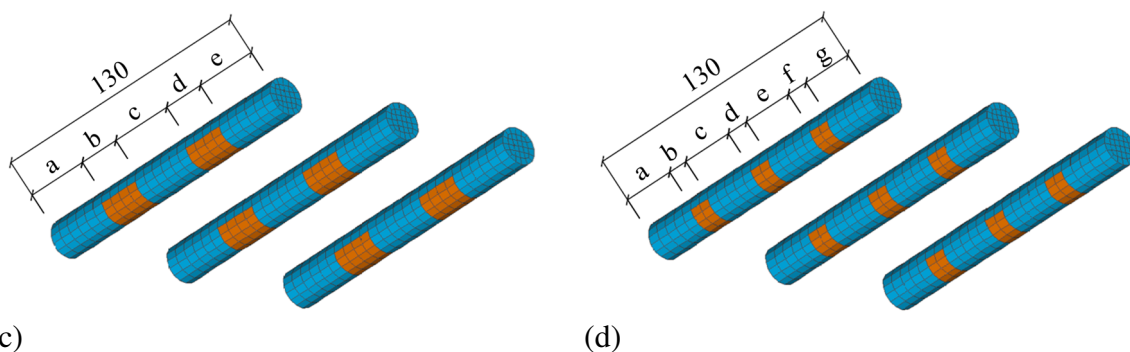


Fig. 7.2 Assumed distribution of the anodic and cathodic part: (a) over the circumference; along the reinforcement bar: (b) configuration A, (c) configuration B and (d) configuration C

Table 7.1 Summary of the investigated cases according to the extent of the anodic and cathodic area

| Investigated cases according to the extent of the anodic and cathodic area | | | | | | | | | |
|--|--------------------------------------|--|-------|------|------|------|------|------|------------------|
| Config. | Anodic region over the circumference | Anodic and cathodic regions over the length of the rebar | | | | | | | Area ratio |
| | | a | b | c | d | e | f | g | |
| | α ($^{\circ}$) | (mm) | (mm) | (mm) | (mm) | (mm) | (mm) | (mm) | A_A/A_C (-) |
| A-1 | 180 | 65.0 | 5.0 | 60.0 | - | - | - | - | 0.020 |
| A-2 | 180 | 55.0 | 20.0 | 55.0 | - | - | - | - | 0.083 |
| A-3 | 180 | 50.0 | 30.0 | 50.0 | - | - | - | - | 0.130 |
| A-4 | 180 | 40.0 | 50.0 | 40.0 | - | - | - | - | 0.238 |
| A-5 | 180 | 30.0 | 70.0 | 30.0 | - | - | - | - | 0.368 |
| A-6 | 180 | 15.0 | 100.0 | 15.0 | - | - | - | - | 0.625 |
| A-7 | 180 | 0.0 | 130.0 | 0.0 | - | - | - | - | 1.000 |
| A-8 | 360 | 65.0 | 5.0 | 60.0 | - | - | - | - | 0.040 |
| A-9 | 360 | 55.0 | 20.0 | 55.0 | - | - | - | - | 0.182 |
| A-10 | 360 | 50.0 | 30.0 | 50.0 | - | - | - | - | 0.300 |
| A-11 | 360 | 40.0 | 50.0 | 40.0 | - | - | - | - | 0.625 |
| A-12 | 360 | 30.0 | 70.0 | 30.0 | - | - | - | - | 1.167 |
| B-1 | 45 | 30.0 | 20.0 | 30.0 | 20.0 | 30.0 | - | - | 0.040 |
| B-2 | 90 | 30.0 | 20.0 | 30.0 | 20.0 | 30.0 | - | - | 0.083 |
| B-3 | 135 | 30.0 | 20.0 | 30.0 | 20.0 | 30.0 | - | - | 0.130 |
| B-4 | 180 | 30.0 | 20.0 | 30.0 | 20.0 | 30.0 | - | - | 0.182 |
| B-5 | 360 | 30.0 | 20.0 | 30.0 | 20.0 | 30.0 | - | - | 0.444 |

continued

continued

| | | | | | | | | | |
|-----|-----|------|------|------|------|------|------|------|-------|
| B-6 | 360 | 25.0 | 25.0 | 30.0 | 25.0 | 25.0 | - | - | 0.625 |
| B-7 | 360 | 20.0 | 35.0 | 20.0 | 35.0 | 20.0 | - | - | 1.167 |
| C-1 | 45 | 25.0 | 10.0 | 25.0 | 10.0 | 25.0 | 10.0 | 25.0 | 0.030 |
| C-2 | 90 | 25.0 | 10.0 | 25.0 | 10.0 | 25.0 | 10.0 | 25.0 | 0.061 |
| C-3 | 135 | 25.0 | 10.0 | 25.0 | 10.0 | 25.0 | 10.0 | 25.0 | 0.095 |
| C-4 | 180 | 25.0 | 10.0 | 25.0 | 10.0 | 25.0 | 10.0 | 25.0 | 0.130 |
| C-5 | 360 | 25.0 | 10.0 | 25.0 | 10.0 | 25.0 | 10.0 | 25.0 | 0.300 |
| C-6 | 360 | 20.0 | 15.0 | 20.0 | 20.0 | 20.0 | 15.0 | 20.0 | 0.625 |
| C-7 | 360 | 15.0 | 25.0 | 15.0 | 20.0 | 15.0 | 25.0 | 15.0 | 1.167 |

Computational modeling and solution of Eq. (4.75) (see Section 4.5) is a challenging task, especially considering the interaction between the transport processes, the complexity of the geometry and the external boundary conditions. Therefore, the processes before depassivation of reinforcement are here not computed. It is assumed that at the start of the analysis the reinforcement is already depassivated and positions of anode and cathode as well as their surfaces are specified in advance (see Tab. 7.1). For each combination the total rate of energy dissipation at steady state is calculated using Eq. (4.75). Moreover, the related phenomena such as corrosion induced damage of concrete and related current intensity are calculated as well.

The initial concentration of dissolved oxygen is taken as 0.0085 kg/m^3 of pore solution. This coincides with the values at the free boundaries of the beam, assuming the beam fully saturated with oxygen. Electrical conductivity and diffusivity of oxygen as a function of the water saturation are given in Table 7.2, while the other relevant parameters used in the computations of corrosion current density are the same as in Table 5.5 (see Section 5). The active corrosion phase is computed for the time period of $t = 7$ years.

Table 7.2 Electrical conductivity ($10^{-3} \Omega^{-1} \text{m}^{-1}$) and oxygen diffusivity ($10^{-8} \text{m}^2/\text{s}$) of concrete with $w/c=0.4$, according to Gjrv et al. (1977)

| Electrical conductivity of concrete and oxygen diffusivity | | | | | | | | | |
|--|------|------|------|------|------|------|------|-------|-------|
| Saturation (%) | 50 | 55 | 60 | 65 | 70 | 75 | 80 | 85 | 90 |
| σ_{natural} | 0.20 | 0.25 | 0.53 | 0.75 | 1.00 | 2.00 | 6.00 | 10.00 | 11.20 |
| D_o | 1.55 | 1.30 | 1.20 | 1.00 | 0.75 | 0.45 | 0.30 | 0.20 | 0.13 |

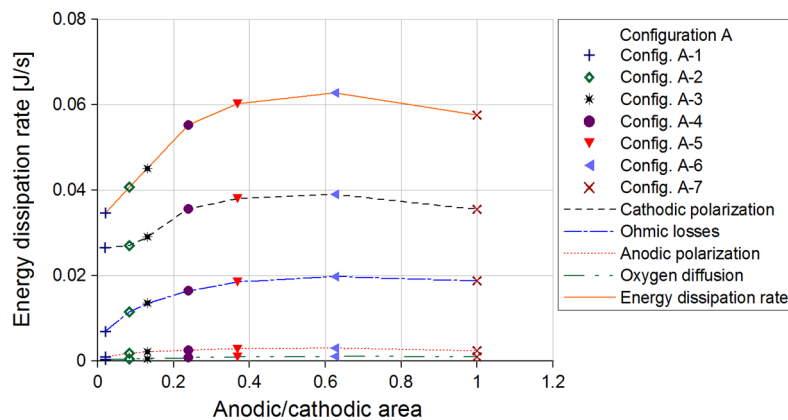
The adopted mechanical properties of concrete are: modulus of elasticity $E_c = 26.2 \text{ GPa}$, Poisson's ratio $\nu_c = 0.18$, uniaxial compressive strength $f_c = 31 \text{ MPa}$, tensile strength $f_t = 1.92 \text{ MPa}$ and fracture energy $G_F = 40 \text{ J/m}^2$. Steel is assumed to be linear elastic with modulus of elasticity $E_s = 200 \text{ GPa}$ and Poisson's ratio $\nu_s = 0.33$. As mentioned before, the

analyses are carried out only considering the processes after depassivation of reinforcement for an un-cracked good quality concrete ($w/c = 0.4$) assuming constant water saturation of 50%.

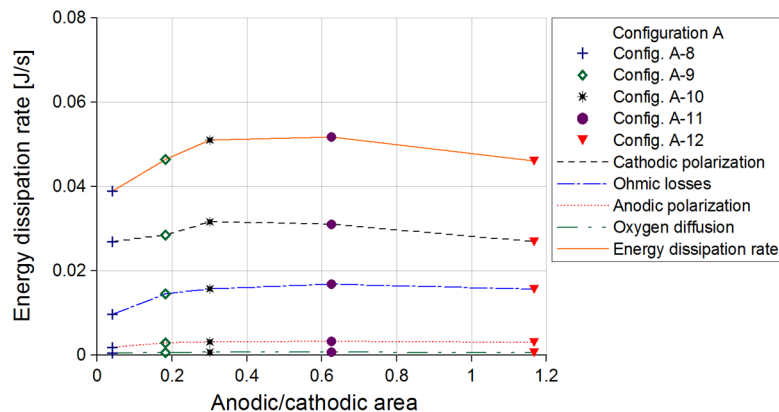
7.1.2 Results and discussion

The steady state energy dissipation rates computed using Eq. (4.74) are plotted for all configurations in Fig. 7.3 as a function of the ratio between anodic and cathodic areas. Shown is the total energy dissipation rate and separate contributions of: (i) oxygen molecular diffusion, (ii) ion flow through electrolyte, (iii) anodic polarization and (iv) cathodic polarization, for the three cases A, B, C, respectively.

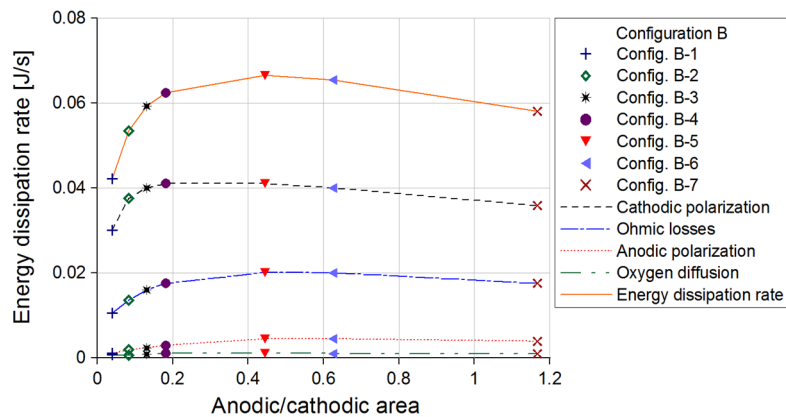
From the comparison of different contributions shown in Fig. 7.3 can be seen that the contribution of the cathodic polarization and ion flow through electrolyte are dominant. On the contrary, the contribution of the anodic polarization and oxygen molecular diffusion represent as maximum only 8.5% of the total energy dissipation. The numerical results show that with the increase of the ratio between anodic/cathodic areas the energy dissipation increases up to a certain critical value. With further increase of the ratio energy dissipation decreases. This effect is more pronounced for configurations B and C, and less for the case A.



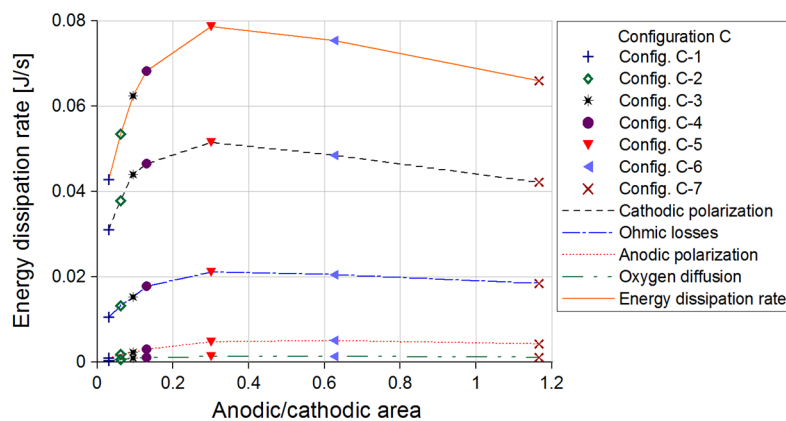
(a)



(b)



(c)



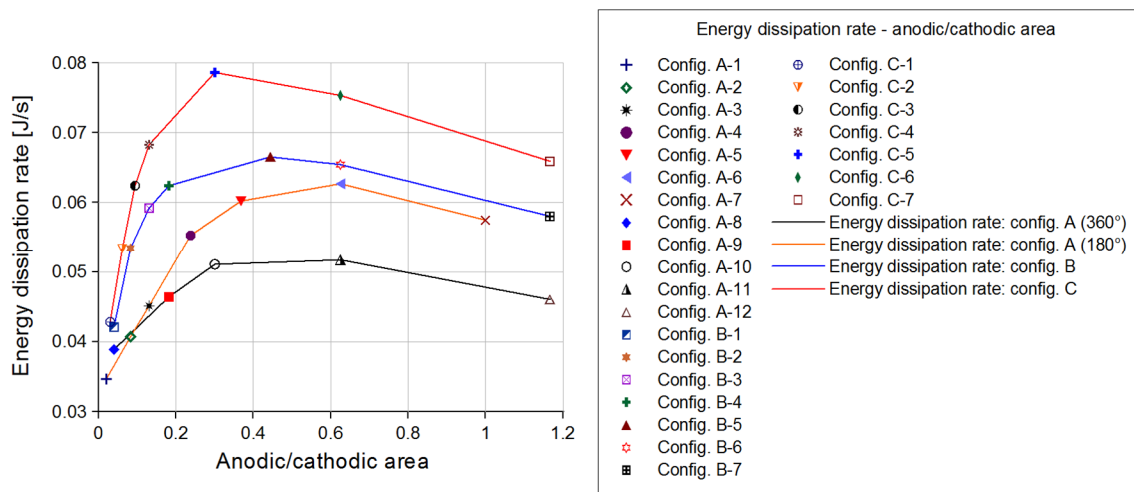
(d)

Fig. 7.3 Numerical values of the energy dissipation rate related to the entropy production as a function of the anodic/cathodic area ratio: (a), (b) configuration A; (c) configuration B and (d) configuration C

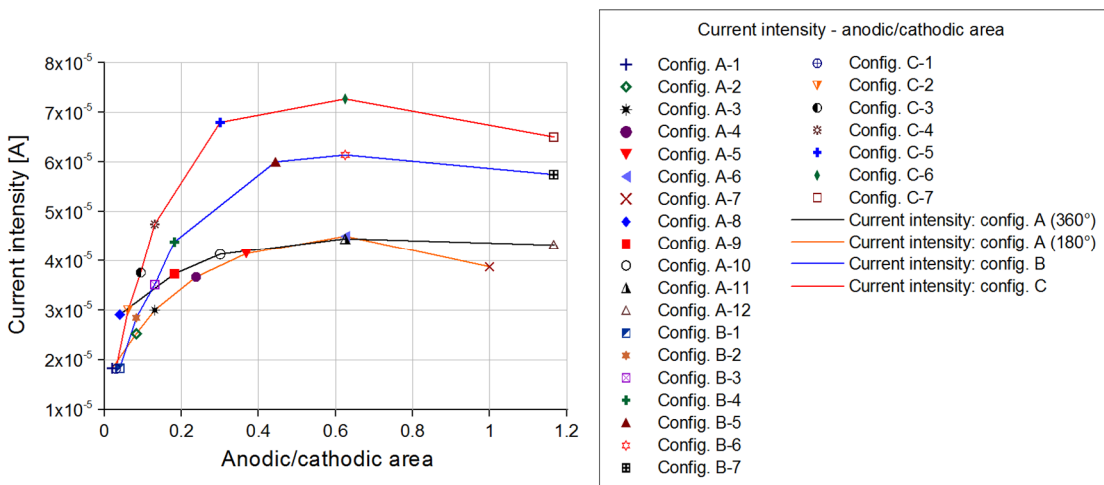
The maximum entropy production is reached for the anodic/cathodic area ratio of 0.63, 0.44 and 0.30, for the configuration A, B and C, respectively. The absolute maximum of energy dissipation is obtained for the case C (C-5, see Table 7.1). Furthermore, it can be seen that different area distribution along the longitudinal bars strongly influences the contribution of cathodic polarization and ion flow through electrolyte. It is also important to note that for the same area ratio, the distribution of anodic area over the circumference and length has a strong influence on the total energy dissipation.

In Figs. 7.4a,b the calculated energy dissipation rate and current intensity are plotted for all analyzed cases as a function of the anodic/cathodic area ratio. As can be seen, the current intensity exhibits similar trend as the dissipated energy. However, except for the configuration A, the peak values of current intensity do not coincide with the peak values of dissipated energy. The maximum current intensity is observed for the case C (C-6, see Table 7.1), similar as for the entropy. It is interesting to observe that the maximum current intensity is obtained for all configurations, at the same anodic/cathodic area ratio (0.63). In contrary to this, maximum of dissipated energy for different configurations depends also

on the anodic/cathodic area ratio. Increasing a number of cathodic zones the ratio at which entropy production reaches maximum decreases, i.e. it varies from 0.63 to 0.30.



(a)



(b)

Fig. 7.4 Energy dissipation rate (a) and current intensity as function of the anodic/cathodic area ratio (b)

The effect of changes in the anodic/cathodic area ratio on the corrosion rate is determined by the type of governing of the corrosion process. If governing is mixed, as in here presented model, the change in corrosion rate (or entropy production) due to the change in the anodic/cathodic area ratio, depends on the contribution of anodic, cathodic and the ohmic governing mode as well as the geometry of the system.

In the engineering practice the criteria based on the maximum current intensity is generally accepted as the relevant criteria for the measure of the highest corrosion rate of reinforcement in concrete (Ghods et al., 2007). However, from the theoretical point of view the criteria based on the maximum entropy production should be relevant (Bažant,

1979a). The results of the present numerical study confirm this and indicate that the criterion for the most critical corrosion rate based on the current intensity cannot be always applied.

To demonstrate the effect of distribution of cathodic and anodic areas on the corrosion induced damage in concrete, development of the corrosion induced damage (crack patterns) for the cases A-6, A-11, B-5 and C-5 are shown in Fig. 7.5.

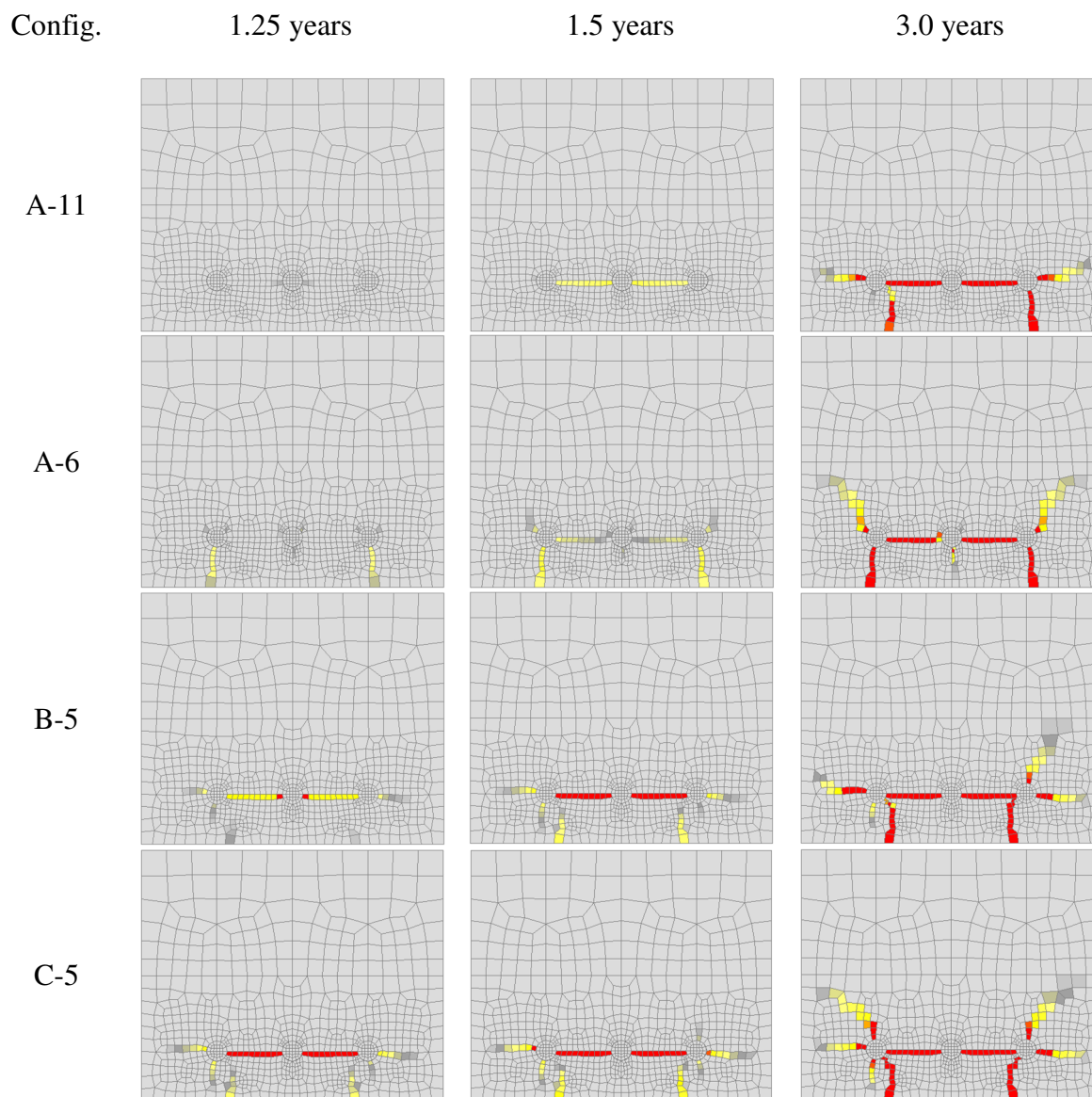


Fig. 7.5 Predicted corrosion induced crack pattern in the beam cross section, 1.25, 1.5 and 3.0 years after depassivation, for the configurations which exhibit the highest energy dissipation: A-6, A-11, B-5 and C-5 (red = critical crack opening of 0.10mm)

It can be seen that the distribution of the anode/cathode regions significantly influences time of the appearance of the first visible crack. Crack patterns for these four cases after

1.25, 1.5 and 3.0 years are similar, however, the level of the corrosion induced damage is significantly different. Comparing the four cases, it can be seen that the numerical results show good agreement with the principle of maximum entropy production. It can be observed that maximum damage of concrete after 3 years coincide with the maximum of dissipated energy.

Furthermore, in Fig. 7.6 is shown for the configuration C, case in which the maximum entropy production is observed, the crack development for the cases C-1, C-5 and C-7. Note that the entropy production is the lowest in the case C-1 and the highest for the case C-5. The crack patterns from Fig. 7.6 show that maximum damage is obtain for the case C-5, i.e. maximum entropy production coincides with the maximum corrosion induced damage of concrete beam.

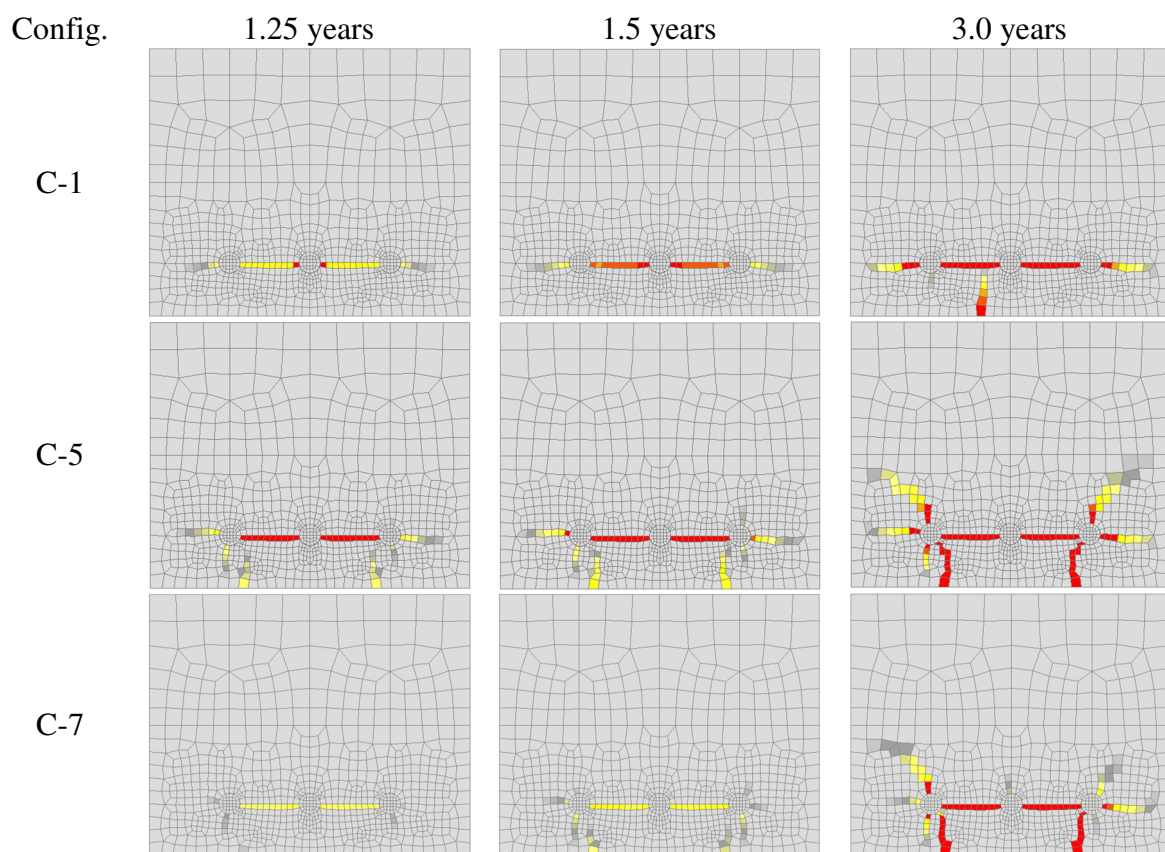


Fig. 7.6 Predicted corrosion induced crack pattern in the beam cross section, 1.25, 1.5 and 3.0 years after depassivation, for the configurations: C-1, C-5, and C-7 (red=critical crack opening of 0.10mm)

7.2 Conclusions

The mathematical formulation of the entropy production in corrosion cells and its relative relation with corrosion rate and corrosion induced damage is discussed. The numerical study is performed on RC multi-rebar reinforced beam without stirrups. Based on the results of the study the following conclusions can be drawn out.

The computation of entropy production is carried out assuming that the main dissipative processes are: ion flow through electrolyte, anodic and cathodic polarization and oxygen diffusion process. The results of the study show that among these four dissipative processes the contribution of cathodic and ohmic heating to entropy production is dominant whereas the contribution due to oxygen diffusion and anodic polarization are much lower.

It is typically observed that for all investigated configurations the entropy production first increases with the increase of the anodic/cathodic surface ratio up to the maximum value and subsequently there is a decrease. For the assumed boundary conditions and geometry, the entropy production and anodic/cathodic ratio at which dissipation is maximum depends on the assumed position of cathodic and anodic surfaces. Generally it is shown that the entropy production increases with increasing number of anodic and cathodic regions.

Comparing the corrosion induced damage of concrete it can be concluded that maximum entropy production is directly correlated with the highest corrosion induced damage in concrete element.

It is shown that the shape of the relationship between current intensity vs. anodic/cathodic surface ratio is similar with the relationship between entropy production vs. anodic/cathodic surface ratio. Moreover, maximum of current intensity is obtained for the same anode-cathode combinations (Case C). However, it is interesting to observe that maximum of current intensity for all investigated cases is obtained for the anodic/cathodic surface ratio of approximately 0.60 whereas the same ratio for the entropy energy production depends on the geometry, i.e. it is different in all three here investigated cases (A, B and C).

It should be pointed out that for each geometry and boundary conditions there are an infinite number of possible anodic-cathodic combinations and to find the critical one is a rather demanding task. However, the main aim of the present study was to demonstrate that maximum entropy production coincides with the maximum of corrosion induced damage of concrete. Therefore, the principle of maximum entropy production can be considered as an important theoretical tool to find the most critical combination between anodic and cathodic surfaces of reinforcement.

8. CONCLUSIONS AND OUTLOOK

In the framework of the present work, recently developed 3D Chemo-Hygro-Thermo-Mechanical (CHTM) model for concrete is further improved. The work is focused on the calibration of the model parameters with particular reference to the transport of the corrosion products in cracks and diffusion in pores and voids in the vicinity of the reinforcement.

An extensive experimental program is proposed to quantitatively verify and calibrate the 3D CHTM model, in the first part of the study. Concrete cylinders with different geometric ratios (cover/reinforcement diameter) are investigated under natural and laboratory controlled conditions. In the experiments, evaluation of the mass loss and monitoring of the crack pattern and width, at different level of corrosion induced damage, as well as readings of the average current density are shown. Under accelerated corrosion conditions, two different environmental exposures are investigated. Specifically, some specimens are subjected to wetting/drying cycles (1 day wetting, 6 days drying) and some are constantly immersed in water. It is shown that the environmental settings in accelerated corrosion conditions strongly influence cracking time and the development of the corrosion induced damage.

The expansion of the corrosion products and the subsequent compressive pressure on the concrete cover is accurately evaluated by means of microscope analysis and Raman spectroscopy, employed to characterize the nature of the corrosion compounds. It is shown that in submerged specimens, mainly Magnetite is identified at the concrete/steel interface as result of the low concentration of dissolved oxygen. Under cyclic wetting/drying, Goethite and Akaganeite are detected. Furthermore, at high level of saturation, penetration in the cement paste is more pronounced than in wetting/drying exposure. This explains the difference in terms of cracking time and corresponding crack growth.

The performed numerical analysis, employing the developed 3D CHTM model, shows that the predicted corrosion rate is significantly affected by the hysteretic moisture behaviour of concrete, by the geometry of the specimen and by transport of corrosion products in pores and cracks. Further on, the calibration of the volume expansion factor based on the corrosion products characterization plays an important role in determining the cracking time.

The influence of distribution of relative humidity and water content on predicted current density is studied for different geometric ratios. Numerical results show a very good agreement with the experimental tests in which, for the wetting/drying exposure, sudden increase of current density is noted during wetting and progressive decrease during drying. Moreover, hysteretic moisture behaviour is much more pronounced in the presence of concrete damage.

The study of different imposed potential confirmed the influence of the impressed current density on the accommodation of corrosion products in pores and voids close to the reinforcement bar. It is shown that initial diffusion coefficient in un-cracked concrete is a non-linear function of the current density, which can significantly influence the formation and migration of the corrosion compounds. On the other hand, distribution of the products in cracks is considered dependent on the crack width and level of saturation. It is shown that diffusivity increases with the crack width (logarithmic trend) following different curves depending on the water content. Further on, the performed parametric study shows that in case of submerged specimen, higher initial diffusivity of corrosion products is detected, leading to larger critical corrosion depth. Additionally, it can be concluded that even though the process is modeled as convective diffusion problem, diffusion can be considered dominant for migration of products.

The crack pattern and development of the corrosion induced damage in time corresponds nicely with the experimental results for all the investigated geometric ratios. It is shown that as consequence of the transport of corrosion products, the increase of the crack widths becomes progressively slower. Due to the fact that a relatively large amount of corrosion products is distributed over the cracks, the corrosion induced pressure is less pronounced.

Currently, in simulation of natural corrosion, the position of the anodic and cathodic regions is assumed in advance. However, there are an infinite number of possible anode-cathode combinations. The influence and the effect of their distribution is a complex aspect of the corrosion modelling and it is still not solved. Therefore, a mathematical formulation of the entropy production in corrosion cells and its relative relation with corrosion rate and corrosion induced damage is proposed. The computation of entropy production is carried out on a multi-rebar reinforced concrete beam considering that the main dissipative processes are: ion flow through electrolyte, anodic and cathodic polarization and oxygen diffusion process. It is demonstrated that the maximum entropy production is directly correlated with the highest corrosion induced damage in concrete element. It is typically observed that for all investigated configurations the entropy production first increases with the increase of the anodic/cathodic surface ratio, up to the maximum value, and subsequently there is a decrease. For the assumed boundary conditions and geometry, the entropy production and anodic/cathodic ratio at which dissipation is maximum depends on the assumed position of cathodic and anodic surfaces. Generally, it turns out that the entropy production increases with increasing number of anodic and cathodic regions.

Although all of the presented numerical studies give a good agreement with the experimental data, further work is needed to compare the results of the accelerated corrosion tests with the tests under natural corrosion conditions. Evaluation of running experiments in natural environment is needed in order to correctly calibrate the modelling parameter and highlight the differences with the laboratory controlled conditions.

However, the diffusivity of compounds in the induced cracks can be supposed to be the same as in accelerated corrosion test, under the assumption that the effect of the water circulation has a stronger influence than the imposed current density. Furthermore, considering a maximum current density of 0.20-0.30 A/m² reached in natural environment, an initial diffusivity of approximately 10⁻¹⁵ m/s², according to the proposed relationship, can be used for numerical simulations of corrosion of reinforcement in concrete. However, the assumed value and the corresponding effects should be analysed and verified with the experimental data.

BIBLIOGRAPHY

Ababneh, A., Benboudjema, F., & Xi, Y. (2003). Chloride penetration in nonsaturated concrete. *Journal of Materials in Civil Engineering*, 15(2), 183-191.

Åhs, M. (2007). Moisture redistribution in screeded concrete slabs. Report TVBM 3136.

Aldea, C. M., Ghandehari, M., Shah, S. P., & Karr, A. (2000). Estimation of water flow through cracked concrete under load. *ACI Materials Journal*, 97(5), 567-575.

Al-Harthy, A. S., Stewart, M. G., & Mullard, J. (2011). Concrete cover cracking caused by steel reinforcement corrosion. *Magazine of Concrete Research*, 63(9), 655-667.

Aligizaki, K. K., de Rooij, M. R., & Macdonald, D. D. (2000). Analysis of iron oxides accumulating at the interface between aggregates and cement paste. *Cement and Concrete Research*, 30(12), 1941-1945.

Alisa, M., Andrade, C., Gehlen, C., Rodriguez, J., & Vogels, R. (1998). Modelling of degradation. Brussels: Brite-Euram, 174.

Allan, M. L. (1995). Probability of corrosion induced cracking in reinforced concrete. *Cement and Concrete Research*, 25(6), 1179-1190.

Alonso, C., Andrade, C., Rodriguez, J., & Díez, J. M. (1998). Factors controlling cracking of concrete affected by reinforcement corrosion. *Materials and structures*, 31(7), 435-441.

Anderberg, A. (2004). Moisture properties of self-levelling flooring compounds. Report TVBM 3120.

Anderberg, A. (2004). Moisture properties of self-levelling flooring compounds. Report TVBM 3120.

Andrade, C., Alonso, C., Gonzalez, J. A., & Rodriguez, J. (1989). Remaining service life of corroding structures. In *DURABILITY OF STRUCTURES. IABSE SYMPOSIUM, SEPTEMBER 6-8 1989, LISBON (IABSE REPORT VOLUME 57/1)*.

Andrade, C., Alonso, C., & Molina, F. J. (1993). Cover cracking as a function of bar corrosion: Part I-Experimental test. *Materials and structures*, 26(8), 453-464.

Andrade, C., & Alonso, C. (1996). Progress on design and residual life calculation with regard to rebar corrosion of reinforced concrete. In *Techniques to Assess the Corrosion Activity of Steel Reinforced Concrete Structures*. ASTM International.

Andrade, C., Díez, J. M., & Alonso, C. (1997). Mathematical modeling of a concrete surface "skin effect" on diffusion in chloride contaminated media. *Advanced Cement Based Materials*, 6(2), 39-44.

Andrade, C., & Alonso, C. (2004). Test methods for on-site corrosion rate measurement of steel reinforcement in concrete by means of the polarization resistance method. *Materials and Structures*, 37(9), 623-643.

- Andrade, C., Cesetti, A., Mancini, G., & Tondolo, F. (2016). ESTIMATION OF CORROSION ATTACK IN REINFORCED CONCRETE BY MEANS OF CRACK OPENING. *Structural Concrete*. John Wiley & Sons.
- Angst, U., Elsener, B., Larsen, C. K., & Vennesland, Ø. (2009). Critical chloride content in reinforced concrete - a review. *Cement and Concrete Research*, 39(12), 1122-1138.
- Angst, U., Elsener, B., Jamali, A., & Adey, B. (2012). Concrete cover cracking owing to reinforcement corrosion—theoretical considerations and practical experience. *Materials and Corrosion*, 63(12), 1069-1077.
- Apostolopoulos, C. A., Demis, S., & Papadakis, V. G. (2013). Chloride-induced corrosion of steel reinforcement—Mechanical performance and pit depth analysis. *Construction and Building Materials*, 38, 139-146.
- Baroghel-Bouny, V. (2007). Water vapour sorption experiments on hardened cementitious materials: Part I: Essential tool for analysis of hygral behaviour and its relation to pore structure. *Cement and Concrete Research*, 37(3), 414-437.
- Bazant, M. Z., & Bažant, Z. P. (2012). Theory of sorption hysteresis in nanoporous solids: Part II Molecular condensation. *Journal of the Mechanics and Physics of Solids*, 60(9), 1660-1675.
- Bažant, Z. P. & Najjar, L. J. (1972). Nonlinear water diffusion in nonsaturated concrete. *Matériaux et Construction*, 5(1), 3–20.
- Bažant, Z. P. (1975). Pore pressure, uplift, and failure analysis of concrete dams. *Int. Commission on Large Dams*.
- Bažant, Z. P. (1979a). Physical model for steel corrosion in concrete sea structures—theory. *Journal of the Structural Division*, 105(6), 1137-1153.
- Bažant, Z. P. (1979b). Physical model for steel corrosion in concrete sea structures--application. *Journal of the structural division*, 105(ASCE 14652 Proceeding).
- Bažant, Z. P. & Kaplan, M. F. (1996). *Concrete at high temperatures*. Longman Essex, UK.
- Bažant, Z. P., Hauggaard, A. B., Baweja, S., & Ulm, F. J. (1997). Microprestress-solidification theory for concrete creep. I: Aging and drying effects. *Journal of engineering Mechanics*, 123(11), 1188-1194.
- Bažant, Z. P., Adley, M. D., Carol, I., Jirásek. M., Akers, S. A., Rohani, B., Cargile, J. D. & Caner, F. C. (2000). Large-strain generalization of microplane model for concrete and application. *Journal of engineering mechanics*, 126(9), 971–980.
- Bear, J., & Bachmat, Y. (1991). *Introduction to modeling of transport phenomena in porous media* (Vol. 4). Springer Science & Business Media.
- Bertolini, L., Elsener, B., Pedferri, P., Redaelli, E. & Polder, R. B. (2004). *Corrosion of steel in concrete*. John Wiley & Sons.

- Bertolini, L., Elsener, B., Pedersen, P., Redaelli, E., & Polder, R. B. (2013). *Corrosion of steel in concrete: prevention, diagnosis, repair*. John Wiley & Sons.
- Bhargava, K., Ghosh, A. K., Mori, Y., & Ramanujam, S. (2005). Modeling of time to corrosion-induced cover cracking in reinforced concrete structures. *Cement and Concrete Research*, 35(11), 2203-2218.
- Böckris, J., Reddy, A., & Gamboa-Aldeco, M. (2000). *Modern Electrochemistry, 2A: Fundamentals of Electrode Processes*. Modern Electrochemistry, 2A: Fundamentals of Electrode Processes.
- Böhni, H. (Ed.). (2005). *Corrosion in reinforced concrete structures*. Elsevier.
- Broekhoff, J. C. P. (1969). *Adsorption and capillarity* (Doctoral dissertation, TU Delft, Delft University of Technology).
- Broomfield, J. P. (2002). *Corrosion of steel in concrete: understanding, investigation and repair*. CRC Press.
- Browne R. (1982). Design prediction of the life for reinforced concrete in marine and other chloride environments. *Durability of Building Materials*, 1(2), pp. 113–125.
- Brunauer, S., Emmett, P. H., & Teller, E. (1938). Adsorption of gases in multimolecular layers. *Journal of the American chemical society*, 60(2), 309-319.
- Cabrera, J. G., & Ghoddoussi, P. (1992, October). The effect of reinforcement corrosion on the strength of the steel/concrete bond. In *Int. Conf., Bond in Concrete—from Res. to Pract* (Vol. 3, pp. 10-11).
- Cairns, J. (1998). State of the art report on bond of corroded reinforcement. Tech Rep No. CEB-TG-2/5, CEB.
- Cairns, J., Plizzari, G. A., YINGANG, D., Law, D. W., & Franzoni, C. (2005). Mechanical properties of corrosion-damaged reinforcement. *ACI Materials Journal*, 102(4), 256-264.
- Cairns, J., Du, Y., & Law, D. (2008). Structural performance of corrosion-damaged concrete beams. *Magazine of Concrete Research*, 60(5), 359-370.
- Chan, S. H., Khor, K. A., & Xia, Z. T. (2001). A complete polarization model of a solid oxide fuel cell and its sensitivity to the change of cell component thickness. *Journal of Power Sources*, 93(1), 130-140.
- Chernin, L., & Val, D. V. (2011). Prediction of corrosion-induced cover cracking in reinforced concrete structures. *Construction and Building Materials*, 25(4), 1854-1869.
- Collins, F. G., & Grace, W. R. (1997). Specifications and testing for corrosion durability of marine concrete: the Australian perspective. *Special Publication*, 170, 757-776.
- Cornell, R. M., & Schwertmann, U. (2003). *The iron oxides: structure, properties, reactions, occurrences and uses*. John Wiley & Sons.

- Coronelli, D. (1997). Bond of corroded bars in confined concrete: test results and mechanical modelling. *Studi e ricerche-Politecnico di Milano. Scuola di specializzazione in costruzioni in cemento armato*, (18), 187-211.
- Coronelli, D., Hanjari, K. Z., Lundgren, K., & Rossi, E. (2011). Severely corroded reinforced concrete with cover cracking: Part 1. Crack initiation and propagation. In *Modelling of Corroding Concrete Structures* (pp. 195-205). Springer Netherlands.
- Dagher, H. J., & Kulendran, S. (1992). Finite element modeling of corrosion damage in concrete structures. *Structural Journal*, 89(6), 699-708.
- De Belie, N., Kratky, J., & Van Vlierberghe, S. (2010). Influence of pozzolans and slag on the microstructure of partially carbonated cement paste by means of water vapour and nitrogen sorption experiments and BET calculations. *Cement and Concrete Research*, 40(12), 1723-1733.
- Derluyn, H., Derome, D., Carmeliet, J., Stora, E., & Barbarulo, R. (2012). Hysteretic moisture behavior of concrete: Modeling and analysis. *Cement and Concrete Research*, 42(10), 1379-1388.
- Dong, W., Murakami, Y., Oshita, H., Suzuki, S., & Tsutsumi, T. (2011). Influence of Both Stirrup Spacing and Anchorage Performance on Residual Strength of Corroded RC Beams. *Journal of Advanced Concrete Technology*, 9(3), 261-275.
- Du, Y. (2001). Effect of reinforcement corrosion on structural concrete ductility (Doctoral dissertation, University of Birmingham).
- Duffó, G. S., Morris, W., Raspini, I., & Saragovi, C. (2004). A study of steel rebars embedded in concrete during 65 years. *Corrosion science*, 46(9), 2143-2157.
- El Maaddawy, T. A., & Soudki, K. A. (2003). Effectiveness of impressed current technique to simulate corrosion of steel reinforcement in concrete. *Journal of materials in civil engineering*, 15(1), 41-47.
- El Maaddawy, T., & Soudki, K. (2007). A model for prediction of time from corrosion initiation to corrosion cracking. *Cement and concrete composites*, 29(3), 168-175.
- Elkey, W., & Sellevold, E. J. (1995). Electrical resistivity of concrete.
- Espinosa, R. M., & Franke, L. (2006). Influence of the age and drying process on pore structure and sorption isotherms of hardened cement paste. *Cement and concrete research*, 36(10), 1969-1984.
- Feldman, R. F., & Sereda, P. J. (1964). Sorption of water on compacts of bottle-hydrated cement. I. The sorption and length-change isotherms. II. Thermodynamic considerations and theory of volume change. *Journal of applied Chemistry*, 14, 87-104.

- Feldman, R. F., & Sereda, P. J. (1968). A model for hydrated Portland cement paste as deduced from sorption-length change and mechanical properties. *Materiaux et construction*, 1(6), 509-520.
- Fenaux, M. (2013). Modelling of chloride transport in non-saturated concrete: from microscale to macroscale (Doctoral dissertation, Caminos).
- Fischer, C. (2012). Auswirkungen der Bewehrungskorrosion auf den Verbund zwischen Stahl und Beton. Universität Stuttgart, Institut für Werkstoffe im Bauwesen, Doktorarbeit.
- Foerst, W. (1955). Ullmanns Encyclopädie der Technischen Chemie, Urban and Swarzenberg.
- Funahashi, M. (1990). Predicting corrosion-free service life of a concrete structure in a chloride environment. *Materials Journal*, 87(6), 581-587.
- Gehlen, C., & Banholzer, B. (2000). Time to initiate a corrosion-induced crack after depassivation of the reinforcement. In A. Sarja (Ed.), *International Symposium on Intergrated Life-Cycle Design of Materials and Structures* (pp. 361-366). RILEM Publications SARL.
- Ghods, P., Isgor, O. B., & Pour-Ghaz, M. (2007). A practical method for calculating the corrosion rate of uniformly depassivated reinforcing bars in concrete. *Materials and Corrosion*, 58(4), 265-272.
- Giordano, L., Mancini, G., & Tondolo, F. (2011). Reinforced concrete members subjected to cyclic tension and corrosion. *Journal of Advanced Concrete Technology*, 9(3), 277-285.
- Gjørv, Vennesland and El-Busaidy, 1977: Electrical Resistivity of Concrete in the Oceans. The 9th Annual Offshore Technology Conference in Houston May 2-5 1977, pp 581-588.
- Glass, G. K., & Buenfeld, N. R. (2000). The influence of chloride binding on the chloride induced corrosion risk in reinforced concrete. *Corrosion Science*, 42(2), 329-344.
- Gulikers, J. (2005). Theoretical considerations on the supposed linear relationship between concrete resistivity and corrosion rate of steel reinforcement. *Materials and Corrosion*, 56(6), 393-403.
- Gulikers, J., & Raupach, M. (2006). Modelling of reinforcement corrosion in concrete. *Materials and Corrosion*, 57(8), 603-604.
- Hansen, K. K. (1986). Sorption isotherms: a catalogue (Doctoral dissertation, Technical University of Denmark, Danmarks Tekniske Universitet, Department of Structural Engineering and MaterialsInstitut for Bærende Konstruktioner og Materialer).
- Hansen, E. M., & Kjelstrup, S. (1996). Application of nonequilibrium thermodynamics to the electrode surfaces of aluminum electrolysis cells. *Journal of The Electrochemical Society*, 143(11), 3440-3447.
- Harker, A. H., Sharland, S. M., & Tasker, P. W. (1987). A mathematical model of uniform corrosion of intermediate level radioactive waste canisters in concrete.

- Isgor, O. B., & Razaqpur, A. G. (2004). Finite element modeling of coupled heat transfer, moisture transport and carbonation processes in concrete structures. *Cement and Concrete Composites*, 26(1), 57-73.
- Isgor, O. B., & Razaqpur, A. G. (2006a). Advanced modelling of concrete deterioration due to reinforcement corrosion. *Canadian Journal of Civil Engineering*, 33(6), 707-718.
- Isgor, O. B., & Razaqpur, A. G. (2006b). Modelling steel corrosion in concrete structures. *Materials and Structures*, 39(3), 291-302.
- Jacob, A. (2008). Composite bridge decks cut life cycle costs. *Reinforced Plastics*, 52(9), 30–32.
- Jaffer, S. J., & Hansson, C. M. (2009). Chloride-induced corrosion products of steel in cracked-concrete subjected to different loading conditions. *Cement and Concrete Research*, 39(2), 116-125.
- Jamali, A., Angst, U., Adey, B., & Elsener, B. (2013). Modeling of corrosion-induced concrete cover cracking: A critical analysis. *Construction and Building Materials*, 42, 225-237.
- Kjelstrup, S., & Bedeaux, D. (2008). *Non-equilibrium thermodynamics of heterogeneous systems*. World Scientific.
- Kobayashi, K., & Shuttoh, K. (1991). Oxygen diffusivity of various cementitious materials. *Cement and concrete research*, 21(2), 273-284.
- Koch, G. H. (2002). *Historic congressional study: corrosion costs and preventive strategies in the united states* (No. FHWA-RD-01-156).
- Kranc, S. C., & Sagiüés, A. A. (2001). Detailed modeling of corrosion macrocells on steel reinforcing in concrete. *Corrosion science*, 43(7), 1355-1372.
- Kwiatkowski, J., Woloszyn, M. & Roux, J.J. (2009). Modelling of hysteresis influence on mass transfer in building materials. *Building and Environment*, 44(3), 633–642.
- Lambert, P. (1983). *Corrosion and passivation of steel in concrete* (Doctoral dissertation, Aston University).
- Lambert, P., Page, C. L., & Vassie, P. R. W. (1991). Investigations of reinforcement corrosion. 2. Electrochemical monitoring of steel in chloride-contaminated concrete. *Materials and Structures*, 24(5), 351-358.
- Langmuir, I. (1916). THE CONSTITUTION AND FUNDAMENTAL PROPERTIES OF SOLIDS AND LIQUIDS. PART I. SOLIDS. *Journal of the American Chemical Society*, 38(11), 2221-2295.
- Leech, C., Lockington, D., & Dux, P. (2003). Unsaturated diffusivity functions for concrete derived from NMR images. *Materials and Structures*, 36(6), 413-418.

- Liu, Y. (1996). Modeling the time-to-corrosion cracking of the cover concrete in chloride contaminated reinforced concrete structures. Virginia Polytechnic Institute and State University.
- Liu, Y., & Weyers, R. E. (1998). Modeling the time-to-corrosion cracking in chloride contaminated reinforced concrete structures. *ACI Materials Journal*, 95(6), 675-681.
- Lopez, W., & Gonzalez, J. A. (1993). Influence of the degree of pore saturation on the resistivity of concrete and the corrosion rate of steel reinforcement. *Cement and concrete research*, 23(2), 368-376.
- Lu, C., Jin, W., & Liu, R. (2011). Reinforcement corrosion-induced cover cracking and its time prediction for reinforced concrete structures. *Corrosion Science*, 53(4), 1337-1347.
- Maage, M. A. G. N. E., Helland, S. T. E. I. N. A. R., & Carlsen, J. E. (1995). Practical non-steady state chloride transport as a part of a model for predicting the initiation period. *Chloride Penetration into Concrete, RILEM*, 398-406.
- Maekawa, K., Ishida, T., & Kishi, T. (2008). *Multi-scale modeling of structural concrete*. CRC Press.
- Marsavina, L., Audenaert, K., De Schutter, G., Faur, N., & Marsavina, D. (2009). Experimental and numerical determination of the chloride penetration in cracked concrete. *Construction and Building Materials*, 23(1), 264-274.
- Martin-Pérez, B. (1999). *Service life modelling of RC highway structures exposed to chlorides* (Doctoral dissertation, University of Toronto).
- Maruyama, I., & Igarashi, G. (2010). Mechanism of moisture sorption hysteresis of hardened cement paste. *Cement Science and Concrete Technology*, 64(1), 96-102.
- Mehta, P. K. (1986). *Concrete. Structure, properties and materials*.
- Mertens, S. (2009). *Hysteresis, Damage and Moisture Effects in Quasi-Brittle Porous Materials* (Hysteresis, schade en vocht invloeden in quasi-brosse poreuze materialen).
- Michel, A., Pease, B. J., Geiker, M. R., Stang, H., & Olesen, J. F. (2011). Monitoring reinforcement corrosion and corrosion-induced cracking using non-destructive x-ray attenuation measurements. *Cement and Concrete Research*, 41(11), 1085-1094.
- Michel A., Lepech M., Stang H., & Geiker M (2016). Multi-physical and multi-scale deterioration modelling of reinforced concrete: modelling corrosion-induced concrete damage. *IA-FraMCoS-9* (2016), 9th International Conference on Fracture Mechanics of Concrete and Concrete Structures, San Francisco.
- Molina, F. J., Alonso, C., & Andrade, C. (1993). Cover cracking as a function of rebar corrosion: part 2—numerical model. *Materials and structures*, 26(9), 532-548.
- Morikawa, M., Seki, H., & Okamura, Y. (1988). Basic study on cracking of concrete due to expansion by rebar corrosion. *Concrete Library of JSCE*, 83-105.

- Morinaga, S. (1990). Prediction of Service Life of Reinforced Concrete Buildings Based on the Corrosion Rate of Reinforcing Steel. Proc. of the 5th International Conference on Durability of Building Materials and Components, Brighton, U.K..
- Nakamura H., Khoa T.K., Ueda N., Kunieda M. (2012). Cracking Propagation Simulation of Concrete due to Rebar Corrosion. SSCS 2012 “Numerical Modeling Strategies for Sustainable Concrete Structures”. Aix an Provence – France.
- Naterer, G. F., Tokarz, C. D., & Avsec, J. (2006). Fuel cell entropy production with ohmic heating and diffusive polarization. *International journal of heat and mass transfer*, 49(15), 2673-2683.
- Neville, A. M. (1973). *Properties of concrete*. Pitman, London.
- Newhouse, C. D., & Weyers, R. E. (1996). Modeling the measured time to corrosion cracking. In *Techniques to Assess the Corrosion Activity of Steel Reinforced Concrete Structures*. ASTM International.
- Newman, J., & Thomas-Alyea, K. E. (2012). *Electrochemical systems*. John Wiley & Sons.
- Nielsen, L. F. (2007). Moisture Sorption in Porous Materials: A best fit description from experimental data. *Nordic Concrete Research*, 36(1-2).
- Nürnberg, U. (1995). *Korrosion und Korrosionsschutz im Bauwesen*. Bau-Verlag.
- Ochs, F., Heidemann, W. & Müller-Steinhagen, H. (2008). Effective thermal conductivity of moistened insulation materials as a function of temperature. *International Journal of Heat and Mass Transfer*, 51(3), 539–552.
- Oh, B. H. & Bažant, Z. P. (1983). Crack band theory for fracture of concrete. *Materials and Structures*, January-February, 155–177.
- Oršanić F. (2015). Chemo-hygro-thermo-mechanical model for simulation of corrosion induced damage in reinforced concrete. Dissertation. Stuttgart.
- Osterminski, K., der von der Ingenieur fakultät, V. A., & Umwelt, B. G. (2013). Zur vollprobabilistischen Modellierung der Korrosion von Stahl in Beton: Ein Beitrag zur Dauerhaftigkeitsbemessung von Stahlbetonbauteilen (Doctoral dissertation, Universitätsbibliothek der TU München).
- Ožbolt, J., Li, Y., & Kožar, I. (2001). Microplane model for concrete with relaxed kinematic constraint. *International Journal of Solids and Structures*, 38(16), 2683-2711.
- Ožbolt, J. & Reinhardt, H. (2002). Numerical study of mixed-mode fracture in concrete. *International journal of fracture*, 118(2), 145–162.
- Ožbolt, J., Balabanić, G., Periškić, G., & Kušter, M. (2010). Modelling the effect of damage on transport processes in concrete. *Construction and Building Materials*, 24(9), 1638-1648.
- Ožbolt, J., Balabanić, G., & Kušter, M. (2011). 3D Numerical modelling of steel corrosion in concrete structures. *Corrosion science*, 53(12), 4166-4177.

- Ožbolt, J., Oršanić, F., Balabanić, G., & Kušter, M. (2012a). Modeling damage in concrete caused by corrosion of reinforcement: coupled 3D FE model. *International journal of fracture*, 178(1-2), 233-244.
- Ožbolt, J., Oršanić, F., Kušter, M., & Balabanić, G. (2012b). Modelling bond resistance of corroded reinforcement. *Bond in concrete*, 437-444.
- Ožbolt, J., Oršanić, F., & Balabanić, G. (2014). Modeling pull-out resistance of corroded reinforcement in concrete: Coupled three-dimensional finite element model. *Cement and Concrete Composites*, 46, 41-55.
- Ožbolt, J., Oršanić, F., & Balabanić, G. (2016). Modeling Influence of Hysteretic Moisture Behavior on Distribution of Chlorides in Concrete. *Cement and Concrete Composites*.
- Page, C., Short, N. R., & El Tarras, A. (1981). Diffusion of chloride ions in hardened cement pastes. *Cement and concrete research*, 11(3), 395-406.
- Page, C. L. & Treadaway, K. W. J. (1982). Aspects of the electrochemistry of steel in concrete. *Nature Publishing Group*, 297, 109 – 115.
- Papadakis, V. G. (2000). Effect of supplementary cementing materials on concrete resistance against carbonation and chloride ingress. *Cement and concrete research*, 30(2), 291-299.
- Pedersen, C. R. (1990). Combined heat and moisture transfer in building constructions (Vol. 214). *Thermal Insulation Laboratory, Technical University of Denmark*.
- Polder, R., Valente M., Cigna R. & Valente T. (1992). Laboratory investigation of concrete resistivity and corrosion rate of reinforcement in atmospheric conditions. *TNO Building and Construction Research*.
- Polder, R., Andrade, C., Elsener, B., Vennesland, O., Gulikers, J., Weidert, R., & Raupach, M. (2000). RILEM TC 154-EMC: electrochemical techniques for measuring metallic corrosion. *Materials and structures*, 33, 603-611.
- Polder, R. B., & Peelen, W. H. (2002). Characterisation of chloride transport and reinforcement corrosion in concrete under cyclic wetting and drying by electrical resistivity. *Cement and Concrete Composites*, 24(5), 427-435.
- Poupard, O., L'hostis, V., Catinaud, S., & Petre-Lazar, I. (2006). Corrosion damage diagnosis of a reinforced concrete beam after 40 years natural exposure in marine environment. *Cement and concrete research*, 36(3), 504-520.
- Pourbaix, M. (1966). *Atlas of electrochemical equilibria in aqueous solutions*.
- Poursaee A. (2016). *Corrosion of Steel in Concrete Structures*, 1st Edition. *Technology & Engineering*.
- Powers, T. C., & Brownyard, T. L. (1946). Studies of the physical properties of hardened Portland cement paste. *Bulletin*, 22.

- Prieto Rábade, M. (2014). Estudio de la adherencia de armaduras corroídas y su influencia en la capacidad resistente de elementos de hormigón armado (Doctoral dissertation, Caminos).
- Rasheeduzzafar, Al-Saadoun, S. S., & Al-Gahtani, A. S. (1992). Corrosion cracking in relation to bar diameter, cover, and concrete quality. *Journal of Materials in Civil Engineering*, 4(4), 327-342.
- Rasheeduzzafar, D. F., Bader, M. A., & Khan, M. M. (1992). Performance of corrosion resisting steels in chloride-bearing concrete. *ACI Materials Journal*, 89(5), 439-448.
- Raupach M., Elsener B., PolderR., Mietz J. (2014). *Corrosion of Reinforcement in Concrete: Monitoring, Prevention and Rehabilitation Techniques*. Woodhead Publishing.
- Richard B., Quiertant M., Bouteiller V., Adelaide L., Tailhan J., Cremona C. (2012). Influence of accelerated corrosion on the reinforced cover concrete cracking behavior: experimental and numerical study. *European Journal of Environmental and Civil Engineering*. Vol. 16, Iss. 3-4.
- Rodriguez, J., Ortega, L. M., Casal, J., & Diez, J. M. (1996). Corrosion of reinforcement and service life of concrete structures. *Durability of building materials and components*, 7(1), 117-126.
- Rodriguez, J., Ortega, L., Izquierdo, D., & Andrade, C. (2006). Calculation of structural degradation due to corrosion of reinforcements. In *Measuring, Monitoring and Modeling Concrete Properties* (pp. 527-536). Springer Netherlands.
- Saetta, A. V., Scotta, R. V., & Vitaliani, R. V. (1993). Analysis of chloride diffusion into partially saturated concrete. *Materials Journal*, 90(5), 441-451.
- Sagoe-Crentsil, K. K., & Glasser, F. P. (1993). "Green rust", iron solubility and the role of chloride in the corrosion of steel at high pH. *Cement and concrete research*, 23(4), 785-791.
- Saifullah, M., & Clark, L. A. (1994, July). Effect of corrosion rate on the bond strength of corroded reinforcement. In *Proceedings of International Conference on Corrosion and Corrosion Protection of Steel in Concrete* (Vol. 1, pp. 591-602).
- Sandberg, P., Pettersson, K., Sørensen, H. E., & Arup, H. (1995). Critical chloride concentrations for the onset of active reinforcement corrosion. *Chloride penetration into concrete: proceedings of the RILEM international workshop* (435-439).
- Schiessl, P., & Raupach, M. (1994). Laboruntersuchungen und Berechnungen zum Einfluss der Rissbreite des Betons auf die chloridinduzierte Korrosion von Stahl in Beton. *Bauingenieur*, 69(11), 439-444.
- Sciacovelli, A. (2010). Thermodynamic optimization of a monolithic-type solid oxide fuel cell. *International Journal of Thermodynamics*, 13(3), 95-103.
- Shi, X., Xie, N., Fortune, K., & Gong, J. (2012). Durability of steel reinforced concrete in chloride environments: An overview. *Construction and Building Materials*, 30, 125-138.

- Shreir, L.L.; Jarman, R.A.; Burstein, G.T. (1994). Corrosion (3rd Edition) Volumes 1-2. Elsevier.
- Stansbury, E. E., & Buchanan, R. A. (2000). Fundamentals of electrochemical corrosion. ASM international.
- Stern, M., & Geary, A. L. (1957). Electrochemical polarization I. A theoretical analysis of the shape of polarization curves. *Journal of the electrochemical society*, 104(1), 56-63.
- Suda, K., Misra, S., & Motohashi, K. (1993). Corrosion products of reinforcing bars embedded in concrete. *Corrosion Science*, 35(5), 1543-1549.
- Tang, L., & Nilsson, L. O. (1996). Service life prediction for concrete structures under seawater by a numerical approach. *Durability of building materials and components*, 7(1), 97-106.
- Taylor, G. (1938). Plastic strain in metals. *Journal of the Institute of Metals*, (62), 307–324.
- Tetsuya I, Prince OI, Ho TLA (2009) Modeling of chloride diffusivity coupled with non-linear binding capacity in sound and cracked concrete. *Cem Concr Res* 39: 913–923.
- Thoft-Christensen, P. (2000). Stochastic modelling of the crack initiation time for reinforced concrete structures. Department of Building Technology and Structural Engineering, Aalborg University.
- Thomas, J. J., Allen, A. J., & Jennings, H. M. (2008). Structural changes to the calcium–silicate–hydrate gel phase of hydrated cement with age, drying, and resaturation. *Journal of the American Ceramic Society*, 91(10), 3362-3369.
- Thomas, M. D., & Bamforth, P. B. (1999). Modelling chloride diffusion in concrete: effect of fly ash and slag. *Cement and Concrete Research*, 29(4), 487-495.
- Toongoenthong, K., & Maekawa, K. (2005). Simulation of coupled corrosive product formation, migration into crack and propagation in reinforced concrete sections. *Journal of Advanced Concrete Technology*, 3(2), 253-265.
- Torres-Acosta, A. A., & Martinez-Madrid, M. (2003). Residual life of corroding reinforced concrete structures in marine environment. *Journal of Materials in Civil Engineering*, 15(4), 344-353.
- Torres-Acosta, A. A., Navarro-Gutierrez, S., & Terán-Guillén, J. (2007). Residual flexure capacity of corroded reinforced concrete beams. *Engineering structures*, 29(6), 1145-1152.
- Tuutti, K. (1982). Corrosion of steel in concrete (No. Monograph).
- Tuutti, K. (1993). The effect of individual parameters on chloride induced corrosion. *Chloride Penetration into Concrete Structures*, 18-25.
- Van Den Abeele, K. A., Carmeliet, J., Johnson, P. A., & Zinszner, B. (2002). Influence of water saturation on the nonlinear elastic mesoscopic response in Earth materials and the

implications to the mechanism of nonlinearity. *Journal of Geophysical Research: Solid Earth*, 107(B6).

Vera, R., Villarreal, M., Carvajal, A. M., Vera, E., & Ortiz, C. (2009). Corrosion products of reinforcement in concrete in marine and industrial environments. *Materials Chemistry and Physics*, 114(1), 467-474.

Walton, J. C., & Sagar, B. (1986). A corrosion model for nuclear waste containers. In *MRS Proceedings* (Vol. 84, p. 271). Cambridge University Press.

Walton, J. C., Plansky, L. E., & Smith, R. W. (1990). Models for estimation of service life of concrete barriers in low-level radioactive waste disposal (No. NUREG/CR-5542; EGG--2597). Nuclear Regulatory Commission, Washington, DC (USA). Div. of Engineering; EG and G Idaho, Inc., Idaho Falls, ID (USA).

Wang, K., Jansen, D. C., Shah, S. P., & Karr, A. F. (1997). Permeability study of cracked concrete. *Cement and Concrete Research*, 27(3), 381-393.

Warkus, J., Raupach, M., & Gulikers, J. (2006). Numerical modelling of corrosion—Theoretical backgrounds—. *Materials and Corrosion*, 57(8), 614-617.

Weydert, R., & Gehlen, C. (1999, May). Electrolytic Resistivity of Cover Concrete: Relevance, Measurement and Interpretation. In *Eighth Int. Conf. on Durability of Materials and Components*. Vancouver, Canada.

Wong, H. S., Zhao, Y. X., Karimi, A. R., Buenfeld, N. R., & Jin, W. L. (2010). On the penetration of corrosion products from reinforcing steel into concrete due to chloride-induced corrosion. *Corrosion Science*, 52(7), 2469-2480.

Yokozeki, K., Motohash, K., & Okada, T. T. I. (1997). A Rational Model to Predict the Service life of RC Structures in Marine Environment n Marine. *Special Publication*, 170, 777-796.

Yunovich M., Thompson N. G., Balvanyos T. and Lave L. (2001). Technical Report Documentation Page. Report No. FHWA-RD-01-XXX. Corrosion Cost and Preventive Strategies in the United States.

Zhao, Y., Yu, J., Hu, B., & Jin, W. (2012a). Crack shape and rust distribution in corrosion-induced cracking concrete. *Corrosion science*, 55, 385-393.

Zhao, Y., Dai, H., Ren, H. & Jin, W. (2012b). Experimental study of the modulus of steel corrosion in a concrete port. *Corrosion Science*, 56, 17–25.